A Pore-Scale Network Modelling Study to Explain the Observed Differences Between Steady-State and Unsteady-State Relative Permeabilities

Juan Li

Submitted for the degree of Doctor of Philosophy

Heriot-Watt University

School of Energy, Geoscience, Infrastructure and Society

02-2016

Abstract

It is widely recognized that multiphase flow through porous media – in particular, hydrocarbon displacement – is controlled by the physics, rock network topology and geometry at the pore scale. Indeed, as early as 1937, one of the pioneers of subsurface flow modelling, Maurice Muskat, suggested that "It is necessary to know the pore geometry of a rock before fluid movement through it can be analyzed" (Muskat, (1937)). Since the 1950s, pore scale network modelling (PNM) has been used to investigate a number of issues in the analysis and modelling of multiphase flow through porous media.

Relative permeability is one of the most important macroscopic properties in reservoir simulations that characterise multiphase flow and this is also determined by the microstructure of porous medium (Oren et al. (1998)). The motivation for the work in this thesis is to utilise PNM to resolve or shed light on the differences between steady-state (SS) and unsteady-state (USS) oil/water relative permeabilities. To do this, two models have been developed in this work: (1) an improved quasi-static model based on the *MixWet* model of McDougall and Sorbie in 1990s (McDougall and Sorbie (1994, 1995)) and (2) a novel dynamic model of water imbibition which has been developed entirely in this thesis. Both of these PNM models simulate 2-phase flow in porous media including a more detailed treatment of film flow in the system.

The modified quasi-static model implements angular pores to accommodate the formation and flow of wetting films. A detailed sensitivity study of wettability and some other parameters is conducted using this model. However, such quasi-static models can only examine the capillary dominated flow regimes. The new dynamic pore-scale network model has been developed to study the effect of flow rate and the balance of viscous to capillary forces, in order to understand all of the parameters that affect two phase imbibition processes and hence relative permeability. The dynamic model concentrates on simulating 2-phase displacement during water imbibition by explicitly modelling intra-pore dynamic bulk and film flows. A new dynamic switching parameter, λ, is proposed within this model which is able to simulate the competition between capillary forces and viscous forces under any flow conditions. This quantity (λ) determines the primary pore filling mechanism in imbibition; i.e. whether the dominant force is (i) piston-like displacement under viscous forces, (ii) film swelling/collapse and snap-off because of capillary forces, or (iii) some intermediate

combination of both mechanisms. Indeed, this λ parameter may vary in different pores in different regions of the network in the same displacement. Using this model, the origin of the observed rate-dependency in unsteady-state displacements has been correctly reproduced and explained. Furthermore, this new dynamic network model quantifies the complex relationships between displacement mechanisms and several process controlling parameters of interest. For example, using this dynamic model, the sensitivities to flow rate (Q), viscosity ratio (μ_o/μ_w), pore-size distribution (PSD), wettability state (contact angle θ), pore geometry (pore half angles β), interfacial tension (σ) and initial water saturation (S_{wi}) have all been examined in both 2D and 3D network models.

Our new dynamic model also provides a set of fractional flows and global pressure data, which can subsequently be used to generate unsteady-state relative permeability (USS-RP) curves for any given conditions specified in terms of the above controlling parameters based on Buckley-Leverett theory. Furthermore, similar to the actual experiments, our model can also select a middle section of the dynamic model, record the fluid configurations at some particular instants, and then apply the quasi-static model on this "lifted-out" section to derive the current relative permeabilities. The comparison between these unsteady-state relative permeability curves with the corresponding steady-state RP can help us to understand the observed differences between SS and USS approaches, and study the ways in which these relate to the underlying pore-scale physics of the various processes.

Acknowledgement

I would like to thank my supervisors Doctor Steven McDougall and Professor Ken Sorbie for their constant support, guidance and encouragement during this study. Without their assistance, this work would have not been accomplished.

I would also like to thank my family for their love and support.

Contents

List of Figures

List of Tables

Nomenclature

Roman

A	cross-sectional area (m^2).
$A_{critical}$	area occupied by bulk oil when snap-off occurs (m^2).
A_o	area occupied by bulk oil in the pore centre (m^2).
A_w	area occupied by corner water (m^2).
C_a	capillary number (-).
C_w	flow resistance factor near the pore wall (-).
d	distance a bulk menisci has travelled within a pore (m).
f	fractional flow (-).
F_d^*	Influence of pore geometry and contact angle in capillary entry pressure of piston-like displacement.
$F_d^{snap-off}$	Influence of pore geometry and contact angle in capillary entry pressure of snap-off.
g	conductance ($m^5/(N \cdot s)$).
G	Conductance pre unit length ($m^4/(N \cdot s)$).
G_{shape}	shape factor (-).
k	permeability (D).
k_{rw}, k_{ro}	water relative permeability/oil relative permeability (-).
l	pore length (μm/m).
M	viscosity ratio (-).
n	number of arc menisci/steps (-).
n_x, n_y, n_z	number of pores in each direction (-).
N_p	the volume of oil produced (m^3).
P	pressure (Pa)
P_c	capillary pressure/capillary entry pressure (Pa).
P_{cow}	global capillary pressure (Pa).
ΔP	pressure drop (Pa).
Q, q	volumetric flow rate (m^3/s)
Q_i	total volume of injected water converted into pore volume (PV).
R, r	radius (μm/m).
r_w	Radius of the curvature of arc menisci (m).

R_{asp}	pore aspect ratio r/l (-).
$R_{C\text{-}T}$	the ratio of the circular switch to the triangular switch (-).
$R_{w\text{-}o}$	indicator of film-swelling potential (-).
S	saturation (-).
S_{wi}	initial water saturation (-).
$S1$	A_w / r_w^2 (-).
t	time (s).
V	volume (m^3).
V_p	total pore volume (m^3).
W	fluid hydraulic resistance
W_i	total volume of injected water (m^3).
x	distance (m).
Z	coordination number (-).

Greeks

α	fraction of oil-wet pores (-).
β	corner half angle (degree/radian)
Δ	difference.
μ	viscosity ((N·s)/m^2).
λ	switching parameter (-).
$\bar{\lambda}$	global average switching parameter (-).
σ	interfacial tension ().
θ	contact angle (degree/radian).
ϕ	porosity (-).
δ^{-1}	effective viscosity ((N·s)/m^2).
π	3.1415926…
∇	gradient.
Σ	cross-sectional area of the network (m^2).

Subscripts

1	network inlet.
2	network outlet.

B	bulk.
c	circular.
e-t	equilateral triangular.
F	film.
i, j	property related to node i/j, to pore i/j, or to corner i/j.
max	maximum.
mean	mean.
min	minimum.
nw	Non-wetting
o	oil
pore	whole pore space
s	single-phase
s-t	scalene triangular.
t	triangle
w	water/wetting/wetting film.

Superscripts

0	false
1	true
in	flowing-in.
new	after updating.
old	before updating.
out	flowing-out.
piston-like	piston-like displacement
snap-off	displacement by snap-off

1 Introduction

The study of multiphase flow is important in a wide range of industries and has great scientific, engineering and economic significance; e.g. in aquifer purification, containment of toxic and nuclear waste, geological flows of magma, chemical reactions in catalysts, enhanced oil recovery and the study of blood flow through capillaries (Love et al. (2001)).

In the petroleum industry, reservoir rocks are often flooded with fluids (mainly brine or aqueous chemical solutions but also gas) that displace oil. Important multiphase displacement processes in hydrocarbon reservoirs include (Marle (1981)):

1. In primary production (i.e. pressure drawdown), water from a neighbouring aquifer may encroach into the oil reservoir.
2. Crude oil often contains dissolved gases which may be released into the reservoir rock when the pressure decreases.
3. Many development techniques use the injection of a fluid (typically water or gas) into some wells to displace the oil towards other wells.

Given the complexity of multiphase flow (due to various flow types, complex physical laws, nonlinear mathematical treatment, complex numerical solutions), this issue is still a very active and fertile area of current scientific, engineering and mathematical research (Van Wachem and Almstedt (2003)).

The two most important parameters of multiphase flow are: residual saturations and relative permeabilities (RP). These quantities determine the rate of recovery and the ultimate recovery of displacement processes and hence they are the most important parameters in reservoir simulations (Al-Gharbi (2004)). Generally, ***two*** experimental methods are used to obtain the RP curves of a particular core sample: viz. steady-state (SS) and unsteady-state (USS) core floods. There are several crucial and controversial questions about relative permeability, despite the familiarity of this concept: What is the "correct" experimental method for measuring appropriate RPs for field application? Considering rate-dependency observed in the experiment results, at what rate should these methods be performed? What are the possible causes of the observed difference between steady-state and unsteady-state RPs?

Differences in both fractional flows and total fluid mobilities have been observed within some SS and USS relative permeability data sets. The origins of these differences and the ways in which these relate to the underlying pore-scale physics of the various processes are currently unknown. The specific motivation for carrying out the research described in this thesis is to explain and model observed experimental differences between steady-state (SS) and unsteady-state (USS) oil/water relative permeabilities. The approach used in this work is to apply pore scale network modelling (PNM) to investigate differences between SS (quasi-static or capillary equilibrium) and USS (dynamic) flow regimes during imbibition; i.e. in water displacing oil from model pore networks. These flow regimes are then linked to the macroscopically derived relative permeabilities under both SS and USS flow conditions.

Pore-scale network model is a commonly applied tool to predict the macroscopic transport properties (such as permeability, formation factor, relative permeability, and capillary pressure) from the associated pore-scale parameters. In principle, this prediction should be possible since these macroscopic properties are determined by the microstructure of a porous medium and the physical characterises of the solid and the fluids occupying the pore space. In PNM, the predicting method is appropriately averaging the equations describing the physical processes occurring on the pore-scale (Oren et al. (1998)).

Two PNM models are presented in this thesis; the first is a modified quasi-static model with angular pores and detailed physics to simulate a range of specific wetting film behaviour over a whole displacement cycle (primary drainage, first (water) imbibition, secondary (water) drainage, second (oil) imbibition, and oil drainage). Relative permeability curves resulting from these ***steady-state*** (SS) cycles are presented and analysed.

Secondly, a novel ***dynamic*** pore-scale network model is developed that can simulate 2-phase imbibition displacements incorporating specific intra-pore bulk and film behaviours, *viz.* piston-like displacement, film swelling/shrinking and snap-off, and coupling between bulk and film flow. A new dynamic switching parameter, λ, is introduced in this unsteady-state model that is able to simulate the competition between capillary forces and viscous forces under a wide range of flow conditions. This dynamic model can then provide a set of fractional flows and global pressure data,

which can subsequently be used to generate unsteady-state relative permeability (RP) curves based on Buckley-Leverett theory. A brief outline of the thesis is as follows.

Chapter 2 reviews the related PNM literature to provide a general background on network modelling covering the basic concepts, and the various pore-scale mechanisms that are observed. The current experimental measurements of relative permeabilities and status of steady-state (SS) and unsteady-state (USS) network models are reviewed. And the ways in which such models can be used to generate relative permeabilites and via Buckley-Leverett theory to produce recovery profiles is described.

Chapter 3 starts with a brief introduction of the basic *MixWet* quasi-static model. This describes all aspects of the steady state approach, including the general structure, the displacement cycles that can be modelled, the underlying governing physical laws, the updating of the pressure field and trapping mechanisms. A modified quasi-static model is then presented which uses angular-pores with explicit wetting film behaviours. The resulting relative permeability and capillary pressure curves are compared and a detailed parametric study is carried out examining the impact of system wettability, pore shape, pore size distribution, coordination number and contact angle.

A full description of the new dynamic (USS) imbibition model, including wetting film flow and transport of mobile bulk menisci, is reported in Chapter 4. Detailed algorithms are described to deal with the more complicated fluid configurations, displacement mechanisms and trapping scenarios which arise in the USS model. By introducing and defining a newly proposed switching parameter, λ, this new dynamic model is able to simulate the local competition between capillary force and viscous forces across all flow conditions from ultra-low flows (where capillarity dominates), through the mixed viscous/capillary regime to very high flows rates where viscous forces prevail.

Chapter 5 presents results from a full parametric sensitivity study in 2D networks using the dynamic imbibition model, examining a wide range of variables, especially their influences on the flow regimes. These factors include: the effect of the dynamic switch parameter (λ) itself, flow rate (Q), viscosity ratio (μ_o/μ_w), pore size distribution (PSD), pore-level aspect ratio, interfacial tension (σ), pore shape, wettability/contact angle (θ), initial water saturation (S_{wi}), coordination number (Z) and random seed.

Chapter 6 introduces the Jones and Roszelle method used to analyse the results from the dynamic model to obtain USS relative permeabilities. In line with the corresponding 2D sensitivities, the sensitivity study is also implemented in the 3D network. Resulting USS relative permeability curves from the dynamic imbibition model are compared with the SS relative permeability data sets and it can be concluded that SS and USS relative permeabilities show different sensitivities to the investigated parameters. Another method to derive the steady-state RP curves of the dynamic imbibition is also introduced. The origins of the observed differences between quasi-static and dynamic relative permeabilities obtained by our models are explained.

The final chapter, Chapter 7, discusses the main findings of this thesis and a number of areas for future study are also proposed.

2 Literature Review

2.1 Network Model

In oil reservoir engineering, macroscopic properties such as capillary pressures and relative permeabilities are of great importance, since they are required to facilitate future predictions of oil recovery from a reservoir. However, these quantities are difficult and expensive to obtain and, even when they are measured experimentally, there are a number of associated uncertainties. Indeed, when experiments using rock samples from the actual reservoir are possible, the results may only reflect the flow functions under specific conditions (viscous/capillary ratios). Furthermore, the core scale (cm) is too small compared with the reservoir scale to be representative of larger-scale behaviour. The financial and time costs of experiments also need to be taken into account.

Therefore, more physically based models are needed to understand, simulate and predict multiphase flow behaviour in porous media. Ideally, these models should be based on an understanding of the pore scale fluid displacement physics of the flow process of interest (e.g. waterflooding) since all processes in an oil reservoir ultimately must relate back to this scale. The earliest attempt to calculate flows from the pore scale was done using a network of capillaries. This first pore network model (PNM) for simulating two phase flow behaviours was developed by Fatt in the 1950s (Fatt, (1956a, 1956b, 1956c)). Using the Young-Laplace equation, Fatt filled the pores and throats in a regular 2D lattice in the order of inscribed radius and successfully produced qualitative forms of capillary pressure and relative permeability curves. He confirmed the overall correctness of the model by comparing the results with those obtained experimentally, and also investigated the influence of network structure and pore size distribution.

Since then, especially since the late 1970s when computer processing power became more readily available, the use of pore network models as investigative tools to study multiphase flow from the pore (μm) to core (mm to cm) scale has grown.

2.2 System Structure and Pore Shape Representation

2.2.1 Regular Lattice

The earliest network models, like those of Fatt, were based on regular lattice structures of capillaries. There are several models that are based on a regular lattice, as discussed below.

Jerauld and Salter (1990) studied relative permeability and explained various trends using a cubic lattice network model with circular capillaries. The relative permeability curves they produced matched those observed in experiments, and they concluded that the factors of most importance in governing the relative permeability curves were the size aspect ratio between pore-bodies and throats, the spatial correlation of pore and throat sizes, and the pore size distribution. All of these factors significantly affected the degree of relative permeability hysteresis between flooding cycles, as well as the shape of the relative permeability curves themselves.

McDougall et al. (1993, 1994, 1995, 1997) investigated the impact of wettability and interfacial tension on relative permeability and capillary pressure curves using a quasi-static, pore-scale model on a regular lattice.

Dixit et al. (1997), again using a regular cubic lattice, found the size aspect ratio between pore-bodies and throats had less influence on the relative permeability hysteresis in less connected media. This was because this aspect ratio strongly affected the balance between the number of piston-like and snap-off displacements in imbibition and this in turn affected the degree and type of hysteresis that was observed.

Random networks were also used to better reflect real porous media: randomly distributed points within the model volume were chosen to then construct a network from Voronoi tessellations of the space (Voronoi (1908); Jerauld et al. (1984a; 1984b)). However, according to their later work, Jerauld and Salter (1990), little difference in relative permeability was observed compared to the results from regular networks. Blunt and King (1990; 1991) applied a similar approach to constructed networks, which were used to investigate the influence of capillary and viscous forces on pore-scale displacements.

2.2.2 Network Derived from Real Porous Media

Bryant et al. (1992; 1993a; 1993b) first constructed a network from a real porous medium by extracting it from a random close packing of equally-sized spheres, in which all sphere coordinates had been measured; this was based on the Finney sphere pack, a dense random pack of identical spheres, arguably one of the most homogeneous granular objects (Finney, (1970)). With this network, they showed that spatial correlation between the hydraulic conductivities existed and they successfully predicted permeability. They also showed the significance of using geologically realistic networks when predicting flow behaviours - permeability was over-predicted from a statistically equivalent but uncorrelated network.

In order to reproduce a topologically and geometrically equivalent network based on a real rock, the 3D image of the rock pore space is required. This 3D image can be obtained by computer tomography (CT) imaging of core samples (Dunsmuir et al. (1991); Spanne et al. (1994); Coker et al. (1996)). There are generally two steps of the approach using micro-CT scanning: first a 3D voxel-based representation of the pore space is created (0 indicates matrix and 1 void space) to capture the structure of the "digital rock". Then an equivalent network (in terms of topology, pore volume, throat radii, clay content, *etc.*) is extracted from this initial digital rock. The resolution of the direct image obtained by means of X-ray computed micro-tomography (micro-CT) can be down to a few microns (Dunsmuir et al. (1991)) and even better using a Synchrotron micro-CT (Coenen et al. (2004)).

However, the conflict between the size of the image and its resolution means that the CT scanning may have limited ability to resolve micro porosity, as found in many carbonate reservoirs. Hence, 2D thin section scanning electronic microscope (SEM) images are often used to reconstruct the 3D pore space with reasonable resolution by means of approaches such as process-based modelling (Bryant et al. (1992; 1993a; 1993b); Bakke and Øren (1997); Øren et al. (1998, 2002, 2003)) or stochastic reconstruction (Wu et al. (2006); Okabe and Blunt (2007)). To reconstruct a 3D rock from 2D thin sections, several statistical methods have been developed (Quiblier (1984); Adler et al. (1990); Roberts (1997)). Multi-point statistical methods (Okabe and Blunt (2004, 2005, 2007)), using 2D thin sections as input training images to derive multi-point statistical information, overcame the problem of former methods but failed to reproduce the long-range connectivity of the original pore space. Wu et al. (2006)

developed a much more efficient single scan stochastical reconstruction algorithm based on Markov Chain Monte Carlo (MCMC) simulation.

There are several types of algorithms for network extraction from 3D images of the pore space to topologically and geometrically represent the real rock; for example, such algorithms include medial-axis based (Lindquist et al. (1996); Lindquist and Venkatarangan (1999); Sheppard et al. (2005, 2006); Jiang et al. (2007)), maximum ball based (Silin et al. (2003); Silin and Patzek (2006); Al-Kharusi and Blunt (2007); Dong et al. (2007); Dong and Blunt (2009)), and Voronoi diagram (Bryant et al. (1992; 1993a; 1993b); Øren and Bakke (2003)).

2.2.3 Pore Shape Representation

Pictures of rocks taken from thin sections show that the geometries of pore cross-sections are highly irregular and hence their representation cannot be precise. Considering the efficiency and cost of each simulation, it is necessary to assume an equivalent idealized geometry for each individual pore in order to reproduce the main features of the pore space and make the problem mathematically tractable. Bryant and Blunt (1992) showed that if the structure of the pore space can be modelled accurately, then network modelling can calculate relative permeability semi-quantitatively from first principles (at least for a strongly water wet rock).

Researchers such as Jerauld and Salter (1990), Heiba et al. (1992), Chaouche et al. (1994) have assumed that circular cylinders and spheres can represent the irregularly shape of throats and pores, respectively. However, micromodel experiments (Lenormand et al. (1983)) have shown that in pores occupied by two phases, the non-wetting phase will be found in the pore centre as a bulk occupying phase and the wetting phase is held in the crevices and corners near the pore walls. Dong and Chatzis (1995) also studied the imbibition of wetting phase in corners of a square tube theoretically and experimentally. They concluded that the imbibition rate depended on fluid properties (surface tension, viscosity), the contact angle, and the geometry of the corner (size and the degree of roughness). Therefore, a non-angular circular pore shape (circular cylinder or sphere) has no capacity to accommodate the wetting film, since it can only accommodate one phase at a time.

To represent the presence of wetting films within a pore, a variety of different types of pore shape have been proposed in the literature. These types are squares or rectangles

(e.g. Fenwick and Blunt (1998), Pereira et al. (1996)), triangles (e.g. Bakke and Øren (1997), Hui and Blunt (2000)) and star-shapes (e.g. Kovscek et al. (1993), Man and Jing (1999), Ryazenov et al. (2009)).

2.3 Fluid and Rock Properties

Here we briefly review the fluid/rock properties that will be used in later chapters.

2.3.1 Single-phase Rock/Fluid Properties and Darcy's Law

The viscosity of a fluid is a measure of the (frictional) energy dissipated when it is in motion resisting an applied shearing force. The SI physical unit of dynamic viscosity is the pascal-second (Pa·s), (equivalent to (N·s)/m^2, or kg/(m·s)); the most common unit in oilfield applications is centiPoise (cP); 1cP=10^{-3} Pa·s.

Porosity (ϕ) is the ratio between the void volume and bulk volume of a certain porous material. In an oil reservoir, it represents the fraction of the total rock volume that is capable of accommodating fluids - either liquids or gases.

Permeability (k) represents the conducting capacity of a rock. The SI unit for permeability is m^2. A practical unit for permeability is the Darcy (D), or more commonly the milliDarcy (mD) (1 Darcy $\approx 10^{-12} m^2$).

In many systems, an empirical relationship between permeability, k, and porosity, ϕ, can be determined - higher permeability rocks generally have a higher porosity, although this is not always the case and a k/ϕ cross-plot often exhibits a lot of scatter.

The unit of permeability, Darcy, is in honour of Henry Darcy who pioneered the mathematical description of water flow through a porous medium (Darcy (1856)). The Darcy law originally described single phase flow and related the total volumetric flow rate (Q) of a fluid through a porous medium to the pressure gradient, the properties of the fluid (viscosity μ), and the porous medium (permeability k and cross-sectional area A). The single phase Darcy law is given below and is used to define absolute permeability.

$$Q = -\left(\frac{k \cdot A}{\mu}\right)\left(\frac{\partial P}{\partial x}\right) \qquad 2\text{-}1$$

2.3.2 Multiphase Rock/Fluid Properties and Darcy's Law

The *saturation* of a phase in a porous medium is the fraction of the *pore space* that it occupies; S_w, S_o, and S_g represent the saturation of water, oil, and gas respectively. Multiphase flow properties such as capillary pressure and relative permeability strongly depend on the saturation of specific phases. For example, water saturation can be calculated as:

$$S_w = \frac{V_w}{V_{pore}} \qquad 2\text{-}2$$

where V_w is the volume occupied by water and V_{pore} is the pore volume. In single-phase flow, the permeability k is mainly determined by the network geometry and in particular its degree of interconnectedness. When there are two immiscible liquids present, however, the saturation of one fluid starts to affect the flow of the other and hence the phase permeability of that other phase. Since it occupies a certain fraction of pore volume, the second liquid will effectively reduce the available space for the first to flow. Hence, as phase saturations change, the permeabilities will alter accordingly. This concept was first postulated by Muskat and Meres (1940), and is based upon an extension of Darcy's law to two-phase flow, namely:

$$q_w = -\frac{k_w}{\mu_w}\nabla P_w$$
$$q_o = -\frac{k_o}{\mu_o}\nabla P_o \qquad 2\text{-}3$$

where k_w and k_o are the ***effective*** permeabilities to water and oil at a given saturation. For convenience, k_w and k_o are usually normalised by the absolute permeability (k), i.e. $k_{rw}=k_w/k$ and $k_{ro}=k_o/k$ to give ***relative*** permeabilities. The two Darcy equations consequently take the form:

$$q_w = -\frac{kk_{rw}}{\mu_w}\nabla P_w$$
$$q_o = -\frac{kk_{ro}}{\mu_o}\nabla P_o \qquad 2\text{-}4$$

Two-phase (oil/water) relative permeabilities are usually plotted as functions of water saturation and will depend (amongst other things) upon the interaction between the two

liquids, characterised by the contact angle at the interface and the value of the interfacial tension. Osoba (1951) concluded that relative permeability-saturation relations may vary from formation to formation, and within the different portions of a heterogeneous formation. In studying the performance of a specific reservoir, it is necessary that the relative permeability characteristics of the individual portions of the reservoir are measured. These measurements may be made in the laboratory on small core samples from the reservoir.

Relative permeability is a direct measure of the ability of the porous medium to conduct one fluid when two or more fluids are present. This flow property is the composite effect of pore geometry, wettability, fluid saturation, saturation history, reservoir temperature, reservoir pressure, overburden pressure, rock types, porosity and permeability types (Gawish (2008)).

When two immiscible fluids are in contact with each other, an infinitesimally thin layer called an interface separates them, leading to an interfacial tension (σ) being established between them. Capillary pressure (P_c) is the difference in pressure between these two phases. And, at equilibrium, this pressure differential can be given through the Young-Laplace equation:

$$\Delta P = \sigma(\frac{1}{R_1} + \frac{1}{R_2}), \qquad 2\text{-}5$$

where R_1 and R_2 are the 2 principal radii of curvature of the interface. Hence, the capillary pressure (P_c), defined as the non-wetting (oil) phase pressure minus the wetting (water) phase pressure, and dependent on saturation, can be written as:

$$P_c = P_o - P_w = \sigma(\frac{1}{R_1} + \frac{1}{R_2}). \qquad 2\text{-}6$$

The representation of capillary pressure is affected by the specific pore geometry, and will be described in later sections.

Wettability is a concept relating to rock/fluid interactions, in which one fluid preferentially wets the surface of the solid. Wettability can strongly affect the fluid mobility and configuration and so has great importance in multiphase flow research.

Wettability can be measured through the value of a contact angle (θ), the angle conventionally measured through the liquid, where a liquid/vapour interface meets a

solid surface (Figure 2-1). For a non-zero contact angle, capillary pressure in a pore is given by $\sigma \cdot \cos\theta \cdot (\frac{1}{R_1} + \frac{1}{R_2})$.

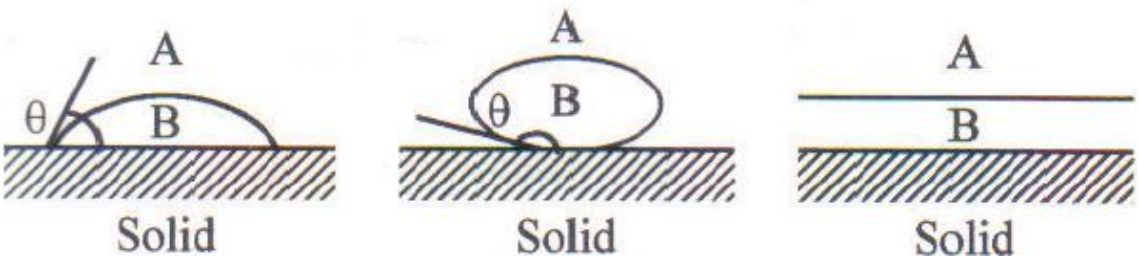

(a) (b) (c)

Figure 2-1 Three possible equilibrium of two fluids (A & B) on a solid surface. (a)- (b) Partial wetting. (c) Complete wetting. After Bear (1972).

Fractional flow of one phase (e.g. f_w and f_o for water and oil flow, respectively) is the volumetric flow rate of that phase (e.g. Q_w and Q_o) divided by the total volumetric fluid flow (Q) under a given pressure gradient, in the presence of another phase, and it depends on the phase saturation; i.e. $f_w = Q_w/Q$ and $f_o = Q_o/Q$ and clearly $f_w + f_o = 1$. Water and oil fractional flows (f_w and f_o) are of great importance in Buckley-Leverett theory which plays a vital role in the calculation of dynamic relative permeabilities, as discussed immediately below.

2.4 Buckley-Leverett Analysis

2.4.1 Theory

Buckley-Leverett theory, proposed by Buckley and Leverett in 1941, is a mathematical theory that describes some of the characteristics of the displacement of oil by a displacing agent (water or gas), and attempts to elucidate the mechanism by which the displacement is effective. The core of this theory is the Buckley–Leverett equation, which is widely used to analyse two-phase flow in porous media. This mathematical equation is derived by starting from material balance and then applying the two-phase Darcy's law to obtain:

$$-(\frac{\partial f_w}{\partial S_w})(\frac{\partial S_w}{\partial x}) = \frac{A\phi}{q}(\frac{\partial S_w}{\partial t}). \qquad 2\text{-}7$$

If the influence of capillary pressure and gravity is neglected, the fractional flow of the displacing phase (water) can be written as

$$f_w = \frac{1}{1 + \frac{k_{ro}\mu_w}{k_{rw}\mu_o}}. \qquad 2\text{-}8$$

Figure 2-2 illustrates the relationship between fractional flow and the Buckley-Leverett theory (S_{wc} is connate (irreducible) water saturation, S_{or} is the residual oil saturation):

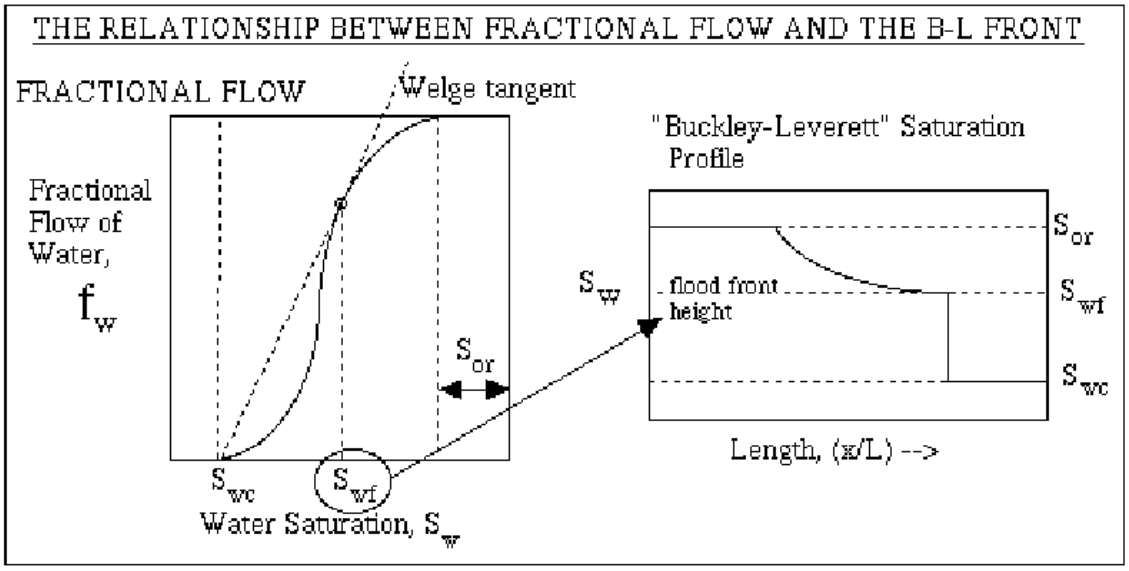

Figure 2-2 Relationship between fractional flow and the Buckley-Leverett theory. After Sorbie (2003).

2.4.2 Calculation of Relative Permeability Using Buckley-Leverett Theory

The methods introduced below are used to calculate individual water and oil relative permeabilities from data obtained during a waterflood experiment, making use of fundamental relationships derived by Buckley and Leverett (1941). All these methods assume the displacing fluid (water or gas) is immiscible with the defending oil, and the effect of capillary pressure and gravity are negligible.

Welge

Welge (1952) proposed an analytical method to compute oil recovery when the oil was displaced from a *linear reservoir* (or one which might be somewhat idealized so that a constant cross-section is exposed to fluid flow) by *an incompressible and immiscible fluid*. Making use of fundamental relationships derived by Buckley and Leverett (1941), the mathematical equations were derived by applying Darcy's law to the flowing phases, and by material balance considerations.

Below are the important equations that were derived in this paper. Near the outlet face of the linear reservoir,

$$\frac{1}{f'_w} = Q_i \qquad 2\text{-}9$$

and

$$\bar{S}_w = \frac{\int_1^2 S_w df'_w}{f'_{w2}} \qquad 2\text{-}10$$

where the subscript *1* and *2* represents the point value of parameters (water saturation or fractional flow) at the inlet or outlet of the 1D system respectively, and Q_i is the total volume of the injected phase W_i converted into pore volume, $Q_i = W_i/V_p$.

The average saturation of displacing phase (water), S_{av}, can be evaluated as:

$$\bar{S}_w - S_{w2} = f_{o2} \cdot Q_i \qquad 2\text{-}11$$

Equation 2-11 readily gives the difference between the average and terminal water saturation, so that only one saturation, the one near the outlet of the sand, need be evaluated for the purpose of calculating oil recovery.

JBN

Johnson et al. (1959) (JBN) developed a method to calculate the individual water and oil relative permeabilities from data obtained during a waterflood experiment. The theory assumes two conditions which must be achieved before the method is applicable. They are: (i) that *the flow velocity be high enough to achieve what has been termed stabilized displacement*, and (ii) that *the flow velocity is constant at all cross sections of the linear porous medium*. In stabilized displacement, the flowing pressure gradient is high compared with the capillary difference between the flowing phases. The high pressure drop insures that the portion of the core in which capillary effects predominate will be compressed to a negligibly small fraction of the total pore space. The assumption of constant flow velocity at all cross sections requires that the phases behave as immiscible incompressible fluids.

Consider a particular instant during a displacement experiment, the oil relative permeability (k_{ro}) can be calculated using the following equation:

$$\frac{d(\frac{1}{W_i I_r})}{d(\frac{1}{W_i})} = \frac{f_o}{k_{ro}} \qquad 2\text{-}12$$

where $I_r = \frac{Q/\Delta P}{Q_s/\Delta P_s}$, and ΔP_s and Q_s are the global pressure drop and flow rate corresponding to this single-phase flooding. And water relative permeability (k_{rw}) can be calculated as

$$k_{rw} = \frac{1-f_o}{f_o}\frac{\mu_w}{\mu_o}k_{ro}. \qquad 2\text{-}13$$

Jones and Roszelle

The method of Jones and Roszelle (1978) is similar to the JBN method (Johnson et al. (1959)) in that it combines the Welge method (Welge (1952)) with pressure drop and flow rate data. However, the Jones-Roszelle method treats data reduction differently. This method uses a graphical approach to data processing which is useful for consistent interpretation of the data. Another unique feature of the Jones and Roszelle contribution is the derivation of the method, which is simpler than those of the Welge and the JBN methods. This method has been used to analyse the results generated by our network model to compute the corresponding dynamic relative permeabilities.

Ignoring gravity effects and capillary pressure, water and oil relative permeability (expressed as functions of saturation) are given by the equations:

$$k_{rw} = \mu_w f_{w2} / \delta_2^{-1} \qquad 2\text{-}14$$

and

$$k_{ro} = \mu_o f_{o2} / \delta_2^{-1} \qquad 2\text{-}15$$

In the above equations, the fractional flow of water or oil, f_{w2} and f_{o2}, and the effective viscosity, δ^{-1}, must be determined as functions of saturation. These quantities must be point values, not averages and the most convenient location for their evaluation is the outlet end of the core because the fractional flow at the outlet is the same as the produced oil or water cut.

The average effective viscosity ($\bar{\delta}^{-1}$) can be calculated as

$$\bar{\delta}^{-1} = \mu_s (\frac{\Delta P}{Q}) / (\frac{\Delta P_s}{Q_s}) \qquad 2\text{-}16$$

where μ_s is the viscosity of the fluid used to find the absolute permeability.

The point effective viscosity at the outlet can be derived as:

$$\delta_2^{-1} = \bar{\delta}^{-1} - Q_i \cdot \frac{d\bar{\delta}^{-1}}{dQ_i} \qquad 2\text{-}17$$

This method will be used by our model to compute the dynamic relative permeabilities in Chapter 6. Clearly, the assumptions in the above simple models – principally on the capillary pressure being negligible – are not good ones for a pore network level calculation. However, in some cases below we will use the mathematical formalities and analysis from such assumptions in order to obtain *effective* relative permeabilities from our network model calculations. For most calculations, it is the Jones and Rozelle method that is used but some further discussion using alternative approaches are also presented below.

2.5 Previous Network Modelling Approaches

2.5.1 Steady-state and Unsteady-state Experimental Background

Measuring relative permeability requires experimental techniques and data reduction skills. Of the experimental methods to date, some have simpler data reduction procedures but are challenging to implement, while those that are less challenging to perform often require detailed data reduction procedures. In general, the experimental methods to measure the relative permeabilities can be categorized as steady-state or unsteady-state methods, based on whether fluid saturations are constant (steady-state) or changing (unsteady-state) during the measurement period (Christiansen and Howarth (1995)).

Steady-state (SS) two phase flow experiments are characterised by simultaneous injection of two phases (e.g. water and oil) at a fixed ratio and known flowrates (Q_w and Q_o). If the inlet and outlet fluxes of each phase have equilibrated, and hence a constant pressure drop has developed across the core, steady-state conditions are reached. Darcy's law is then applied to each phase separately and a pair of relative permeability

values will be found for that particular saturation. The fluid flux ratio is then changed (whilst keeping the total flowrate constant), yielding a second set of data once a new steady-state has been achieved. Repeating this similar measurement for a number of different flux ratios, a set of relative permeability curves spanning the entire saturation range can be obtained. To reach one equilibrium state may take many hours or even days, depending upon the experiment material type and the measurement technique. Thus the time taken to reach equilibrium in each experiment is a serious concern for steady-state measurements.

In unsteady-state experiments, one phase is directly injected into a sample to displace the defending phase, usually at a rate enough high to make capillary pressure effects negligible. Then, the resulting production data can be analysed using Buckley-Leverett frontal advance theory to yield the relative permeability curves of both phases. This is much faster than the steady-state measurement, but the management of the resulting data is more complex, indirect and more open to a certain degree of ambiguity.

Sorbie and Salino (2009) showed systematically how two phase flow could become successively more complex. And during the process, they identified clear cases where both SS and USS RPs should be identical and show no rate dependency, through to where they would not be identical and could in principle show different rate dependencies. The three principal sources of complexity that had strong bearing on relative permeability rate dependency are two phase physics including capillarity, heterogeneous core structure and distributed wettability. In the case when only purely viscous forces were present (no capillarity) and the system was 1D and homogeneous, there would be no difference between a steady-state and an unsteady-state numerical or physical experiment and the resulting relative permeabilities.

Rapoport and Leas (1953) reported that capillary end effect and viscous fingering were two main causes of the observed differences between SS and USS relative permeabilities. In order to minimize capillary end effects, laboratory tests to measure these parameters were often carried out at high rates. And according to Odeh and Dotson (1985), the rates were significantly higher than typical reservoir displacement rates and in applying the measurements to reservoir conditions it was assumed that relative permeability and residual saturation were independent of displacement rate. According to the review of Nguyen et al. (2006), the assumption that relative permeability was independent of rate might be valid for drainage displacements but for

imbibition displacements, it might not be the case. Some authors reported that laboratory imbibition relative permeabilities were independent of rate after accounting for capillary end effects. While other authors concluded that displacement rate was important.

Skauge et al. (2001) questioned if high rate floods, by reducing the influence of capillary pressure, was sufficient to explain the rate effect and reported unexpected effects of flow rates on displacements in intermediate wet cores. They concluded that even when capillary end effect was avoided, relative permeabilities calculated analytically from unsteady state measurements were still influenced by capillary pressure and therefore gave underestimates. They also recommended the use of low flow rate and inclusion of capillary pressure in estimation of relative permeability as the best approach to obtaining data for intermediate wet cores.

Maini et al. (1990) studied experimental measurements of RPs in heavy oil systems. They observed that with minimized capillary end effects, at high flow rates, viscous fingering effects appeared in heavy-oil systems and also had influence on the relative permeabilities. The current techniques (history matching or techniques based on Buckley-Leverett theory) were based on the assumption that the displacement was stable, with the fluid saturations at any cross section perpendicular to the direction of flow were uniform. However, in heavy oil systems, the displacement was often characterized as viscous fingering and highly unstable, which violated one of the most important assumptions of these unsteady-state measurements – the uniform saturation distribution. In practice, this conflict with theory was often ignored. Maini et al. also reported that in light oil systems, there appeared to be good agreement between relative permeabilities measured by the steady-state method and those obtained by the unsteady-state technique. While in viscous oil systems, the two techniques provided different results and the unsteady-state relative permeabilities showed rate dependency due to the viscous fingering effect at high flow rate and capillary end effects at low flow rate.

In the early 1980's, as computers became more powerful, a history-matching approach for processing unsteady-state data evolved. Consequently, new experimental methods evolved with reduced laboratory fluid injection rates which more closely replicated in situ flow rates. At low flow rates, many of the historical concerns about unsteady-state experiments (for instance, wettability changes, fines migration, and emulsion generation) became less important. On the downside, however, capillary end effects

became important and must be properly included in the history matching process at low flow rates (Christiansen and Howarth (1995)). Worse still, the history matching technique did not assure the uniqueness of the solution (Kikuchi et al. (2005)).

Furthermore, unsteady-state measurements only provided RP data after water breakthrough, which limited the water saturation range of the obtained relative permeability curves. Especially in the high-rate unsteady-state measurements for light-oil systems, where both capillary end effects and viscous fingering effects were minimized, the breakthrough occurred when oil saturation was near to the residual value and the obtained relative permeability curves could only provide information within a narrow S_w range (Kikuchi et al. (2005)).

One important feature of steady-state process was the ability to provide relative permeability information for water saturations below unsteady state water breakthrough. According to Kikuchi et al. (2005), unsteady-state simulations were usually performed with interpolated data before water breakthrough, and this interpolated curve might differ from the steady-state curve even when the end points were adjusted to be the same.

There was a great deal of controversy over which method provided data which best represented reservoir process. Unsteady-state measurements were often favoured because of the simplicity of the tests and lower costs compared to steady-state measurements. Measuring relative permeabilities at reservoir conditions often meant operating at high pressures and high temperatures, with fluids sampled from the reservoir or blended to closely resemble reservoir fluids, and with confining or overburden pressures applied to the rock sample. Given these extra experimental complications, the simpler methods for measuring relative permeability were greatly favoured. Thus, the steady-state high-rate method, and the unsteady-state high-rate method had been used more frequently for measurements at reservoir conditions (Christiansen and Howarth (1995)). Some oil operators had a rather specific "company view" on what the "correct method" was for measuring RP for field applications e.g. a large project was active within BP gathering together RP data for field specific purposes mostly using USS low flow rate floods, but sometimes this USS data was supplemented by SS RP measurements. SS floods were usually carried out at a "high" flow rate, but some limited SS data at "low" flow rates was also available. Exxon-Mobil believed that high rate SS RP measurements were "correct" and that these could be supplemented by

some centrifuge measurements to obtain the lower values of k_{ro} (Sorbie and Salino (2009)).

The models described below attempt to simulate fluid behaviour during either steady-state or unsteady-state experiments.

2.5.2 Quasi-static Models

In quasi-static models, capillary pressure is the dominant force and the positions of all fluid-fluid interfaces can be determined at each stage of the displacement. Quasi-static models can be considered as extensions of simple percolation models with drainage floods being modelled through invasion percolation and imbibition through adapted bond percolation. In invasion percolation drainage models, the invading fluid fills a pore or throat in order of its size (more strictly in order of its increasing capillary entry pressure – which may involve wettability through the contact angle). The pore element to be filled in these models must be connected to an element that is already filled with the invading fluid (and therefore connected ultimately to the inlet).

Jerauld and Salter (1990) studied the effected of pore-structure upon two-phase relative permeabilities and capillary pressure of strongly-wetting systems at low capillary number. They built a network of spherical pore-bodies connected by cylindrical tubes. And a central conclusion of their work was that the pore-body to pore-throat aspect ratio strongly affected the pattern of hysteresis between primary drainage, imbibition and secondary drainage. Conversely, the width and shape of the pore-size distribution had little influence.

A succession of models have been proposed by Blunt and coworkers: firstly using a tubes (cylindrical throats) and chambers (spherical nodes or pores) model, (Blunt et al. (1992)), then modelling a granular pore space as an array of wide pores connected by narrow throats (Blunt et al. (1995, 1997a, 1997b)) (Figure 2-3), and finally a network that has 3-D voxel representation of Berea sandstone as its basis (Blunt et al. (2002), Valvatne, (2004)).

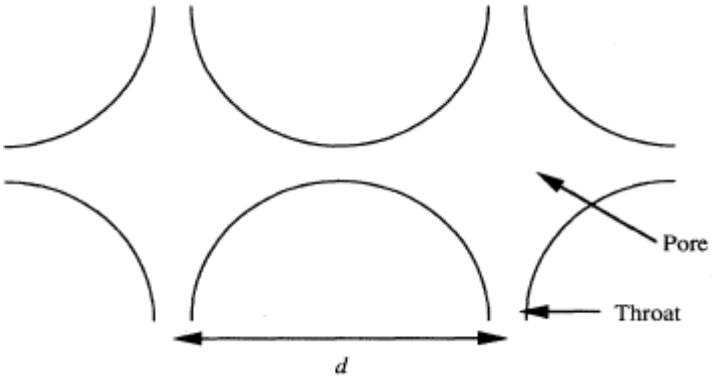

(a)

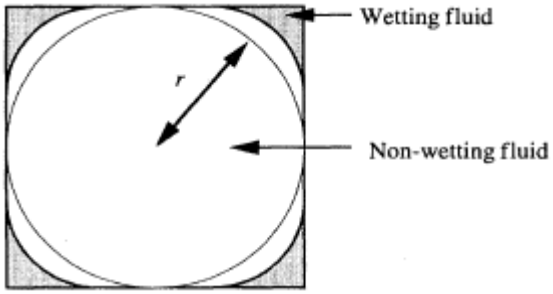

(b)

Figure 2-3 Illustration of a porous medium.
(a) Wide pores are connected by the narrow throats. (b) the pores and throats are assumed to have angular cross-section. (Blunt et al. (1995))

Using the first approach, Blunt et al. (1992) verified percolation-theory results for the effects of buoyancy forces on trapped saturations, derived an expression for the correlation length in displacements perturbed by viscous forces, and concluded that the relative permeabilities measured in quasi-static system at capillary equilibrium are meaningful in viscous-force predominating large-scale displacements. They also tried to simulate the rate-dependent competition between bulk filling and snap-off in imbibition.

Using square elements for both pores and throats, Blunt et al. (1995, 1997a, 1997b) showed that it was possible to simulate specific wetting layers and develop capillary pressure expressions for the different filling events. In a similar approach to that of Kovscek et al. (1993), multiple wetting conditions were allowed to exist within each element, with the corners remaining water-wet while the centre of the pore could become oil-wet. The effects on relative permeability from a wide range of wetting conditions were investigated and results were generated for a variety of advancing and receding contact angles and various oil-wet fractions of the pore space, P_c, RP and residual saturation plots were presented.

Valvatne (2004) successfully predicted flow properties for several porous media, and recognized the importance of wettability on multiphase properties.

Dixit et al. (1998; 1999; 2000) used the same simple quasi-static network model as McDougall et al. (1994, 1995), based on a regular lattice of cylindrical pores connected by volumeless nodes, to introduce a wettability classification system. This system related oil recovery in mixed-wet systems to aging and α, the fraction of oil-wet pores. They also developed analytical expressions to describe the relationship between different wettability indices and different mixed-wetting scenarios. It was suggested that if experimental capillary pressures were available for different flooding cycles, it should be possible to determine whether oil-wet pores were correlated to pore size or just randomly distributed.

Øren et al. (1998) reconstructed 3-D models which realistically described the complex pore space observed in actual sandstones. The predicted transport properties for their model were in good agreement with available experimental data. They also derived general relationships between pore structure, wettability, and capillary pressure for the different pore level displacement mechanisms.

Man and Jing (1999, 2000, 2001) developed a model in which tubular rods were stuck together to form a cubic lattice. The pore cross-section is the star-like grain boundary pore (GBP) shape, which allowed simulation of the generic behaviour of sandstone rocks, with various wetting scenarios. Their results were in close agreement with electrical resistivity and capillary pressure characteristics observed in experiments.

Ryazanov et al. (2009, 2011, 2014) developed a new two-phase flow pore network model, including the new thermodynamically derived criterion for oil layers existence in the pore corners with non-uniform wettability cause by ageing, which was obtained by van Dijke and Sorbie (2006). This model also included two versions of the geometrical criterion (pore shape approximation and oil layers collapse criterion): the conventional geometrical criterion and the new thermodynamically derived criterion for the existence of oil layers introduced above. The network model took as input networks extracted from pore space reconstruction methods or CT images. Furthermore, a new n-cornered star shape characterization technique has been implemented. A number of sensitivities of the residual oil saturation (S_{or}) and relative permeabilities with respect to wettability conditions have been carried out.

2.5.3 Dynamic Models

Under dynamic conditions, the displacement was controlled by both viscous and capillary forces. Based on different conditions, transient behaviour of multi-phase flow could be studied using dynamic pore-network models. Clearly, to simulate the dynamic displacements, much more complicated coding, robust solution methods, and efficient algorithms were required in these models. Problems of numerical convergence and instabilities might cause major difficulties, and the highly non-linear nature of the coupling between viscous forces and capillary forces meant these simulations were much more time-consuming and memory demanding (Joekar-Niasar et al. (2012)).

Mohanty and Salter (1983) developed a pore-level, 3D network model (ignoring wetting film and snap-off) to calculate transverse dispersion and residual oil saturation at high capillary number floods in strongly wet media. They also computed capillary pressure, relative permeability, and mixing parameters in mixed wet media. The results from their model illustrated the effect of wettability on transport properties of a rock.

Lenormand and Zarcone (1984) studied the different flow mechanisms which occurred in an experimental network model constructed with square cross-sectional straight ducts. They assumed that the wetting fluid flowed in the corners and surface roughness of the ducts while the non-wetting fluid occupied the centre of the duct. The purpose of their study was to describe and study the physical mechanisms during the imbibition process at different flow rates. They concluded that for very small capillary numbers (i.e. very low flow rates), the wetting phase flows through the surface roughness and is connected throughout the network. The dominant displacement mechanism of this flow type is snap-off, which results in considerable trapping of the non-wetting fluid. At higher capillary numbers, they observed that, although the wetting fluid was again flowing through corners and roughness, the roughness flow was negligible and the dominant displacement mechanism is pore body filling with some trapping of non-wetting phase. Piston type displacement mechanisms dominate at high capillary numbers, where the wetting phase is flowing in the bulk of the duct displacing the non-wetting phase without any trapping or fingering.

Koplik and Lasseter (1985) used approximate solutions of the Navier-Stokes equations for two-phase flow calculation to study how the microscopic geometry of a pore space affects the macroscopic characteristics of fluid flow in porous media. In their model, pore size, connectedness and wettability are distributed arbitrarily. In their calculation,

Stokes flow results and the Washburn approximation are used to calculate the motion of the individual fluids and microscopic capillary force respectively. The model is restricted of hundreds of pores in 2D due to the scale of the computation. They showed how to calculate the pressure drop along a throat for the case where one or more menisci are present in the pores or the throat connecting them. A similar approach was taken by Chen and Koplik (1985) using a modification of Poiseuille's law for throats of rectangular cross section.

A pore-scale network model was introduced by Dias and Payatakes (1986a, b) to study water flooding for a range of capillary numbers and viscosity ratios. Their network consisted of unit cells of converging-diverging geometry, where the pore walls between the pore centres were assumed to vary sinusoidally. They concluded that the micro-displacement was determined by capillary number and viscosity ratio. At high capillary number and favourable viscosity ratios (oil less viscous than water), the displacement was piston-like and the residual saturation was low. However, at low capillary number and unfavourable viscosity ratios the displacement was ramified and the residual saturation high. They also first simulated the ganglion motion by investigating the effect of stranding, break-up, coalescence, and shape of ganglia for both favourable and unfavourable viscosity ratios. The issue of collision and coalescence of non-wetting ganglion clusters was further addressed in a paper by Constantinides and Payatakes (1991), who used a film drainage model to estimate the time scale for the two processes.

Touboul et al. (1987) compared the results of physical and stochastic network simulators with experiments in micromodels and obtained good agreement between experimental and simulated patterns for several viscosity ratios and capillary numbers (both varied independently over several orders of magnitude).

Lenormand et al. (1988) simulated the dynamics of drainage on 100*100 2-D networks and three basic domains: capillary fingering, viscous fingering, and stable displacement, within which the fluid patterns remained unchanged. They also noted that by including capillary pressure, the system of equations used to solve the pressure at each node became non-linear. Whereas previously reported work (Koplik and Lasseter (1985); Chen and Koplik (1985)) consisted of replacing the nonlinear problem with a sequence of linear problems, Lenormand et al. (1988) again chose to approximate directly the solution to the non-linear problem, using a relaxation technique.

Blunt and King (1991) developed a dynamic two-phase model of drainage, in which pressure drops were calculated numerically using a successive over-relaxation technique. In their model, all the fluid is considered to be contained in the pores and the throats are assumed to be the volumeless connections between pores. This model was mainly used to investigate the effect of viscosity ratio and capillary pressure on pore-scale displacements in both 2D and 3D networks, as well as studying the influence of microscopic flow physics on centimetre-scaled averaged properties. In their model, they used up to 80,000 circular or spherical pores that are connected by non-intersecting straight throats. Across the two-phase interface, the capillary pressure was assumed to be inversely proportional to the throat radius and could be neglected in the pores due to their wider radius. In addition, they considered that the throats were totally filled with one fluid, whilst the pores could contain both fluids. Their simulations showed that drainage relative permeability was a function of both viscosity ratio and capillary number. Chaouche et al. (1994) and Haghighi et al. (1994) developed a dynamic network model similar to the one of Blunt and King (1991) to study drainage in heterogeneous media. Later, Blunt and Scher (1995) extended the model, where pores and throats were modelled as cubic or square shapes to account for wetting layer flow with an assumed constant conductance. They introduced a dimensionless crevice resistance factor α (the ratio of bulk flow in an element to the crevice flow). This parameter in combination with the capillary number was found to have a major influence on the wetting behaviour: when αC_a is of order 0.001, an increase in flow rate led to decrease in the trapped oil saturation.

Hughes and Blunt (2000) studied the effects of flow rate, contact angle and initial wetting phase saturation on imbibition relative permeability curves using a network with irregular pore shapes (square and equilateral triangular) to account for wetting layer flow. In this model, wetting layers were assumed to have a fixed conductance (therefore film swelling was prevented) and pores and throats were filled one at a time without simultaneous filling. They assumed that the non-wetting phase pressure gradient was negligible and so the sorting pressure could be used as the inlet pressure necessary to fill the element. The sorting pressure, controlled by fluid configurations, was periodically recomputed during the displacement. This model was essentially quasi-static with a perturbative rule to include rate effects and was only valid for relatively low flow rates.

Idowu (2009) presented a new method to generate stochastic random networks representing the pore space of various rock samples with given input pore and throat size distributions and connectivity from an analysis of pore-space images, which could be arbitrarily large and hence were not limited by the size of the original image. This network model was rate-dependent that accounted for viscous forces in the similar fashion as Hughes and Blunt (2000) - the local viscous pressure drop was included into the P_{global} of each element, which was used for ranking of all elements for displacement events; but this model allowed film swelling near the advancing flood front and proposed a new time-dependent algorithm by accounting for partial filling of elements (only by film-swelling, the moving bulk menisci were not simulated explicitly). The model was used to study the effects of capillary number and mobility ratio on imbibition displacement patterns, saturation and velocity profiles; as well as the water fractional flow curve, cumulative oil production and residual oil saturation for water-wet and mixed-wet systems.

Vizika et al. (1994) published a theoretical and experimental study that investigated the effect of the viscosity ratio on immiscible, forced imbibition, over a wide range of capillary numbers. The model that they used was akin to the one developed by Dias and Payatakes (1986a, b), and was extended to two layers in order to account for the non-planarity of real porous rocks. They modelled the pore space of the permeable medium as a network of spherical pores, with wall profile to be sinusoidal, connected through long cylindrical throats. With other parameters constant, they observed that the residual oil saturation increased with increasing network size. They reported that at high capillary number, the role of viscosity ratio was very important: in the case of unfavourable viscosity ratio, the wetting fluid was forced into the non-wetting fluid as long micro-fingers and leaving large parts of non-wetting fluid trapped; while many oil ganglia became mobilized. On the contrary, when viscosity ratio was less than one, high micro-displacement efficiency was obtained due to the relatively smooth displacement front. Meanwhile, at low capillary number, unfavourable viscosity ratios case, viscous micro-fingers appeared promptly and lead to high values of residual oil saturation and ganglion mobilization could be observed. In the case of viscosity ratios less than unity and low capillary number, the residual oil saturation was quite high due to the capillary micro-fingers caused by capillary forces. Valavanides et al. (1998) extended the pore-scale model used by Vizika et al. (1994) to account for the ganglion dynamics flow regimes. Then the model was extended again by Valavanides and

Payatakes (2001) to include the drop-traffic flow (DTF) and connected pathway flow (CPF) mechanisms.

An unsteady-state pore-scale process simulator, developed by McDougall et al. (1997), was used it to interpret a number of related laboratory gas-oil displacements performed at different values of interfacial tension, IFT. All of the experimental data, including the oil/gas viscosity ratio, *M*, was available to them as a function of IFT. This model was a 3-D lattice network with circular cylinder pore elements, applying the Rayleigh (truncated normal) pore-size distribution. Both constant rate and constant pressure drop simulations were carried out using this model. Poiseuille's law and a modified Jones and Roszelle technique were used to determine the conductivity of each pore and to analyse the production data respectively. The unsteady-state simulator calculates a net capillary entry pressure for each pore considering the viscous pressure drop across the corresponding pore. By doing this, they were able to reproduce a number of flow regimes (e.g. piston-like displacement, capillary fingering, and viscous fingering) given the particular fluids properties and experiment conditions. The calculated relative permeabilities were found to exhibit the same IFT sensitivities as the experimental datasets. They also found that both capillary number and viscosity ratio played a role in determining the phase distribution during a displacement. Comparing with the dynamic model developed in this work, their dynamic model concentrated on drainage. And with the treatment of using a net capillary entry pressure considering viscous pressure gradient, it was actually a transitional model between quasi-static model and dynamic model. Furthermore, the circular cylinder pores they used limited the ability of this model to simulate explicit wetting film behaviours.

Similar technique of including the local viscous pressure gradient into a net capillary entry pressure was also implemented in the model of Bondino et al. (2011). This model was used to simulate heavy oil depletion experiments at different capillary numbers and depletion rates. Three regimes of bubble growth were identified: (a) the conventional P_c-controlled growth under low C_a, (b) viscous biased growth at intermediate C_a, and (c) bubble mobilization and breakup leading to foamy behaviour at the highest capillary numbers and depletion rates. Gas relative permeabilities and critical gas saturations, associating with these three regimes, were also proposed.

Van der Marck et al. (1997) developed a dynamic model to simulate two-phase drainage flow, subject to three forces: capillary, viscous and gravity. A geometry that resembles

the shape of etched channels (throats) used in the micromodel experiments was introduced into their model. They allowed up to two interfaces to be present between the pore centres. The simulation results were compared with micromodel experiments on saturation and global pressure drop, agreements was obtained except for a high rate, high viscosity ratio case.

A study investigating some of the dynamic phenomena of capillary fingering and viscous fingering was published by Aker et al. (1998). In this study, they simulated primary drainage in a two-dimensional lattice of throats and volumeless pores (i.e. the pore was just a joining point) and film flow was neglected. Local capillary pressure was used to update the pressure in each pore. They performed three types of simulation, where the behaviour of the global capillary pressure and the pressure across the system are discussed qualitatively in terms of three regimes of viscosity ratio, viz. viscous fingering, stable displacement and capillary fingering. Later, the model was extended to study the viscous stabilization of the invasion front (Aker et al. (2000)) and the relation between pressure, saturation and fractional flow (Knudsen et al. (2001), Knudsen and Hansen (2002)).

Dahle and Celia (1999) developed a similar dynamic pore-scale model as the one developed by Aker et al. (1998). In their model, the capillary pressure for a cylindrical tube was given by the Young-Laplace equation, which means that the net capillary force was considered to be zero if two interfaces co-exist in a throat. In addition, they allowed ganglion movements although only one interface was allowed to move in a single throat at any time. The $P_c - S$ curves for drainage were studied based on both the pressure drop over the network and on the internal average phase pressures. They found that the $P_c - S$ curves based on both the global pressure drop and on the internal average phase pressures were in good agreement as long as most of the wetting fluid is connected to the outlet. However, at low wetting phase saturation the wetting phase was represented in the network as ganglia. Therefore, the $P_c - S$ curves defined by reservoir pressure and phase pressure were not the same. The model was extended to study interfacial area and its relation to capillary pressure (Held and Celia (2001a)) and interfacial velocity (Nordhaug et al. (2003)).

Mogensen and Stenby (1998) presented a dynamic pore-scale model of imbibition including wetting layer flow. The effect of viscosity ratio, contact angle, aspect ratio and capillary number on residual oil saturation was investigated in this model. Snap-off

was assumed to happen if $\frac{r_{throat}}{r_{pore}} < \frac{1-\tan\theta\tan\beta}{2f}$, where β is a corner half angle and f is a geometry factor, which showed that the snap-off process was controlled by aspect ratio. They applied an iteration loop for calculating fluid pressures before the displacement simulation. Then the time step was chosen as the minimum time required for a snap-off or a piston like displacement mechanism to occur in a single pore or throat. They concluded that the capillary number, aspect ratio and contact angle all have a significant influence on the competition between piston like advance and snap-off. Snap-off was the dominant mechanism for capillary numbers in range $10^{-8} - 10^{-7}$.

Singh and Mohanty (2003) developed a rule-based dynamic model to simulate two-phase drainage, with film flow incorporated in a novel way. They used a cubic network with cubic bodies (pores) and square cross-section throats. The rules for phase movement and redistribution were based on the pressure field of the network that was solved by applying mass conservation at each node. A pseudo-percolation model was proposed for low but non-zero capillary number (ratio of viscous to capillary forces). The model was used to study primary drainage with constant inlet flow rate and constant inlet pressure boundary conditions. Non-wetting phase front dynamics, apparent wetting residuals (S_{wr}), and relative permeability curves were computed as a function of capillary number (C_a), viscosity ratio (M), and pore-throat size distribution. The displacement front shows three distinct flow regimes—stable, viscous fingering and capillary fingering, given the flow rate and viscosity ratio. S_{wr} - C_a curves depend on the viscosity ratio. It is shown that at high flow rates (or high C_a), relative permeability assumes a linear dependence upon saturation. Pseudo-static capillary pressure curves were also estimated (by using an invasion percolation model) and they were compared with the dynamic capillary pressures obtained from the model. The simulation results are compared with experimental results from the literature.

Al-Gharbi (2004) developed a network with scalene triangle as the cross-section of pores and throats, while the inscribed radius of each element varied sinusoidally. Al-Gharbi's model could predict events such as swelling of the wetting layers, snap-off and meniscus oscillations. They showed that the fraction of disconnected oil flow to overall oil flow is insignificant in primary drainage but has a significant influence in imbibition even at typical reservoir flow rates. Their model was able to predict the trend in relative

permeability and residual oil saturation with capillary number and reproduce the displacement patterns observed in micromodel experiments.

Nguyen et al. (2006) proposed a dynamic network model for imbibition based on a physically realistic description of the complex dynamics of film flow, film swelling and snap-off. The model showed that film swelling was a capillary driven nonlinear diffusive process and that the competition between snap-off and piston-like displacements and resulting relative permeability curves as well as residual saturations were rate dependent. Other than contact angle, their model introduced displacement rate as another mechanism that inhibited snap-off. The complex interaction between relative permeability and displacement rate, contact angle, aspect ratio and pore/throat shapes were analysed by this model. Resulting relative permeabilities and residual saturations were compared with experimental data for strongly water-wet Berea sandstone. They concluded that the magnitude of the relative permeability rate-dependency for a particular rock and wetting state determined largely by the aspect ratio - higher aspect ratios produce larger rate effects than smaller aspect ratios.

Joekar-Niasar et al. (2012) reviewed the dynamic models to date, which focused on their computational aspects and application in investigating dynamics of two-phase flow: geometrical and topological properties of the network, simulation process, and the computational algorithms were reviewed in details, with discussions about the advantages and disadvantages of each model. They explained the possible causes of the less applications of dynamic models compared with the quasi-static pore-scale models: strong numerical instability and tractability, computational costs, limited verification possibility in a 3-D domain, complexities of physics at pore level, and difficulties in casting the pore-level physics into network models.

2.6 Summary and Conclusions

In this thesis, we describe two pore-scale models: a quasi-static model of the whole two phase displacement cycle, and a dynamic model of imbibition (water injection). In this section, we will summarize the methods we have employed in these two models which are related to the reviewed literature, and we discuss the improvement which have been made in our work.

2.6.1 Quasi-static Model

Our modified quasi-static model is based on the *MixWet* model of McDougall et al. (1994, 1995). Hence, many features of the *MixWet* model (such as the model structure, main displacement mechanisms, method to update the pressure field, and trapping algorithm) are shared by the new model. In the *MixWet* model, the porous medium was represented as a network of cylindrical pores with circular cross-sections. However, in order to simulate explicit bulk and film behaviour, triangular pore shapes are included in our new quasi-static model which may be occupied by two phases simultaneously.

As triangular geometries are introduced into the framework of our new models, changes in saturation, conductance, and capillary pressure formulae are required for the co-existence of two phases within a pore element. In order to do this, we use the same model formulae as reported in Øren et al. (1998) and Valvatne (2004).

In some of the reviewed models, the conductance and flow rate of wetting film were calculated separately, which enabled them to simulate the specific film behaviours (Blunt et al. 1997a, 1997b; Valvatne (2004); Øren et al. (1998); Man and Jing (1999, 2000, 2001); Ryazanov et al. (2009, 2011, 2014)).

Our modified quasi-static model simulates the behaviours of corner fluid (swelling, shrinking, and trapping) in greater detail compared with the original *MixWet* model: the film volume, conductance and flow rate will be updated at every P_c step, and more scenarios are considered, as discussed in detail in Chapter 3. And it works as the important preparation for the novel dynamic model that will be introduced later in Chapter 4.

2.6.2 Dynamic Model

The new dynamic model is also based on the MixWet model of McDougall et al. (1994, 1995), and the modifications described above are applied here, including the formulae change for film formation and conductances from Øren et al. (1998) and Valvatne (2004). Below we will compare several dynamic models reviewed earlier with our new unsteady-state model of imbibition. Although we have not yet described our dynamic model, this comparison is aimed at contexting this new model in the light of what has already been published. The full dynamic model is described in detail in Chapter 4.

Pore-Level Events

Lenormand and Zarcone (1984) observed and described the displacement processes operating in imbibition (Figure 2-4): piston-like displacement, snap-off and I_z mechanisms. The I_z mechanism describes the pore body filling events when z of the adjacent bonds are full of the invading phase (water). Table 2-1 presents a brief summary review of the various dynamic pore scale models of imbibition which have been published to date.

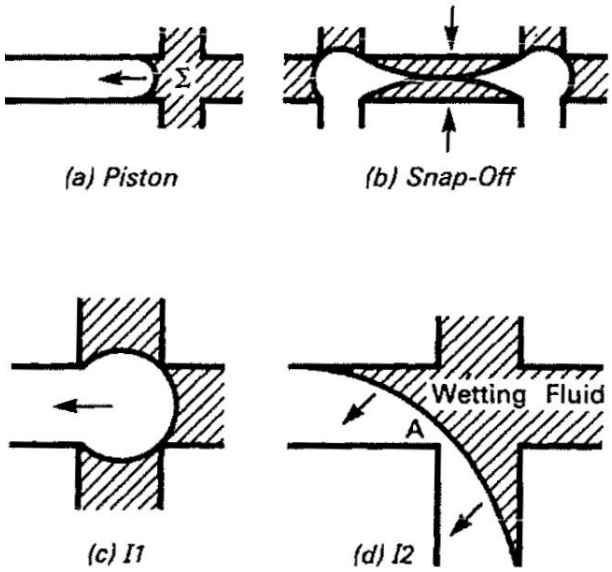

Figure 2-4 Displacing processes in imbibition (Lenormand and Zarcone (1984)).

The model of Aker et al. (1998) only simulated piston-like displacement in drainage; whilst models of Mogensen and Stenby (1998), Singh and Mohanty (2003), and Al-Gharbi (2004) concentrated on piston-like displacement and snap-off only. Other models listed in Table 2-1 have included all three mechanisms: piston-like displacement, snap-off, and I_z mechanism (Hughes and Blunt (2000), Nguyen et al. (2006), Idowu (2009)).

Besides piston-like displacement and snap-off, our newly proposed dynamic model includes another displacing mechanism - the coupling of bulk advancement and film swelling - to simulate the intermediate state between these two mechanisms. This is an important extension to earlier approaches and allows us to account for the rate-dependency seen in dynamic imbibition. The calculated behaviour from this model also goes some way towards explaining the observed difference between SS and USS relative permeabilities.

Table 2-1 Pore-level events of dynamic models

Model	Pore-level events			
	Piston-like displacement	Snap-off	I_z mechanism	Coupling of bulk and film
Aker et al. (1998)	√			
Mogensen and Stenby (1998)	√	√		
Hughes and Blunt (2000)	√	√	√	
Singh and Mohanty (2003)	√	√		
Al-Gharbi (2004)	√	√ (throat)		
Nguyen et al. (2006)	√	√	√	
Idowu (2009)	√	√	√	
Our model	√	√		√

Fluid Configurations

In line with the pore-level events simulated by each model, the considered fluid configurations are listed in Table 2-2. Aker et al. (1998) and Al-Gharbi (2004) simulated the moving bulk menisci in piston-like displacement, and the travelled distances were considered when calculating the conductance. Corner flow in earlier models (Mogensen and Stenby (1998); Hughes and Blunt (2000); Singh and Mohanty (2003)) tended to have fixed thickness and conductance (usually chosen by users), which effectively prevented the wetting film from swelling (although snap-off was allowed under suitable conditions). However, in later models, the film volumes started to be updated based on the local water flow increment and time step (Al-Gharbi (2004); Nguyen et al. (2006)), or the sorting capillary pressure (Idowu (2009)). But in Nguyen et al. (2006) and Idowu (2009) models, the frontal displacement, if possible, will complete within one time step, thus there is no moving bulk meniscus within a single element.

Our new dynamic model will update the moving distances of bulk menisci and the thickness of wetting film automatically at each time step, simulating both piston-like

displacement and film swelling simultaneously, where appropriate. Furthermore, the newly included filling mechanism (coupling of bulk and film) will introduce another configuration (as seen in Table 2-2), and a switch parameter λ will be used to distribute incoming water in the third configuration. Conductance, pressure drop and flow rate will all be updated accordingly.

Table 2-2 Fluid configurations of dynamic models

Model	Fluid configurations				
	Bulk 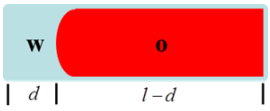		Film 		Bulk and Film 
	Fixed	Updated	Fixed	Updated	
Aker et al. (1998)		√			
Mogensen and Stenby (1998)	√		√		
Hughes and Blunt (2000)			√		
Singh and Mohanty (2003)			√		
Al-Gharbi (2004)		√		√	
Nguyen et al. (2006)				√	
Idowu (2009)				√	
Our model		√		√	√

Flow Rate and Rate-Dependency

In a quasi-static model, the displacement is controlled only by capillary forces, while in a dynamic model, viscous forces are also included. Generally speaking, of the models listed in Table 2-3, there are two methods to implement the viscous forces. The first is

to add capillary pressure into the calculation of local flow rate for two-phase flow (i.e. in pores with one bulk meniscus) (Aker et al. (1998); Mogensen and Stenby (1998); Singh and Mohanty (2003); Al-Gharbi (2004)). The second method is to include the capillary pressure for a specific filling event into the sorting pressure, and then using this sorting pressure to rank and fill all the elements (Hughes and Blunt (2000); Nguyen et al. (2006); Idowu (2009)).

Our new dynamic model will apply the first method, considering capillary pressure in the pores with bulk menisci. As a result, various filling regimes will be obtained under different injection rates. Moreover, the rate-dependent switch parameter λ will be used to distribute the incoming water within the pores, with both a moving meniscus and swelling film, which represents the local competition between piston-like displacement and snap-off.

Furthermore, our new model also applies the method of Aker et al. (1998) to update the global pressure drop for the constant injection rate.

Table 2-3 Flow rate and rate-dependence in each model

Model	Flow rate and rate-dependence	Note
Aker et al. (1998)	Drainage: $q = -g \cdot (\Delta P - \tilde{P}_c)$	$\tilde{P}_c : \begin{cases} \text{one meniscus} : \tilde{P}_c = P_c \\ \text{no menisci} : \tilde{P}_c = 0 \end{cases}$
Mogensen and Stenby (1998)	No menisci: $q_{i,j} = g_{i,j} \cdot (P_i - P_j)$ One menisci: $q_{i,j} = g_{i,j} \cdot (P_i - P_j + P_{c,i,j})$	$g_{i,j} : \begin{cases} \text{open} : g_{i,j} = \text{C (prescribed, positive)} \\ \text{closed} : g_{i,j} = 0 \end{cases}$
Hughes and Blunt (2000)	$Q_{i,j}^{p} = g_{i,j}^{p} \cdot (P_i^{p} - P_j^{p})$ $P_{Sort} = (P_w^{In} - P_w^{i}) - P_c^{i}$	P_c^i is the capillary entry pressure for piston-like displacement, snap-off, or I_z events. P_{Sort} is the displacement sorting pressure.
Singh and Mohanty (2003)	$Q_{ij} = \begin{cases} G_{ij}(P_i^{nw} - P_i^{w} - P_{ctij}), P_i^{nw} - P_i^{w} - P_{ctij} \geq 0 \\ G_{ij}(P_i^{nw} - P_i^{w} - P_{cbi}), P_i^{nw} - P_i^{w} - P_{cbi} \leq 0 \\ 0 \end{cases}$	Drainage from pore i to j Imbibition from pore j to i Otherwise
Al-Gharbi (2004)		

	$Q_{total} = \frac{P_{pore} - P_{throat} + P_c}{W_{eq}}$	
Nguyen et al. (2006)	$q_{i,j} = g_{i,j}(P_i - P_j)$ (Film flow) $P_w^{*,n} = \frac{q + \sum_{i,j} g_{i,j}^n P_{i,j}^n}{\sum_{i,j} g_{i,j}^n}$ $P_c^{*,n} = P_{nw} - P_w^{*,n}$	$g_{i,j}^n$ is the film conductance. Summation: all pores and throats (film) connected to the displacement front.
Idowu (2009)	$Q_{i,j}^p = g_{i,j}^p \cdot (P_i^p - P_j^p)$ $P_{global} = P_c^{local} - P_o^{local} - \Delta P_w$	$\Delta P_w = P_w^{inlet} - P_w^{local}$ Rank all possible elements using the $P_{global.}$
Our model	No menisci: $q_{i,j} = g_{i,j} \cdot (P_i - P_j)$ One menisci: $q_{i,j} = g_{i,j} \cdot (P_i^w - P_j^{nw} + P_{c,i,j})$ $\lambda = \frac{P_c}{P_c + \Delta P}$	A rate-dependent switch parameter λ is used to distribute the arriving water

In conclusion, in this work, we will present two models: (i) a quasi-static model simulating the specific film behaviours in angular pores, and (ii) a novel dynamic model of imbibition.

In the quasi-static model, we will focus our sensitivities on pore shape, pore size distribution (PSD), coordination number (Z), contact angle (θ). These calculations are conducted as a preparation for later comparisons with the dynamic results. These comparisons will help us to explain the observed differences between SS and USS relative permeability data.

In our dynamic model of imbibition, a new filling mechanism that includes both bulk and film flow is applied. This model introduces a rate-dependent switch parameter λ, which represents the competitions between capillary forces and viscous forces at the pore-scale, and between bulk advancement and film swelling. Analysis based on the Jones and Rozelle version of the Buckley-Leverett theory will be used to obtain the dynamic relative permeabilities. However, some alternative approaches to the calculation of relative permeability are also considered and discussed.

3 Quasi-static Pore Network Models (PNMs)

In this thesis, both the quasi-static model with explicit film behaviours and the dynamic model of water imbibition are based on the mixed-wet model of McDougall and Sorbie (*MixWet*) (McDougall and Sorbie (1993; 1995); McDougall et al. (1997); Dixit et al. (1998)) and share many features of it: such as the model structure and main displacement mechanisms. However, the fact that pore elements in *MixWet* are circular cylinders with no ability to contain expandable wetting film limits the ability of *MixWet* to simulate the explicit film behaviours. To relax this limitation of *MixWet* and prepare the pore geometries for the later dynamic model, a modified quasi-static model with angular pores and explicit film behaviours will be introduced in this chapter, followed by some preliminary results.

Similar to *MixWet*, the modified quasi-static model also simulates the two-phase displacement based on invasion percolation algorithm: the invading fluid fills a pore or throat in descending/ascending order of its size (more strictly in order of its increasing/decreasing capillary entry pressure). With the consideration of trapping, the pore element to be filled in these models must be connected ultimately to the inlet, and the defending phase within must be connected to the outlet. At each P_c level, when steady-state conditions are reached, Darcy's law will be applied to each phase separately and a pair of relative permeability values will be calculated for that particular saturation.

3.1 The *MixWet* Network Model

The *MixWet* model is a quasi-static model in which the flow is dominated by capillary forces and hence pore filling sequences (of say water displacing oil or vice versa) occur in the order of capillary entry pressure increasing or decreasing based on the particular displacement process (drainage or imbibition). Wetting phase and non-wetting phase co-exist in the system, but due to the lack of crevices in each pore (for simple cylindrical pores), film along the pore wall is volumeless and each pore can only accommodate one bulk phase at a time. Later, we will introduce angular pores, which can describe 2-phase occupancy in a single pore, with one as the bulk phase and the other in films in the corners.

3.1.1 Network Structure

The porous medium is represented as a 2D or 3D network of pore elements that are connected to one another through volumeless nodes. The most basic network structure is regular but can be distorted in accordance with measured distortion numbers. The 2D and 3D coordination number (Z) in the fully-connected model would naturally be 4 and 6, respectively; and smaller coordination number can be achieved through randomly removing pore elements. The size of the network is given by the number of nodes in three directions which are denoted as n_x, n_y, n_z (as indicated in Figure 3-1), and all of the pores are circular cylinders, where each is randomly assigned a radius (r) and a length (l). The cross sectional area and volume of a pore element, which will be used to calculate the saturation and conductance, are as follows:

$$A = \pi r^2, \qquad V = A \cdot l = \pi r^2 l \tag{3-1}$$

The pore-size distribution is defined by the value of pore-size distribution exponent (n), where $f(r) \sim r^n$. *n=0* refers to a Uniform distribution, *n=3* gives a Cubic distribution, and a value of *n=10* is used by the *MixWet* input interface to choose the Truncated Normal (TN) distribution.

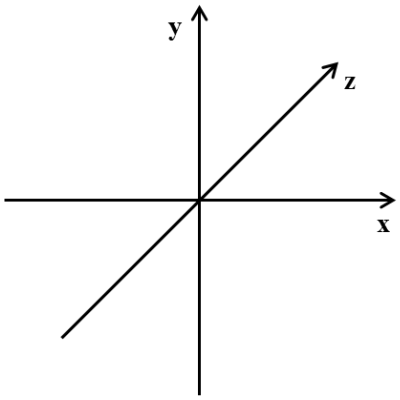

Figure 3-1 Illustration of x-direction, y-direction, z-direction

3.1.2 Displacement Cycles

At the start of a *MixWet* simulation, the system is assumed to be purely water-wet and completely filled with water. There are then five displacement cycles in the *MixWet* model, starting from primary drainage (PD).

Primary drainage (PD): oil displaces water from a 100% water-wet network. This can also be used to examine other generic 2-phase incompressible drainage displacements (e.g. gas-oil drainage). Successively higher (positive) capillary pressure is applied to the system and this drives the displacement. Invasion will first occur in the biggest pore elements that are accessible from the inlet face, since the largest pore is characterised by the lowest threshold entry pressure, followed by the next largest accessible pores, and so on.

Aging: following primary drainage to some state of the system (defined by a given chosen S_{wi}, a final P_c or other criterion), aging occurs and the wettability of the network is modified according to pre-selected wetting rules. Based on the value of the fraction of oil-wet pores (α) and wettability type (*mixed-wet Large - MWL, mixed-wet small - MWS, and fractionally wet - FW*), a number of oil-filled pores will change from a water-wet to an oil-wet condition and the wetting condition will remain unchanged until the end of simulation. Notice that we currently assume that the wettability is uniform within a given pore.

Water imbibition (WI): following aging, water is allowed to imbibe along water-wet pathways in the system and snaps off in the smallest oil-filled pores. The displacement is controlled by reducing the pressure in the oil phase (i.e. successively lower (positive) capillary pressures are applied to the system). In contrast to drainage, displacement first occurs in the smallest pore with the highest entry pressure.

Both piston-like displacement and snap-off will occur during water imbibition. Note the circular pores are actually not explicitly able to accommodate the wetting film to enable snap-off to occur. However, in the *MixWet* model, snap-off is still allowed to occur wherever topology makes this possible with the suitable threshold pressure and wettability connectivity.

Water drainage (WD): after spontaneous WI ceases, the next stage of this cycle proceeds by applying successively negative capillary pressures and water is forced into sequentially smaller oil-wet pores. This process then carries on until a final residual oil saturation ("S_{or}") is reached; it is denoted as "S_{or}" here since this can be defined in a number of ways as discussed in Ryazanov et al (Ryazanov et al. (2014)).

Oil imbibition (OI): after the WD stage, then the next cycle is oil imbibition (OI) where oil imbibes along oil-wet pathways, snapping-off the smallest water-filled pores. This

is driven by a gradual reduction in water pressure - capillary pressures are negative and rising successively back to zero.

Oil drainage (OD): after the OI stage, the oil pressure is increased once again and oil is forced into water-wet pores until some final S_w value is reached according to some final criterion as before.

3.1.3 Wettability Alteration

Wettability is a measure of the preference of the system surface to be wetted by a particular phase – preferentially the aqueous or oleic phase to some degree; this is described by the water/oil contact angle in the pore, θ_{ow} – usually denoted simply as θ in this work. The wettability of a porous medium determines the actual fluid phase distributions in the network model and hence the form of both the capillary pressure and the relative permeability curves. Both the *MixWet* model and the new models proposed below define various wettability types, as discussed below:

Water-wet: where water is the preferential wetting phase. In an angular pore, the wetting phase can occupy the pore corners as arc menisci, *AMs*, whereas the non-wetting phase stays in the centre of the pore. These wetting films can swell/shrink as the result of a decreasing/increasing capillary pressure. In a cylindrical water wet pore occupied by oil, the oil occupies the pore centre (practically the entire pore) and a notional water film exists on the wall but this has no bulk volume.

Oil-wet: in this system, instead of water, oil becomes the preferred wetting phase and occupies the corners as films. In a cylindrical oil wet pore occupied by water, the water phase occupies the pore centre and a notional oil film exists on the wall (but again this has no bulk volume).

Mixed-wet: where some degree of water wetness and oil wetness are shown in the same system. Our model has three possible types: *mixed-wet large - MWL, mixed-wet small - MWS* and *fractionally-wet - FW*. The first two wetting types (MWL and MWS) are self-explanatory in that that some portion of the largest or smallest oil-filled pores will turn from water-wet to oil-wet in the aging process after primary drainage, based on the predefined fraction of oil-wet pores α. In the fractionally-wet (FW) system, the fraction of oil-filled pores is uncorrelated with pore size and wetting change occurs throughout the entire pore size range.

The wettability can also be classified based on the value of contact angle– contact angles in water-wet, oil-wet or intermediate-wet systems are less than 90°, greater than 90° or close to 90°, respectively. The *MixWet* model allows us to predefine the value of contact angle and change it automatically in the aging process based on the chosen wettability type. We set the contact angle in the initially water-wet, completely water-filled system to be 0°. In addition any random range of contact angles can be specified in the oil wet pores (where $-1 < \cos\theta < 0$) and in the water wet pores (where $0 < \cos\theta < 1$). Using such simple rules, a very wide range of wetting conditions can be generated in the network model, which appear from experience to capture a wide range of behaviours observed in experimental systems.

3.1.4 Solving for the Pressure Field

Since all the pore elements are connected to volumeless nodes, then mass conservation at each node leads to the expression:

$$\sum q_i = 0 \qquad 3\text{-}2$$

where *i* runs over all the connected pores of the target node, and *q* is the volumetric flow rate into the node. Note: in the *MixWet* model, each pore can be occupied by only one phase, thus the *q* here is actually a single-phase flow rate.

The flow rate of each individual pore element is as follows:

$$q = g \cdot (P_i - P_j)\,. \qquad 3\text{-}3$$

When aggregated across the entire network, equations 3-2 and 3-3 give rise to a set of linear equations for the pressure field and local flow rates.

In the *MixWet* model, and the later modified quasi-static model, a constant pressure drop is assigned across the system. Then, at each capillary pressure step, the changing fluid configurations control the detailed pressure field for each phase in turn, and thus feeds through to changes in flowrates.

3.1.5 Trapping

In quasi-static model, bulk phase and wetting films are treated separately during the trapping process. At each step, the system will generate clusters of topologically connected bulk water and bulk oil. Each cluster, and the pores contained therein, is

assigned a unique number - the cluster number. If a pore has the same cluster number as at least one outlet pore, then the defending fluid within it can be displaced via the continuous path to the outlet and the pore is labelled as an 'untrapped' pore. Similarly, pores containing the invading phase and having a matched cluster number as any one inlet pore will then be labelled as connected with the inlet. Also, based on specific displacing cycle, connectivity of wetting (water or oil) films to the system inlet or outlet will also be considered through the similar technique conducting on bulk phase.

3.1.6 Relative Permeabilities

The model records the total water flow Q_t at 100% water saturation (single-phase), and uses it to calculate the relative permeabilities:

$$k_{rw} = \frac{Q_w}{Q_t} \cdot \frac{\mu_w}{\mu_s} \qquad 3\text{-}4$$

and

$$k_{ro} = \frac{Q_o}{Q_t} \cdot \frac{\mu_o}{\mu_s} . \qquad 3\text{-}5$$

Where Q_w/Q_o is total water/oil outflux at the system outlet. Note here, $\mu_s=\mu_w$ since the initial single-phase flood was using water.

All of the foregoing details pertain to the basic cylindrical *MixWet* network model. Whilst this model proved successful in the past in capturing a wide range of multiphase flow phenomena at the pore scale, particular film flow processes and unsteady-state dynamics are not included in it. Thus, some substantial theoretical and code developments were required in order to incorporate this additional important physics. The first limitation to be relaxed was that of having a circular geometry of the pores. Angular pores were introduced in order to be able to model the impact of including explicit corner flow.

3.2 Quasi-static Model with Specific Film Behaviours

To accommodate films appropriately, triangular pore geometries were introduced into the network framework. The inclusion of explicit corners into each pore element is vital for tracking film-flow and expansion. Furthermore, as capillary pressure varies, we can also simulate the corresponding volume changes of wetting fluid in the corners, which will also impact the wetting phase conductance as the flood proceeds.

3.2.1 Geometry

In the triangular pore model, the cross-sectional shape is characterized by the radius *r* of the inscribed circle and the half-angles of three corners. In simulating the fluid behaviour in triangular pores, we must make some changes in the formulae for capillary pressure, pore saturation, and pore conductances. Regarding the geometry and simple volumetrics, different equations must be used when calculating the cross sectional area of a pore.

The area of a generalised triangle is given by the equation $A_t = r^2 \sum_{i=1}^{3} \frac{1}{\tan \beta_i}$, where *r* is the inscribe radius and $\beta_1 \geq \beta_2 \geq \beta_3$, $\beta_1 + \beta_2 + \beta_3 = 90^o$ are the half angles. We can define the range of half angles to constrain the pore shape. For example, equilateral triangular pores can be produced or we can assign the angles randomly and produce pores of arbitrary triangular cross-section.

Changes in saturation and conductance formulae are required for the co-existence of two phases within a pore element. According to Oren et al. (1998) and Valvatne (2004), when water is present as arc menisci (*AMs*) in the corners of a pore body or throat, the area occupied by the water is given by:

$$A_w = r_w^2 \sum_{i=1}^{n} [\frac{\cos\theta \cos(\theta + \beta_i)}{\sin \beta_i} + \theta + \beta_i - \frac{\pi}{2}] \qquad 3\text{-}6$$

where θ is the contact angle, $r_w = \frac{\sigma}{P_c}$ is the radius of curvatures of the *AMs*, and *n* is the number of corners that have corner water.

If we denote S_1 as a dimensionless parameter:

$$S_1 = \sum_{i=1}^{n} [\frac{\cos\theta \cos(\theta + \beta_i)}{\sin \beta_i} + \theta + \beta_i - \frac{\pi}{2}], \qquad 3\text{-}7$$

the corner water area can be written as

$$A_w = r_w^2 \cdot S_1 . \qquad 3\text{-}8$$

The area of the central part of a pore occupied by bulk nonwetting fluid follows immediately:

$$A_{nw} = A_t - A_w \tag{3-9}$$

In the calculation of saturation, we need to consider the volume occupied by corner fluid and bulk fluid separately. Moreover, when we update relative permeability, the bulk flow and flow in the wetting layer must also be treated separately.

It should also be noted that the number of *AMs* does not always match the number of corners. As shown in Figure 3-2, the distance the *AM* moves, *AB*, is determined by the curvature and can be calculated from geometry

$$AB = r_w \frac{\cos(\theta + \beta)}{\sin \beta} \tag{3-10}$$

To be physical, the *AB* needs to be positive, thus $\theta < \frac{\pi}{2} - \beta$.

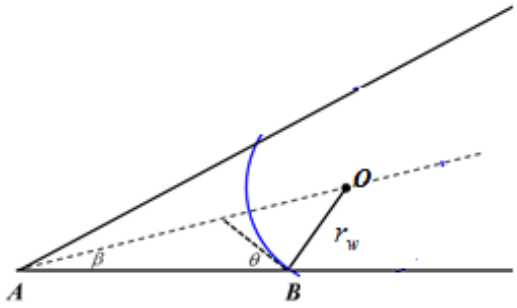

Figure 3-2 Illustration of arc menisci, blue curve represents the arc menisci.

In this model, if the corner does not satisfy the above condition, then it will be assumed to have no corner water at all. Therefore, in a particular pore element with half angles $\beta_1 \geq \beta_2 \geq \beta_3$, the value of contact angle will determine the number and curvature of *AMs* (see Figure 3-3).

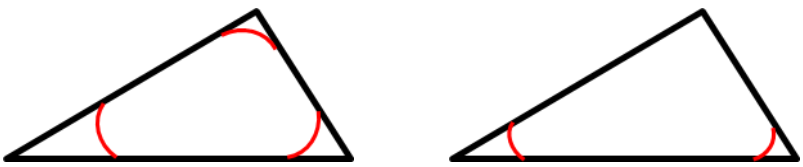

(a) $0 \leq \theta < \frac{\pi}{2} - \beta_1$ (b) $\frac{\pi}{2} - \beta_1 \leq \theta < \frac{\pi}{2} - \beta_2$

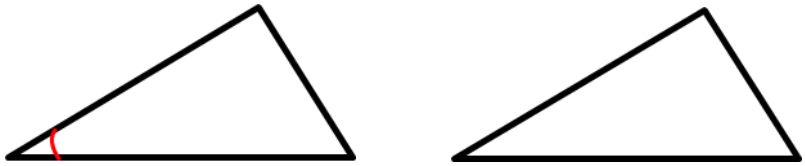

(c) $\frac{\pi}{2}-\beta_2 \le \theta < \frac{\pi}{2}-\beta_3$ (d) $\frac{\pi}{2}-\beta_3 \le \theta < \frac{\pi}{2}$

Figure 3-3 Number and curvature of *AMs*, red curves represent *AMs*.

The hydraulic conductance of completely filled pore bodies and throats is computed by assuming a Poiseuille-like law between the flow rate q and the pressure gradient ∇P,

$$q = -g\nabla P. \tag{3-11}$$

The conductance of circular pores is well known to be:

$$g = \frac{\pi r^4}{8\mu l} \tag{3-12}$$

For non-circular geometries, Oren et al. (1998), the full pore conductance can be approximated as:

$$g = \frac{3A^2 G_{shape}}{5\mu l} = \frac{3r^2 A}{20\mu l} \tag{3-13}$$

where G_{shape} is a shape factor that depends upon the cross sectional geometry and A represents cross sectional area. If we denote s as the corresponding perimeter length, the shape factor G_{shape} can be represented as:

$$G_{shape} = \frac{A}{s^2}. \tag{3-14}$$

And for a particular triangle:

$$G_{shape} = \frac{1}{4}\left(\sum_{i=1}^{3} \frac{1}{\tan\beta_i}\right)^{-1}. \tag{3-15}$$

If nonwetting fluid occupies only the centre of a pore body or throat, however, with water present as *AMs* in the corners, the nonwetting conductance is found from the equation above, but with A replaced by the cross-sectional area occupied by nonwetting phase only, A_o. The conductance of the corresponding wetting phase in the film is given by:

$$g_w = \frac{r_w^2 A_w}{C_w \mu_w l} \tag{3-16}$$

where C_w is a dimensionless flow resistance factor which accounts for the reduced water conductivity close to the pore walls (notionally accounting for wall surface roughness and zero slip boundaries).

Numerical solutions of the corner flow problem show that C_w depends on the corner geometry, the contact angle, and the boundary condition at the oil-water interface. Its value for different θ and boundary conditions has been estimated by Ransohoff and Radke (1988). Later, Zhou et al. (1997) developed an analytical expression for C_w which approximates the data of Ransohoff and Radke quite well using the expression:

$$C_{w,i} = \frac{12\sin^2\beta_i (1-B)^2 (\psi_1 - B\psi_2)[\psi_3 + f_2 B\psi_2 - r_d(1-f_1 B)]^2}{(1-\sin\beta_i)^2 B^2 [\psi_1 - B\psi_2 - (1-B)r_d^2]^3} \tag{3-17}$$

where

$$\psi_1 = \cos^2(\beta_i + \theta) + \cos(\beta_i + \theta)\sin(\beta_i + \theta)\tan\beta_i \tag{3-18}$$

$$\psi_2 = 1 - \frac{\theta}{\pi/2 - \beta_i} \tag{3-19}$$

$$\psi_2 = \frac{\cos(\beta_i + \theta)}{\cos\beta_i} \tag{3-20}$$

$$B = (\pi/2 - \beta_i)\tan\beta_i \tag{3-21}$$

r_d represents the degree of "roundedness": $r_d = 0$ for the sharp corners and f_1 and f_2 are determined by the boundary conditions at the interface, with value ranging from 0 to 1. The solid/wetting phase contact line is assumed to have a no-slip boundary condition ($f_1 = 1$), whilst the wetting/non-wetting fluid boundary may be no-slip ($f_2 = 1$), no-stress ($f_2 = 0$) or some combination of the two, implying that ($0 < f_2 < 1$).

We initially assume C_w is equal in all the corners with AMs, and assign it a relatively large value ($O(10^2)$ compared with 20/3 in the bulk conductance formula), and so, for the corners and bulk with identical cross-sectional area, the corner conductance is appreciably smaller than the bulk value, in keeping with reality. A sensitivity study of

C_w was carried out and this will be discussed later. Note in the later sensitivity study, the value of C_w is still assumed to be constant throughout the system; the more involved representation given by Equation 3-17 may be included in the models in the future.

The total conductance of a pore element is calculated by simply summing bulk and corner conductances.

3.2.2 Pore Scale Two-phase Displacement Mechanisms

Piston-like displacement

Piston-like advance is the pore scale displacement mechanism whereby the invading fluid pressure is high enough to allow it to enter the bulk (centre) of the element by pushing the displaced fluid ahead of it. There are three conditions for a (two phase) piston-like displacement to happen in a pore: (i) the invading bulk fluid needs to be connected with the inlet, (ii) the defending fluid should be connected with the outlet, and (iii) the threshold pressure of the pore should be smaller (larger) than the current capillary pressure during drainage (imbibition). The entry pressure for piston-like displacement in a circular pore is given by the Young-Laplace equation:

$$P_{c,entry}^{piston-like} = \frac{2\sigma\cos(\theta)}{r}. \qquad 3\text{-}22$$

However, in triangular pores where the wetting fluid remains in the corners of pores in the form of arc menisci (*AM*s), the capillary entry pressure expressions become more complex. Entry pressures are found by calculating the force balance acting on the interface in the triangular duct. The method for doing this by balancing the interfacial forces is known as the Mayer, Stowe and Princen method (MS-P), Mayer and Stowe (1965), Princen (1969a, b, 1970) and we follow the presentation of Oren et al. (1998):

For piston-like displacement,

$$P_c^{piston-like} = \frac{\sigma\cos\theta(1+2\sqrt{\pi G_{shape}})}{r}\cdot F_d(\theta_r, G_{shape}, \beta) \qquad 3\text{-}23$$

where θ is the contact angle, σ is the interfacial tension (IFT), and

$$F_d(\theta_r, G, \beta) = \frac{1+\sqrt{1-\frac{4G_{shape}S_1}{\cos^2\theta_r}}}{(1+2\sqrt{\pi G_{shape}})}. \quad 3\text{-}24$$

S_1 is given by Equation 3-7, and if we assign

$$F_d^* = \cos\theta + \sqrt{\cos^2\theta - 4G_{shape}S_1} \quad 3\text{-}25$$

then capillary pressure can be written as

$$P_c^{piston-like} = \frac{F_d^* \cdot \sigma}{r}. \quad 3\text{-}26$$

Note here, as seen in Figure 3-3, if $\frac{\pi}{2} - \beta_3 \le \theta < \frac{\pi}{2}$, there will be no *AM* in the triangular pore, consequently, the capillary entry pressure of piston-like displacement will be given by Equation 3-22 like in circular pores.

This type of displacement predominates during drainage but can also occur during imbibition if the fluid topologies and capillary pressure conditions are suitable. Since this mechanism requires a bulk water supply, it will lead to a continuous water path starting from the inlet.

Snap-off

In imbibition, a second displacement type known as snap-off may occur. Snap-off is a mechanism that is controlled by wetting layer flow. Water accumulates in layers until oil no longer contacts the solid and water spontaneously fills the centre of the throat separating the oil into two droplets. Fluid starts accumulating in the wetting layers as a result of a drop in the capillary pressure which allows the film to swell. The capillary pressure at which snap-off occurs is lower than that of piston-like displacement due to the morphology of the associated meniscus; for example, in a circular pore, the snap off conditions is:

$$P_{c,entry}^{snap-off} = \frac{\sigma\cos\theta}{r}. \quad 3\text{-}27$$

In a scalene triangle, when 2 *AMs* in corner *i* and *j* meet (as seen in Figure 3-4, possible *i-j* combinations can be 1-2, 1-3, and 2-3), then r_w can be represented by pore geometry and contact angle as follows:

$$r_w^{snap-off} = r \cdot \frac{\frac{\cos\beta_i}{\sin\beta_i} + \frac{\cos\beta_j}{\sin\beta_j}}{\frac{\cos(\theta+\beta_i)}{\sin\beta_i} + \frac{\cos(\theta+\beta_j)}{\sin\beta_j}} \qquad 3\text{-}28$$

and the two *AMs* that will have the minimum r_w give:

$$r_{w,\min}^{snap-off} = r \cdot \frac{\frac{\cos\beta_2}{\sin\beta_2} + \frac{\cos\beta_3}{\sin\beta_3}}{\frac{\cos(\theta+\beta_2)}{\sin\beta_2} + \frac{\cos(\theta+\beta_3)}{\sin\beta_3}} \qquad 3\text{-}29$$

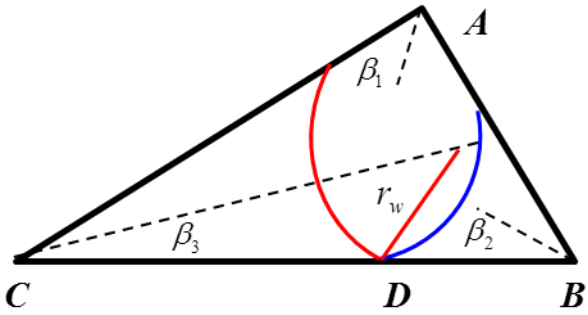

Figure 3-4 Illustration of *AMs* meeting with each other.
Red and blue curvature indicate the two merging *AMs*, red line represents the radius of the red *AM*.

From the above formula, we can conclude:

(1) In a strongly water-wet system when $\theta = 0$, $r_w^{snap-off} = r$ is true for any two corners, i.e. all three *AMs* meet spontaneously at the inscribe circle, regardless the pore shape.

(2) In an equilateral triangle, where $\beta_1 = \beta_2 = \beta_3$, the three *AMs* will merge with each other at the same time.

(3) 2 menisci in the sharpest corners will meet first.

(4) In the system with angular pores, if the contact angle is sufficiently large ($\theta \geq \frac{\pi}{2} - \beta_3$), no arc meniscus (*AM*) can be found in the pore corner (Figure 3-3 (d)), then snap-off is completely suppressed.

In a particular scalene triangle, if the contact angle is big enough, it is possible that only the sharpest corner contains one *AM*. Then snap-off will occur when the meniscus reaches to the most obtuse corner (as shown in Figure 3-5).

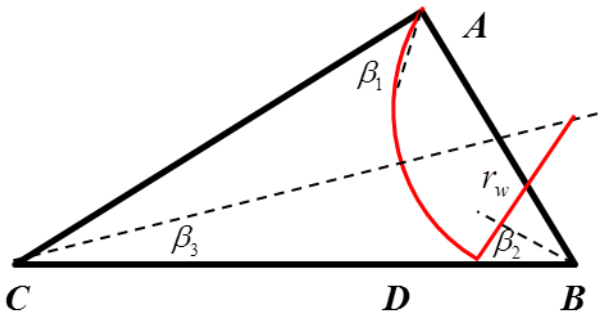

Figure 3-5 Illustration of snap-off in pores with one *AM*.

Thus

$$r_w^{snap-off} = r \cdot \frac{\frac{\cos\beta_1}{\sin\beta_1} + \frac{\cos\beta_3}{\sin\beta_3}}{\frac{\cos(\theta+\beta_3)}{\sin\beta_3}} \qquad 3\text{-}30$$

Furthermore, in the rare case with a large β_1 and two *AMs*, it is possible that the arc menisci corresponding to the sharpest corner approaches the most obtuse corner before it meets with the other menisci; in this case, snap-off will occur with the smallest radius of *AMs* characterised by Equation 3-30 (correspondingly the highest capillary entry pressure). To summarise:

$$r_w^{snap-off} = \min\left(r \cdot \frac{\frac{\cos\beta_2}{\sin\beta_2} + \frac{\cos\beta_3}{\sin\beta_3}}{\frac{\cos(\theta+\beta_2)}{\sin\beta_2} + \frac{\cos(\theta+\beta_3)}{\sin\beta_3}}, r \cdot \frac{\frac{\cos\beta_1}{\sin\beta_1} + \frac{\cos\beta_3}{\sin\beta_3}}{\frac{\cos(\theta+\beta_3)}{\sin\beta_3}}\right). \qquad 3\text{-}31$$

Similar to the simplified expression of piston-like capillary entry pressure, if we denote

$$F_d^{snap-off} = \frac{r}{r_w^{snap-off}}, \qquad 3\text{-}32$$

the corresponding capillary entry pressure for snap-off will be:

$$P_{c,entry}^{snap-off} = \frac{\sigma}{r_{w,\min}^{snap-off}} = \frac{F_d^{snap-off} \cdot \sigma}{r}. \quad 3\text{-}33$$

The oil-occupied area in the centre when snap-off occurs, $A_{critical}$, can be calculated using $r_w^{snap-off}$, as follows:

$$A_{critical} = A - A_w^{snap-off} = A - (r_w^{snap-off})^2 \cdot S_1 \quad 3\text{-}34$$

Based on a more refined categorisation of triangles, the existence and shape of *AMs* is described in the table below (Table 3-1).

Table 3-1 Illustration of *AMs* when snap-off occurs with various contact angles. Red curves represent *AMs*.

Half angles	Shape	$\theta = 0$	3 *AMs*	2 *AMs*	1 *AM*	$\theta = \frac{\pi}{2} - \beta_3$
$\beta_1 = \beta_2 = \beta_3$				NA	NA	
$\beta_1 > \beta_2 = \beta_3$					NA	
$\beta_1 = \beta_2 > \beta_3$				NA		
$\beta_1 > \beta_2 > \beta_3$					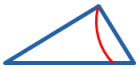	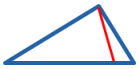

Given the capillary pressure for piston-like displacement is larger than that of snap-off in the same pore (for example, for an equilateral triangular pore, the value of F_d^* and $F_d^{snap-off}$ are shown in Figure 3-6), the former is always more likely to happen when it is topology possible. Snap-off can only occur in elements that are without an immediately available bulk water supply. However, snap-off via film-flow can occur anywhere in a water-wet system where the appropriate conditions – untrapped oil and capillary pressure – are met.

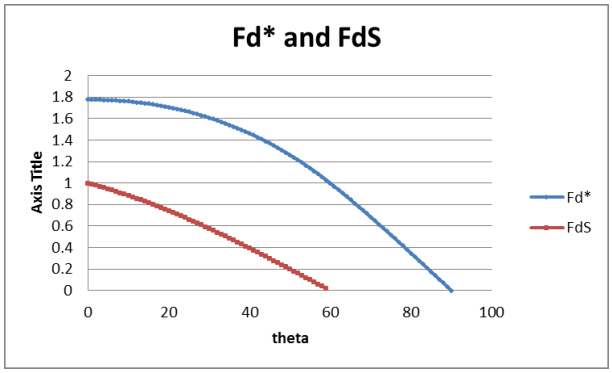

Figure 3-6 F_d^* and $F_d^{snap-off}$ in equilateral triangular pore with various contact angles. (see Equation 3-25 and 3-32 respectively)

3.2.3 Corner Fluid Behaviours in Mixed-wet Networks

During low-rate imbibition, wetting fluid gradually accumulates in pore corners by film swelling until snap-off occurs. Conversely, during drainage cycles, the increasing capillary pressure will push the wetting layer towards the corner of the pore and hence the corner fluid level shrinks. From the equations for the area occupied by wetting phase and non-wetting phase, we can see that, with fixed interfacial tension and contact angle, the areas of corners and centre of each pore are determined by the radius of the curvature of *AMs*, which is itself inversely proportional to the value of capillary pressure. Thus, the above areas are ultimately functions of P_c and so when absolute P_c increases in drainage and decreases in imbibition, the wetting film shrinks and swells accordingly.

In snap-off, wetting films gradually swell and eventually block the pore throat. Blocking of multiple pores can lead to considerable entrapment of the non-wetting phase, as a portion of the displaced phase can become entirely surrounded by the injected phase. In the case of a 3D waterflood, the trapped oil generally consists of smaller blobs, or ganglia, each occupying a few adjoining pores of the void space. Note that we have not considered ganglia movement in the current model – the trapped fluid will remain 'frozen' and cannot subsequently move.

However, it is not only bulk fluid that can become trapped by the invading phase. We also note that the wetting layers can become trapped after wettability alteration, since corner fluid may not be entirely connected across the system if the network contains pores of different wettabilities. This effect can also hinder the accumulation or shrinking of *AMs*.

The existence of wetting films will activate more complex shrinking, swelling, and trapping mechanisms, and more involved equations to calculate the corresponding saturations and conductances are required. The main challenge is to relate the appropriate capillary pressure based on the different regimes of trapping. Thus, it is necessary to record the exact value of P_c when each kind of trapping occurs.

Consider the following pores with wetting films in the corners: oil-filled pores containing a water film (Type A) and water-filled pores containing an oil film (Type B). The active film in order to swell requires two conditions: a sufficient source of invading phase *via the films* (connected to the inlet) and a continuous connected "gateway" or path of the *bulk* defending phase to the outlet. Similarly, two conditions have to be satisfied for the wetting film to shrink: *bulk* invading phase connected to the inlet and the untrapped *film*. Note the role of each phase as invading or defending phase depends on the specific filling process.

As a result of each filling process, several pore types with specific configurations and connectivity are created. The possible film dynamic of each pore can be predicted by the connectivity of bulk phase and film: each pore type is denoted based on the following rules: in each type, the first phase is the invading phase and the second one is the defending phase - take $O_B^1W_F^0$ as an example: *O* means oil is the invading phase (supply), and water (*W*) is the defending phase that flows out of the network (gateway). The subscript *B* and *F* stand for bulk and film respectively: as in $O_B^1W_F^0$, bulk oil will flow into this pore and displace water through the shrinking water film. And the superscript *1* means the relevant phase is open to inlet or outlet based on the nature of the mentioned phase (invading or defending); similarly, the superscript *0* means the related phase is closed/ trapped: for $O_B^1W_F^0$ pores, bulk oil is connected with the inlet, but water in films is trapped. Based on the involved configuration and specific *film* behaviour, the pores can be classified as in Table 3-2. Note in Table 3-2, only the configuration newly created in each corresponding displacement cycle is listed as primary configuration.

Table 3-2 Displacement cycle, primary configuration and possible film behaviours
Blue as water and red as oil

Displacement Cycle	Configuration	P_c	Film behaviour	Newly Created Pore type
PD		Positive, increasing	Water, shrinking	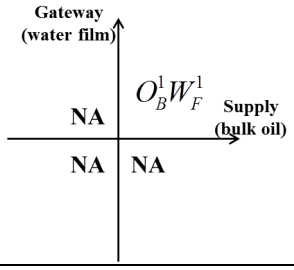
WI		Positive, decreasing	Water, swelling	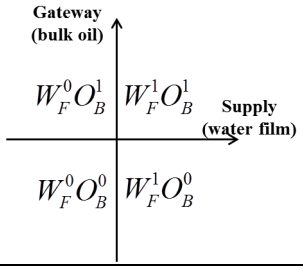
WD		Negative, decreasing	Oil, shrinking	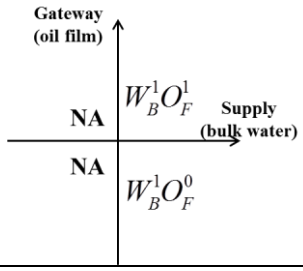
OI		Negative, increasing	Oil, swelling	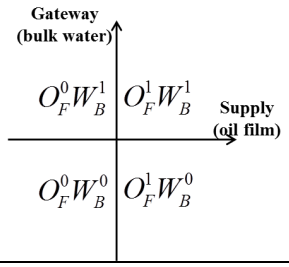
OD		Positive, increasing	Water, shrinking	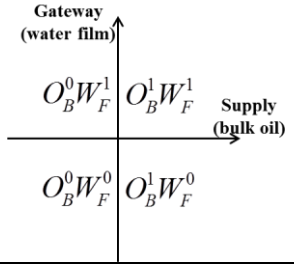

We now examine the flooding cycle with respect to the new wetting film dynamics (film swelling, shrinking, and trapping controlled by capillary pressure) compared to the original *MixWet* model.

Primary Drainage (PD):

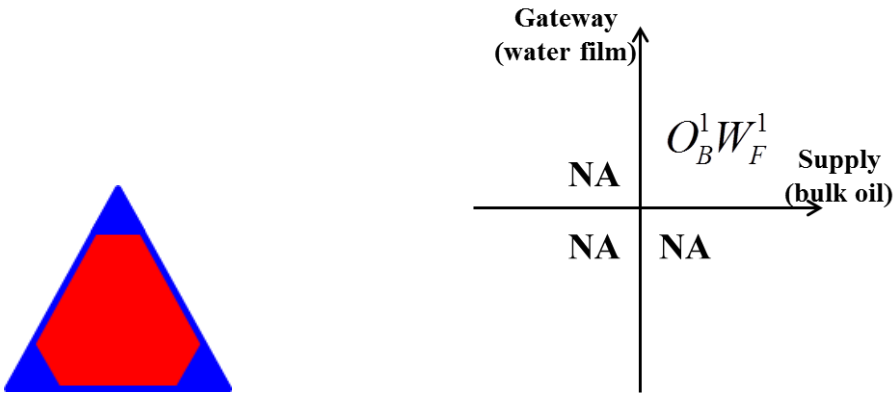

(a) (b)

Figure 3-7 Primary fluids configuration and film-related pore type in primary drainage. Blue as water and red as oil. Each quadrant in Figure 3-7 (b) indicates the possible connectivity of supply or gateway phase (same as in Figure 3-10, Figure 3-12, Figure 3-14, and Figure 3-17): first quadrant: both supply and gateway are open; second quadrant: supply closed, gateway open; situations in third and fourth quadrants are the opposite of those in first and second quadrants respectively.

The initial network is purely water-wet and filled by water, i.e. cos θ = 1 in all pores. Then, during primary drainage, bulk oil invades the system and creates water-wet, bulk oil-filled pores, Type A, with water in the corners as *AMs*. The nature of the displacement ensures that bulk oil connectivity must occur with the inlet. Also, the water film is guaranteed to be connected throughout the system since the system is now assumed to be purely water-wet (and corner films will therefore exist in every pore). Consequently, during PD, there are only $O_B^1W_F^1$ pores hosting oil – all the wetting film can safely shrink. At the end of PD, capillary pressure will have increased to its maximum value, $P_{c,\max} = \frac{F_d^* \cdot \sigma}{r_{\min}}$, and all pores will turn into Type A pores with the minimum corner water (as illustrated in Figure 3-8). In Figure 3-8 (and following diagrams), labels below arrows (e.g. invaded by oil in Figure 3-8) indicate the possible bulk invasion that lead to configuration alteration. And labels above arrows represent the conditions like: (1) current phase connectivity (e.g. $O_B^1W_F^1$ in Figure 3-8) and (2) comparison between local capillary entry pressure and global capillary pressure (e.g. $|P_c| \geq |P_{c,invasion}|$ in Figure 3-15 (c)) - pores that satisfy these conditions can have configuration changes that are indicated by corresponding arrows. Note corner water in

all invaded pores will have an identical cross-sectional area (all pores are at the same capillary pressure). However, if we artificially set a higher end S_w in PD, it is possible that some smallest pores are still filled by water due to their high entry pressure (they will remain untouched by the oil drainage process), and the water film in other pores will be thicker than the minimum value.

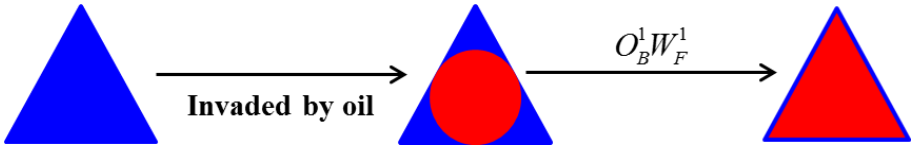

Figure 3-8 Diagram of Primary Drainage. Blue as water and red as oil.

After PD, aging occurs, *i.e.* the wettability alteration takes place. Based on the value of the fraction of oil-wet pores required, the number of oil-filled pores will change from a water-wet to an oil-wet condition. Note that only oil-filled pores can become oil-wet during this process. Also note that the process of aging will cause some notional water loss, as resident water films are assumed to drain from the system during the wettability alteration process (Figure 3-9).

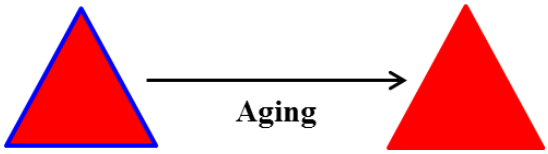

Figure 3-9 Diagram of aging. Blue as water and red as oil.

Water Imbibition (WI):

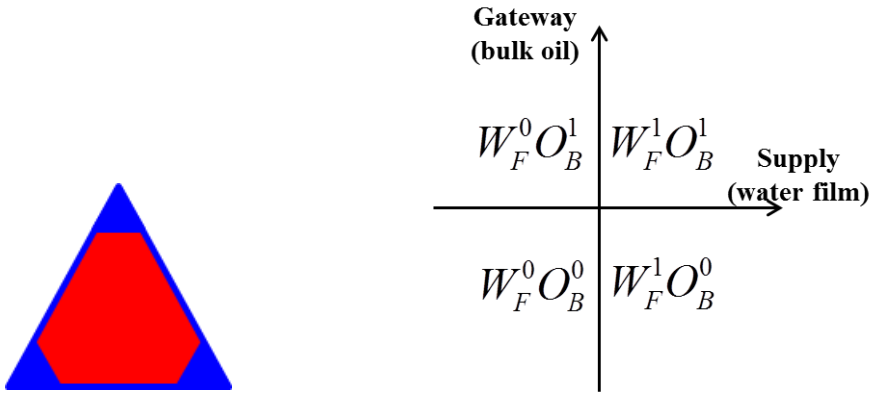

(a) (b)

Figure 3-10 Primary fluids configuration and film-related pore type in water imbibition. Blue as water and red as oil.

In this step of the flooding cycle, water imbibes into the system by invading water-wet, oil-filled pores through piston-like displacement, and/or by the accumulation (swelling) of water films and subsequent snap-off. Thus no *new* Type A pores are created during WI, and no Type B pores can appear at this stage (they only appear once the water has been over-pressured and then invades oil-wet pores).

A $W_F^1O_B^1$ pore has water supply from the inlet and a guaranteed oil pathway to the outlet which facilitates the continuous accumulation of water films until either piston-like displacement or snap-off occurs.

Wettability alteration may lead to the disconnection of a water film from the inlet in some Type A pores. For these pores ($W_F^0O_B^1$), *water films* cannot swell due to their lack of water supply. Thus their corner/centre areas remain unchanged throughout WI and maintain meniscus configurations as determined by the maximum P_c reached at the end of PD. During WI, water cannot flow into $W_F^0O_B^1$ pores through wetting layer accumulation and snap-off, but the untrapped oil in them may still be displaced by water in a piston-like fashion, as long as these pores have access to the invading *bulk* water (as indicated in Figure 3-11). *Note that we do not currently consider the 'sandwich' situation, in which small amount of oil may exist between the corner water and the newly invading bulk water – we allow these pores to become fully-water-filled.* This assumption may be relaxed later. Obviously, $W_F^0O_B^0$ pores with neither water supply nor oil gateways to the outlet will stay in their same status as at the end of PD.

As the displacement proceeds, bulk oil in some $W_F^1O_B^1$ pores may then get trapped due to bulk displacement and/or snap-off occurring in surrounding pores. Further, swelling of water films in these pores (termed here $W_F^1O_B^0$ pores) is not possible; and for each pore, the value of P_c when the trapping occurs is noted in order to maintain its water volume. In addition to prohibiting film accumulation and snap-off, trapped bulk oil also prohibits the pore being displaced through a piston-like mechanism (Figure 3-11).

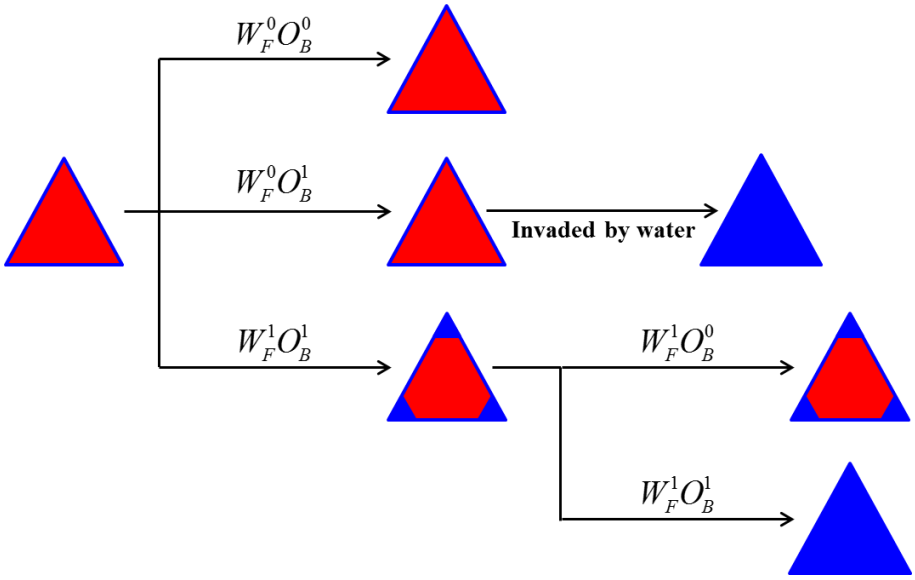

Figure 3-11 Diagram of Water Imbibition. Blue as water and red as oil.

Water Drainage (WD):

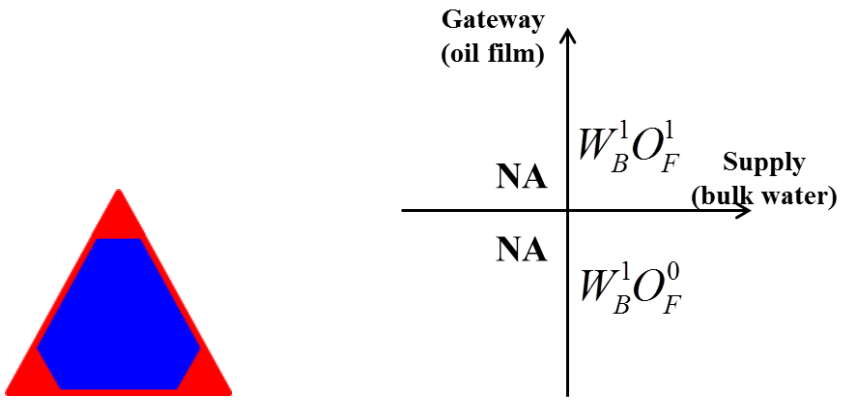

(a) (b)

Figure 3-12 Primary fluids configuration and film-related pore type in water drainage. Blue as water and red as oil.

During water drainage, bulk water invades oil-filled, oil-wet pores, and creates Type B elements. Note that Type B pores have not appeared up to this stage in the flooding cycle. Similar to bulk oil invasion during primary drainage, bulk water in Type B pores must be connected to the inlet for oil to be displaced and the only pores that become trapped during WD will be of $W_B^1O_F^0$ type – the disconnection of corner oil from the outlet prohibits its shrinking thus it remains as an immobile oil film (the value of P_c when water invaded this type of pore, $P_{c,invasion}$, is noted and this allows us to calculate the exact volume of fluids within these pores). In the other Type B pores – classified as

$W_B^1O_F^1$ – the oil film will retreat towards the corners as P_c becomes increasingly negative (Figure 3-13 (a)).

During the previous water imbibition, capillary pressure decreased to 0 and so all possible snap-off and piston-like displacements had already occurred in pores with water supply through film and untrapped bulk oil ($W_F^1O_B^1$) - no $W_F^1O_B^1$ pore will be left in the current water drainage process. During WD, water still cannot flow into $W_F^0O_B^1$ or $W_F^0O_B^0$ pores through wetting layer accumulation, but displacement through piston-like mechanism in $W_F^0O_B^1$ pores is still possible (Figure 3-13 (b)).

Moreover, the lack of oil intrusion also makes it impossible to re-connect bulk oil in $W_F^1O_B^0$ pores with the outlet; hence they will remain trapped and will have no alteration in their fluid configurations as displacement continues (Figure 3-13 (c)).

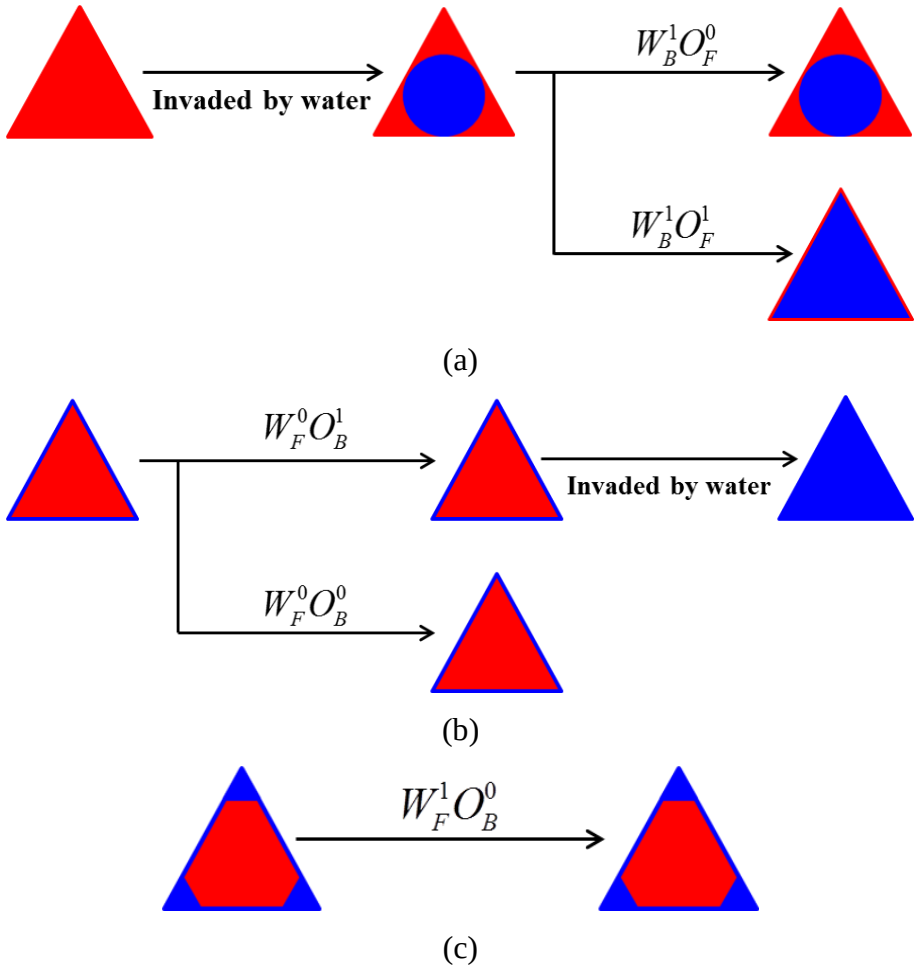

Figure 3-13 Diagram of Water Drainage. Blue as water and red as oil.

Oil Imbibition (OI):

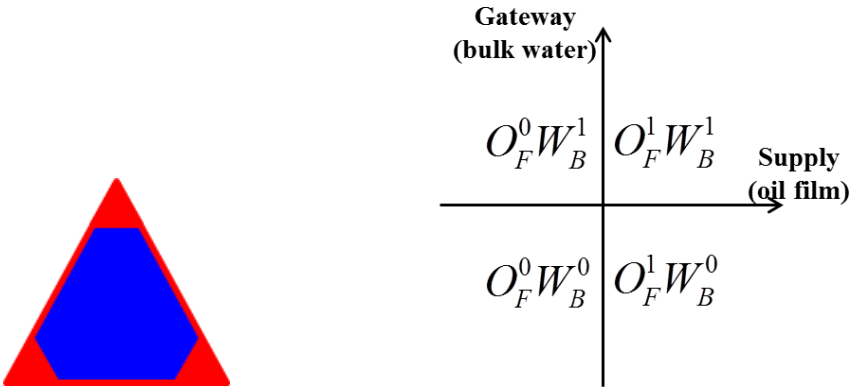

(a) (b)

Figure 3-14 Primary fluids configuration and film-related pore type in oil imbibition. Blue as water and red as oil.

In oil imbibition, oil enters the system through bulk piston-like invasion into water-filled, oil-wet pores; or this same final state occurs by the accumulation and snap-off of corner oil. Therefore, no new Type A or Type B pores can be produced at this stage.

Bulk water trapped pores ($O_F^1W_B^0$ or $O_F^0W_B^0$), either present originally or created during the displacement process, will no longer have any fluid configuration change, and the "frozen status" of such pores will be determined by the value of P_c when the trapping occurred. Untrapped water in $O_F^0W_B^1$ pores (no oil film connection to the inlet) can only be displaced by bulk displacement rather than snap-off. Furthermore, in $O_F^1W_B^1$ pores (continuous path of oil-wet pores from the inlet and untrapped bulk water) corner oil will accumulate from its current volume until piston-like displacement or snap-off occurs. Note that the initial position of *AMs* in the above pores is determined by their final status in the earlier WD process – either at the corners or in the inscribed circle (Figure 3-15).

For the pores that are classified as both $W_B^1O_F^0$ (in WD) and $O_F^1W_B^1$ (in OI) then, with the help of an adequate film oil supply and a bulk oil gateway, their oil films can keep swelling until piston-like displacement or snap-off occurs, just like regular $O_F^1W_B^1$ pores. However, the details require one slightly subtle nuance as follows: as we already know, the former trapping status of those $W_B^1O_F^0$ pores means that their *AMs* are in a critical status where the *AMs* just meet (characterized by $P_{c,invasion}$ which is higher than the negative final P_c of water drainage). To avoid an unrealistic instantaneous reduction in

oil saturation, we assume that fluids in such pores only alter their configuration until the value of P_c becomes larger than their recorded trapped $P_{c,invasion}$ value during WD –as illustrated in Figure 3-15 .

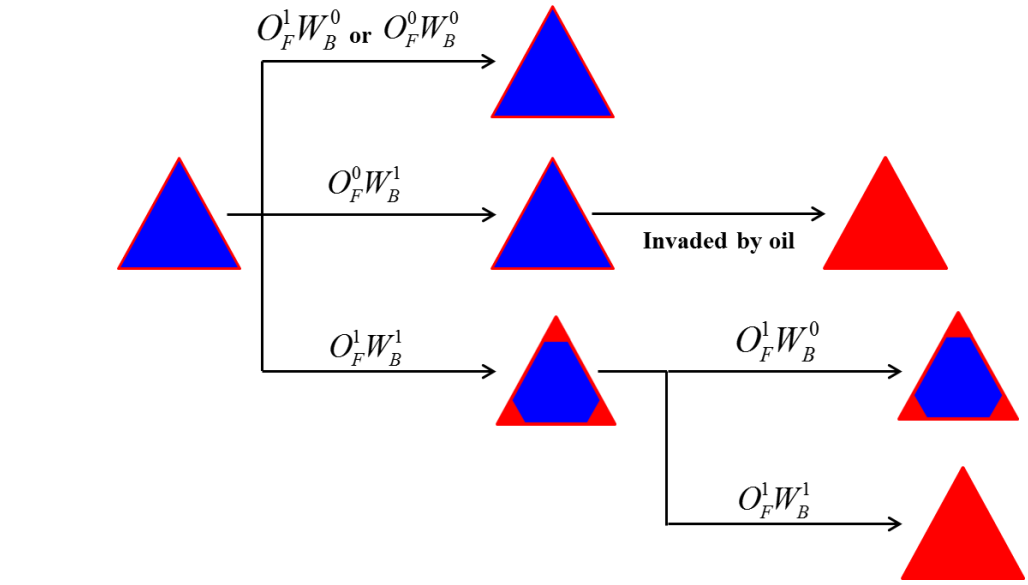

(a)

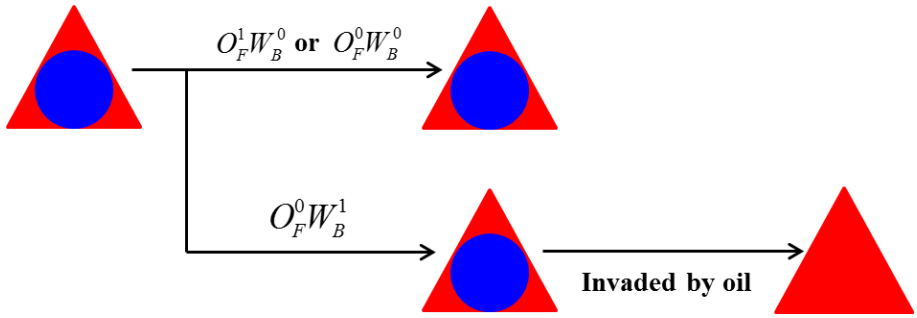

(b)

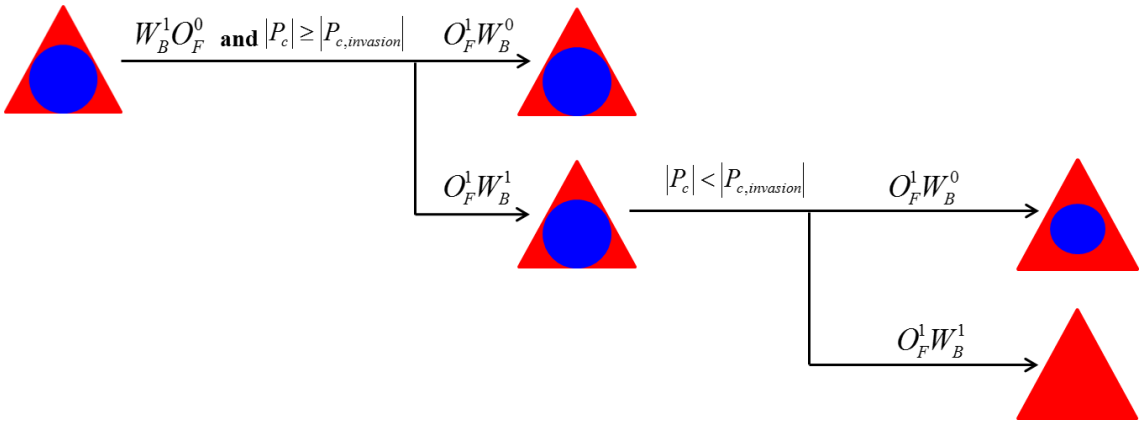

(c)

Figure 3-15 Diagram of Oil Imbibition (Type B pores). Blue as water and red as oil.

In this oil imbibition process, Type A pores ($W_F^1O_B^0$, $W_F^0O_B^1$ and $W_F^0O_B^0$) will remain frozen in their former state (Figure 3-16) – for the least thick water films (characterised

by $P_{c,max}$), no further shrinking is possible; while for bulk oil trapped pores, invading oil still cannot contact them at this stage.

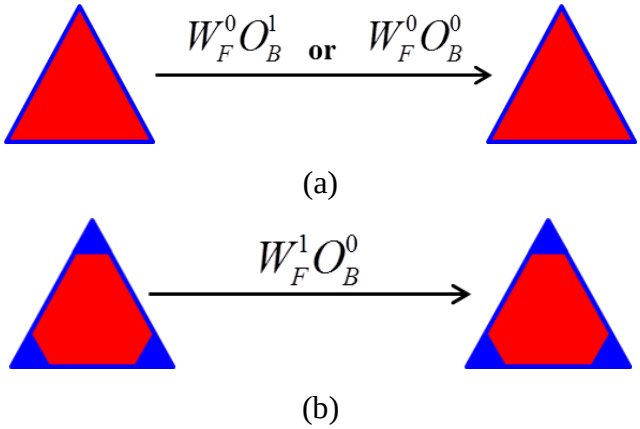

Figure 3-16 Diagram of Oil Imbibition (Type A pores). Blue as water and red as oil

Oil Drainage (OD):

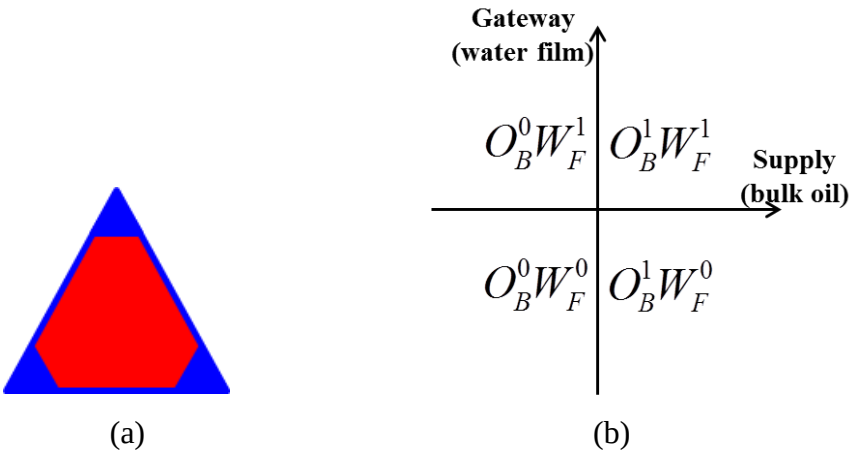

Figure 3-17 Primary fluids configuration and film-related pore type in oil drainage. Blue as water and red as oil

During oil drainage (OD), bulk oil is forced into water-filled, water-wet pores and creates some new Type A pores. To differentiate the Type A pores, we have an array to record if one of them is either newly produced during OD or was trapped during an earlier part of the flooding cycle. For the newly produced pore type, the only trapping scenario that can occur is if its corner water is disconnected from the outlet – this makes its designation $O_B^1W_F^0$ – and its pore saturation will remain unchanged from that point onwards. The other pores are $O_B^1W_F^1$ and their bulk oil will occupy the maximum central volume of the pores at the end of OD (Figure 3-18).

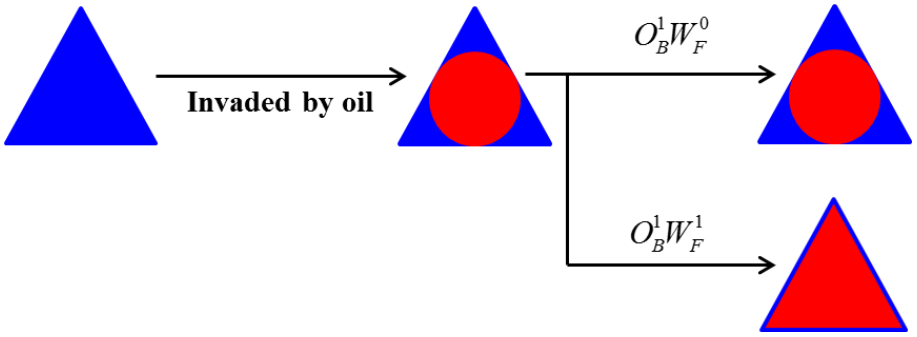

Figure 3-18 Diagram of Oil Drainage (newly produced Type A pores). Blue as water and red as oil

Type A pores created in the former process are the results of disconnected water film or bulk oil, whose fluids distributions are decided by the P_c at the moment of trapping – thus further water film shrinking, if possible, can only start after P_c increases beyond their recorded trapping capillary pressure value (Figure 3-19 (a)). Additionally, in some pores, the corner water volume is already characterized by the maximum P_c; thus even if these pores have proper connectivity to permit oil to flow into them, the process cannot lead to any saturation changes (Figure 3-19 (b)).

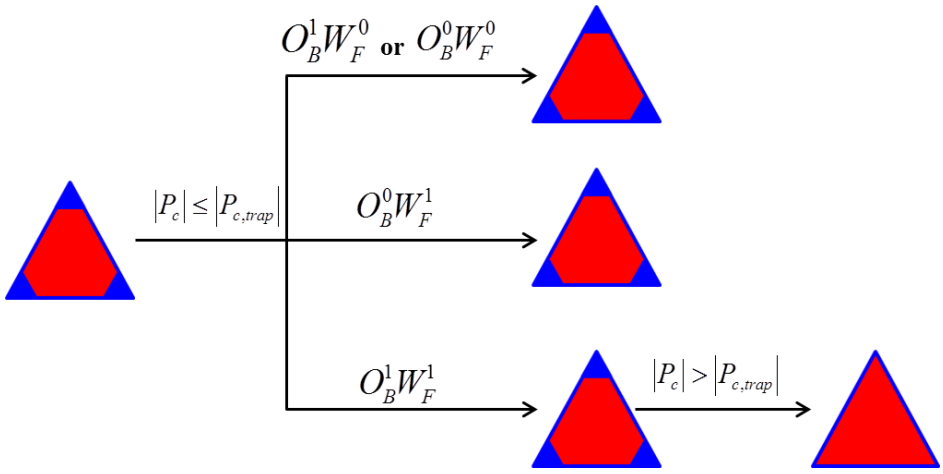

(a)

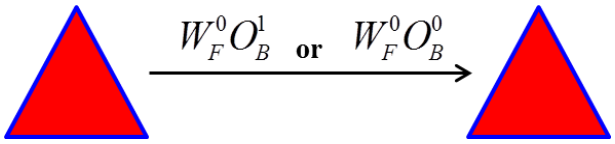

(b)

Figure 3-19 Diagram of Oil Drainage (Type A pores produced in former process). Blue as water and red as oil

Type B pores in OD will remain frozen; but piston-like displacement may possibly occur in pores with untrapped bulk water ($O_F^0W_B^1$ and $O_F^0W_B^0$), as illustrated in Figure 3-20.

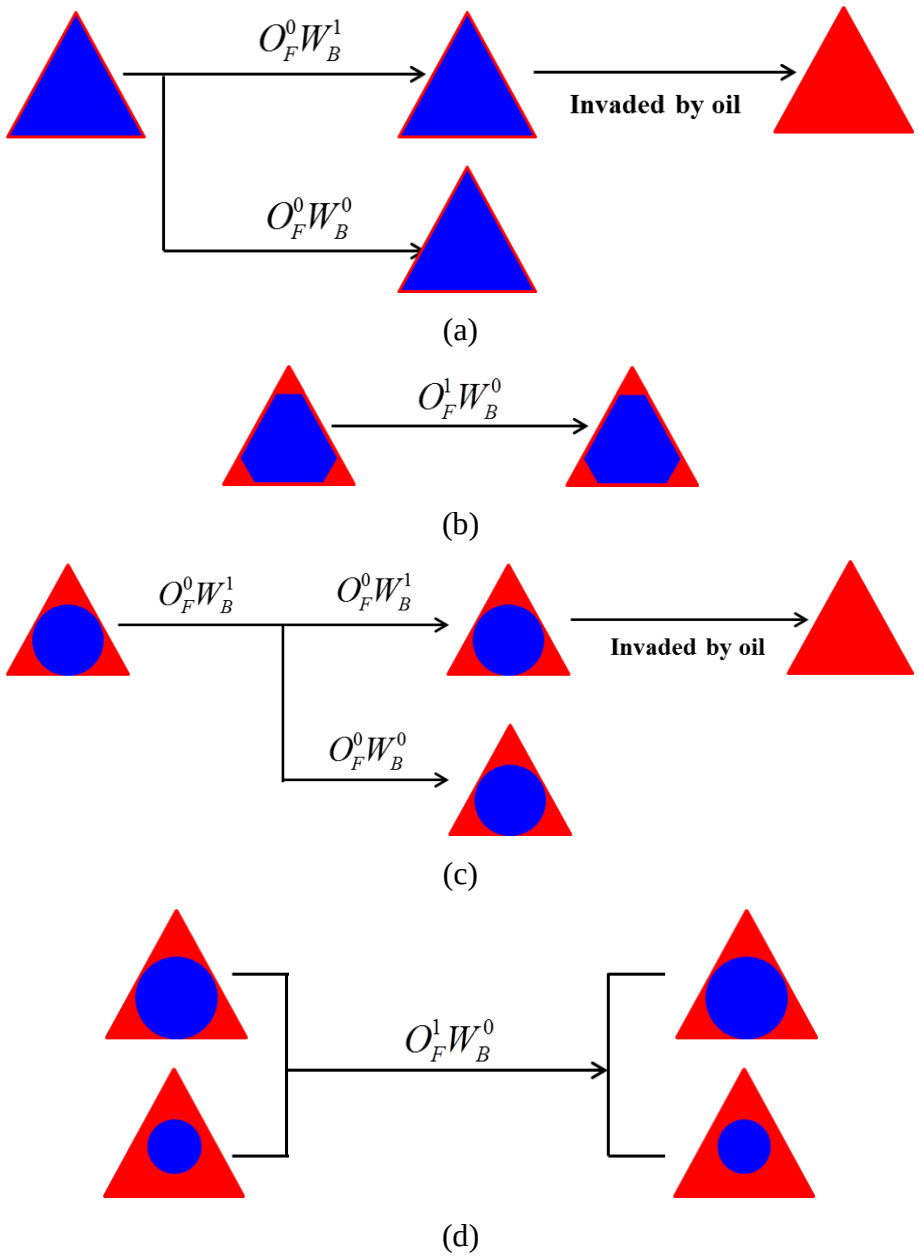

Figure 3-20 Diagram of Oil Drainage (Type B pores). Blue as water and red as oil

A complete diagram of the whole displacement cycle tracking the entire list of possible fluid events, fluid configurations, trapping scenarios, as well as the pore type is given below (Figure 3-22). We note again that the oil-lens "sandwich" case (as seen in Figure 3-21) has not been considered here because this case requires a more complex algorithm to simulate and track the fluids configuration alteration and it doesn't have much influence on the displacing result. As the reader can see, this is a complex tree of events

but we believe that it covers most of the physical processes that can occur in a standard flooding cycle in a mixed-wet system, i.e. PD, "aging" (wetting change), WI, WD, OI and OD.

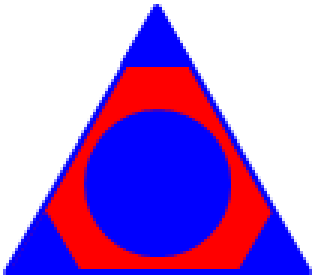

Figure 3-21 Illustration of the oil-lens "sandwich" case. Blue as water and red as oil.

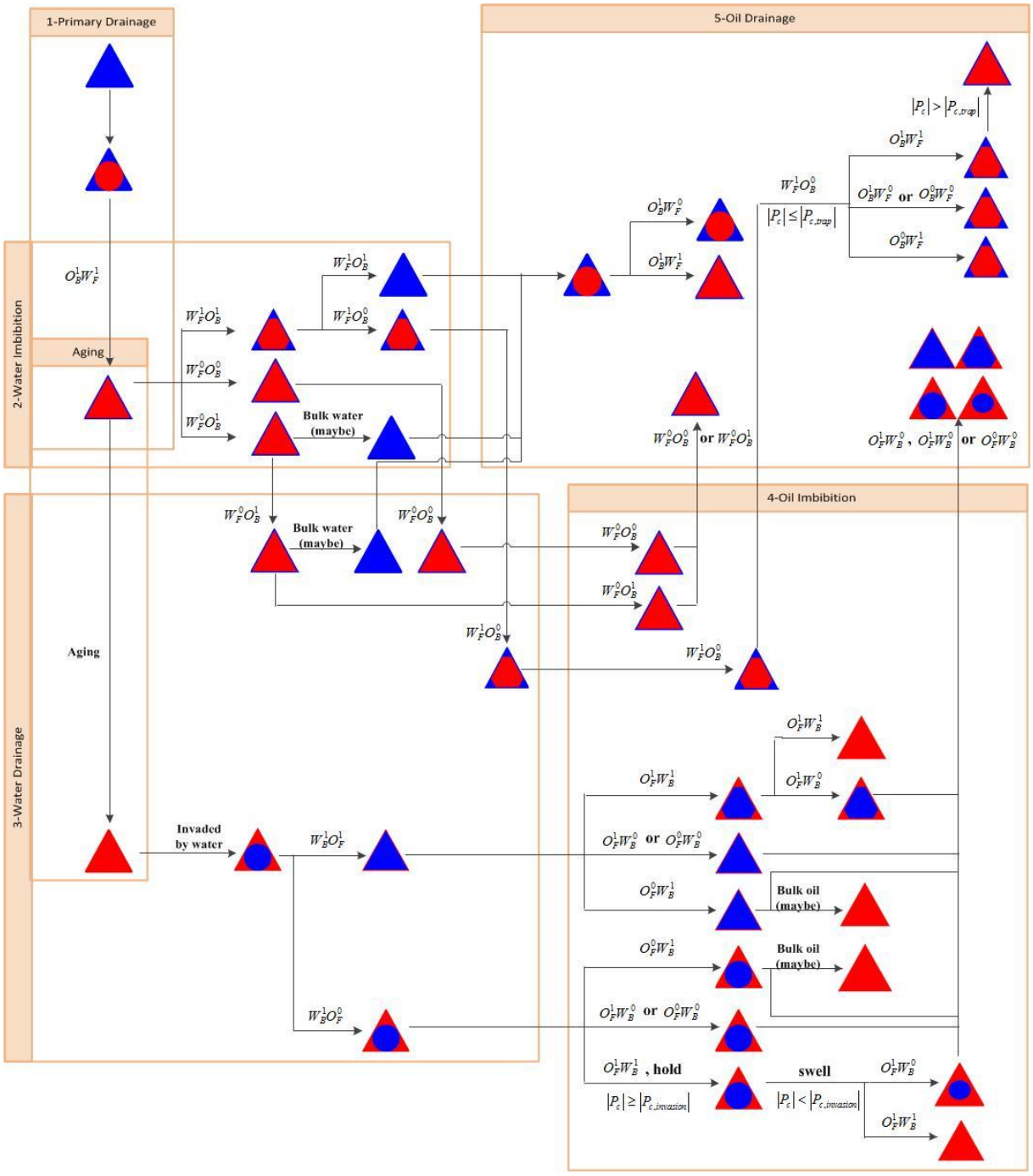

Figure 3-22 Diagram of the entire displacement circle. Blue as water and red as oil

3.3 Results for Quasi-statically Modelling Flooding Cycles in Mixed-wet Cases

The following scoping study compares capillary-dominated (quasi-static) flooding cycles highlighting the effect of wettability. In these calculations, the modelled capillary pressures and relative permeabilities will be analysed and any hysteresis which is observed will be noted. The focus of the work will then study primary drainage and water imbibition in much more detail and the influence of various parameters will be further studied. In this quasi-static model, the simulation time is positively correlated to

the network size: for a typical 20*20*20 network, it will take about 10 minutes to finish the whole displacement cycle.

3.3.1 Wettability and Hysteresis

Following on from the *MixWet* model described above, our new model can also distribute wettability after primary drainage in three ways: *mixed-wet large - MWL*, *fractional-wet-FW*, and *mixed-wet small-MWS* (Section 3.1.3). We examine the way in which different fractions of oil wet pores (α) and the pore size distribution of these oil-wet pores will affect the hysteresis in the capillary pressure and relative permeability curves.

Capillary pressure

In purely water-wet systems, water-films with perfect connectivity can swell and snap-off in water imbibition wherever topologically possible at a sufficiently high capillary pressure. The snap-off process will start from the smallest pores since they have the highest P_c. With the wide PSD range (1 to 50 micron), the S_w hysteresis at the beginning of WI is not dramatic, since the S_w increment brought in by snap-off in the smallest pores is quite small. However, at the beginning of WI, the capillary entry pressure for snap-off is significantly smaller than P_c for piston-like displacement, as shown in Figure 3-23 (a). But a high level of snap-off can also result in significant oil trapping and hence relatively high levels of residual oil saturation at the end of water imbibition. Under such circumstances, then, without oil-wet pores being present, there will be no saturation change in water drainage (WD) and oil imbibition (OI) processes. Not until the oil drainage stage, when oil is again forced into the system, is water displaced by oil from water-wet pores (Figure 3-23 (a)).

In a purely oil-wet system, all the oil-filled pores are oil-wet and so the absence of water films makes water imbibition impossible. Then the WD, OI, and OD processes are virtually the mirror images of PD, WI and WD in a purely water-wet model respectively (treat oil as wetting phase and water as non-wetting phase). This can be seen in the modelled capillary pressure curves for these processes (see Figure 3-23 (b)).

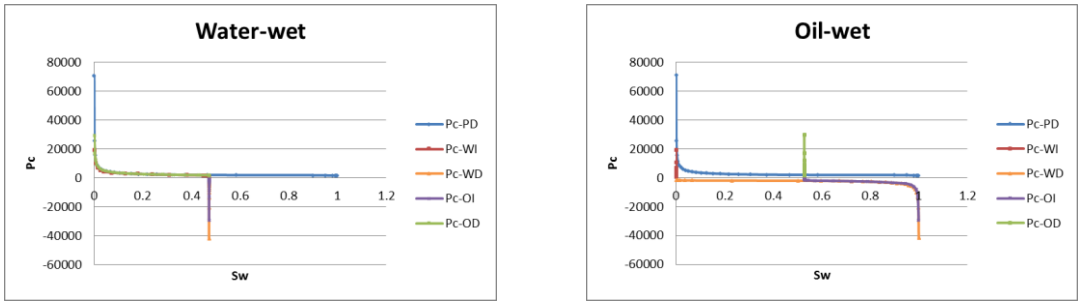

(a) water-wet (b) oil-wet

Figure 3-23 Capillary pressure hysteresis of water-wet and oil-wet system

After primary drainage, the system will alter the wettability of a fraction (α) of the oil-filled pores from water-wet to oil-wet. Invading water in the water imbibition (WI) stage of the cycle will completely ignore these oil-wet pores and the oil in these pores will reside in the system unchanged during WI. Therefore, under the same aging method, increasing the fraction α will result in a smaller water saturation increment since less oil is mobile in WI. Meanwhile, these resident oil-wet pores will reduce the connectivity of water films and consequently limit the extent of snap-off, which will reduce the oil trapping and enhance the oil recovery. Therefore, compared with a purely water-wet system, the presence of a fraction α of oil wet pores (α=0.25 or α=0.5) may enhance or reduce oil production, according to the specific aging criteria. The *Mixed-wet small* (MWS) wetting alteration (which is a user choice) changes the smallest pores to oil-wet. This limits the influence of residual oil in oil-wet pores and exaggerates the positive effect on oil recovery due to the lower degree of snap-off. A *mixed-wet large* (MWL) wetting change will have an opposite effect to that of the *mixed-wet small* change; and the *fractional wet* (FW) change will have an intermediate effect. Compared with a purely water-wet system, water invasion in a mixed wet system with a higher oil wet fraction (α=0.75) is limited by the reduced volume of oil resident in water-wet pores, regardless of the aging method (as shown by the red curves in Figure 3-24, Figure 3-25, and Figure 3-26). Statistically, according to the explicit aging method and fraction of oil-wet pores (α), the theoretical water saturation (as the ratio of the volume of oil resident in water-wet pores to the total pore volume, assuming all the oil residing in the water-wet pores can be displaced by the invading water, i.e. no oil-trapping) at the end of WI (ignoring oil-trapping) is listed below in Table 3-3, and the corresponding actual S_w at the end of WI is listed in Table 3-4. The differences between corresponding data ($S_{w,actual} < S_{w,theoritical}$) are caused by oil trapping – when α=0.25 and α=0.5, the differences are quite small and they are mostly the result of trapping in $W_F^1 O_B^0$ (water

film is connected to the inlet, bulk oil is disconnected from the outlet) pores; but when α=0.75, a large portion of water films are disconnected from the system inlet, the resulting oil trapping in $W_F^0 O_B^0$ (isolated pores with disconnected water film and bulk oil) and $W_F^0 O_B^1$ (oil is mobile but the water supply is cut off) pores cause the large differences observed.

Table 3-3 Theoretical S_w at the end of WI (ignoring oil-trapping)

	MWS	FW	MWL
α=0.25	0.97940	0.75486	0.42943
α=0.5	0.86044	0.50313	0.13246
α=0.75	0.55431	0.24243	0.01873

Table 3-4 Actual S_w at the end of WI

	MWS	FW	MWL
α=0.25	0.916741	0.680727	0.397835
α=0.5	0.856223	0.500841	0.132456
α=0.75	0.08078	0.042625	0.001869

After WI, the water drainage stage (WD) starts and oil-wet pores start to be invaded by bulk water; the extent of S_w change in this process is essentially determined by the volume of oil resident in the oil-wet pores. Under the same aging method, a larger volume of oil associated with the higher fraction α will lead to a larger S_w increment. Also, with the same fraction, a *mixed-wet large* (MWL) wetting change, by accommodating more oil in the larger pores, will encourage water displacing oil better than in other scenarios. The former trapped $W_F^1 O_B^0$ and $W_F^0 O_B^0$ pores in WI will remain trapped in WD, but with the water supply, oil in the $W_F^0 O_B^1$ pores may be displaced by the bulk water (if there is bulk water in surrounding elements). Oil then imbibes through swelling oil-films or by bulk piston-like displacement (OI) and then once again displaces water in water-wet pores in OD. The extent of S_w hysteresis is affected by both the aging method (MWL, MWS, FW) and the value of α; the analysis in OI and OD is similar to that of water imbibition and water drainage, (treat oil as wetting phase

and water as non-wetting phase) (as shown in Figure 3-24, Figure 3-25, and Figure 3-26).

The radius step and P_c step are chosen by the user and independent from the wettability status in each system. However, according to the earlier analysis, at each P_c step, wettability *will* affect the S_w increment; thus the hysteresis observed in the P_c curves. Taking WI as an example, with the same aging method, as the fraction of oil-wet pores (α) increasing, less pore elements will be open to the invading water. Thus within a certain P_c step, the number of events (piston-like displacement or snap-off) will be reduced and the resulting S_w increase will be less. And with the same α, as P_c decreases during WI, displacements will first occur in the MWL system, since the smallest pores (water-wet and characterised by the highest capillary entry pressure) are open to the invading water; but the displacement will terminate at the smallest S_w, since the oil will be left in the largest, oil-wet pores. On the contrary, the network for the MWS system cannot have much oil displacement at the beginning of WI (when P_c is high); but as capillary pressure decreases, more and more oil in the larger water-wet pores can be displaced and cause the largest S_w increment. Similar analysis can be conducted for other processes.

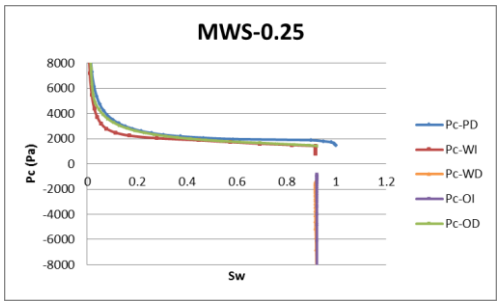

(a) α=0.25

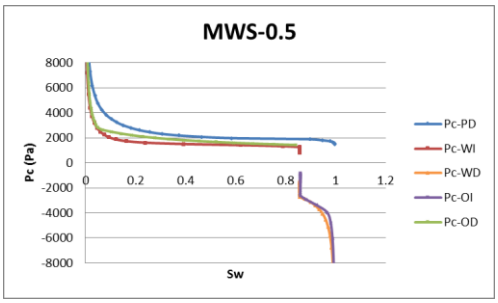

(b) α=0.5

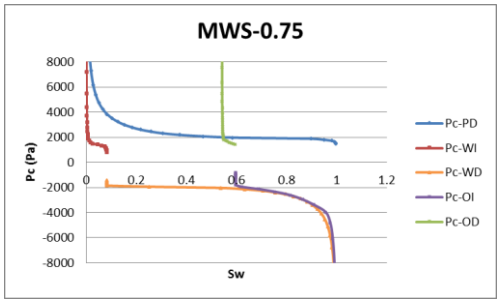

(c) α=0.75

Figure 3-24 Capillary pressure hysteresis of *mixed-wet small* system

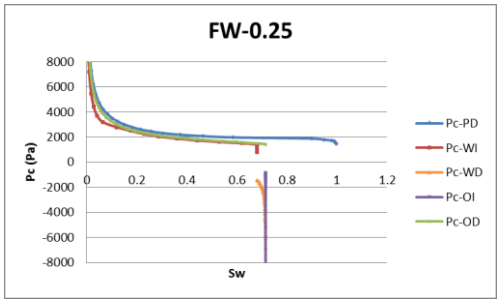

(a) α=0.25

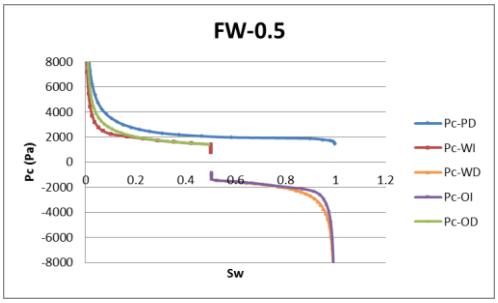

(b) α=0.5

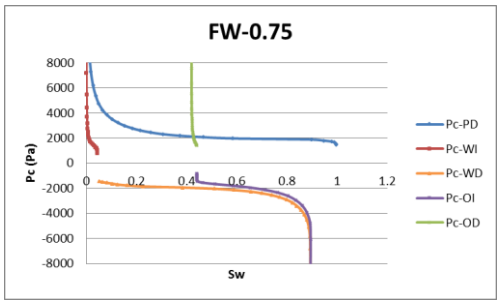

(c) α=0.75

Figure 3-25 Capillary pressure hysteresis of *fractional-wet* system

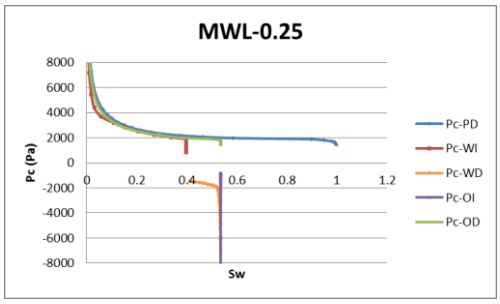

(a) α=0.25

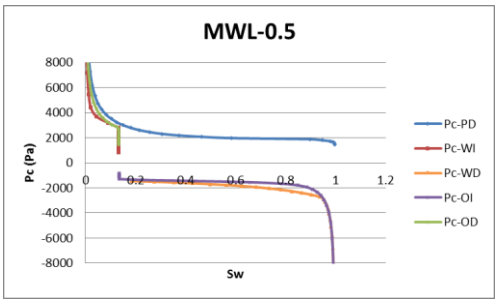

(b) α=0.5

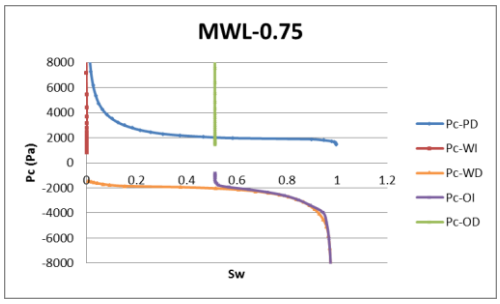

(c) α=0.75

Figure 3-26 Capillary pressure hysteresis of *mixed-wet large* system

Relative permeability hysteresis in heterogeneously-wet systems

In "pure" (non-forced) water imbibition, the injected water can only displace bulk oil resident in water-wet pores; therefore, a purely oil-wet system will imbibe no water and relative permeabilities will not change in this process (Figure 3-27 (b)). In a purely water-wet system, however, oil will have lower permeability in WI than that in PD due

to snap-off and oil trapping, and water permeability curves in PD and WI almost overlap with each other (because C_w limits the film conductance) (Figure 3-27 (a)).

Later in water drainage, the invading water will be forced to displace the bulk oil resident in oil-wet pores through piston-like displacement and continue displacing oil by pushing the oil film towards the pore corners (oil film shrinking). Without oil-wet pores, the purely water-wet system will have no water saturation change at all during WD (Figure 3-27 (a)). In a purely oil-wet network, however, the displacement is almost the mirror image of primary drainage (treating oil as the wetting phase and water as the non-wetting phase) (Figure 3-27 (b) and (c)).

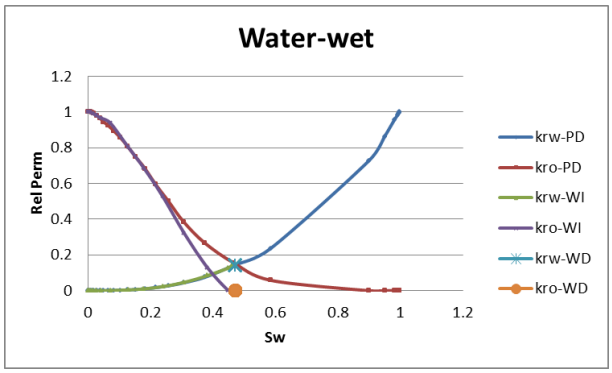

(a) water-wet

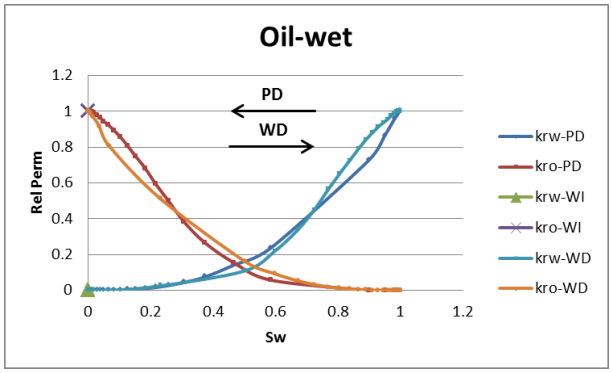

(b) oil-wet (Rel perm vs S_w)

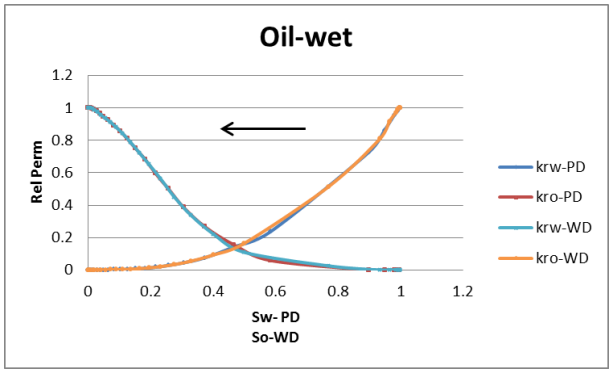

(c) oil-wet (Rel perm vs S_w (PD)/ S_o (WD))

Figure 3-27 Relative permeabilities hysteresis of water-wet and oil-wet system

In accordance with the discussion in the last section, it can also be observed in the relative permeability hysteresis that oil in oil-wet pores will be ignored by invading water in WI: under each aging method, S_w alteration decreases as the fraction α grows (since less and less oil will be available to the invading water); and with the identical fraction, a *mixed-wet* large (MWL) wetting change will have the biggest volume of immobile oil in oil-wet pores and least S_w increment (as seen in Figure 3-28, Figure 3-29, and Figure 3-30).

At the beginning of WI, k_{ro} in MWS systems is slightly higher than oil relative permeability at the same S_w in PD – hardly any displacement occurs in WI when P_c is high, since the *smallest* pores in this system are all oil-wet. When P_c decreases to a particular value, displacements start to occur in the larger pores in a MWS system – a large S_w increment and a sudden drop in k_{ro} curve can be observed. In MWL and FW systems, the initial k_{rw} and k_{ro} have similar values as their counterparts in PD. Initially, the displacements which occur in the smallest pores can only cause a small S_w increment and oil-trapping then is rare. As P_c decreases, the smaller k_{ro} (comparing with k_{ro} in PD at the same S_w) observed is the result of oil-trapping. In the system with higher α, the k_{ro} reduction tends to be smaller because the larger fraction of oil-wet pores reduces the connectivity of the water-film and the degree of snap-off. The water-films are disconnected by the presence of oil-wet pores, hence the lower water relative permeabilities (Figure 3-28, Figure 3-29 and Figure 3-30).

During WD, the former immobile oil during WI can now be displaced. With the same aging method, the increasing fraction α means more oil is mobile in this process and a larger S_w increment can be observed. At the beginning of WD, both the k_{ro} and k_{rw} are smaller than the corresponding k_{ro} and k_{rw} in PD at the same S_w value (considering oil-trapping and less-connected water films in WI). During water drainage, the invading bulk water can re-connect the former isolated water films and invade the previous trapped $W_F^0 O_B^1$ pores (water film disconnected from the inlet, bulk oil is connected to the outlet). Also, oil in oil-wet pores that was frozen in WI can participate the displacement in WD – hence the k_{rw} and k_{ro} observed in Figure 3-28, Figure 3-29, and Figure 3-30.

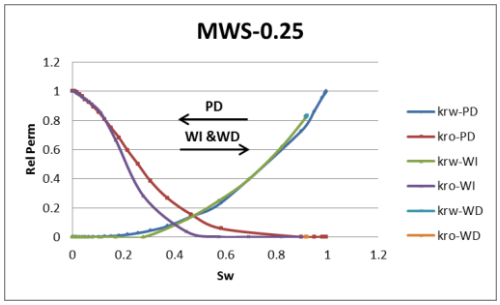

(a) α=0.25

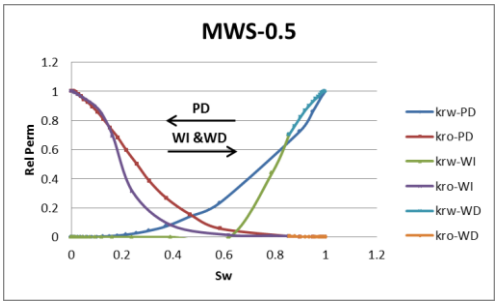

(b) α=0.5

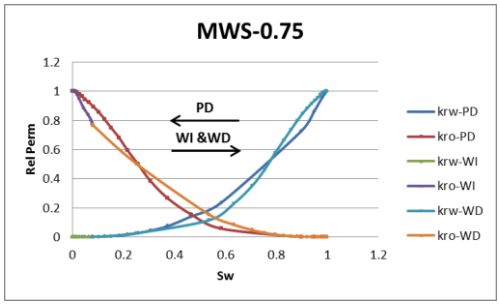

(c) α=0.75

Figure 3-28 Relative permeabilities hysteresis of *mixed-wet small* system

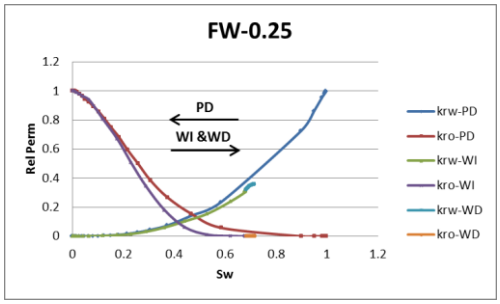

(a) α=0.25

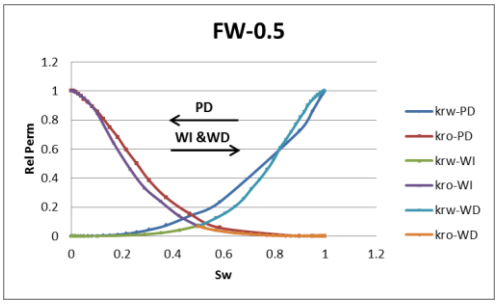

(b) α=0.5

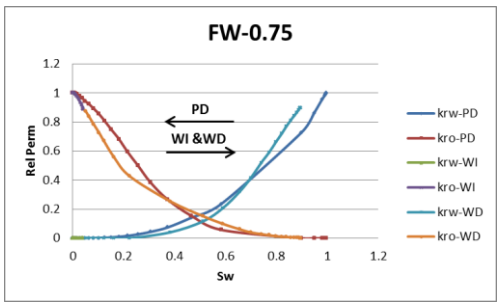

(c) α=0.75

Figure 3-29 Relative permeabilities hysteresis of *fractional-wet* system

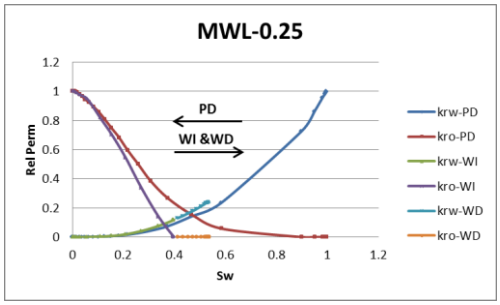

(a) α=0.25

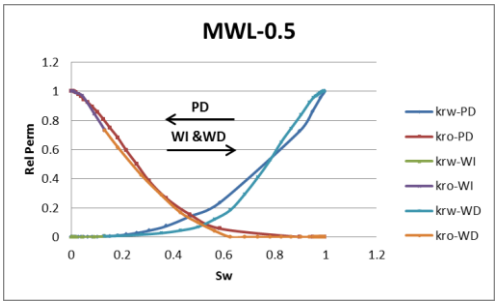

(b) α=0.5

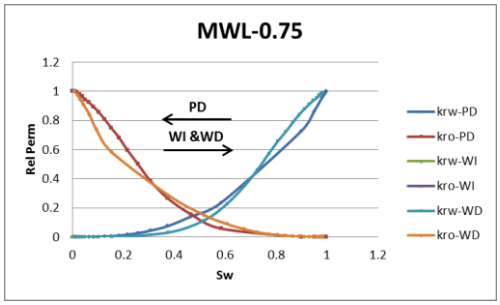

(c) α=0.75

Figure 3-30 Relative permeabilities hysteresis of *mixed-wet large* system

In conclusion, the S_w at the end of water imbibition (WI) is determined by (1) the volume of mobile oil present in the water-wet pores, and (2) the degree of oil-trapping. Note that when α=0.25 and α=0.5, the residual oil is mostly trapped in $W_F^1O_B^0$ pores, but when α=0.75, a large portion of water films are disconnected from the system inlet, the resulting oil trapping in $W_F^0O_B^0$ and $W_F^0O_B^1$ pores can result in a large volume of oil frozen in water-wet pores. The volume of oil in oil-wet pores determines the oil recovery (S_w) at the end of WD, and the bulk oil trapped in $W_F^1O_B^0$ and $W_F^0O_B^0$ pores will remain immobile.

The P_c step is independent of the wettability status in each system. However, at each P_c step, wettability *will* affect the S_w increment since within a certain range of pore sizes, some pores may be oil-wet and cannot have any oil displacement.

Compared with the relative permeabilities for PD, both k_{ro} and k_{rw} in WI are smaller – oil trapping and immobile oil in oil-wet pores will limit the oil relative permeability, and the less connected water films will reduce the mobility of water. During WD, the invading bulk water can re-connect the former isolated water films. Previously immobile oil in oil-wet pores and $W_F^0O_B^1$ pores (providing bulk water can be found in neighbouring elements) regain its mobility during this forces water flooding.

3.3.2 Parametric Study Using Angular Pore Shapes

In this section, several factors that may affect the PD and WI results are investigated. These will be revisited later and compared with the dynamic results, in an attempt to explain the observed difference between SS and USS relative permeability (RP) curves.

Pore shape

It is clear that the displacement result will affected by both the pore shape and contact angle, in this section, for simplicity, we only discuss the influence of pore shape with constant contact angle ($\theta=0^o$).

In a circular-pore system (*MixWet*), the bulk oil will occupy the whole pore volume of an individual cylindrical pore, while in triangular pores (this quasi-static model) the non-wetting phase can only fill the central part of the pore due to the existence of corner films. Hence at a given P_c, a larger corner water volume and higher water saturation exists in the angular pore system. The corner water area and the corresponding local water saturation ($S_w^*=A_{corner}/A_{total}$) differences are governed by the value of S_1 and shape factor (Figure 3-31). Therefore, generally speaking, going from a circular (C) pore systems to an equilateral-triangular (E-T) pore systems to a scalene-triangular (S-T) pore systems (i.e. with decreasing shape factor), the corresponding P_c and relative permeability curves will shift to right with higher S_w.

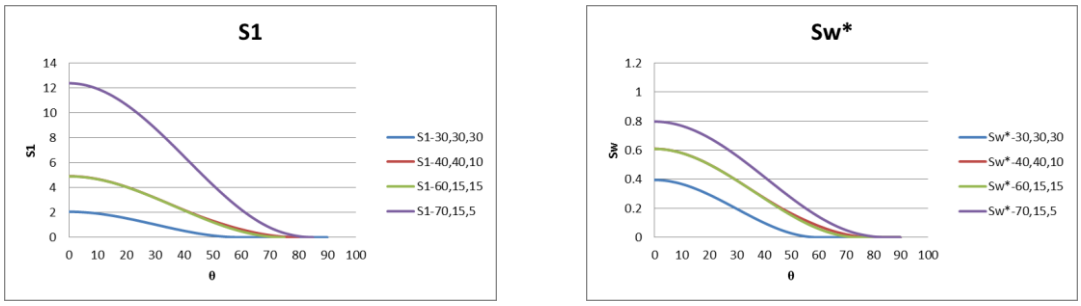

(a) S_1 (b) S_w

Figure 3-31 S_1 and S_w of different pore shape. For different triangles, the values of their half angles β_1, β_2, β_3 are shown in the legend.

Capillary entry pressures of piston-like displacement and snap-off are computed using different expressions of F_d^* and $F_d^{snap-off}$ in circular pores and angular pores (as seen in Section 3.2.2). Based on Figure 3-32 (a), with other conditions fixed, for piston-like displacement, circular pores have the highest capillary entry pressure and equilateral triangular pores come second. For snap-off, however, due to $\theta=0^o$, snap-off will occur

when 3 *AMs* meet at the inscribed circle, thus all the pore shapes will have the identical capillary entry pressure (Figure 3-32 (b)).

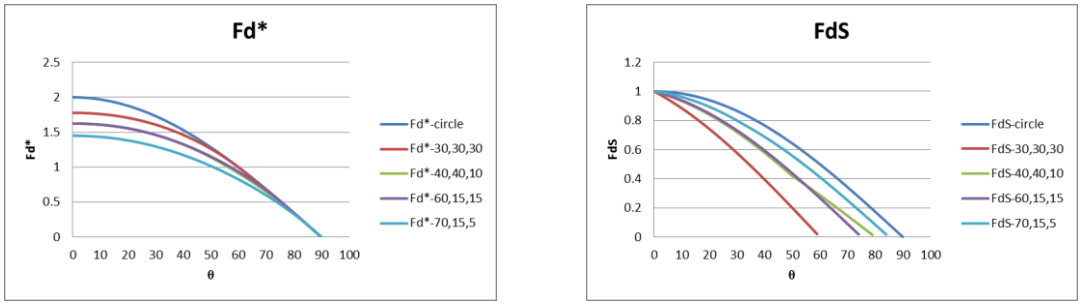

(a) F_d^* (b) $F_d^{snap-off}$

Figure 3-32 F_d^*, and $F_d^{snap-off}$ of different pore shape. For different triangles, the values of their half angles β_1, β_2, β_3 are shown in the legend.

In primary drainage, as more water-filled pores are invaded by oil, the S_w difference between corresponding curves increases. In the later stages of primary drainage (lower S_w), however, we expect the shift to get progressively smaller, since increasing P_c leads to a decreasing radius of *AMs* and thus a smaller volume of corner water in the triangular pore system. Alternatively, throughout water imbibition, the swelling water film increases these shifts (Figure 3-33).

From Figure 3-33, it can also be seen that the differences between oil relative permeability curves are clear, while the shifts of the k_{rw} curves are much smaller since the water film conductance is limited by the resistance of the solid, C_w. Note, although wetting films cannot expand in circular pores, snap-off is possible – as long as it is topology possible with untrapped oil and suitable capillary entry pressure.

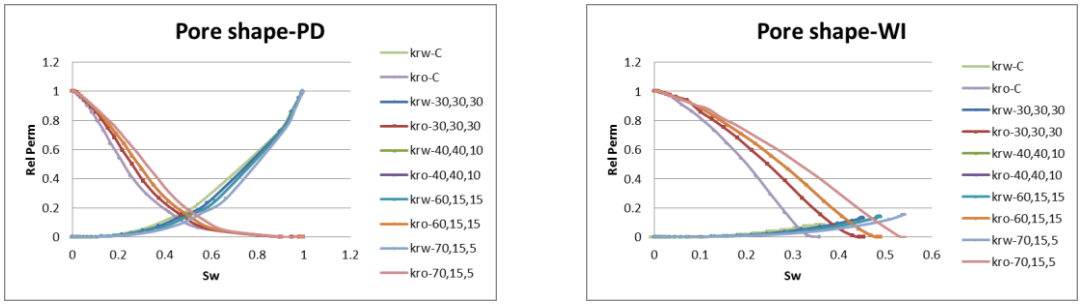

(a) PD (b) WI

Figure 3-33 Relative permeability comparisons of systems with different pore shapes. Various pore shapes (circle (C), equilateral-triangle (E-T), scalene-triangle (S-T)) are shown in the legend.

Contact angle

After primary drainage, contact angle can be altered to produce a wide range of wetting condition, the discussion below will focus on the water-wet system $0^o \le \theta < 90^o$.

For circular pores, although both piston-like displacement and snap-off are possible in imbibition (water displacing oil), no film alteration will occur. Displacement occurs in ascending order of pore radii (or descending order of capillary entry pressure), and therefore it is independent of the contact angle if a single contact angle is specified, i.e. contact angle uniformly affects the capillary pressure in each pore without changing the order (Figure 3-34 (a)). The relative permeabilities are therefore independent of θ (Figure 3-34 (b)).

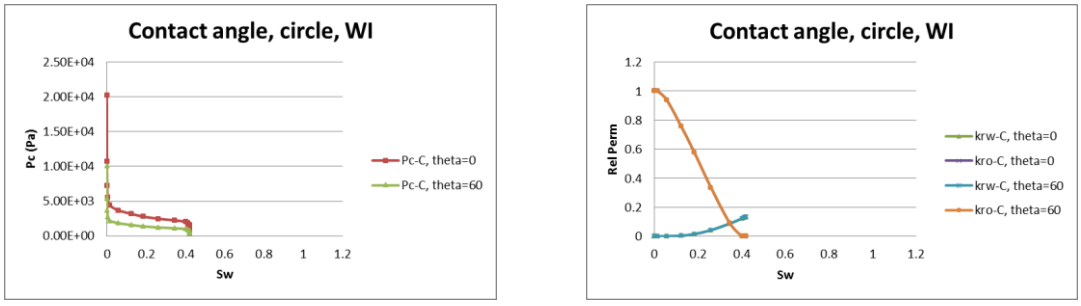

(a) P_c (b) Rel Perm

Figure 3-34 Capillary pressure and relative permeability comparisons of circular pore systems with different contact angle.

In triangular pores, at the same radius level, an increasing value of contact angle will reduce the capillary entry pressure for piston-like displacement and snap-off through F_d^* and $F_d^{Snap\text{-}off}$ (Figure 3-35 and Figure 3-36 (a)). The ratio of $\frac{F_d^*}{F_d^{snap-off}}$ represents the difference between capillary entry pressures of piston-like displacement and snap-off. During WI, when snap-off occurs in the smallest pores, the current capillary pressure will be $P_c = \frac{F_d^{snap-off} \cdot \sigma}{r_{\min}}$, which is low enough to allow piston-like displacement occurs in pores with radius smaller than $r^{piston-like} = \frac{F_d^*}{F_d^{snap-off}} \cdot r_{\min}$, where applicable. Therefore, with higher value of $\frac{F_d^*}{F_d^{snap-off}}$, a larger fraction of pores will be filled through piston-like displacement at the beginning of WI, before snap-off event occurs. And in the

extreme case where $\frac{F_d^* \cdot \sigma}{r_{\max}} \geq \frac{F_d^{snap-off} \cdot \sigma}{r_{\min}}$, snap-off will be suppressed completely. Figure 3-35 (b) shows that as contact angle increases, the value of $\frac{F_d^*}{F_d^{snap-off}}$ increases as well (as long as there is at least one *AM* presenting in the pore). Consequently, fewer number of snap-off events will be observed in the high θ cases (as verified by Figure 3-36 (c)).

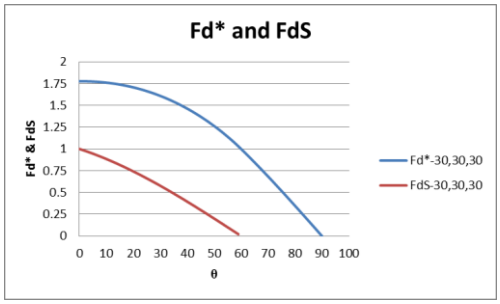

(a) F_d^* and $F_d^{snap-off}$

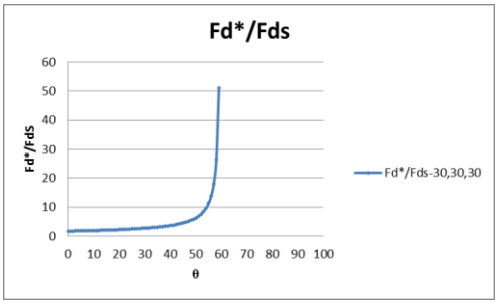

(b) $\frac{F_d^*}{F_d^{snap-off}}$

Figure 3-35 F_d^*, $F_d^{snap-off}$, and $\frac{F_d^*}{F_d^{snap-off}}$ in equilateral triangular pore with various contact angles.

From Figure 3-31 (b), it can be seen that S_w decreases with increasing contact angle, until θ increases above 60 degree where the equilateral triangular pore loses its ability to accommodate any wetting film (assuming that this pore has unit inscribed radius).

Hence, in a manner similar to the analysis of pore shape, at the same *radius* level, P_c and relative permeability curves are expected to move to the left (lower S_w) as contact angle increases, due to the smaller area occupied by corner water at the same radius step (although there will be less snap-off events) (Figure 3-36). Note here, in order to be compared with the unsteady-state displacement results later, snap-off is not allowed to occur in $\theta=60^o$ case without corner water. Similar to other cases, the limited water film conductance reduces the k_{rw} difference compared with k_{ro} curves.

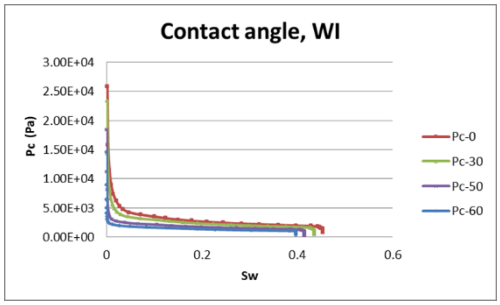

(a) P_c

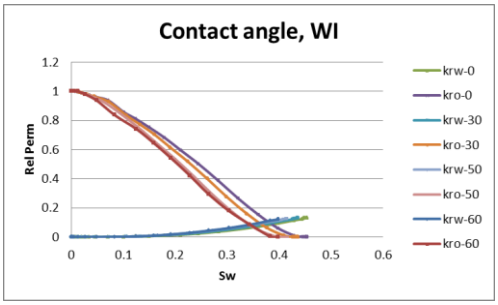

(b) Rel Perm

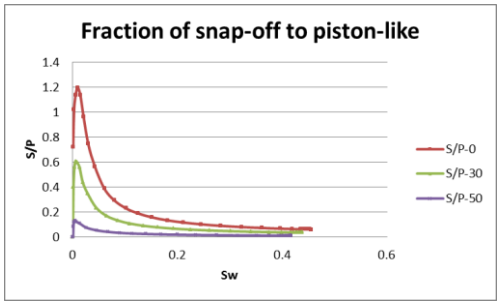

(c) Fraction of counts of snap-off and piston-like displacements (S/P)

Figure 3-36 Capillary pressure and relative permeability comparisons of systems with different contact angle in equilateral-triangular pore system.

Pore size distribution

As discussed above, the value of capillary pressure is inversely proportional to the pore radius. Hence, comparing with the base case (PSD (1,50)) (in which pore size ranging from 1 micron to 50 microns uniformly), a system characterised by a minimum inscribed pore radius of 11 microns will require a smaller P_c at the end of primary drainage to complete all the possible bulk piston-like displacements. As a result, in the triangular pore system, with radii varying from 11 to 40 microns, we can expect a larger volume of corner water and thus a larger S_w when PD ends (Figure 3-37).

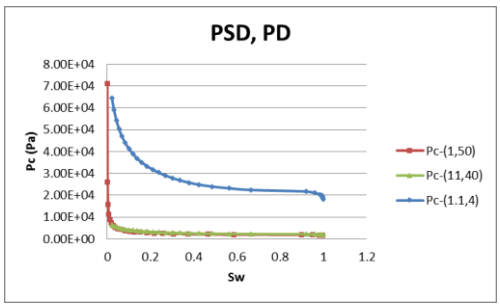

(a) PD

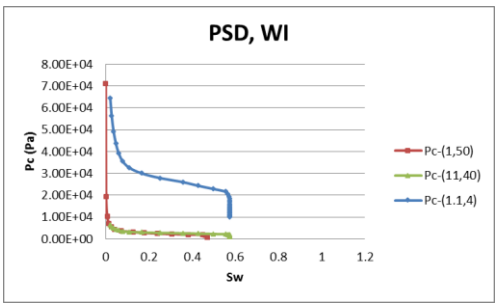

(b) WI

Figure 3-37 Capillary pressure comparisons of systems with different pore size distributions.

Other than contact angle, the value of $\frac{r_{\max}}{r_{\min}}$ can also control the fraction of numbers of snap-off to piston-like displacement: as discussed in last section, when snap-off occurs in the smallest pores, piston-like displacement can occur in pores with radius smaller than $r^{piston-like} = \frac{F_d^*}{F_d^{snap-off}} \cdot r_{\min}$, where applicable. Therefore, in the system with narrower radius range, a higher fraction of pores will be filled through piston-like displacement, as seen in Figure 3-38 (b). On top of the less snap-off, water-filled pores in the (11,40) system have larger pore volume and better influence on the global S_w than in the (1,50) network, hence the horizontal shift observed in Figure 3-38 (a).

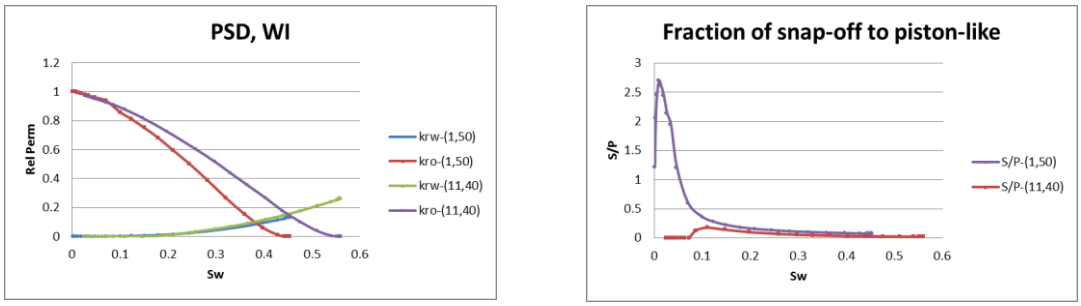

(a) Rel Perm (b) S/P

Figure 3-38 Relative permeability comparisons of systems with different pore size distributions.

Meanwhile, comparing the (11,40) system with (1.1,4) system (same R_{max}/R_{min} but higher mean radii), the resulting RP curves are overlapping since a uniform effect in each pore; the filling order remains the same (Figure 3-38 and Figure 3-37), although the capillary pressure curves differ by 3 orders of magnitude.

Coordination number, Z

A fully connected 3D system (Z=6) has more continuous paths for both bulk oil and water films and hence results in higher relative permeabilities in both primary drainage and in water imbibition. In addition, this better connected network can effectively reduce the degree of oil trapping by providing the non-wetting phase with more downstream outflow pathways, eventually resulting in a better oil recovery following water imbibition (Figure 3-39).

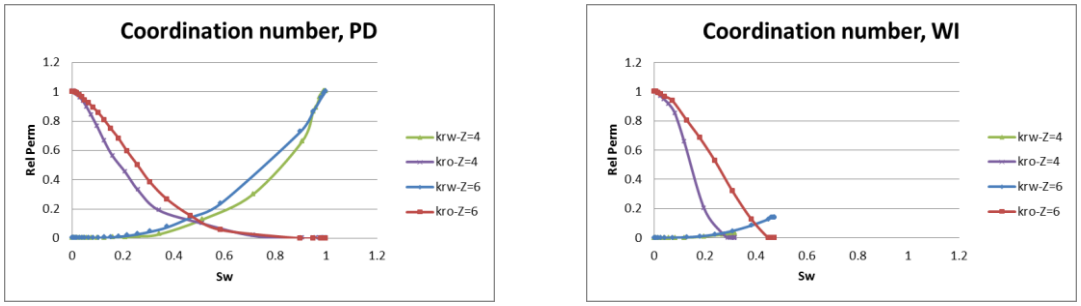

(a) PD (b) WI

Figure 3-39 Relative permeability comparisons of systems with different coordination numbers.

The resistance factor of solid, C_w

Taking different values of C_w will have no influence on the filling order, which is determined by the capillary entry pressure. Therefore, the capillary pressure curves and oil relative permeability curves are independent of this quantity (C_w). However, C_w is able to impact the k_{rw} curves through its effect on the film conductances, i.e. a higher resistance of the solid (higher C_w) will reduce the film mobility and hence lower the water relative permeability (Figure 3-40). The effect is not great but is observable in these results.

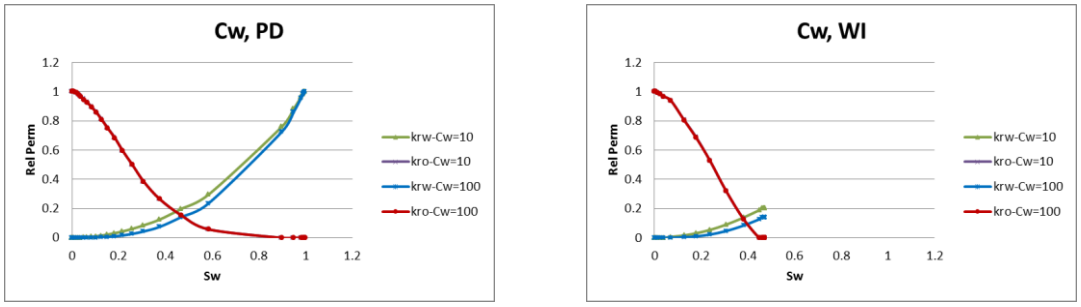

(a) PD (b) WI

Figure 3-40 Relative permeability comparisons of systems with different C_w.

Additional Sensibilities

Finally, the various parameters listed in Figure 3-41 will have no influence on the filling results in this quasi-static model; but as discussed later in Chapter 5 and 6, they *will* affect the displacement in dynamic water imbibition. These parameters are pressure drop (ΔP), pore length (L), water/oil interfacial tension (IFT or σ) and viscosity ratio ($M=\mu_o/\mu_w$). They affect each pore uniformly; hence, they have no influence on the resulting relative permeability curves, since both the filling order and specific film behaviours are independent of these parameters (ΔP, L, σ and μ_o/μ_w) ***in this quasi-***

static model. For example, interfacial tension, IFT, determines the value of capillary entry pressure without changing the filling order.

Viscosity ratio is the ratio of defending phase viscosity to the invading phase viscosity, particularly, in water imbibition, $M = \mu_o / \mu_w$. Although various viscosity ratios can affect the conductance (less viscous phase will flow faster), the influences on bulk water and wetting film are equal; thus, relative permeabilities are unchanged. Viscosity ratio is an important parameter in 2-phase flow in porous media but it is not important in a quasi-static model. However, $M = \mu_o / \mu_w$ will play an important role as explained later in the dynamic model.

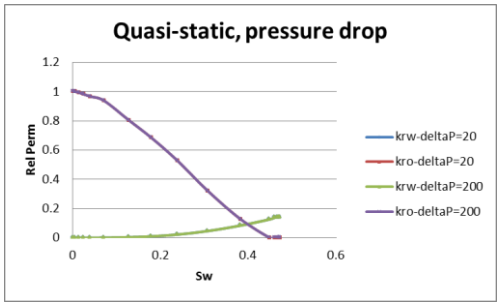

(a) pressure drop

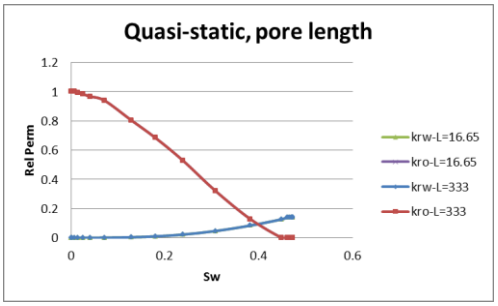

(b) pore length

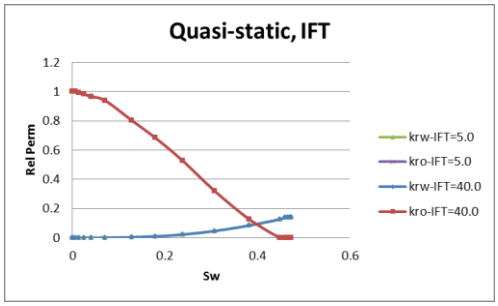

(c) IFT

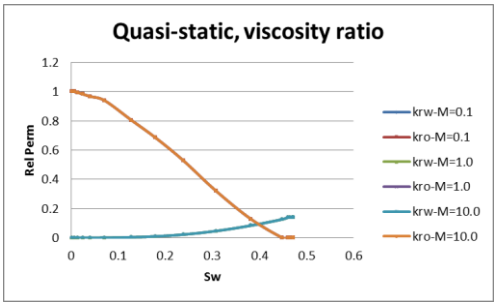

(d) viscosity ratio

Figure 3-41 Parameters that have no influence on relative permeabilities

3.4 Summary and Conclusions

In this chapter, we have presented an updated quasi-static pore network model now incorporating angular pore shapes to simulate specific bulk and film behaviours. Formulae of important parameters were modified according to pore geometry and more detailed film behaviours (swelling, shrinking and trapping) were simulated in each displacing cycle.

The following conclusions can be obtained from our parametric wettability study:

1. Under the same aging method, oil recovery in water imbibition (WI) is subsequently reduced as the fraction of oil-wet pores (α) grows, while larger S_w increment in water drainage (WD) will be observed in system with high α.
2. The *Mixed-wet small* (MWS) wetting change limits the influence of residual oil in oil-wet pores and exaggerates the positive effect on oil recovery due to the lower degree of snap-off. A *mixed-wet* large (MWL) wetting change will have an opposite effect to that of the *mixed-wet small* change; and the *fractional wet* (FW) change will show an intermediate range of behaviours.
3. Considering water snap-off and oil trapping, oil relative permeability in WI is lower than that in PD. Moreover, regardless the aging method and fraction of oil-wet pores, water relative permeability in a mixed wet system in WI is lower than that in PD because the water films are less-connected.
4. In water drainage, the forced bulk water will displace the oil present in oil-wet pores and re-connected the water films in mixed-wet systems, thus k_{rw} and k_{ro} may be found to be higher than the corresponding RPs in PD.

In an attempt to explain the observed difference between SS and USS relative permeability (RP) results (later in this thesis), several factors that may affect the displacements have been investigated and will be revisited later in the context of the new dynamic model proposed below:

1. Going from a circular (C) pore system to an equilateral-triangular (E-T) pore system to a scalene-triangular (S-T) pore system, a larger volume of corner water will result in higher S_w, and lower capillary pressure because of the subsequently smaller F_d^*.
2. In systems with angular pores, as contact angle (θ) increases, P_c and relative permeability curves are expected to be shifted to lower S_w and relatively fewer snap-off events can be observed.
3. For an identical mean radius, a narrower radii range will result to less snap-off, and the water-filled pores have larger pore volume and better contribution to the global water saturation.
4. Higher coordination number (Z) can effectively reduce the degree of oil trapping by providing more continuous paths for both oil and water phases to escape through – hence the higher relative permeabilities and better oil recovery in WI.
5. Higher resistance of solid (C_w) will reduce the film mobility and water relative permeability.

6. In this quasi-static model, factors such as pressure drop (ΔP), pore length (L), water/oil interfacial tension (IFT or σ), viscosity ratio ($M=\mu_o/\mu_w$), and mean radii (R_{mean}), have no influence on the resulting relative permeability curves, which is not the case in the later dynamic model.
7. Due to the limited conductance of water film, under most of the investigated factors (except C_w), the differences seen between k_{rw} curves are far smaller than those between k_{ro} curves.

4 Dynamic Network Model of Imbibition

In this chapter, we will introduce the novel dynamic model of imbibition: the invading phase (water) is injected into the system at constant flow rate and displaces the defending phase (oil) through advancing bulk water/oil menisci and/or swelling wetting film. The primary filling mechanism and filling order are determined by the competition between viscous forces and capillary forces. This model correctly reproduces the flow regimes that were observed in the micromodel experiments of imbibition (Lenormand and Zarcone (1984)) and is used to study the influence of various parameters on flow regimes (Chapter 5) and relative permeabilities (Chapter 6).

4.1 Assumptions of the Model

In this model, we assume that the flow is immiscible and laminar. There is a linear relationship between local pressure drop and flow rate, but in pores with bulk water/oil menisci, the local capillary entry pressure will be considered in the calculation of local flow rate (Section 4.4.2). This model is based on the following assumptions (which may be relaxed in the future work):

1. For simplicity, this model only focuses on the purely water-wet system, wettability alteration (ageing) after primary drainage will not be considered here. In the later study of contact angle, θ will be constant throughout the system or distributed within the (0^o, 90^o) range.
2. The primary filling mechanism (piston-like displacement and snap-off) is determined by the pore-level competition between capillary forces and viscous forces. To capture this, the model introduces a novel switching parameter, λ, to control the displacement event locally. The form of λ in this thesis represents the linear relationship between dominant forces - a form that is simple and correctly reproduces the filling regimes under various conditions.
3. Mass (oil and water) must be conserved at each volumeless node; however, spare water from the upstream adjacent pores will be used to swell the downstream wetting films, thus flow rate of each phase needs to be considered separately and mass of single phase may not be balanced at some nodes (Section 4.5 and 4.6). Note here, since the total mass is still conserved, the model only focuses on the water phase, while the oil phase will be managed simultaneously.

4. Because of the current pressure solver, during this imbibition process, bulk oil cannot penetrate into the water-filled pores, thus this model cannot simulate the mobile oil ganglion and the retreating bulk menisci: bulk oil will remain trapped in these two situations.

4.2 Imbibition (Water Displacing Oil)

In the previous chapter, we have discussed a variety of pore-scale issues in the context of steady-state flow in mixed-wet systems. We now go on to describe a new *dynamic* model of imbibition and restrict our discussion to water-wet media. Note, however, that much of the development undertaken in Chapter 4 will inform the unsteady-state formulation. During water flooding, water is usually injected from the inlet at a constant rate and displaces a defending oil phase occupying the centre of water-wet pores. Water-wet triangular pores will initially have water in their corners as wetting films and the imbibition mechanism will generally be more complex compared with primary drainage, Lenormand et al, (1983). The three main filling mechanisms characterising the imbibition process are piston-like displacement, snap-off, and pore body filling events. This model will concentrate on the first two mechanisms, leaving pore body filling to later.

4.2.1 Piston-like Displacement

For piston-like displacement, water will flow into the pore element forming a bulk water/oil meniscus perpendicular to the flow direction. In the calculation of local flow rate, this mechanism requires a capillary entry pressure to be taken into account, which will always help the displacement in imbibition (in contrast to drainage). Therefore, in most cases, regardless of the capillary pressures, piston-like displacement can occur in each pore as long as there is upstream adjacent bulk water available (in water-filled neighbouring pores or at the system inlet). To avoid the retreat of menisci, pores with a counter-current flow direction are considered to be trapped, i.e. the bulk meniscus can only penetrate if $\Delta P > -P_c$, where ΔP is the pressure drop from the water-filled end to the oil-filled end of the pore. The system records the advancing flow direction in each partially-filled element – the flow direction when the penetration of bulk menisci just occurs – and at each time step the system will trap any pores exhibiting counter-current flow.

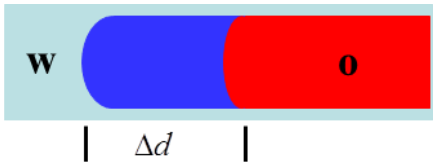

Figure 4-1 Illustration of the bulk menisci advancing.
Blue (both light and dark) is water, red is oil; dark blue represents the water volume increment in the displacement.

Now, in each pore, considering water influx and outflux, q_w^{in} and q_w^{out}, the water volume increment associated with that pore, ΔV_w is:

$$\Delta V_w = (q_w^{in} - q_w^{out}) \cdot \Delta t \qquad 4\text{-}1$$

Note here, for piston-like events, q_w^{in} is actually equal to the total influx, and water can only escape from these pores through wetting films; hence for pores with no films, q_w^{out} is zero until the meniscus reaches the end of the pore.

Defining Δd as the incremental distance the bulk meniscus has travelled along a pore, and A_o the oil-occupied cross-sectional area, all of the incremental water is used to propel the bulk meniscus through the oil (Figure 4-1), i.e.

$$\Delta d = \Delta V_w / A_o \qquad 4\text{-}2$$

Once a pore is fully-filled by water, the bulk meniscus can then move into all downstream oil-filled pores. Note that this model does not consider moving oil ganglia, hence the bulk meniscus can only penetrate a specific pore at most once.

4.2.2 Film Swelling and Snap-off

In angular pores, water will accumulate in corners as arc menisci (*AM)* and wetting films can expand as water flows along the pore edges. If it swells sufficiently so that the fluid/fluid interface becomes unstable, then snap-off occurs. Snap-off can only happen if there is no bulk water in the upstream neighbours (as piston-like displacement would be favoured in such cases). Unlike in the steady-state model, where the swelling film is controlled by decreasing capillary pressure, our new unsteady-state model will simulate this phenomenon dynamically through film flow gradients in the system.

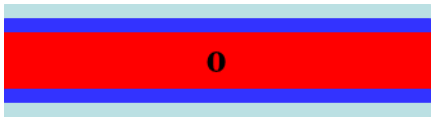

Figure 4-2 Illustration of the film swelling.

Blue (both light and dark) is water, red is oil; dark blue represents the water volume increment in the displacement.

The existence of a good water supply near the inlet means that wetting films in upstream untrapped pores will swell first and subsequently act as new water sources to expand the downstream films. In a given pore element, different water flows q_w^{in} and q_w^{out} at the pore inlet and outlet will alter the water volume as per Equation 4-1.

Then the entire increment will be used to swell the wetting films, and so,

$$\Delta A_o = -\Delta V_w / l \qquad 4\text{-}3$$

In each pore, q_w^{in} and q_w^{out} are determined by the pore-level fluid configurations and surrounding conditions; details of how the specific water flows are obtained will be introduced later in Section 4.5.

Considering local flow direction and topology, piston-like displacement is always favoured over snap-off wherever bulk displacement is possible. However, snap-off does not have the requirement of adjacent upstream bulk water, therefore it can occur anywhere in the network as long as the water supply is adequate and oil is untrapped.

The water configuration when dominated by piston-like displacements leads to continuous water paths from the inlet. However, snap-off will generate scattered clusters of water-filled pores and may cause increased trapping of the oil phase.

4.2.3 Coupling of Piston-like Advancement and Film Swelling

In a dynamic model, pore elements can be found in various intermediate states before becoming fully filled; *i.e.* there may be partially-filled pores with water/oil menisci partly intruded into the pore together with possible corner water (see Figure 4-3). Since circular pores cannot contain expandable wetting films and can only experience piston-like displacement, this section will focus on triangular pores from now onwards.

Figure 4-3 Illustration of partial-filled pores. Blue is water, red is oil.

Generally, bulk menisci advancement and wetting film swelling will co-exist in a dynamic imbibition model and the rate-dependent competition between these two mechanisms is determined by the dominating force, either viscous or capillary. In each pore, the existence of a partially advanced water/oil meniscus, as in Figure 4-3, is solely determined by the presence of bulk water in upstream adjacent elements and is independent of injection rate. However, local fluid velocity *will* affect the precise water partition (between the piston like advance and the film) after the bulk meniscus partially penetrates the pore. At high-rates, where the viscous force is more dominant, a large portion of the water would be expected to stay in the pore centre, pushing the meniscus along the pore with negligible film swelling, as in Figure 4-4 (a). Conversely, at low-rates, capillary forces dominate and most of the incoming water would tend to swell the water films, as in Figure 4-4 (b).

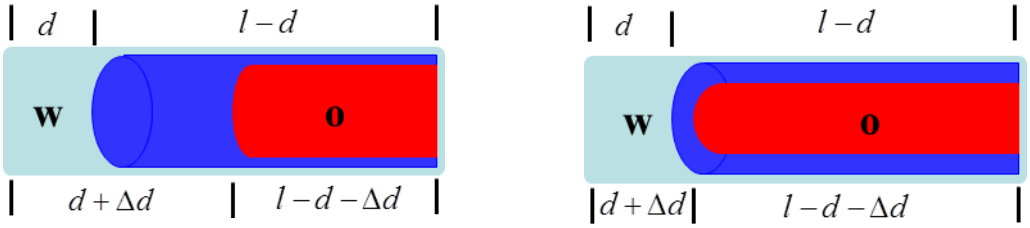

(a) viscous force dominant (b) capillary force dominant

Figure 4-4 Illustration of the coupled piston-like/film swelling displacement mechanisms. Light blue denotes the old existing water, dark blue is for the newly entering water, red is for oil.

To capture the above scenarios, a local force balance 'switch', λ, is introduced in each element to describe the competition between viscous and capillary forces. We define, the quantity, λ, as follows:

$$\lambda = \frac{P_{c,enrey}}{P_{c,entry} + (P_i - P_j)} \qquad 4\text{-}4$$

where $P_{c,entry}$ is the capillary entry pressure of piston-like displacement in one particular element (see Equation 3-26), P_i is the nodal pressure at the water-filled end of the pore,

and P_j is the nodal pressure of the oil-occupied end. Note here, we assume that the inclusion of viscous forces will have no influence on the local capillary entry pressure.

After bulk water flows into a pore, the switch λ can be used to partition the water increment as follows (λ portion of the invading water will be used to swell the wetting film):

$$\Delta V_w = (q_w^{in} - q_w^{out}) \cdot \Delta t \qquad 4\text{-}5$$

$$V_o^{new} = V_o^{old} - \Delta V_w, \qquad 4\text{-}6$$

$$A_o^{new} = A_o^{old} - \frac{\Delta V_w \cdot \lambda}{l - d^{old}}, \qquad 4\text{-}7$$

and

$$d^{new} = l - \frac{V_o^{new}}{A_o^{new}}. \qquad 4\text{-}8$$

From the above equations, it can be seen that the value of λ is positively correlated to the extent of film swelling, with λ = 1 giving only film swelling (capillary dominated) and $\lambda \rightarrow 0$ giving pure piston like advance (viscous dominated). Therefore, as well as representing the competition between capillary and viscous forces, this switch can also control the distribution of incoming water and determine the favoured filling mechanism. Through λ, this model will be able to reproduce the filling regimes reported by Lenormand and Zarcone (1984) through micro-model displacement experiments: snap-off predominates the low-rate simulations and will be suppressed in high-rate cases. It can also be used to study the influence of different flow and network conditions on displacement regimes and relative permeabilities.

4.3 Calculation of Hydraulic Conductance

The hydraulic conductance describes the ability of a fluid to flow through a given pore element under the influence of a viscous pressure gradient and it is clearly strongly determined by the local fluid distribution. Four possible wetting fluid configurations are simulated by the dynamic model proposed here as follows: 1. fully-filled with water, Figure 4-5 (a); 2. oil filled with a wetting film and no bulk meniscus, Figure 4-5 (c); 3.

partially filled with a bulk meniscus and negligible film, Figure 4-5 (e); and 4. partially filled with both a bulk meniscus and a wetting film, Figure 4-5 (g).

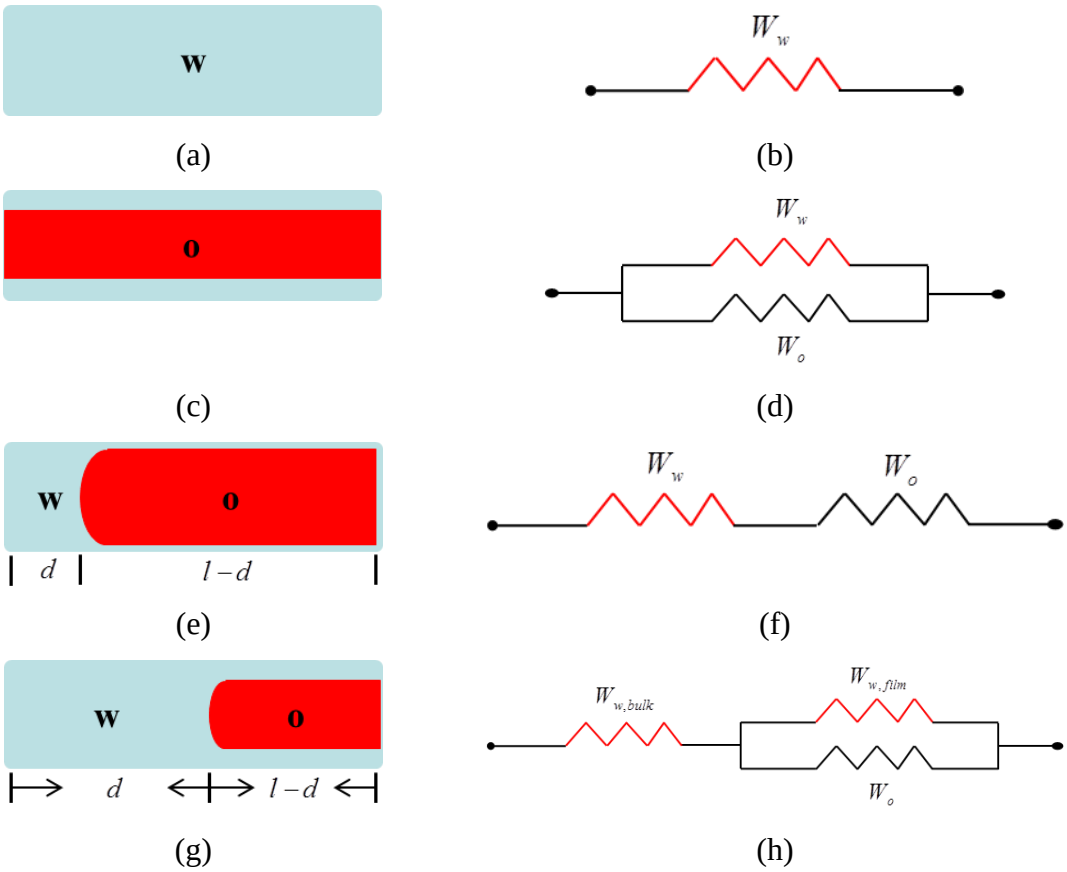

Figure 4-5 Fluid configuration and equivalent electrical conductance diagrams to represent the form of the fluid conductivity calculation.

Calculating the fluid conductance is a complicated problem for some of these configurations but we adapt the approach of Al-Gharbi (2004), using an equivalent electrical resistor network to help simplify the computations, Figure 4-5 (b), (d), (f), (g) are the equivalent electrical diagrams of Figure 4-5 (a), (c), (e), (g), respectively.

Pores in this model are cylinders with triangular cross-section and fixed inscribed radius and so the conductance in each region per unit length, G_{region}, has no correlation with distance, where the subscript *region* stands for the 4 configurations illustrated in Figure 4-5, thus the general form of the fluid hydraulic resistance, W, over a length (x) can be written as:

$$W = \frac{x}{G_{region}}. \qquad 4\text{-}9$$

where *x* can be pore length (*l*), bulk menisci travelling distance (*d*), or *l*-*d* based on the specific fluid configuration and the conductance of interest.

For pores with bulk oil and wetting film (Figure 4-5 (c)), it is equivalent to the circuit with resistors in parallel, and the total hydraulic resistance, W_{total}, would be,

$$\frac{1}{W_{total}} = \frac{1}{W_w} + \frac{1}{W_o}. \tag{4-10}$$

and so the total conductance is:

$$g = \frac{G_w}{l} + \frac{G_o}{l} \tag{4-11}$$

For pores with advancing menisci and no wetting film (Figure 4-5 (e)), the hydraulic resistance in the pore with both bulk water and bulk oil is equivalent to the series circuit.

Hence,

$$W_{total} = W_w + W_o. \tag{4-12}$$

and the conductance of the pore is given by:

$$g = \frac{1}{\frac{d}{G_w} + \frac{l-d}{G_o}} \tag{4-13}$$

The configuration shown in Figure 4-5 (g) is naturally the combination of (c) and (e) and, as a result:

$$W_{total} = W_{w,bulk} + \frac{1}{\frac{1}{W_{w,film}} + \frac{1}{W_o}} \tag{4-14}$$

and the total conductance is given by the expression:

$$g = \frac{1}{\frac{d}{G_{w,bulk}} + \frac{l-d}{G_o + G_{w,film}}} \tag{4-15}$$

Conductance per unit length for each phase is represented by various expressions associating with the particular fluid configurations. First, for circular pores without corner water, the conductance is

$$G = \frac{\pi r^4}{8\mu} \qquad 4\text{-}16$$

i.e. simple Poiseuille-type flow.

While for angular pores and considering film swelling and snap-off, water can exist in 4 possible cross-sectional configurations as shown in Figure 4-6.

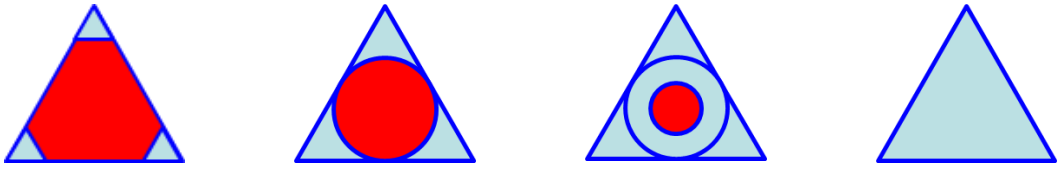

(a) (b) (c) (d)

Figure 4-6 Fluid configurations of intersection. Blue as water and red as oil

In a pore containing a mobile film, water will initially exist in pore corners as thin and stable lenses (Figure 4-6 (a)). If oil in the centre is untrapped, then water in corners will accumulate through film swelling until two or more menisci meet (Figure 4-6 (b)). Following this, "spontaneous" water filling occurs (Figure 4-6 (d)), although it is possible that snap-off in some pores cannot finish during a particular time step and stage (c) (Figure 4-6 (c)) is used to describe this intermediate state. For this latter case, the meniscus is unstable but there is insufficient water available to complete the snap-off event at this instant.

Similar to the quasi-static model with angular pores, the single-phase conductance expressions for non-circular geometries can be approximated by the following expression (Oren et al. (1998)):

$$G_{whole} = \frac{3r^2 A}{20\mu} \qquad 4\text{-}17$$

where A represents the cross-sectional area of the pore, and μ is the viscosity of the phase occupying the pore element.

The conductance of corner water can be approximated by the expression:

$$G_{corner} = \frac{r_w^2 A_w}{C_w \mu_w} \qquad 4\text{-}18$$

Unlike in quasi-static models, where the thickness of the wetting films is controlled by the changing capillary pressure, film expansion in this dynamic model is the result of water flow gradients, and so no specific r_w is monitored. However, the curvature of the arc meniscus is related to A_w through the pore geometry and wettability, $A_w = r_w^2 \cdot S_1$. Consequently, the conductance expression for corner water flow in this model can be calculated via the actual area of corner water recorded by the system:

$$G_{corner} = \frac{A_w^2}{C_w \mu_w S_1}. \qquad 4\text{-}19$$

For the configuration shown in Figure 4-6(b), the water conductance, G_{II}, is the corner conductance when $A_w = A - A_{critical}$ ($A_{critical}$ is given by Equation 3-34):

$$G_{II} = \frac{(A - A_{critical})^2}{C_w \mu_w S_1} \qquad 4\text{-}20$$

Whilst the water conductance in Figure 4-6 (c) is the sum of G_{II} and the volume-weighted ring-region conductance, G_{ring}.

$$G_{III} = G_{II} + G_{ring} = G_{II} + \frac{A_{critical} - A_o}{A_{critical}} \cdot (G_{whole} - G_{II}) \qquad 4\text{-}21$$

For all of the above cases with bulk oil, the formula to calculate the conductance of non-wetting phase is the same as that corresponding to the single phase conductance, but with *A* replaced by the oil-occupied central area A_o.

4.4 Updating Pressure and Flow Fields

4.4.1 Local Pressure Gradients

Given that the nodes are volumeless in this model, mass conservation for each node implies:

$$\sum q_{ij} = 0 \qquad 4\text{-}22$$

At each junction, the mass conservation of water alone is invalid since it is the gradient of water flow that drives the film swelling process in downstream pore elements. However, the balance of *total* (oil and water) flow must be maintained; hence the pressure gradient is updated using total flow.

In pores without bulk menisci, the local flow rate is computed by assuming a Poiseuille-type relationship between the flow rate q and the pressure gradient as follows:

$$q = g \cdot (P_i - P_j). \qquad 4\text{-}23$$

In pores containing bulk menisci, capillary pressure must be introduced into the calculation of local flow rate (note that during water imbibition, P_c assists the flow), and so:

$$q = g \cdot (P_i - P_j + P_{c,entry}) \qquad 4\text{-}24$$

where P_i is the nodal pressure at the water-filled end of the pore, P_j is the nodal pressure of the oil-occupied end, and $P_{c,entry}$ is the capillary entry pressure of the corresponding pore (Equation 3-26).

Applying the above Equation 4-23 and 4-24 in each pore and mass conservation at each node, we obtain a set of linear equations and, by solving these, the pressure field and flow field can be updated. Note that the sign of the flow represents the flow direction and the capillary pressure that helps move the bulk menisci should have the same sign as the flow from water to oil.

4.4.2 Global Pressure Drop for Constant Injection Rate

Ignoring capillary pressure, the relationship between the global pressure drop across the lattice, ΔP , and injected flow rate Q is given by

$$Q = a\Delta P \qquad 4\text{-}25$$

This is simply a pseudo single-phase Darcy's law with the constant a depending on the configuration of the fluids and the conductances of each pore.

Now considering the inclusion of capillary pressure, Equation 4-25 can be modified to:

$$Q = a(\Delta P + \overline{P}_{c,entry}) = a\Delta P + b \qquad 4\text{-}26$$

where $\overline{P}_{c,entry}$ is the average capillary entry pressure in the system. The first term on the RHS of this equation, $a\Delta P$, is Darcy's Law, while the second term, *b*, includes the capillary pressure between the two fluids.

In this model, water is injected from the inlet at a fixed flow rate. However, as the displacement proceeds, the changing fluid configurations require a constant adjustment of the global pressure drop to maintain this predefined injection rate. Aker et al (1998; 2000) proposed a method to obtain the target rate as summarised below:

(1) Apply a pressure drop to the network. Based on the current ΔP, update the pressure field and flow rate in each pore; then calculate the resulting total flow rate Q at the inlet.

(2) Change the pressure drop to $\Delta P'$ and determine the new injection rate Q'.

(3) Insert the pairs of values (ΔP, Q) and ($\Delta P'$ Q') into the equation $Q = a\Delta P + b$ and solve this set of simultaneous equations to calculate *a* and *b*.

(4) Use the calculated *a* and *b* to assign the correct pressure drop $\Delta P^* = \dfrac{Q_{target} - b}{a}$ that is now consistent with the predefined inject rate.

The above problem seems to be linear, but in actual simulations, especially when the constant injection rate is low, *a* and *b* in above method are highly sensitive to the assigned pressure drop and may change accordingly. Therefore the guess of $\Delta P'$ in step (2) should be as close to the target ΔP^* as possible and the above method implemented in our model will be iterated until the actual injection rate is equal to the predefined rate within a specified accuracy.

Al-Gharbi has proposed another simplified method by assuming that the required pressure drop to maintain the constant flow rate will not change very much between time steps. With the actual injection rate Q^n and pressure drop ΔP^n at the nth time step, the pressure drop at the (n+1)th time step can be approximated as:

$$\Delta P^{n+1} = \Delta P^n \times (1 + 0.5(\frac{Q_{target} - Q^n}{Q_{target}})) \qquad 4\text{-}27$$

Comparing with Aker et al's method, which requires solving the pressure field twice, this algorithm only involves one pressure field update and is simpler. However, the 'small pressure drop change between time steps' assumption only works well in high-rate, viscous-dominated cases. Hence, Al-Gharbi's method is faster than Aker's method in high-rate cases, but less efficient in low-rate cases, since each method will be iterated in our model until the error between the resulting flow rate and the target rate is sufficiently small.

In the low rate case, where capillary forces play a more important role, negative flows may be found at the network inlet/outlet. These phenomena can sometimes be seen in the laboratory experiment and cause problem in the calculation of relative permeability later. To simplify the relative permeability calculation, the system will check the flow direction of all inlet/outlet pores at each time step, remove the negative cases, solve the pressure field again, and find a new pressure drop that is consistent with the fixed injection rate.

The work flow of finding the appropriate pressure drop is presented in Figure 4-7 below:

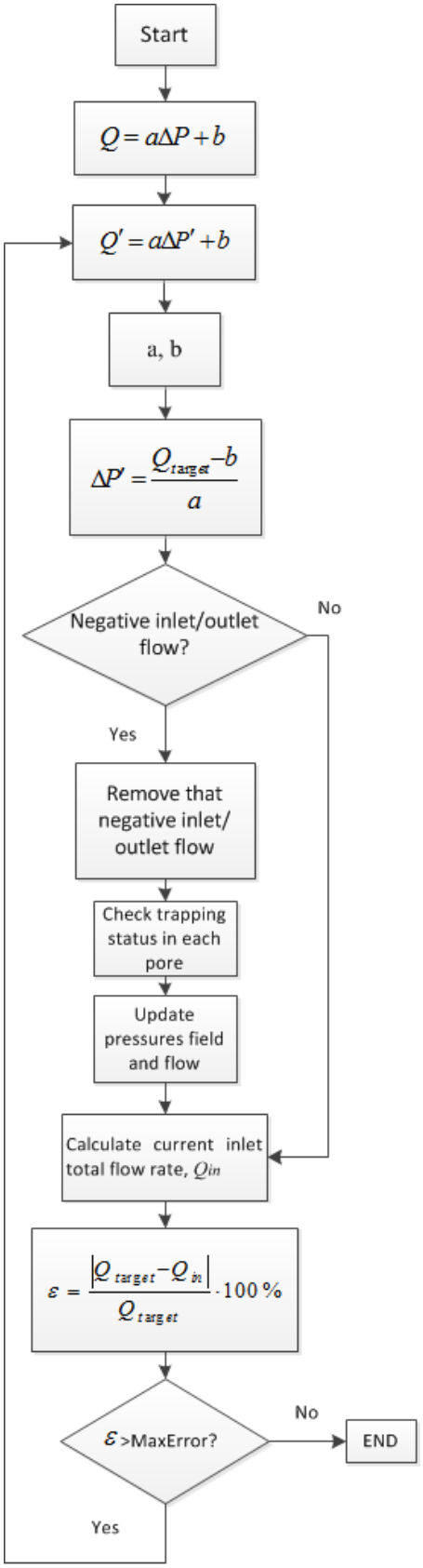

Figure 4-7 Work flow to find the appropriate pressure drop for a fixed injection rate

4.5 Local Water Flow

The assignment of total flow rate (q) in each pore has been described previously (Section 4.4.1). Now, based on the explicit fluid configuration in each pore, local water influx (q_w^{in}) and outflux (q_w^{out}) can be calculated (as seen in Table 4-1).

Table 4-1 q_w^{in} and q_w^{out} in pores with explicit fluids configuration.

Blue represents water, red represents oil.

No			A	B	C
Configuration				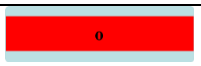	
Water Film Untrapped	Oil Untrapped	q_w^{in}	q	$q \cdot \frac{g_w}{g}$	q
		q_w^{out}	q	$q \cdot \frac{g_w}{g}$	$q \cdot \frac{G_{w,film}}{G_{w,film}+G_o}$
	Oil Trapped	q_w^{in}	NA	q	q
		q_w^{out}		q	q
Water Film Trapped	Oil Untrapped	q_w^{in}	NA	0	q
		q_w^{out}		0	0
	Oil Trapped	q_w^{in}		0	0
		q_w^{out}		0	0

NA means oil-trapping and water-film trapping are not applicable in water-filled pores.

Although trapped oil has already been considered in the previous calculation of hydraulic conductances, its effect on water flow needs to be managed carefully. Furthermore, in the more complicated cases with distributed pore shapes and/or contact angles, it is possible that one element with a wetting film will find that none of its downstream neighbours are able to accommodate corner water, i.e. the water film becomes trapped. This type of trapping must also be handled very carefully and the specific trapping mechanisms, both of bulk oil and wetting film, will be explained later in Section 4.8.

(1) For water-filled pores (Table 4-1 A), only water flows in and out, and thus:

$$q_w^{in} = q_w^{out} = q\,. \tag{4-28}$$

(2) In a pore with a wetting film and no bulk meniscus (Table 4-1 B):

(i) If both the bulk oil and water film are untrapped, q_w^{in} and q_w^{out} can be calculated based on the conductance ratio of existing water films to bulk conductance:

$$q_w^{in} = q_w^{out} = q \cdot \frac{g_w}{g}\,. \tag{4-29}$$

(ii) If the water film is untrapped but the bulk oil present in it is disconnected from the outlet, water can flow through this pore via the film without displacing oil. Water influx and outflux in this scenario are equal and

$$q_w^{in} = q_w^{out} = q\,. \tag{4-30}$$

(iii) However, if the wetting film in it is trapped, regardless the mobility of bulk oil, water cannot flow through this pore, thus

$$q_w^{in} = q_w^{out} = 0\,. \tag{4-31}$$

(3) For a pore with bulk meniscus (Table 4-1 C) then:

(i) If both the bulk oil and wetting film are connected to the outlet, the inflowing bulk water determines the water influx:

$$q_w^{in} = q\,, \tag{4-32}$$

and the water outflux is controlled by the thickness of the wetting film:

$$q_w^{out} = q \cdot \frac{G_{w,\,film}}{G_{w,\,film} + G_o}\,. \tag{4-33}$$

(ii) In pores with untrapped water film and immobile bulk oil, water will flow around the oil phase and

$$q_w^{in} = q_w^{out} = q\,. \tag{4-34}$$

(iii) If the wetting film is trapped, there will be no water outflux:

$$q_w^{out} = 0\,. \tag{4-35}$$

In this scenario, bulk water can still flow into the pore and accumulate within it by displacing the bulk meniscus, providing the bulk oil is untrapped:

$$q_w^{in} = q \tag{4-36}$$

(iv) If both bulk oil and water film are trapped, water flow in this pore will be impossible:

$$q_w^{in} = q_w^{out} = 0\,. \tag{4-37}$$

4.6 Distributing Water at a Node

Volumetric water changes in pores are updated through the pore-level gradients in water flow: $\Delta V_w = (\left|q_w^{in}\right| - \left|q_w^{out}\right|) \cdot \Delta t$. There are two causes of the local water flow gradient: (1) in pores with *advancing* bulk menisci, the fluids configuration itself (bulk water at the inlet, water film at the outlet) guarantees the positive water flow influx (as discussed in Section 4.5). And, (2) in pores *with mobile water film*, their water influxes (q_w^{in}) can be altered by distributing the water flow gradient present at their upstream adjacent nodes.

In water imbibition, we always assume that the upstream water supply into a node is no smaller than the downstream demand, *i.e.* the water flow gradient in each junction is non-negative along the flow direction. However, in some particular cases, due to the surrounding fluid configurations, the flow direction in some pores may reverse, which may lead to a negative water flow differential. In this scenario, the upstream water is not sufficient to maintain the water volume in downstream pores, let alone increase them. In such cases, the model will allow the downstream film to shrink in order to conserve mass. Furthermore, for pores with retreating bulk menisci, the wetting films are also allowed to shrink using a technique introduced below.

Note the distribution technique introduced here only alters the water influxes (q_w^{in}) in pores with untrapped water film, q and q_w^{out} will not be affected by the calculations in this section. Also, since the total flow rate (q) in each pore is invariant, by altering the water influx, the corresponding oil influx is actually changed simultaneously ($q_o^{in} = q - q_w^{in}$).

At a junction, the total water influx and outflux can be obtained as:

$$Q_{tot}^{in} = \sum_{upstream} \left| q_w^{out} \right| \tag{4-38}$$

and

$$Q_{tot}^{out} = \sum_{downstream} \left| q_w^{in} \right| . \tag{4-39}$$

Thus, the difference of water flow rate at the node, denoted as ΔQ is:

$$\Delta Q = Q_{tot}^{in} - Q_{tot}^{out} . \tag{4-40}$$

Based on the potential alteration of water films, the downstream pores can be classified into 3 groups: (a) pores with possible swelling films – if both the bulk oil and water films are untrapped; (b) pores with possible shrinking films – if the wetting films are untrapped, regardless the mobility of bulk oil (including pores with untrapped water film and retreating bulk menisci) (as seen in Table 4-2); and (c) pores without mobile water films - only single phase (bulk water or bulk oil) can flow into this group of pores due to the invading bulk water ($q = q_w^{in}$) or trapped water film ($q_w^{in} = 0$), thus their water influxes cannot be altered.

Table 4-2 Fluid configurations with possibly swelling or shrinking water films

Configuration	Description	Group (a) - swelling	Group (b) - shrinking
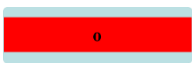	Oil untrapped Film untrapped	√	√
	Oil trapped Film untrapped		√
	Retreating bulk menisci. Film untrapped		√

For each group of downstream pores, required water influxes can be calculated as:

$$Q_{tot}^{out-(a)} = \sum_{\substack{downstream \\ group(a)}} \left| q_w^{in} \right| \quad 4\text{-}41$$

$$Q_{tot}^{out-(b)} = \sum_{\substack{downstream \\ group(b)}} \left| q_w^{in} \right| \quad 4\text{-}42$$

$$Q_{tot}^{out-(c)} = \sum_{\substack{downstream \\ group(c)}} \left| q_w^{in} \right| \quad 4\text{-}43$$

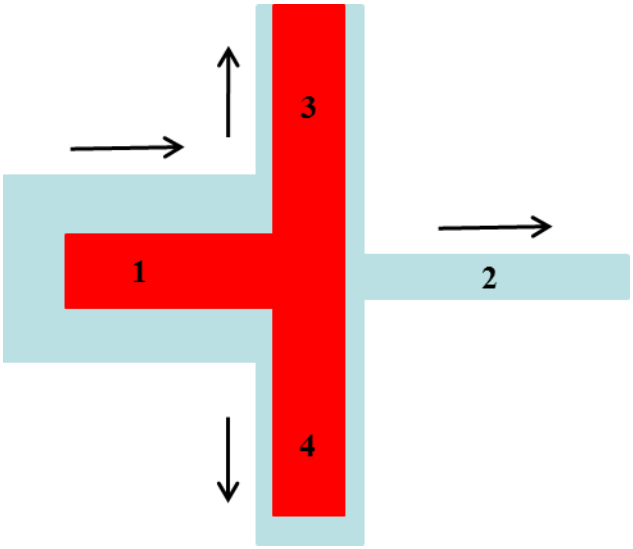

Figure 4-8 Illustration of the distribution of water at each node.
Blue is water, red is oil, black arrow representation flow direction. Pore 1 and pore 3: untrapped oil and water; pore 2: fully-filled by water; pore 4: water untrapped, exhibiting counter-current flow.

For the schematic example in Figure 4-8, based on the local flow direction, $Q_{tot}^{in} = \left| q_{w-1}^{out} \right|$, and $Q_{tot}^{out} = \left| q_{w-2}^{in} \right| + \left| q_{w-3}^{in} \right| + \left| q_{w-4}^{in} \right|$; and according to the description of each pore in the caption of Figure 4-8, for the downstream pores: $Q_{tot}^{out-(a)} = \left| q_{w-3}^{in} \right|$, $Q_{tot}^{out-(b)} = \left| q_{w-3}^{in} \right| + \left| q_{w-4}^{in} \right|$, and $Q_{tot}^{out-(c)} = \left| q_{w-2}^{in} \right|$.

The technique of distributing water at a node is described below:

(1) If $\Delta Q > 0$, the spare water provided by the upstream pores can be used to swell the *untrapped* water films present in downstream *group (a)* pores:

$$q_{w-new}^{in} = q_w^{in} + \Delta Q \cdot \frac{q_w^{in}}{Q_{tot}^{out-(a)}} \qquad 4\text{-}44$$

(2) However, if the total water influx is not sufficient to feed the downstream pores ($\Delta Q < 0$), but is large enough to maintain the water influxes of group (c) pores ($Q_{tot}^{in} \geq Q_{tot}^{out-(c)}$), then the mass balance can be regained through shrinking the wetting film in *group (b)* pores:

$$q_{w-new}^{in} = q_w^{in} + \Delta Q \cdot \frac{q_w^{in}}{Q_{tot}^{out-(b)}} \qquad 4\text{-}45$$

Note here that $\Delta Q < 0$, hence the reassigned water influxes in related pores are in fact smaller than their corresponding water outflux and film shrinking occurs.

(3) In the rare cases when the total water influx in this node is too low to maintain the required water influxes of group (c) pores ($Q_{tot}^{in} < Q_{tot}^{out-(c)}$), mass cannot be conserved through swelling or shrinking film: the conductance of *all* downstream water will be temporarily reduced:

$$g_w = g_w \cdot \frac{Q_{tot}^{in}}{Q_{tot}^{out}} \qquad 4\text{-}46$$

Then the pressure field and local flows of the entire system are updated, and the above calculations will be conducted again.

Note that after redistributing the water influx of eligible downstream pores, we will have $Q_{tot-new}^{out} = \sum_{downstream} \left| q_{w-new}^{in} \right| = Q_{tot}^{in}$, *i.e.* the water flow regains its balance at each node. To summarise, the above process effectively moves the water-flow imbalance from the node to the downstream pores and uses this pore-level gradient to update the downstream wetting films.

4.7 Time Step

The time step is chosen to conserve mass and guarantee that at most ***one*** pore can be filled by invading water in a single time step (or, in the case of a shrinking wetting film, the *AMs* can at most retreat to the corners of the pore). Also, note that the formulae for calculating the water conductances are different between pores with a thin film and a thick film after *AM*s merge. Thus, in a time step, *AMs* in at most one pore can reach (swelling or shrinking to) the coalescence point, $A - A_{critical}$.

Referring to the possible fluid configurations in Table 4-3, we note the following (where letters A, B, C etc. refer to the individual cases in this table):

Table 4-3 Fluid configurations to update the time step.

Blue as water and red as oil

No	Configuration	Description
A		Water-filled pores
B		Oil-contained pores with volume-less film
C		Oil-contained pores with thin film
D		Oil-contained pores with films just meet
E		Oil-contained pores with thick film before snap-off
F		Partial-filled pores with volume-less film

G		Partial-filled pores with thin film
H		Partial-filled pores with films just meet
I		Partial-filled pores with thick film before snap-off

Below, Δt_i (i=1, 2, 3, 4, 5, 6, 7) is the minimum time step that can be found within the corresponding group of pores listed in Table 4-3:

(1) For water-filled pores, type (A), and oil-trapped pores with a volumetric water film, (C)-(E), we require:

$$\Delta t_1 = \min\left(\frac{V_w}{\left|q_w^{in}\right|}\right) \tag{4-47}$$

(2) For oil-filled pores containing a thin and dynamic film, (B) and (C), the film can expand until two or three arc menisci meet. So,

$$\Delta t_2 = \min\left(\frac{(A_o - A_{critical})\cdot l}{\left|q_w^{in} - q_w^{out}\right|}\right) \tag{4-48}$$

In the rare film shrinking scenario, (cases (C) and (D)), *AMs* can at most reach the corners of the pore and:

$$\Delta t_2 = \min\left(\frac{V_w}{\left|q_w^{in} - q_w^{out}\right|}\right) \tag{4-49}$$

(3) The shortest time for one of the untrapped (D) and (E) pores to snap-off is given by:

$$\Delta t_3 = \min\left(\frac{V_o}{\left|q_w^{in} - q_w^{out}\right|}\right) \tag{4-50}$$

If the films shrink, (case (E)), then *AMs* can at most retreat to case (D) and:

$$\Delta t_3 = \min\left(\frac{(A_{critical} - A_o)\cdot l}{\left|q_w^{in} - q_w^{out}\right|}\right) \quad 4\text{-}51$$

(4) For untrapped (F) and (G) pores with both piston-advancement and film swelling, there are two possible events as the concluding outcomes of a time step: (a) for cases characterised by a small switch, where piston-like advance is the primary mechanism, bulk menisci may travel to the pore ends and fully fill the related pores with little film swelling; and (b) for cases with film-swelling as the main mechanism (characterised by a large switch), the *AMs* may merge (Type (H)) before the advancing meniscus moves to the pore outlet.

For event (a), invading water will fill the concerned pores, hence $\Delta V_w = V_o$.

For event (b), however, based on the formula for distributing invading water (Equation 4-6 to 4-8), the water volume increment would be:

$$\Delta V_w = \frac{(A_o - A_{critical})\cdot(l-d)}{\lambda}. \quad 4\text{-}52$$

Since the event involving the least water volume increment will occur first, for each pore, the actual water volume change ΔV_w^* can be represented as:

$$\Delta V_w^* = \min\left(V_o, \frac{(A_o - A_{critical})\cdot(l-d)}{\lambda}\right). \quad 4\text{-}53$$

And the corresponding time step is:

$$\Delta t_4 = \min\left(\frac{\Delta V_w^*}{\left|q_w^{in} - q_w^{out}\right|}\right) \quad 4\text{-}54$$

(5) The shortest time for the untrapped (H) and (I) pores to be fully filled is given by:

$$\Delta t_5 = \min\left(\frac{V_o}{\left|q_w^{in} - q_w^{out}\right|}\right) \quad 4\text{-}55$$

(6) For pores with bulk menisci, and immobile wetting films, (G)-(I), water can only flow along the film and so we have:

$$\Delta t_6 = \min\left(\frac{(A - A_o)\cdot l}{\left|q_w^{in}\right|}\right), \tag{4-56}$$

(7) For the rare film shrinking cases that can occur in configurations (G) and (H),

$$\Delta t_7 = \min\left(\frac{A_w \cdot (l - d)}{\left|q_w^{in} - q_w^{out}\right|}\right) \tag{4-57}$$

and in case (I),

$$\Delta t_7 = \min\left(\frac{(A_o - A_{critical})\cdot (l - d)}{\left|q_w^{in} - q_w^{out}\right|}\right) \tag{4-58}$$

So, in order to determine the actual time-step for the next displacement, we must calculate:

$$\Delta t = \min(\Delta t_1, \Delta t_2, \Delta t_3, \Delta t_4, \Delta t_5, \Delta t_6, \Delta t_7) \tag{4-59}$$

Considering all above events in the calculation of time step, Δt may be very small, especially in the low-rate simulations with all the film behaviours – it may take several time steps for one single pore to be fully filled. Consequently, the simulation time will be prolonged.

Figure 4-9 illustrates the time step choice associated with each configuration change described above:

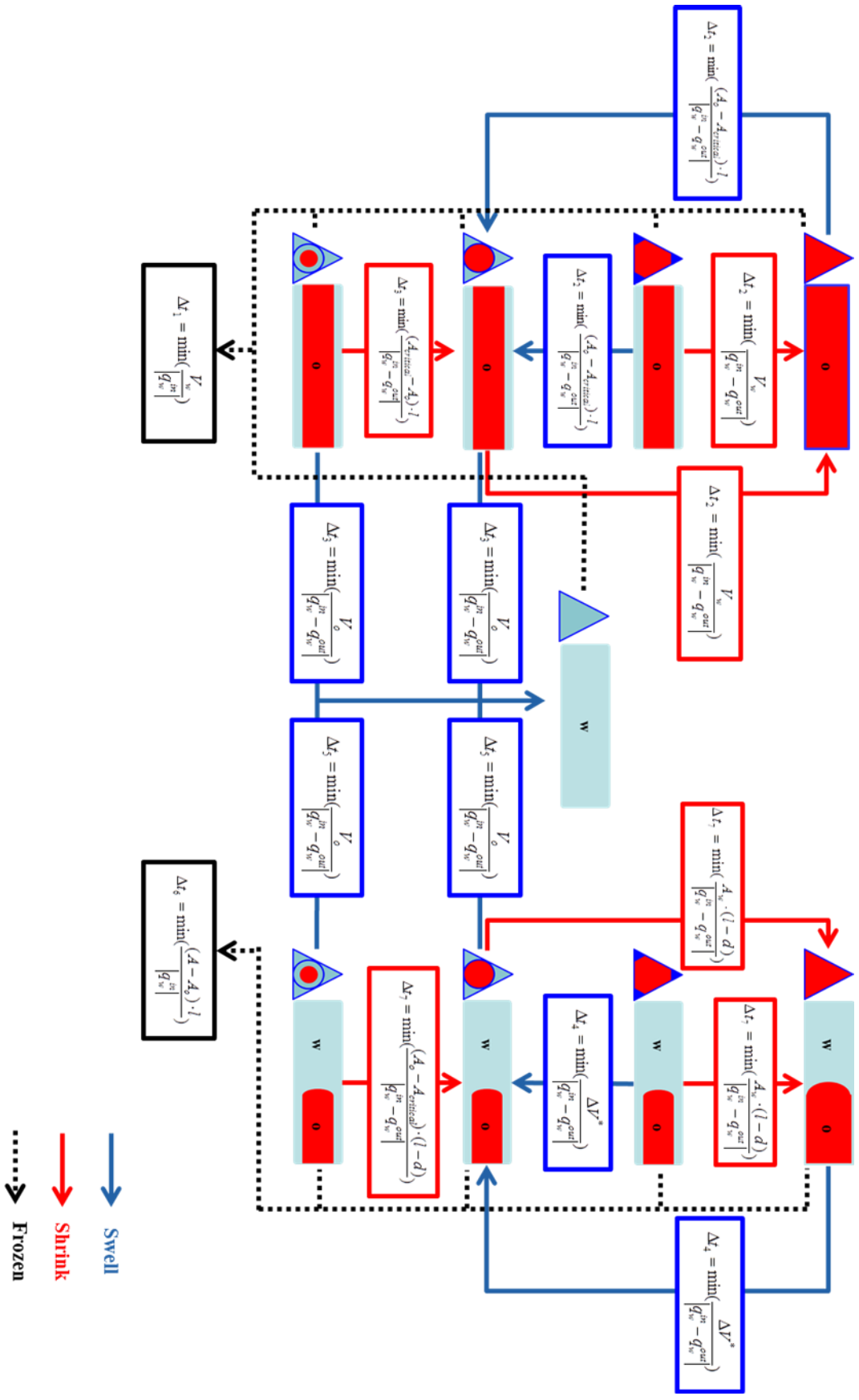

Figure 4-9 Time step associating with particular configuration changes

4.8 Trapping

4.8.1 Bulk-oil Trapping

Bulk oil is considered as being trapped when it becomes disconnected from the outlet and so water encountering trapped oil can only flow around it through water films - a process which involves no oil displacement.

Whilst the earlier topology-based trapping protocol (following Hoshen and Kopelman (1976)) is fine for the steady-state model described earlier in Chapter 3, it is no longer applicable here. Each pore in a fully connected 3-D cubic structure has 10 adjacent elements, while in the dynamic model, the existence of partially-filled pores introduces a more complex topological situation.

Now, for a pore containing a bulk meniscus, only the 5 elements that are connected to the oil-occupied end of the pore (green in Figure 4-10) matter. The other 5 pores at the opposite water-filled end of the pore (black in Figure 4-10), whatever the fluid configurations within them, have no effect on the trapping status of the partially-filled pore of interest. Furthermore, to eliminate retreating bulk menisci, if the partially-filled pore has a flow direction from its oil-filled end to its water-filled end, it will be considered trapped, regardless of the surrounding fluid configurations.

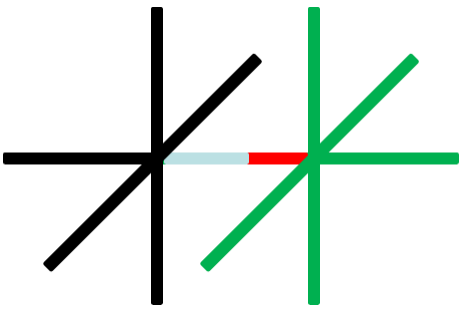

Figure 4-10 Illustration of new topology brought in by partial-filled pores
Red is oil, blue is water. Green represents pores of interest; and the black elements have no effect on the connectivity of the partial-filled pores.

Besides topological considerations, *local flow direction* will also have an impact on oil trapping. For the schematic example in Figure 4-11, the circled pores containing oil are all topologically connected to the outlet. However, given their flow directions, they are actually trapped due to the lack of an available *downstream* path – hence, a new

trapping algorithm is required. This new trapping approach is somewhat more involved than our earlier clustering-based approach.

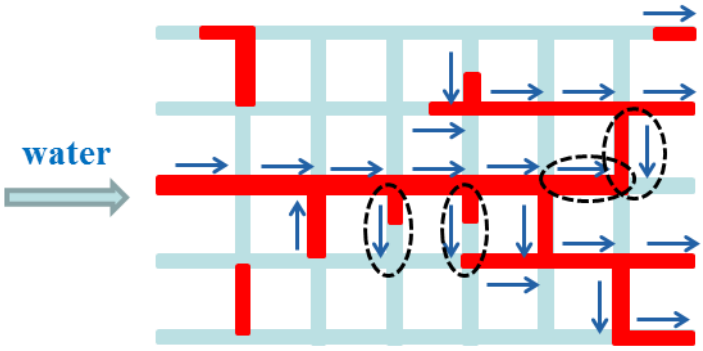

Figure 4-11 Illustration of the clustering algorithm.
Red is oil and blue is water. Arrows represent the flow directions, and the circled pores will exhibit opposing oil-trapping statuses based on two trapping mechanisms.

Now, a *Depth-First Search* (*DFS*) backtracking algorithm is applied to find out all the oil-trapped pores based on both topology and local flow direction. First the system will label all the pores as being oil-trapped and then, starting from the outlet oil-occupied pores, the search will go as far as possible against the flow direction to identify (and "un-trap") all upstream oil-occupied pores. The model will search each upstream neighbour in the order of west (x), east (x), south (y), north (y), down (z), and up (z); it should also remember the element it has explored and will not visit it again. The backtracking point is when the search reaches either (i) an inlet pore, (ii) a partially-filled pore, or (iii) a point where all the upstream neighbours have been visited and managed.

During the search of upstream neighbours, given the local flow direction (marked by a red arrow in Figure 4-12), oil pores without bulk menisci will only consider 5 upstream neighbours instead of the 10 topologically connected elements. Additionally, the candidates (green pores) must have the right flow direction (marked by black arrows) to be chosen as upstream neighbours.

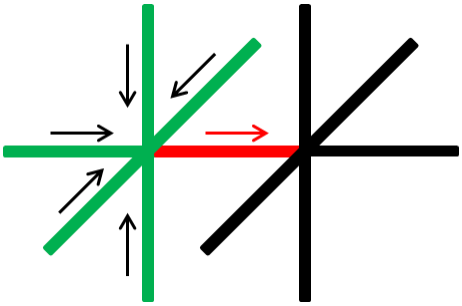

Figure 4-12 Illustration of finding the ***upstream*** neighbours.
Red is oil, green are pores of interest; and the black elements having no effect on the connectivity of the partial-filled pores.

Thus, in Figure 4-11, the real clusters of un-trapped, oil-occupied pores, are dendritic structures, each with a consistent flow direction as shown in Figure 4-13.

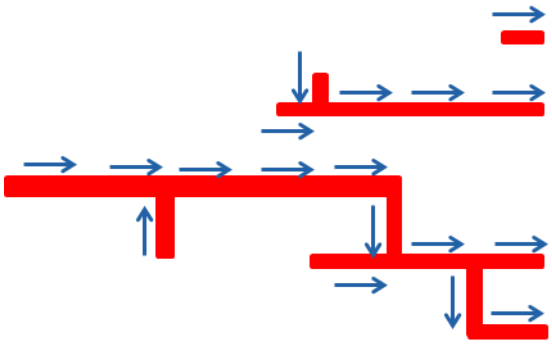

Figure 4-13 clusters of pores with untrapped oil

This new flow-direction based trapping mechanism will apply *DFS* iteratively and the full details of the DFS scheme are shown schematically in Figure 4-14 and listed below:

(1) Label all the pores as ‘trapped’ and ‘un-assigned’;
(2) Select an outlet pore,
    (a) if it is oil-filled with positive flow, apply *DFS* to this pore;
    (b) if it is partial-filled with positive flow, un-trap it and label it as ‘assigned’;
    (c) otherwise, just label it as ‘assigned’;
(3) If there are still un-visited outlet elements, go back to step 2; otherwise, search stops.

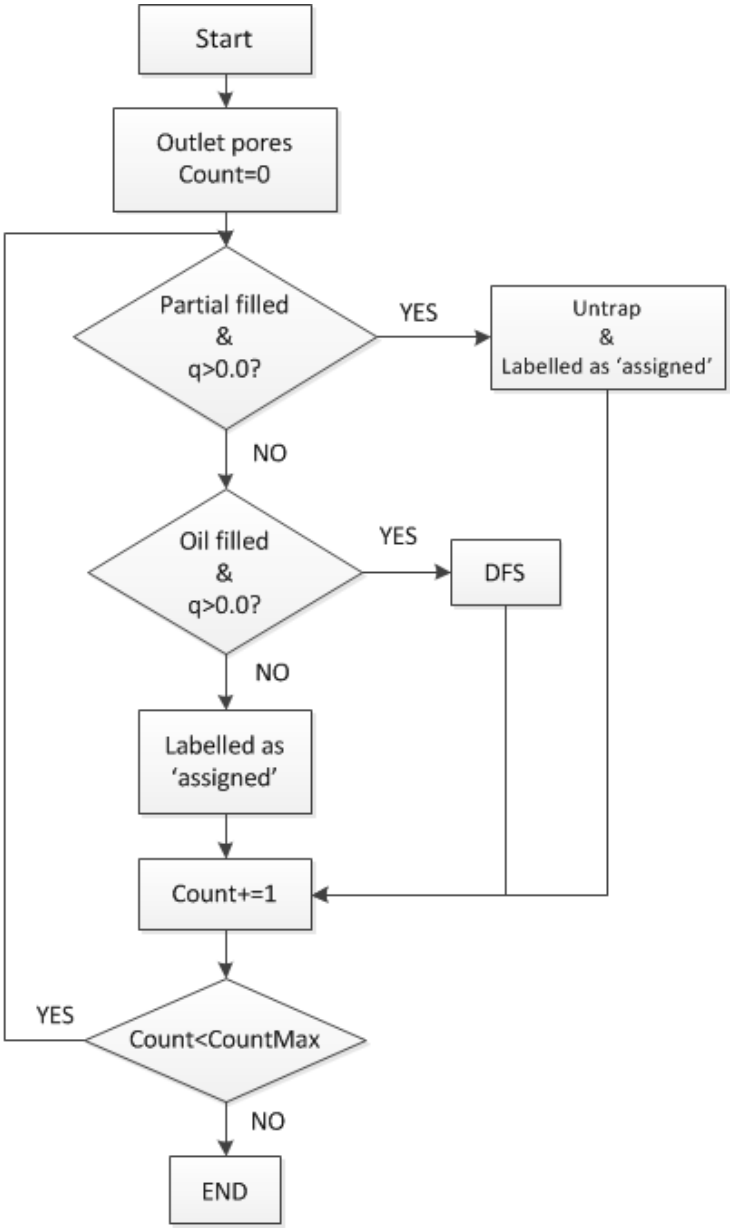

Figure 4-14 Work flow of clustering.

DFS will treat the current element as the root/start-point of the searching tree and, based on the pore type, x-pore, y-pore, or z-pore, there are three corresponding algorithms (*DFS x-direction*, *DFS y-direction*, *DFS z-direction*). The generic algorithm is:

(1) Based on the pore type, choose the appropriate algorithm in *DFS*, here we assume the current pore, 'root', is an x-pore and take the *DFS x-direction* as an example;

(2) If the current 'root' is an inlet pore

(a) if there is oil in it and the flow direction is positive, un-trap it and label it as 'assigned';

(b) otherwise, just label it as ‘assigned’.

Then return.

(3) If the current ‘root’ is an oil-filled pore and has not been visited before: un-trap it and label it as ‘assigned’. Find out all the upstream neighbours of the current ‘root’, apply *DFS* to each one in the aforementioned order;

If all the neighbours have been visited, return.

(4) If the current ‘root’ is partially-filled, un-visited, and with the right flow direction: un-trap it, label it as ‘assigned’.

Then return.

(5) Otherwise, label the pore as ‘assigned’ and return.

The work flow, with all the details of *DFS x-direction* is shown in Figure 4-15. The algorithms for y-pores and z-pores are essentially the same as that used for x-pores, only with a little modification to identify the upstream neighbours.

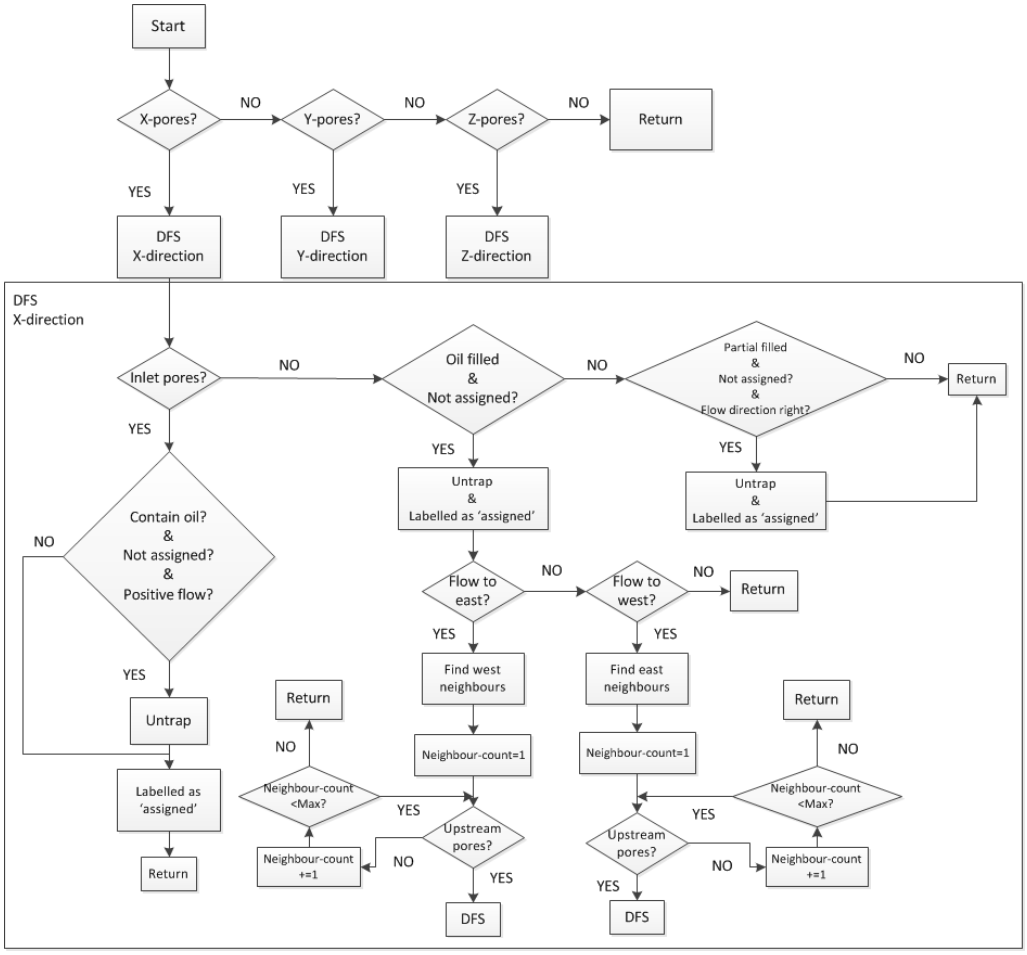

Figure 4-15 Work flow of DFS

The old topological trapping algorithm will not only underestimate the extent of trapped oil, it also leads to mass conservation errors and affects water configurations. According to former sections, fluid trapping status is a major concern when we distribute mass and update fluid configurations. Therefore a suitable trapping algorithm is crucial.

Oil trapping needs to be checked in every time step after configuration changes and during the process of finding the pressure drop to maintain the constant flow rate (Section 4.4.2). However, based on the requirement of accuracy or efficiency, this checking may be conducted in every several time steps, especially in the high-rate, piston-like displacement dominated cases.

4.8.2 Wetting-film Trapping

In a system with distributed contact angle and/or pore shapes, it is possible that some pore elements with wetting films find all their downstream neighbours have no ability to accommodate corner water. In such cases, their films will be trapped and water outflux is cut off. Furthermore, if for a particular pore, all its downstream neighbouring elements contain trapped film, the film within will be trapped as well.

Similar to the bulk-oil trapping, the wetting-film trapping also requires a flow-direction based depth-first-searching mechanism. Wetting film in a particular pore, if present, can only be untrapped if, along the flow direction, it is connected to at least one pore at the outlet.

4.9 The Capillary/Viscous Switch, λ, in a Single Pore

Following earlier work, we note that ***two*** dimensionless numbers help us characterise two phase flow through porous media. The first is the **capillary number** C_a, which represents the competition between capillary and viscous forces (see Aker and Maloy, for example) and one form of this quantity is:

$$C_a = \frac{\mu_w Q}{\sigma_{ow} \sum} \qquad 4\text{-}60$$

where μ_w ($\mathrm{N \cdot s/m^2}$) is the advancing phase (water) viscosity, Q ($\mathrm{m^3/s}$) is the volumetric flow rate, σ ($\mathrm{N/m}$) is the interfacial tension, and $\sum$ ($\mathrm{m^2}$) is the cross

sectional area of the inlet face of the medium (in this work , we approximate $\sum$ as $n_y \cdot 2r_{mean} \cdot l$ in 2D network (the thickness of the network is taken to be the average diameter of the pores) and $n_y \cdot n_z \cdot l^2$ in 3D network).

The second important dimensionless number characterising porous media flow is the **viscosity ratio**, M, defined as the ratio of defending phase viscosity, μ_o, to advancing phase viscosity, μ_w, as follows:

$$M = \frac{\mu_o}{\mu_w} \qquad 4\text{-}61$$

In this model, the water viscosity will be held fixed at $1.0e^{-3}$ $\mathrm{N \cdot s/m^2}$; (i.e. 1cP or 1mPa.s) and, by altering the oil viscosity, we can simulate water injection experiments in "light oil" (lower μ_o) and "heavy oil" (higher μ_o) systems.

As an important supplement of C_a and M, we introduce the automatic switch, λ (see Equation 4-4), to simulate the local competition between viscous and capillary forces. λ is also used to distribute the incoming water in a pore element (see Equation 4-7), therefore the value of λ is restricted in the [0.0,1.0] range.

Note that, with the help of capillary pressure, the viscous pressure gradient from the water-filled end of a pore to its oil-filled end, $P_i - P_j$, does not need to be positive to have a positive flow rate. If $P_i - P_j < -P_{c,entry}$, the pore will be considered trapped (as the flow will be counter-current). If $-P_{c,entry} < P_i - P_j < P_{c,entry}$, the displacement is capillary dominated, while the importance of P_c decreases as the pressure drop increases further. If $P_i - P_j > P_{c,entry}$, viscous forces begin to dominate the displacement.

For pores with bulk meniscus, the local flow rate is given by Equation 4-24, thus the representation of this switching parameter can also be written as:

$$\lambda = \frac{P_{c,entry}}{q} \cdot g\,. \qquad 4\text{-}62$$

To explore the exact relationship between λ and other parameters of interest, we will start from a single pore, in which water is injected at a constant rate q at one end and the

other end functions as an outlet. We also assume that there is no initial water in this water-wet pore, and that the cross section is a triangle.

The capillary entry pressure $P_{c,entry}$ in a triangular pore is given by Equation 3-26, and the total conductance of this triangular pore is:

$$g = \frac{3r^2 A}{20\bar{\mu}l} \tag{4-63}$$

where $\bar{\mu}$ is the average viscosity of the system, which is governed by the volume ratio of the phases and particular configuration of each phase. As the displacement progresses, the value of $\bar{\mu}$ will alter accordingly. Therefore, for the simplicity of analysis, we choose the moment when the bulk meniscus just enters this pore, $\bar{\mu} = \mu_o$ (thus, we can eliminate the effect of particular fluid configurations and ensure that each pore can have a constant switch value given the values of the set parameters). In addition, the cross-sectional area can be calculated as $A = r^2 \sum_{i=1}^{3} \frac{1}{\tan\beta_i}$. The expression of λ can be expanded as

$$\lambda = \frac{3F_d^* \cdot \sum_{i=1}^{3} \frac{1}{\tan\beta_i}}{20} \cdot \frac{\sigma_{ow} \cdot r^3}{\mu_o q l} \tag{4-64}$$

This equation now defines the relationship between the initial switch value and all the pore-scale parameters of importance.

If we denote the pore-scale aspect ratio to be the ratio of inscribed radius to pore-length

$$R_{asp} = \frac{r}{l}, \tag{4-65}$$

and consider capillary number and viscosity ratio (Equation 4-60 and Equation 4-61), then the above equation for the λ switch can be expressed in terms of wettability, capillary number, viscosity ratio and aspect ratio, as follows:

$$\lambda = \frac{3F_d^*}{20} \cdot \frac{R_{asp}}{M \cdot C_a} \tag{4-66}$$

In a larger network, in addition to the local switch, we can also have an averaged *global* switch. We already know that the global pressure drop can be updated using Equation 4-26. Thus, an expression for a global average switch can be approximated by:

$$\bar{\lambda} = \frac{\bar{P}_c}{Q} \cdot \bar{g} = \frac{b}{Q} \qquad 4\text{-}67$$

4.10 Indicator of Film-Swelling Potential

As discussed in Section 4.6, the ability of pores with wetting films to provide water is determined by their water outfluxes. Hence with increasing water outflux, the invading water prefers to flow along and expand films as it goes, rather than remaining in the pores and displacing bulk menisci (see also Equation 4-1).

Since the outflux of water from films is controlled by the ratio of film conductance and total conductance, then we can assign a dimensionless quantity, R_{w-o}, as follows:

$$R_{w-o} = \frac{G_w}{G_w + G_o}. \qquad 4\text{-}68$$

This represents the ratio of film conductance to the total conductance at the pore outlet and so the extent of film swelling can be indicated through the value of R_{w-o}. More film swelling is associated with higher values of $R_{w\text{-}o}$, and hence it can work as an indicator of film-swelling potential.

Applying the equation of water/oil conductance per unit length (as seen in Equation 4-17, 4-19), before snap-off, a more detailed representation of $R_{w\text{-}o}$ can be derived as follows:

$$R_{w-o} = \frac{\dfrac{A_w^2}{C_w S_1}}{\dfrac{A_w^2}{C_w S_1} + \dfrac{3r^2(A - A_w)}{20\dfrac{\mu_o}{\mu_w}}}. \qquad 4\text{-}69$$

And the expression of $R_{w\text{-}o}$ after *AMs* merging can be given by Equation 4-17, 4-20, and 4-21.

Figure 4-6 shows how $R_{w\text{-}o}$ changes as film swelling increases in one particular equilateral triangular pore. Naturally, for one pore, water outflux will grow as the film gets thicker – i.e. $R_{w\text{-}o}$ increases. The very significant changing point (especially in the *M=1.0* and *M=10.0* cases) is when *AMs* meet. At this moment, for an equilateral triangle:

$$\frac{A_w}{A} = \frac{(A - \pi r^2)}{A} \approx 0.3954 . \qquad 4\text{-}70$$

Thereafter, water in the central ring area has a very high conductance compared with the water films, as the corresponding total water conductance is computed by Equation 4-21.

Figure 4-16 also illustrates that, with other conditions identical, water in pores with unstable viscosity ratio (*M=10.0*) will preferentially flow along the film.

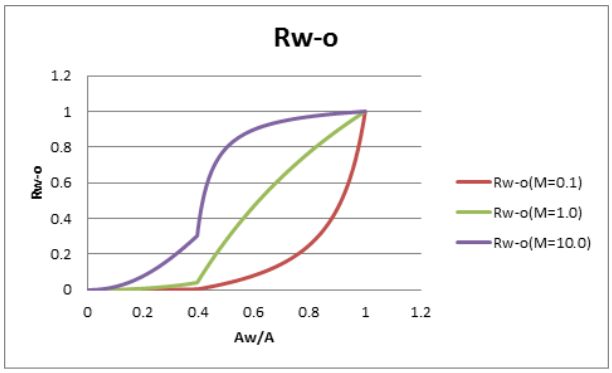

Figure 4-16 Plot of $R_{w\text{-}o}$ *vs.* normalised water cross sectional area for different viscosity ratios.

Therefore, with the same water volume in the corners, it is possible to analyse the influence of each parameters on the extent of film-swelling through the value of $R_{w\text{-}o}$. $R_{w\text{-}o}$ is a local parameter indicating the film-swelling potential, from the view of the whole system, the global equivalent of $R_{w\text{-}o}$ would be water fractional flow, f_w.

4.11 Summary and Conclusions

A novel dynamic model of imbibition is presented in this chapter. In this model, three displacing mechanisms are considered: piston-like displacement, snap-off, and the coupling of these two mechanisms. A switch parameter, λ, is introduced which represents the pore-level competition between capillary and viscous forces. Through the parameter, λ, the invading water is distributed between the piston like advance and

the film after the bulk meniscus partially penetrates the pore. The value of λ is positively correlated to the extent of film swelling, with λ = 1 giving only film swelling (capillary dominated) and $\lambda \rightarrow 0$ giving pure piston like advance (viscous dominated). The expanded expression of λ indicates the influence of various fluid and network conditions on the filling regime. In addition, an indicator of film-swelling potential (denoted $R_{w\text{-}o}$) has also been introduced, which is a quantity that describes the mobility of wetting films. This has been introduced as a "supplement" to λ.

Parameters in this dynamic model, like capillary entry pressure, conductance of fully-filled pore element and corner area occupied by water, are identical to those of the quasi-static model introduced in Chapter 3, since these two models share the same network structure and pore geometry.

However, when considering the more complex fluid configurations (including both wetting film and bulk menisci) and the trapping status associated with the dynamic modelling, careful management of pore conductance, local water flow and time step are required. Moreover, in this dynamic model, (i) capillary entry pressures are considered when updating the local flow rates of pores that contain advancing menisci; and (ii) the global pressure drop needs to be updated at each time step to maintain the preassigned constant injection rate. Topological trapping in the quasi-static model is not sufficient to handle the more complex trapping in this dynamic case. More involved fluid configurations and specific flow directions require a more advanced trapping algorithm and this has been described here. To overcome this difficulty, a *Depth-First Search* (*DFS*) backtracking algorithm has been applied in this dynamic model to identify all the oil-trapped pores based on both topology and local flow direction. Furthermore, water film trapping has also been included to simulate the situations in more complicated networks with distributed pore shapes and/or wettability.

5 Parametric Sensitivities in 2-D Systems

5.1 Introduction and Background

In this chapter, results of a detailed parametric study are presented surveying all of the quantities which appear in the dynamic model. This study is carried out in 2D network models for several reasons; the 2D systems is simpler and larger networks can be studied, it allows a simpler visual comparison of the flow regimes to be made and it also allows us to compare our results to earlier similar 2D studies examining viscous/capillary flow regimes (e.g. for dynamic drainage that of Lenormand et al. (1990)).

In the dynamic imbibition simulations below, the liquids flow from the inlet (left side) to the outlet (right side) of the system, other boundaries of the network are sealed like in the imbibition micromodel experiments. Unless otherwise indicated, the parameters of importance in this model will be assigned with the default values, which are listed in Table 5-1. *Also, initially, there is no water in the system, i.e.* all pores start with volumeless films. All simulations continue until all outlet pores become filled with water (at which point no further displacement of oil is possible).

Table 5-1 List of default parameters used in this study

Parameter	Default value	Unit
Network size (2D)	100*50	Node
Coordination number (Z)	4	-
Pore size (uniform) (r)	1-50	μm
Distortion number	0.3	-
Average pore length (l)	333	μm
Pore shape/half angles (β_i)	30,30,30	degree
Wettability class	Water wet	-
Water viscosity	$1.0e^{-3}$	$N \cdot s/m^2$
Contact angle (θ)	0	degree
Interfacial tension (σ)	40.0	mN/m
Initial water saturation (S_{wi})	0.0	-
The resistance factor of solid (C_w)	100	-

As mentioned by Joekar-Niasar et al. (2012), in dynamic model, the strong nonlinearity at the pore scale made the unsteady-state simulations time-consuming, and the running time was highly correlated to the capillary number and viscosity ratio. The dynamic model in this thesis suffers from the same issues. Furthermore, as discussed in Section 4.7, it may take several time steps to fully-fill one single pore, which further prolongs the simulation time. For a 100*50 2D network, the total simulation time is determined by particular parameters (especially the flow rate): it takes about 1 hour to finish the displacement in high-rate cases; while in low-rate cases, the running time may increase to 6 hours and more.

5.2 Influence of the Capillary/viscous Force Balance (λ) During Network Flow

By default, the model automatically calculates the capillary/viscous switch based on the local pressure drop and local capillary pressure. However, this model also allows us to *predefine* the value of the switch, enabling us to *force* the displacement to be purely piston-like or purely snap-off, regardless of the capillary number. This is a useful construct that allows us to analyse more realistic cases more easily. In this section, we will investigate the influence of switch parameter (λ) using unfavourable viscosity ratio (the invading water is less viscous than the defending oil phase, $M=10.0$) since the difference brought in by various switch values will be emphasized in this case.

Figure 5-1 (a), (c), (e) and Figure 5-2 (a), (c), (e) show snapshots of displacements in which red represents the water-filled pores and white represents the pores that are oil-filled or partially oil-filled (with or without a wetting film). In both figures, (b), (d), (f) illustrate the local water saturation in each pore. As S_w increases, the colour changes in the order: white, light blue, light purple, dark purple, to dark blue; the black region corresponds to water-free pores.

In both figures, (a) and (b) are the results when λ=0.0 (only piston-like displacement is possible); (c) and (d) are the results of implementing the automatic switch, whilst (e) and (f) show the results of the system where snap-off is forces to be the primary filling mechanism (λ=1.0).

In the high-rate ($Q=1.0e^{-3}m^3/s$, $C_a=2.94e^{1}$) model with automatic switch, λ in each pore is found to be close to 0.0 due to the high pore-scale pressure drop - the displacement pattern is similar to that in the bulk-dominated model (Figure 5-1 (a) and (c)). While

for the model which only has snap-off as the filling mechanism, the configuration changes are dramatic (Figure 5-1 (e)).

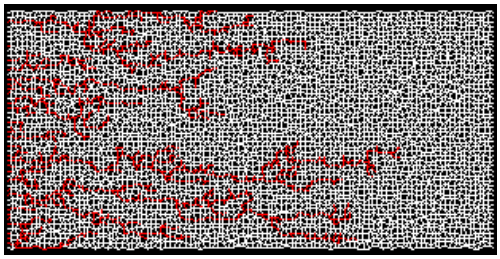

(a) λ=0.0, piston-like

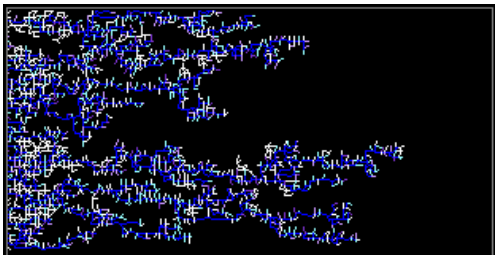

(b) λ=0.0, piston-like, S_w map

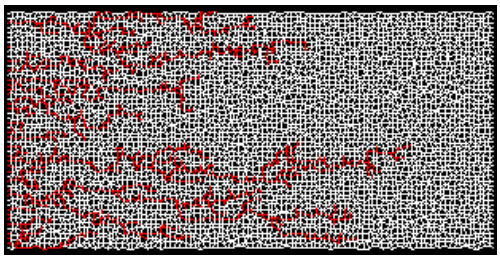

(c) automatic λ

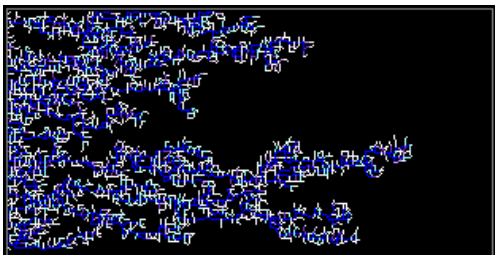

(d) automatic λ, S_w map

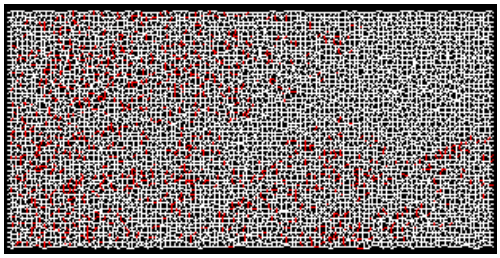

(e) λ=1.0, snap-off

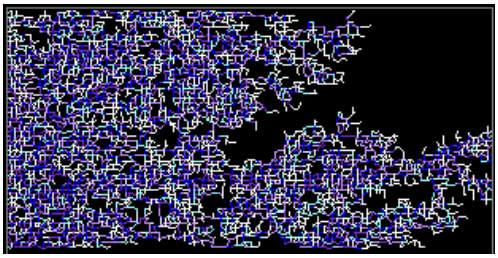

(f) λ=1.0, snap-off, S_w map

Figure 5-1 Illustrate the influence of ***switch***, ***Q=1.0e^{-3}m^3/s, M=10.0***.
Above figures are taken when identical amount of water (0.192 PV) has been injected into each network. (a), (c), (e) are figures of pores filled by different phases. Red is water-filled pores, white is oil-containing pores. (b), (d), (f) are figures showing the local water saturation. As S_w increases, the colour will change in the order of black, white, light blue, light purple, dark purple, to dark blue. The black region is composed of pores with volumeless film and the dark blue pores are filled with invading water.

Furthermore, at the intermediate-rate ($Q=1.0e^{-6}m^3/s$, $C_a=2.94e^{-2}$), as the value of the switch increases, more film swelling and snap-off occurs. Thus the water configuration changes from continuous bulk paths to scattered clusters (Figure 5-2 (a)-(c)-(e)). When the switch is larger than 0.0, thin films appear that connect the water-filled clusters (Figure 5-2 (d)-(f)).

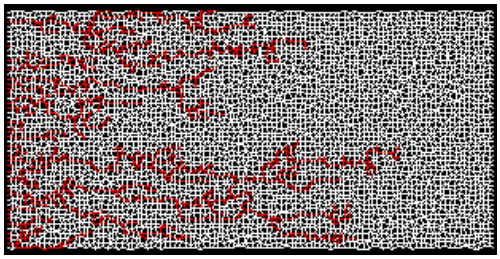

(a) λ=0.0, piston-like

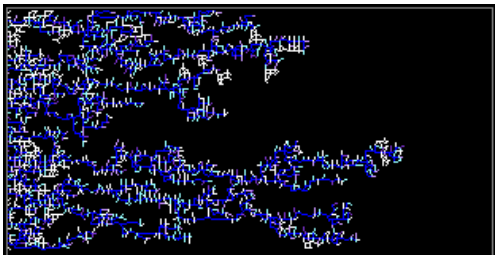

(b) λ=0.0, piston-like, S_w map

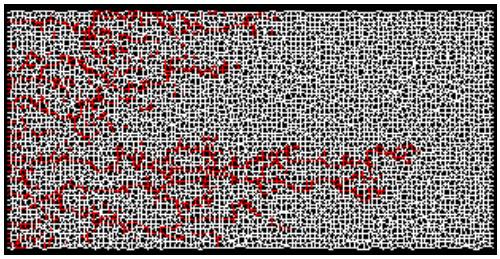

(c) automatic λ

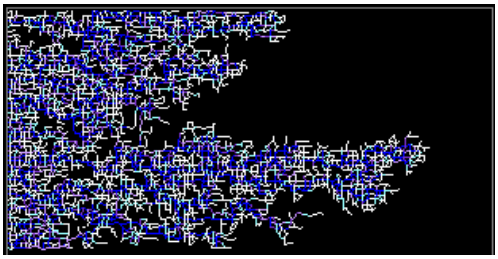

(d) automatic λ, S_w map

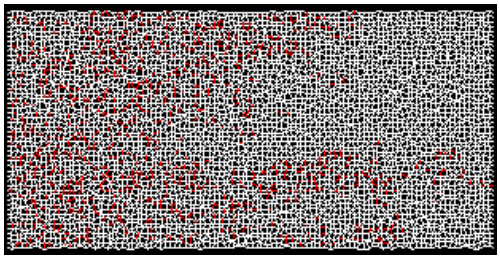

(e) λ=1.0, snap-off

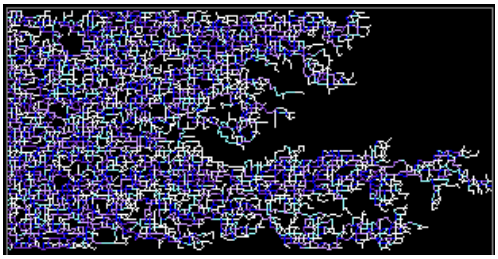

(f) λ=1.0, snap-off, S_w map

Figure 5-2 Illustrate the influence of ***switch***, ***Q=1.0e^{-6}m^3/s, M=10.0***.

Above figures are taken when identical amount of water (0.192 PV) has been injected into each network. (a), (c), (e) are figures of pores filled by different phases. Red is water-filled pores, white is oil-containing pores. (b), (d), (f) are figures showing the local water saturation. As S_w increases, the colour will change in the order of black, white, light blue, light purple, dark purple, to dark blue. The black region is composed of pores with volumeless film and the dark blue pores are filled with invading water.

The dramatic effect of the switch can be seen on the pore occupancy patterns of each phase during water injection, which is shown in the bar charts of the water-filled pores (Figure 5-3). In these figures, the red bars represent the pore size distribution (PSD) of all the pores while the blue bars represent the water-filled pores only. It is clear that the bulk displacement will primarily fill the larger pores (λ=0.0), while the film swelling and snap-off will firstly fill the smaller pores (λ=1.0) – in the case with automatic λ, under the current flow rate, *Q=1.0e^{-6}*, these two filling mechanisms are more balanced (Figure 5-3 (b)). Note that the blue bars only represent the count of water fully-filled pores (Table 4-3 A), there is also water residing in other partial-filled pores as the

wetting films or bulk water (Table 4-3 C-I) – the blue bars cannot represent the current system water saturation.

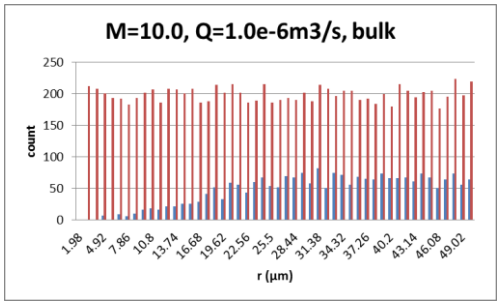

(a) λ=0.0, piston-like

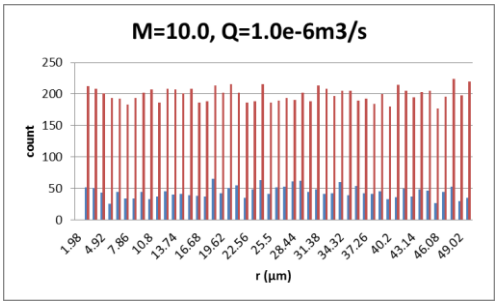

(b) automatic λ

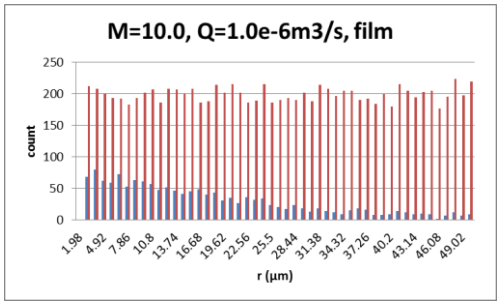

(c) λ=1.0, snap-off

Figure 5-3 PSD bar chart at the end of simulations with various ***switches***, ***Q=1.0e^{-6}m^3/s, M=10.0***. The red bars represent the PSD of all the pores, the blue bars represent the water-filled pores only.

The water fractional flow curves at the outlet of the network model reflect the characteristics of the water displacement fronts. For example, viscous fingering will lead to a "ragged" water effluent curve, and the more stable displacements lead to smoother F_w-S_w curves. Furthermore, more film swelling and snap-off associating with the larger λ will result in more trapped oil and worse oil recovery (Figure 5-4).

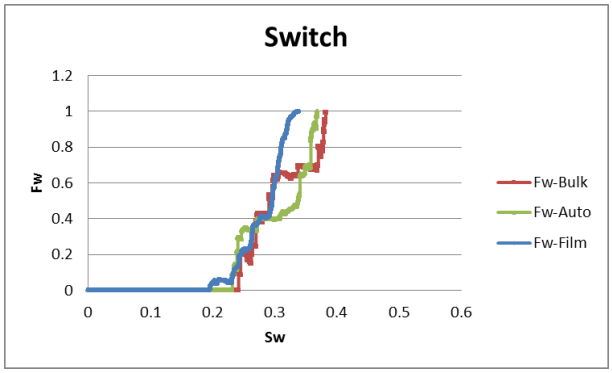

Figure 5-4 Water fractional flow curves of simulations with various ***switches***, ***Q=1.0e^{-6}m^3/s, M=10.0***.

In the numerical experiments where water is injected into the porous medium containing a more viscous oil phase (*M=10.0*), the pressure drop decreases more over time to counteract the growing global conductance (due to the decreasing global average viscosity) and maintain the flow rate. Compared to piston-like displacement, snap-off is more likely to cause oil trapping and reduce the global conductance, which has the opposing effect of the less viscous invading water. Therefore, although with identical injection rate, the global pressure drops are quite different (Figure 5-5), to be specific, smallest pressure drop reduction is observed in the purely snap-off case. We can immediately deduce that the dynamic balance between capillary and viscous forces (i.e. λ) will lead to different USS relative permeability curves. Precisely how this occurs and the detailed results on this matter will be discussed in Chapter 6.

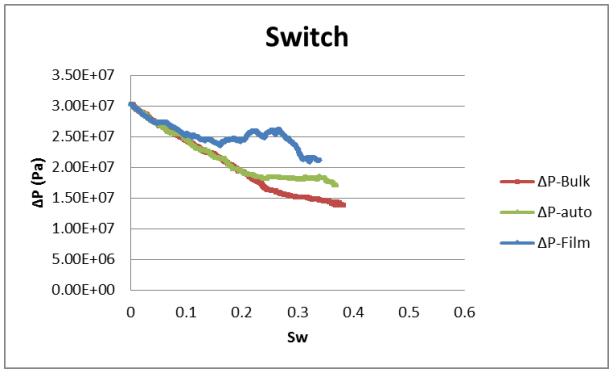

Figure 5-5 Global pressure drop of simulations with various ***switches***, ***Q=1.0e^{-6}m^3/s, M=10.0***.

5.3 Influence of Flow Rate (*Q*)

If we change the injection rate in our simulator, then the pressure drop across the whole system (as well as across each pore) will alter accordingly. This means that the *local* switch will be affected by the *global* flow rate. Rather, by distributing the incoming water into wetting film or bulk water, the *local* switch will also have influence on the *global* displacement regimes. In a high rate case with a large pressure drop, viscous forces will control the displacement and relatively small λ values will dominate locally. Therefore, in each partially-filled pore, most of the invading water for such cases would be used to propel the bulk meniscus forward and less water would be left to swell the local wetting film and this will also reduce downstream film-swelling and snap-off. Conversely, low-rate, capillary-dominated floods will be characterised by larger switch values and better water supply to feed downstream swelling films. The overall

complexity of the imbibition process is in large measure a result of the competing influences just described.

Unit Viscosity Ratio

Figure 5-6 shows the fluid configurations of unit viscosity ratio imbibition displacements at 3 injections rates ($Q=1.0e^{-3}m^3/s$; $Q=1.0e^{-6}m^3/s$; $Q=5.0e^{-9}m^3/s$). Snap-off and trapping are clearly becoming more prevalent as flow rate decreases. In the high rate case (a), most of the waterflood occurs through the advancement of bulk menisci, whereas the low injection rate case (e) is mainly characterised by the swelling of wetting films. For the intermediate flow rate case, both mechanisms operate together.

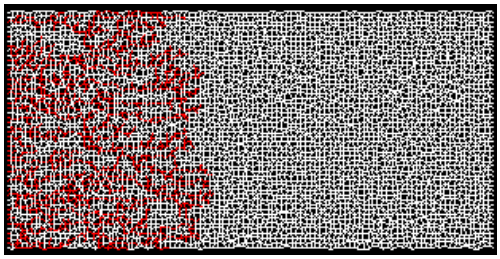

(a) $Q=1.0e^{-3}m^3/s$, $C_a=2.94e^{1}$

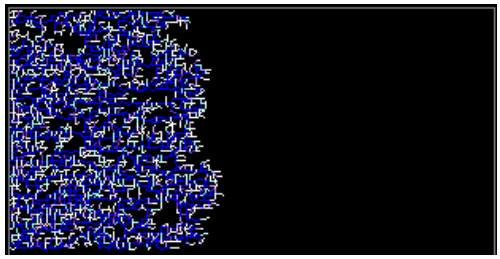

(b) $Q=1.0e^{-3}m^3/s$, $C_a=2.94e^{1}$, S_w map

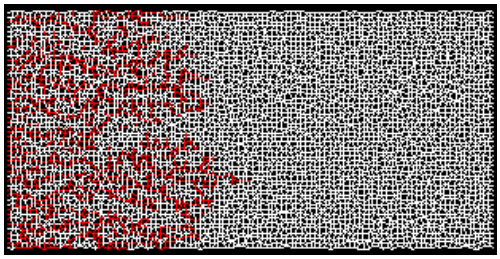

(c) $Q=1.0e^{-6}m^3/s$, $C_a=2.94e^{-2}$

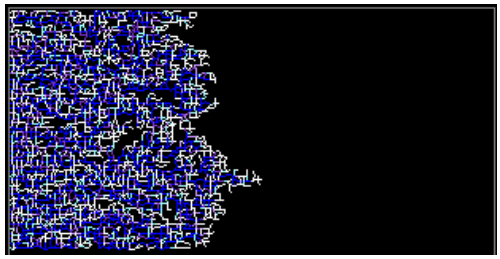

(d) $Q=1.0e^{-6}m^3/s$, $C_a=2.94e^{-2}$, S_w map

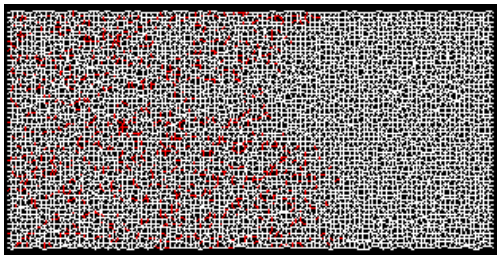

(e) $Q=5.0e^{-9}m^3/s$, $C_a=1.47e^{-4}$

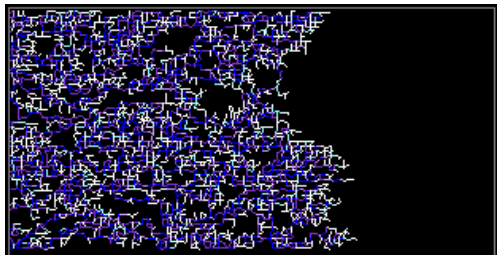

(f) $Q=5.0e^{-9}m^3/s$, $C_a=1.47e^{-4}$, S_w map

Figure 5-6 Fluids configuration with various ***injection rates*** and ***M=1.0***.
Above figures are taken when identical amount of water (0.192 PV) has been injected into each network. (a), (c), (e) are figures of pores filled by different phases. Red is water-filled pores, white is oil-containing pores. (b), (d), (f) are figures showing the local water saturation. As S_w increases, the colour will change in the order of black, white, light blue, light purple, dark purple, to dark blue. The black region is composed of pores with volumeless film and the dark blue pores are filled with invading water.

As before, piston-like displacement will fill the larger pores first, while snap-off will primarily occur in smaller pores. Pore occupancy bar charts of water-filled pores for different injection rates (Figure 5-7) also highlight the dramatic influence of flow rate on pore filling preferences as rate changes.

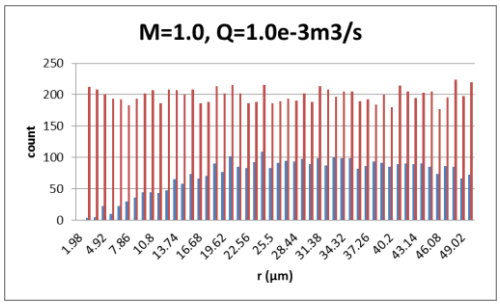

(a) $Q=1.0e^{-3}m^3/s$

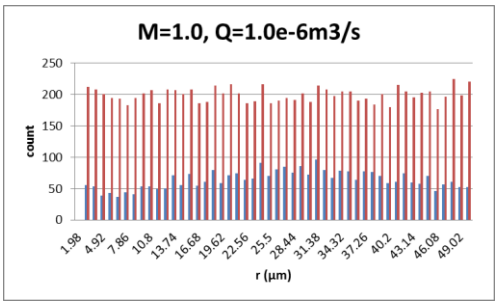

(b) $Q=1.0e^{-6}m^3/s$

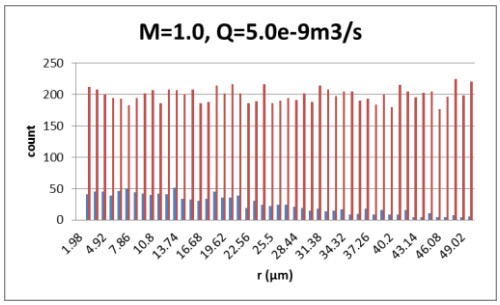

(c) $Q=5.0e^{-9}m^3/s$

Figure 5-7 Bar chart of pore size distribution at the end of each simulation with various ***injection rates*** and ***M=1.0***. Red is the number of all the pores within each range. Blue is the water-filled pores in each range.

In low-rate floods, the disconnected nature of the water clusters leads to early breakthrough of the water front and increased trapping. This is reflected in the curve of water fractional flow f_w (Figure 5-8). Since these simulations are carried out under the assumption that no initial water is present, f_w will be 0 until water breakthrough, after which f_w will gradually increase to 1. The earlier breakthrough of the water front in the low rate model is highlighted by the earlier increase in f_w – the smaller endpoint water saturation corresponds to the more severe oil trapping at low rates.

In these unit viscosity ratio runs, the water front is relatively smooth, as is the fractional flow curve – this means that, shortly after breakthrough, all outlet pores have been filled with water and at this point the flood is essentially over (water injected afterwards will flow through the network via connected water path without any further displacement). Thus the water saturation will not change very much post breakthrough, and hence these datasets cannot provide a great deal of useful information on USS relative permeability

curves (the method to obtain the USS relative permeability curves will be introduced later in Section 6.1).

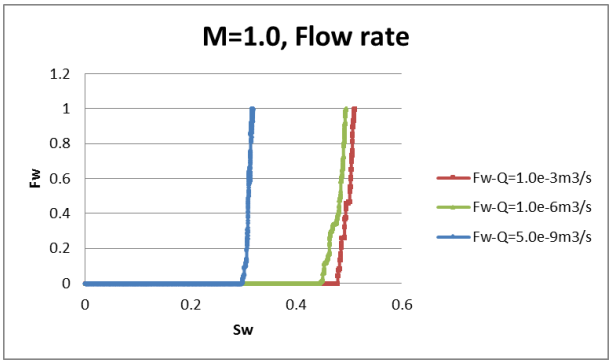

Figure 5-8 F_w-S_w curve of each simulation with various ***injection rates*** and ***M=1.0***.

It should be noted that the global pressure drops required to maintain the constant injection rates are positively correlated to the flow rate. In the cases with unit viscosity ratio, the global pressure drops will increase because of the oil trapping which occurs during the displacements (Figure 5-9) – steeper growth of the low-rate curve verifies the higher level of snap-off and trapping in that case. Note in each figure of global pressure drop (Figure 5-9 (a)-(c)), the upper bound of the y-axis is proportional to the corresponding injection rate, and this proportional relationship is used to obtain the combined figure with a normalised ΔP (as seen in (Figure 5-9 (d)) for better comparison.

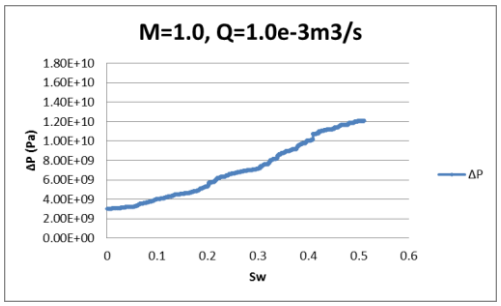

(a) $Q=1.0e^{-3}m^3/s$

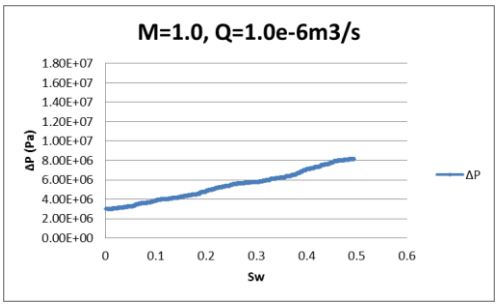

(b) $Q=1.0e^{-6}m^3/s$

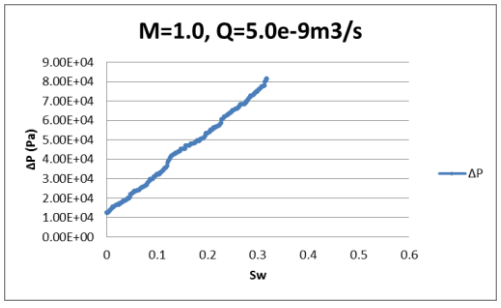

(c) $Q=5.0e^{-9}m^3/s$

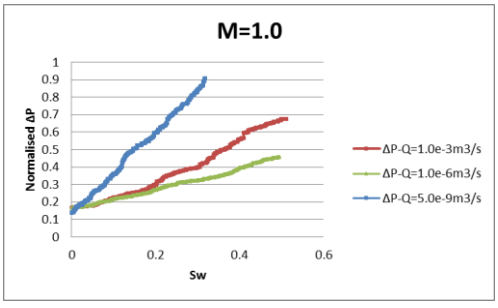

(d) Normalised ΔP

Figure 5-9 Global pressure drop of each simulation with various ***injection rates*** and ***M=1.0***.

The local distribution of the pore-scale switch during the displacement can be visualized. Since the network model only calculates λ in a pore when it has both the bulk menisci and mobile oil present, the map of local switch values at any given time actually outlines the water front. As λ increases, the colour will change in the order of white (λ=0.0), light blue, light purple, dark purple, to dark blue (λ=1.0). From Figure 5-10 (b), (d), (f), we can find that the local switches increase in general as flow rate decreases.

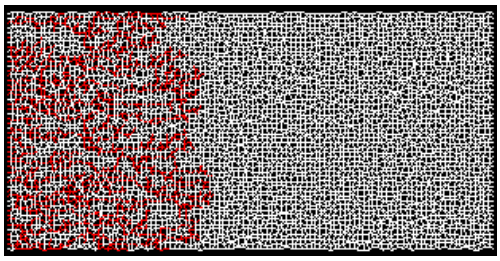

(a) $Q=1.0e^{-3}m^3/s$

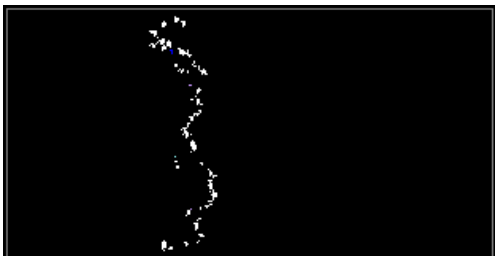

(b) $Q=1.0e^{-3}m^3/s$, local λ

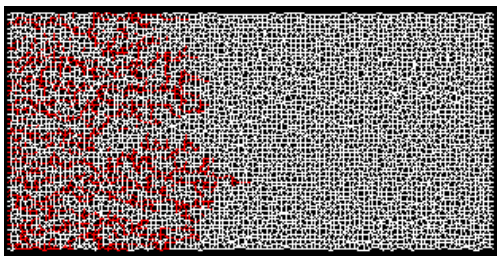

(c) $Q=1.0e^{-6}m^3/s$

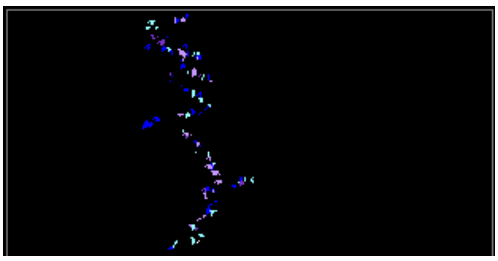

(d) $Q=1.0e^{-6}m^3/s$, local λ

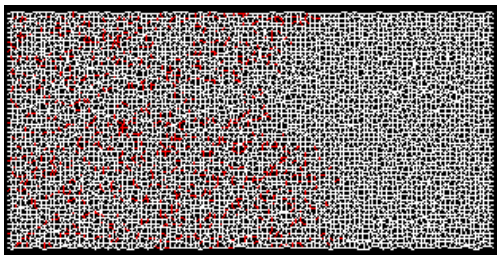

(e) $Q=5.0e^{-9}m^3/s$

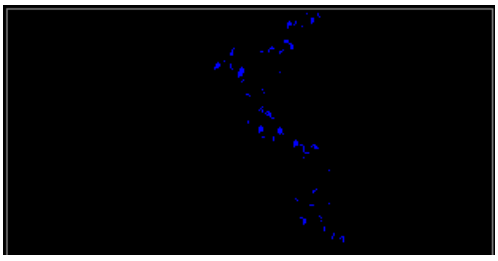

(f) $Q=5.0e^{-9}m^3/s$, local λ

Figure 5-10 Fluids configuration and switch map with various ***injection rates*** and ***M=1.0***.

Above figures are taken when identical amount of water has been injected into each network. (a), (c), (e) are figures of pores filled by different phases. Red is water-filled pores, white is oil-containing pores. (b), (d), (f) are figures of corresponding local switch map. As λ increases, the colour will change in the order of white (λ=0.0), light blue, light purple, dark purple, to dark blue (λ=1.0).

Furthermore, based on the number of selected pores (a quantity that is predefined by the user), the model can randomly choose several pores (note with the same random seed, the model will actually choose the same pores in each simulation) and record the values of their switch at each time step if the pores contains bulk menisci and mobile oil. Each curve in Figure 5-11 tracks the switch changing of one particular pore, and the x-axis represents the number of time steps. The increasing tendency of the local switch as injection rate decreases is once again verified by the results in Figure 5-11: in the high-rate model (a), the initial switch of each selected pore is 0.0; while in the low-rate model (c), the switch in each pore remains as 1.0 (only film swelling); and in the intermediate-rate case (b), the starting values of local switch are distributed between 0 and 1. It can also be concluded that in the cases with unit viscosity ratio, surrounding fluid configurations may affect the local force balance and cause a sudden jump in λ (Figure 5-11).

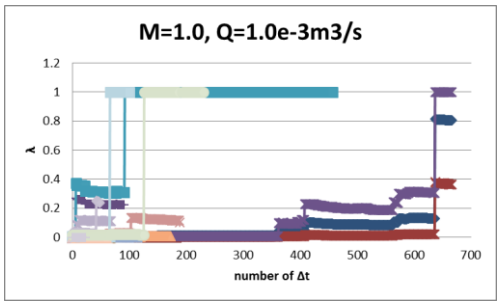

(a) $Q=1.0e^{-3}m^3/s$

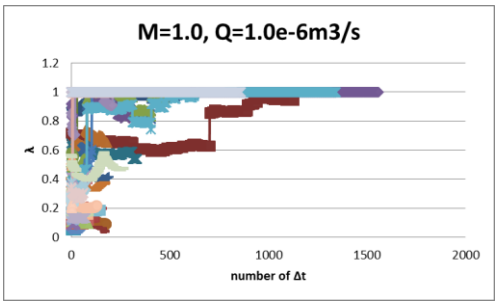

(b) $Q=1.0e^{-6}m^3/s$

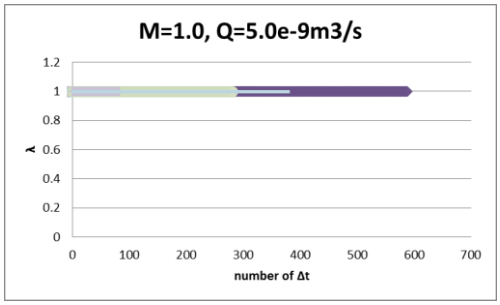

(c) $Q=5.0e^{-9}m^3/s$

Figure 5-11 Local Switch evolution in each simulation with various ***injection rates*** and ***M=1.0***. Each curve represents the value of switch in a particular pore at each time step, the x-axis is the number of time steps.

Unfavourable Viscosity Ratios

A series of adverse mobility ratio displacements with $M = 10.0$ are shown in Figure 5-12 under various flow rates (i.e. $Q=1.0e^{-3}m^3/s$; $Q=1.0e^{-6}m^3/s$; $Q=1.0e^{-9}m^3/s$). When less viscous water is injected into the network model ($M=10.0$), the high-rate model is

dominated by viscous fingering, while at lower rates growing numbers of disconnected water-filled clusters caused by snap-off are observed– the capillary forces become increasingly important as flow rate decreases and the wetting front becomes more transversely disperse (Figure 5-12).

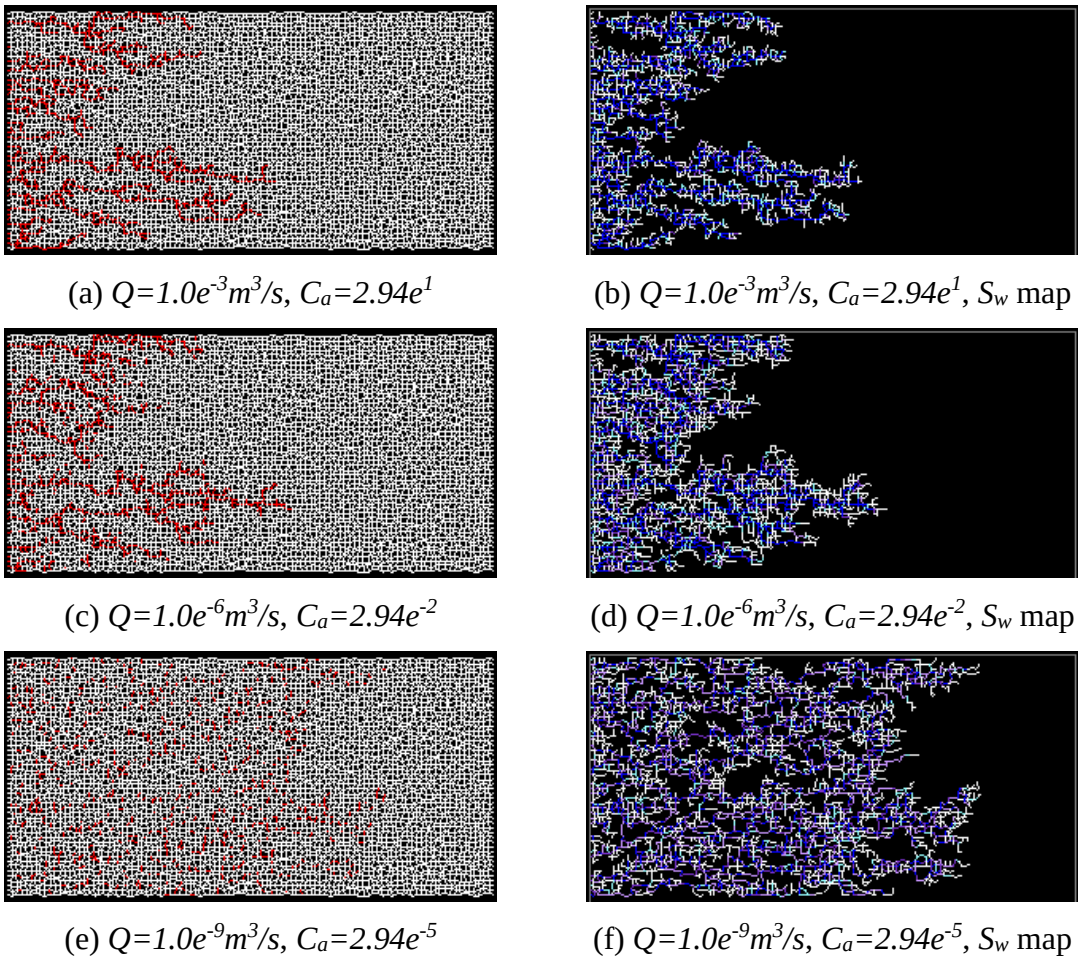

(a) $Q=1.0e^{-3}m^3/s$, $C_a=2.94e^{1}$ (b) $Q=1.0e^{-3}m^3/s$, $C_a=2.94e^{1}$, S_w map

(c) $Q=1.0e^{-6}m^3/s$, $C_a=2.94e^{-2}$ (d) $Q=1.0e^{-6}m^3/s$, $C_a=2.94e^{-2}$, S_w map

(e) $Q=1.0e^{-9}m^3/s$, $C_a=2.94e^{-5}$ (f) $Q=1.0e^{-9}m^3/s$, $C_a=2.94e^{-5}$, S_w map

Figure 5-12 Fluids configuration with various ***injection rates*** and ***M=10.0***. Above figures are taken when identical amount of water (0.192 PV) has been injected into each network. (a), (c), (e) are figures of pores filled by different phases. Red is water-filled pores, white is oil-containing pores. (b), (d), (f) are figures showing the local water saturation. As S_w increases, the colour will change in the order of black, white, light blue, light purple, dark purple, to dark blue. The black region is composed of pores with volumeless film and the dark blue pores are filled with invading water.

Bar charts of pore phase occupancy within the pore size distribution demonstrate the competition between viscous forces (large pores) and capillary force (small pores) – significant differences in the size distribution of water-filled pores are again evident (Figure 5-13).

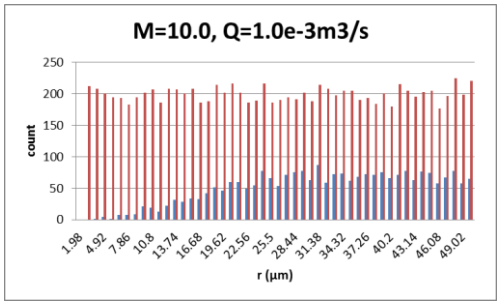

(a) $Q=1.0e^{-3}m^3/s$

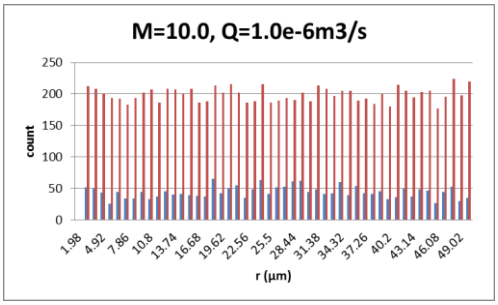

(b) $Q=1.0e^{-6}m^3/s$

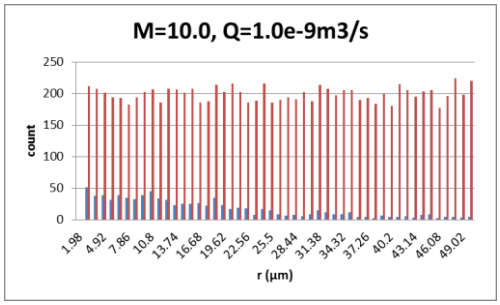

(c) $Q=1.0e^{-9}m^3/s$

Figure 5-13 Bar chart of pore size distribution at the end of each simulation with various ***injection rates*** and ***M=10.0***.

Red is the number of all the pores within each range. Blue is the water-filled pores in each range.

The slope and smoothness of the corresponding fractional flow curves after breakthrough highlight the effects of pore scale heterogeneities on the water front. As flowrate is decreased, and the flow regime moves from viscous fingering to film swelling, the water front flattens, breakthrough occurs at a lower S_w and final recovery is reduced (Figure 5-14).

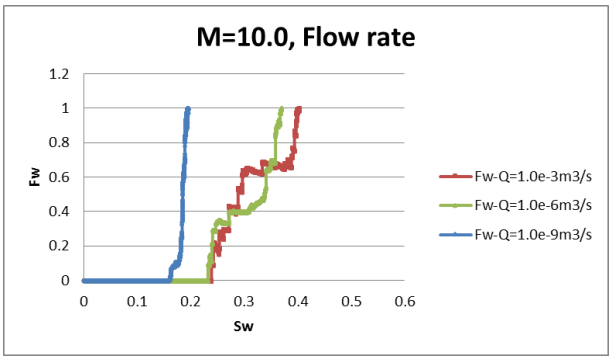

Figure 5-14 F_w-S_w curve at the end of each simulation with various ***injection rates*** and ***M=10.0***.

The global pressure drops to maintain the constant injection rates are positively correlated to the specific rate. In cases with unfavourable viscosity ratio, although the

trapping will induce an increase in ΔP, the decreasing average viscosity – as less viscous fluids is injected into the system – will bring down the global pressure drop overall. Hence the pressure drop plot is the net result of 2 competing effects (Figure 5-15).

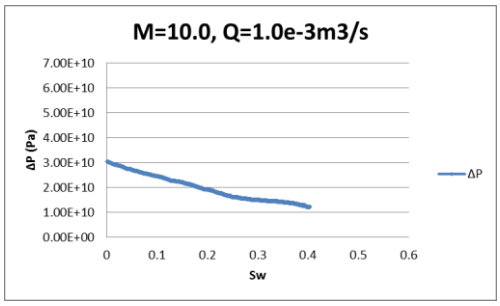

(a) $Q=1.0e^{-3}m^3/s$

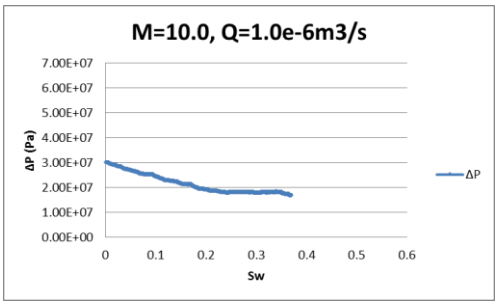

(b) $Q=1.0e^{-6}m^3/s$

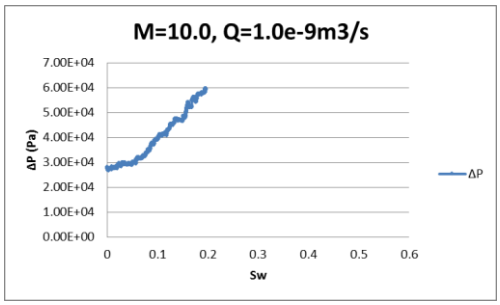

(c) $Q=1.0e^{-9}m^3/s$

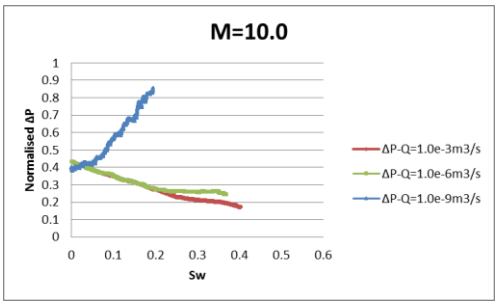

(d) Normalised ΔP

Figure 5-15 Global pressure drop of each simulation with ***various injection rates*** and ***M=10.0***.

Figure 5-16 shows the local switch map in the simulations at the same 3 injection rates as studied above (i.e. $Q=1.0e^{-3}m^3/s$; $Q=1.0e^{-6}m^3/s$; $Q=1.0e^{-9}m^3/s$). The switch map draws the outline of the heterogeneous water front (viscous fingering) of the high rate and intermediate rate models, as well as the relatively smoother front of the low rate, film-swelling model.

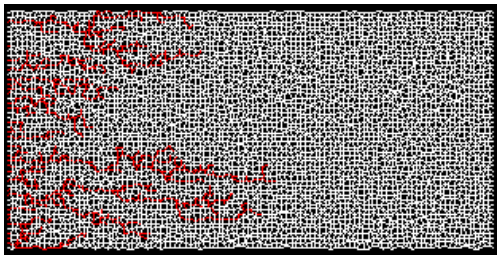

(a) $Q=1.0e^{-3}m^3/s$

(b) $Q=1.0e^{-3}m^3/s$, local λ

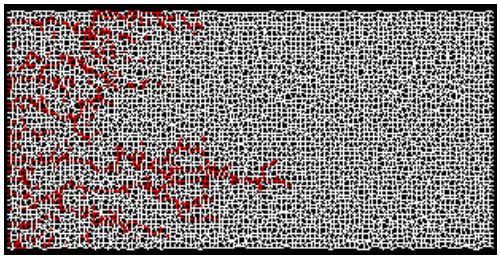

(c) $Q=1.0e^{-6}m^3/s$

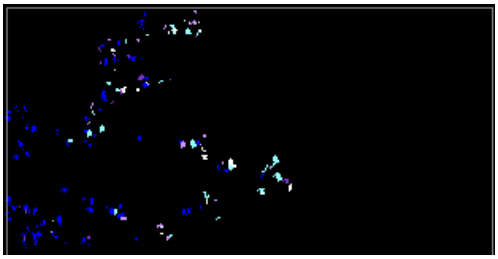

(d) $Q=1.0e^{-6}m^3/s$, local λ

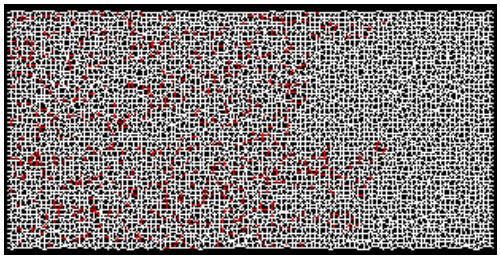

(e) $Q=1.0e^{-9}m^3/s$

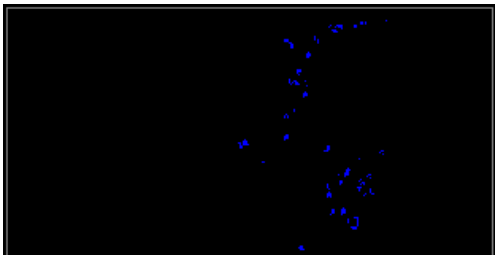

(f) $Q=1.0e^{-9}m^3/s$, local λ

Figure 5-16 Fluids configuration and switch map with various ***injection rates*** and ***M=10.0***.

Above figures are taken when identical amount of water (0.192PV) has been injected into each network. (a), (c), (e) are figures of pores filled by different phases. Red is water-filled pores, white is oil-containing pores. (b), (d), (f) are figures of corresponding local switch map. As λ increases, the colour will change in the order of white (λ=0.0), light blue, light purple, dark purple, to dark blue (λ=1.0).

Figure 5-17 shows the switch curves of selected representative pores. Note that, for each pore, with the help of decreasing average viscosity (as less viscous water invades), the value of the automatic switch will *go up* during the displacement, Figure 5-17 (a) and (b). In the corresponding very low flow rate displacements (Figure 5-17 (c)), the switch remains constant at λ = 1 since all displacements are dominated entirely by capillarity (i.e. film swelling mechanisms).

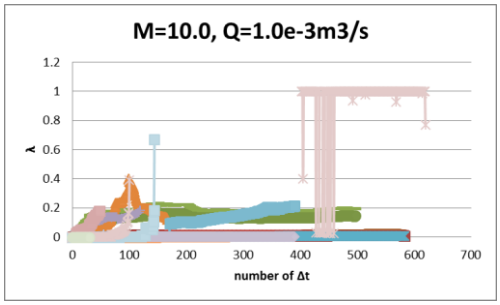

(a) $Q=1.0e^{-3}m^3/s$

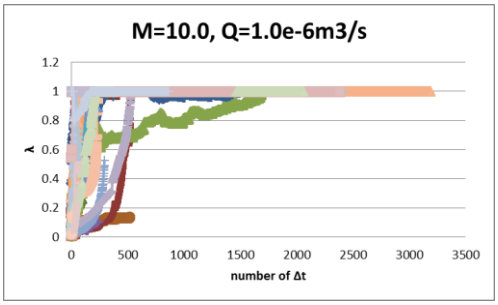

(b) $Q=1.0e^{-6}m^3/s$

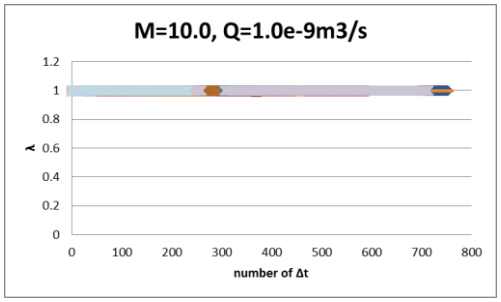

(c) $Q=1.0e^{-9}m^3/s$

Figure 5-17 Local Switch evolution in each simulation with various ***injection rates*** and ***M=10.0***.

Favourable Viscosity Ratios

When more viscous water is injected into the network model (*M=0.1*), it will tend to propagate through the system with a flat front, since it is a highly stable displacement. Different levels of film-swelling and snap-off can still be observed in each of the cases with various flow rates (i.e. $Q=1.0e^{-3}m^3/s$; $Q=1.0e^{-6}m^3/s$; $Q=5.0e^{-8}m^3/s$). However, as the wetting film flows slower than the bulk oil, the observed difference will be less obvious than the corresponding comparisons at *M=1.0* or unfavourable *M=10.0* viscosity ratios (Figure 5-18).

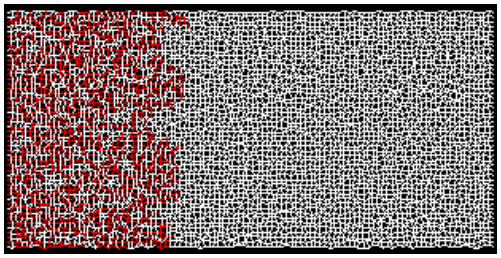

(a) $Q=1.0e^{-3}m^3/s$, $C_a=2.94e^{1}$

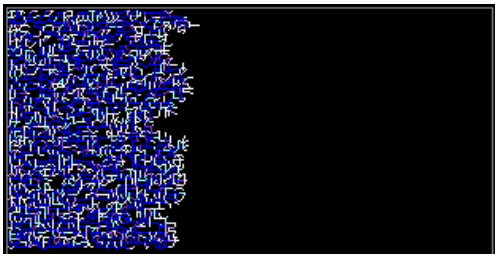

(b) $Q=1.0e^{-3}m^3/s$, $C_a=2.94e^{1}$, S_w map

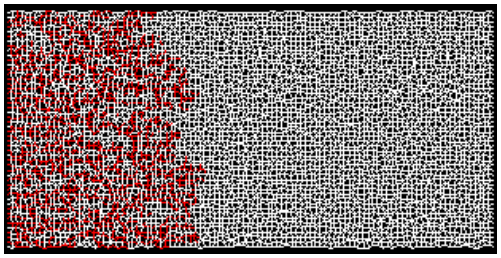

(c) $Q=1.0e^{-6}m^3/s$, $C_a=2.94e^{-2}$

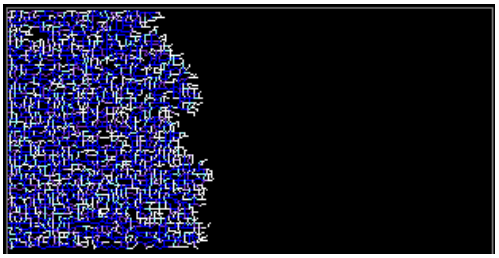

(d) $Q=1.0e^{-6}m^3/s$, $C_a=2.94e^{-2}$, S_w map

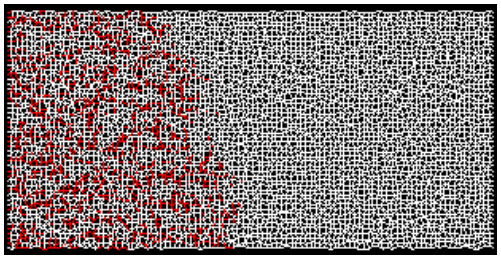

(e) $Q=5.0e^{-8}m^3/s$, $Ca=1.47e^{-3}$

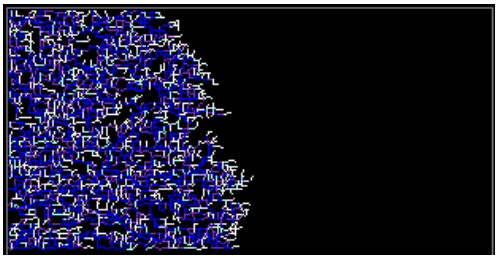

(f) $Q=5.0e^{-8}m^3/s$, $Ca=1.47e^{-3}$, S_w map

Figure 5-18 Fluids configuration with various ***injection rates*** and ***M=0.1***.

Above figures are taken when identical amount of water (0.192PV) has been injected into each network. (a), (c), (e) are figures of pores filled by different phases. Red is water-filled pores, white is oil-containing pores. (b), (d), (f) are figures showing the local water saturation. As S_w increases, the colour will change in the order of black, white, light blue, light purple, dark purple, to dark blue. The black region is composed of pores with volumeless film and the dark blue pores are filled with invading water.

Bar charts of the phase pore occupancies within the pore size distribution demonstrate the competition on water occupancy between viscous forces (large pores) and capillary force (small pores) (Figure 5-19).

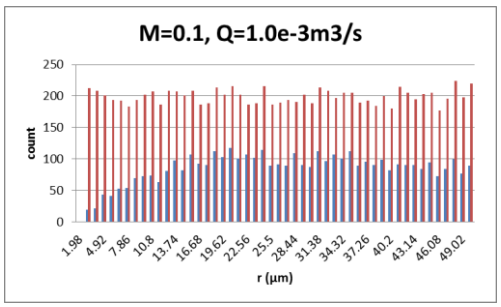

(a) $Q=1.0e^{-3}m^3/s$

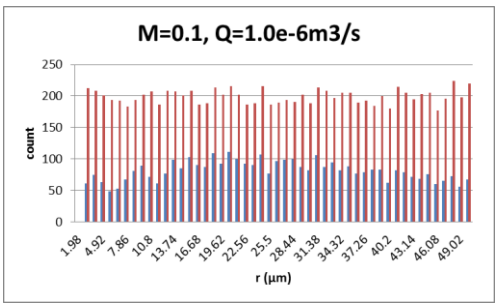

(b) $Q=1.0e^{-6}m^3/s$

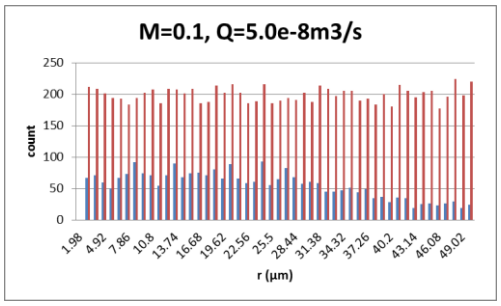

(c) $Q=5.0e^{-8}m^3/s$

Figure 5-19 Bar chart of pore size distribution at the end of each simulation with various ***injection rates*** and ***M=0.1***.

Red is the number of all the pores within each range. Blue is the water-filled pores in each range.

Figure 5-20 shows the F_w-S_w curves for these 3 flow rates for the *M=0.1* case – the low rate flood leads to more trapping and a lower oil recovery.

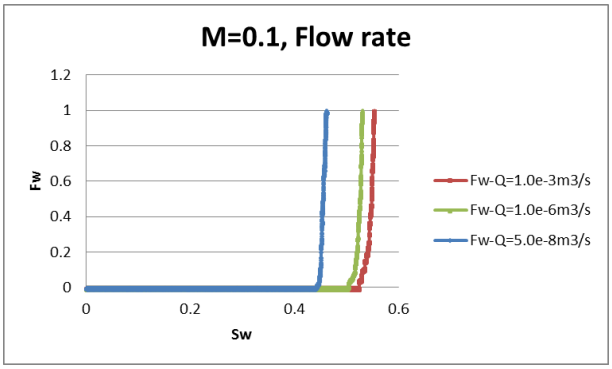

Figure 5-20 F_w-S_w curve at the end of each simulation with various ***injection rates*** and ***M=0.1***.

The global pressure drops will increase to counteract the decreasing global conductance brought about by both trapped oil and increasing average viscosity – as the more viscous phase (water) is injected into the system (Figure 5-21).

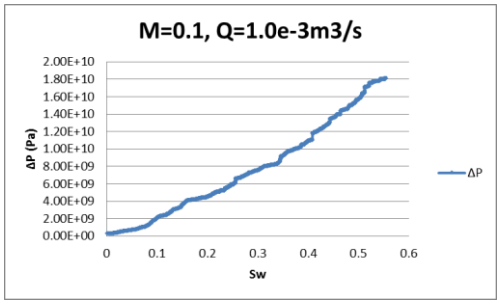

(a) $Q=1.0e^{-3}m^3/s$

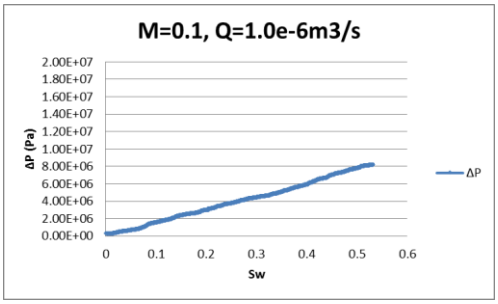

(b) $Q=1.0e^{-6}m^3/s$

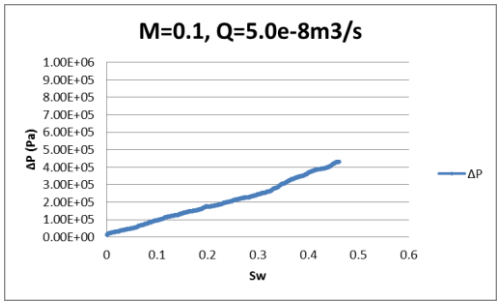

(c) $Q=5.0e^{-8}m^3/s$

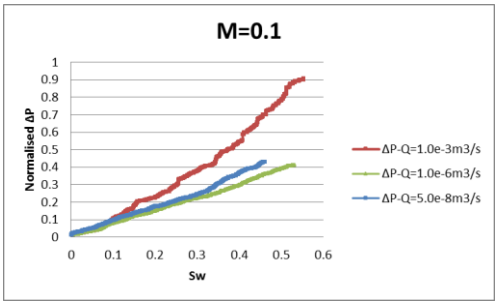

(d) Normalised ΔP

Figure 5-21 Global pressure drop of each simulation with various ***injection rates*** and ***M=0.1***.

Figure 5-22 shows the local switch map in the simulations with various injection rate and favourable viscosity ratio (*M=0.1*).

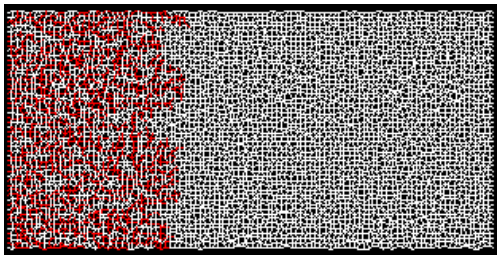

(a) $Q=1.0e^{-3}m^3/s$

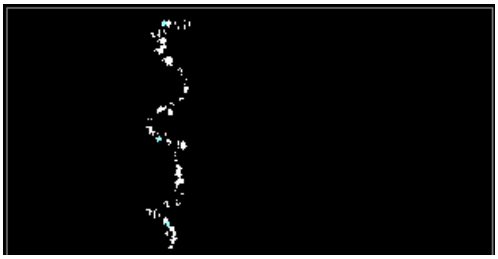

(b) $Q=1.0e^{-3}m^3/s$, local λ

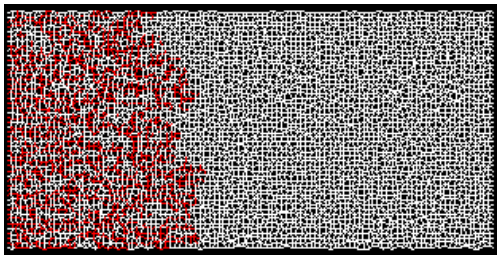

(c) $Q=1.0e^{-6}m^3/s$

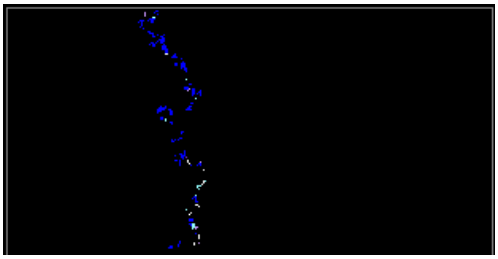

(d) $Q=1.0e^{-6}m^3/s$, local λ

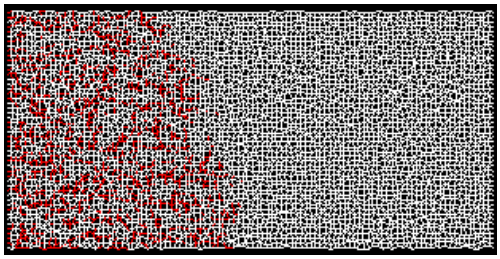

(e) $Q=5.0e^{-8}m^3/s$

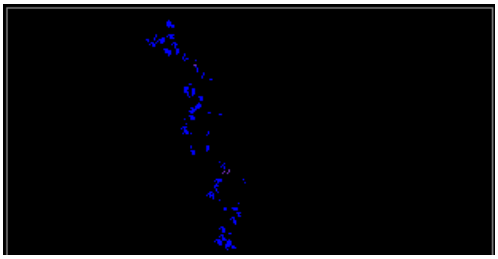

(f) $Q=5.0e^{-8}m^3/s$, local λ

Figure 5-22 Fluids configuration and switch map with various ***injection rates*** and ***M=0.1***.

Above figures are taken when identical amount of water has been injected into each network. (a), (c), (e) are figures of pores filled by different phase. Red is water-filled pores, white is oil-filled or partial-filled pores with wetting film. (b), (d), (f) are figures of corresponding local switch map. As λ increases, the colour will change in the order of white (λ=0.0), light blue, light purple, dark purple, to dark blue (λ=1.0).

Figure 5-23 shows the switch curves (λ vs. Δt) of selected representative pores. In this case, for each pore the increasing average viscosity will *reduce* the local λ.

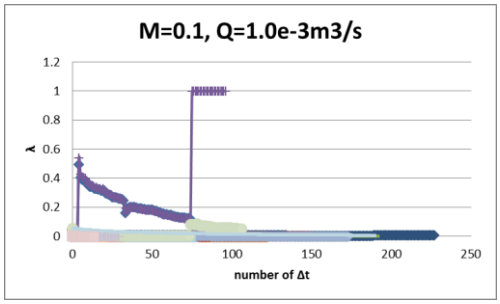

(a) $Q=1.0e^{-3}m^3/s$

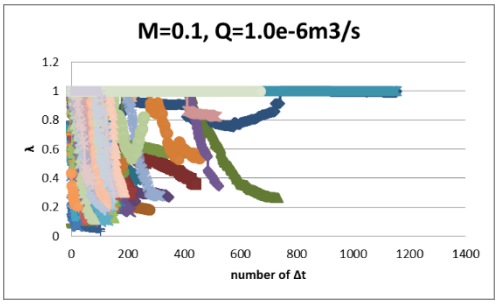

(b) $Q=1.0e^{-6}m^3/s$

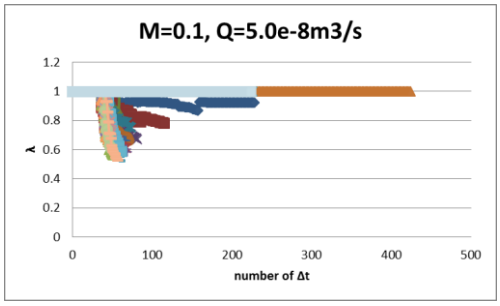

(c) $Q=5.0e^{-8}m^3/s$

Figure 5-23 Local Switch evolution in each simulation with various ***injection rates*** and ***M=0.1***.

5.4 Influence of Viscosity Ratio (*M*)

5.4.1 High-rate Model ($Q=1.0e^{-3}m^3/s$, $Ca=2.94e^{1}$)

The impact of viscosity ratio on waterflood behaviour is now studied by varying the oil viscosity while keeping the water viscosity constant. Note in the simulations where μ_w and μ_o increase simultaneously with constant viscosity ratio (M), roughly the same filling regime (stable front displacement or viscous fingering) can be expected. However, at the same Q, less snap-off events will be observed since the increasing global viscosity will require a higher pressure drop across the system to maintain the constant flow rate.

In the high-rate case, we expect viscous forces to dominate the displacement and wetting films should be suppressed. When the invading water is more viscous than the defending phase ($M<1$), a stable displacement occurs – as shown in Figure 5-24 (a). Conversely, if a less viscous phase is injected into the system ($M>1$), viscous forces in the defending phase will be the dominating factor, and a typical pattern of finger growth along the pressure gradient emerges (Figure 5-24 (c)).

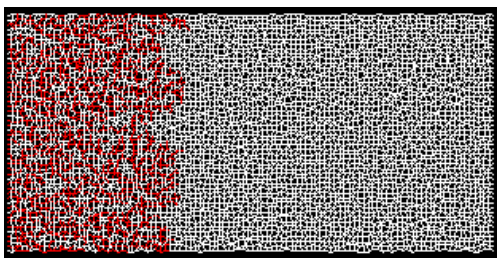

(a) $M=0.1$

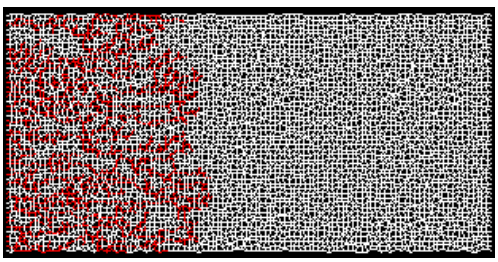

(b) $M=1.0$

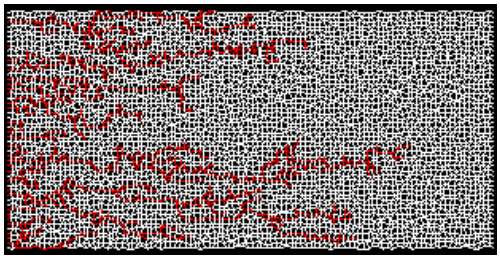

(c) *M=10.0*

Figure 5-24 Fluids configuration of ***high-rate model*** ***(Q=1.0e^{-3}m^3/s***, C_a*=2.94e^1)* with various ***viscosity ratios***.

Above figures represent pores filled by different phases, and are taken when identical amount of water (0.192PV) has been injected into each network. Red is water-filled pores, white is oil-containing pores.

In Figure 5-25, the formation of an unstable water front, the corresponding early water breakthrough and the poorer oil recovery caused by viscous fingering can be seen in the fractional flow curves.

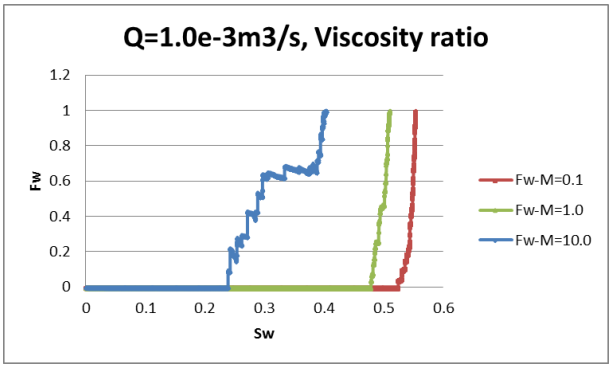

Figure 5-25 F_w-S_w curve of ***high-rate model*** ***(Q=1.0e^{-3}m^3/s***, C_a*=2.94e^1)* with various ***viscosity ratios***.

Figure 5-26 illustrates the local switch maps (λ *vs.* Δt), where it can be seen that although the local switch always starts from 0, the surrounding configuration changes may cause sudden jumps.

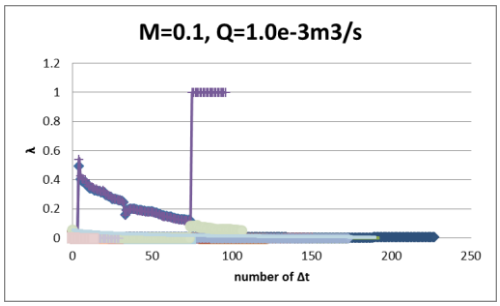

(a) *M=0.1*

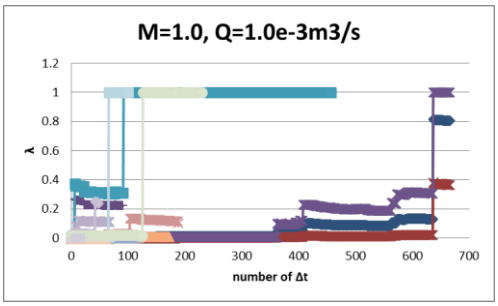

(b) *M=1.0*

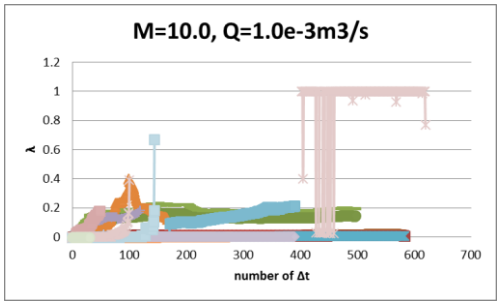

(c) *M=10.0*

Figure 5-26 Local Switch evolution in each ***high-rate model*** ***(Q=1.0e^{-3}m^3/s***, C_a*=2.94e^1)* with various ***viscosity ratios***.

5.4.2 Intermediate-rate Model (Q=1.0e^{-6}m^3/s, Ca=2.94e^{-2})

At an intermediate flow rate (*Q=1.0e^{-6}m^3/s*, C_a*=2.94e^{-2}*), broadly the same displacement regimes and water fractional flow curves are observed (Figure 5-27, Figure 5-28) as in high-rate cases (Figure 5-24, Figure 5-25), although snap-off starts to appear at the unfavourable viscosity ratio (*M=10.0*) (Figure 5-27 (c)).

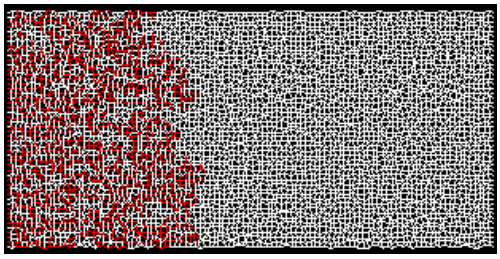

(a) *M=0.1*

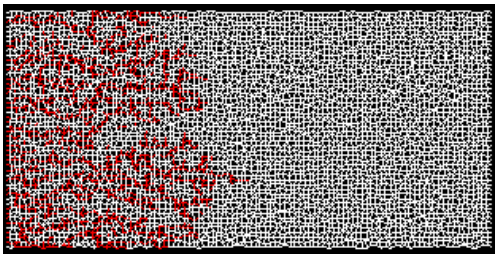

(b) *M=1.0*

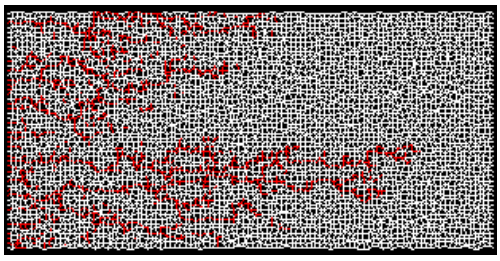

(c) *M=10.0*

Figure 5-27 Fluids configuration of ***intermediate-rate model*** (***Q=1.0e^{-6}m^3/s***, C_a*=2.94e^{-2}*) with various ***viscosity ratios***.

Above figures represent pores filled by different phases, and are taken when identical amount of water (0.192PV) has been injected into each network. Red is water-filled pores, white is oil-containing pores.

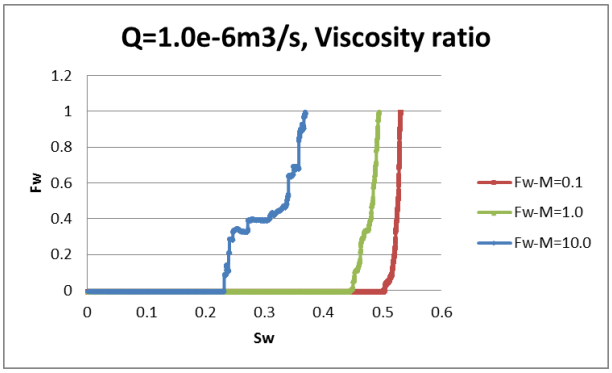

Figure 5-28 F_w-S_w curves of ***intermediate-rate model*** (***Q=1.0e^{-6}m^3/s***, C_a=*2.94e^{-2}*) with various ***viscosity ratios***.

Unlike the high-rate case, where λ starts from 0 everywhere in the network, the intermediate flow rate case will begin to exhibit non-zero initial λ locally allowing us to study the relationship between viscosity ratio and the capillary/viscous switch in greater detail (Figure 5-29). Note here the λ analysis concentrates on the initial value as the advancing water/oil menisci just move into a specific pore. Very broadly for this flow rate, this initial λ is inversely proportional to the viscosity ratio; for example the case with M =0.1 shows a mainly decreasing λ vs Δt trend starting from higher λ (more film swelling) and a generally increasing trend for the *M=10* viscosity ratio from the smaller initial λ (more bulk displacement).

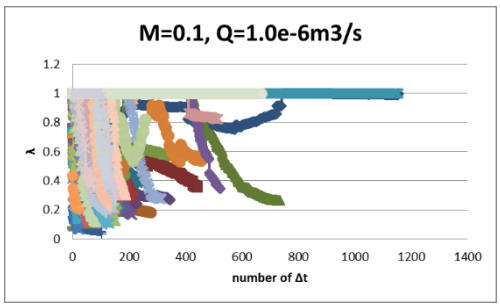

(a) *M=0.1*

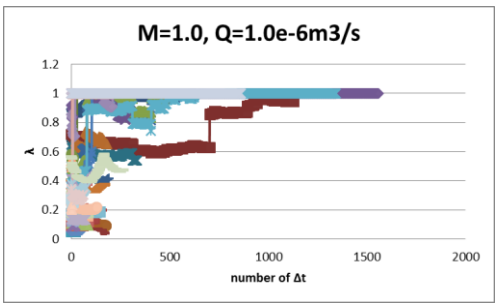

(b) *M=1.0*

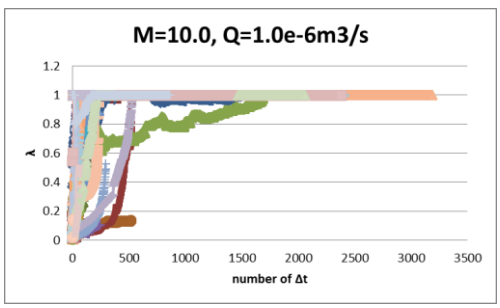

(c) *M=10.0*

Figure 5-29 Local Switch evolution in each ***intermediate-rate model*** (***Q=1.0e^{-6}m^3/s***, C_a=*2.94e^{-2}*) with various ***viscosity ratios***.

Furthermore, other than local λ values, the indicator of film swelling can also be affected by the viscosity ratio. It was shown earlier (Section 4.10) that R_{w-o} can be written as:

$$R_{w-o} = \frac{\frac{A_w^2}{C_w S_1}}{\frac{A_w^2}{C_w S_1} + \frac{3r^2(A - A_w)}{20\frac{\mu_o}{\mu_w}}} \qquad 5\text{-}1$$

Therefore, for the same volume of corner water, as viscosity ratio increases in the order of 0.1, 1.0, 10.0, R_{w-o} will grow as well; thus the wetting films will have greater mobility and greater impact in the unstable viscosity ratio case.

So, as *M* increases, there is a competition between the smaller initial λ and larger R_{w-o}; and based on the results shown in Figure 5-27, the increased mobility of the wetting films appears to prevail for the case studied.

In the normal expression for capillary number, only water (advancing phase) viscosity is considered, hence it fails to capture the water/oil viscosity difference here – we keep the μ_w constant while changing the defending oil phase viscosity.

5.4.3 Low-rate Model ($Q=5.0e^{-8}m^3/s$, $Ca=1.47e^{-3}$)

In the low-rate case ($Q=5.0e^{-8}m^3/s$, $Ca=1.47e^{-3}$), where capillary forces dominate the displacement, the extent of snap-off is still controlled to some degree by the viscosity ratio (Figure 5-30). As a result of increasing viscosity ratio, the wetting films will have greater mobility (R_{w-o}) and cause a higher level of film swelling/snap-off, regardless the current value of local λ.

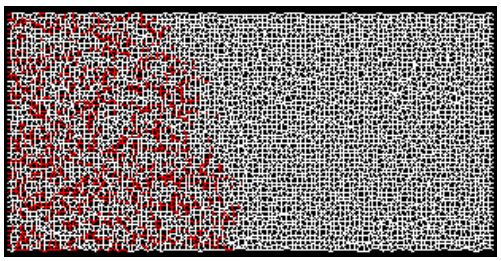

(a) *M=0.1*

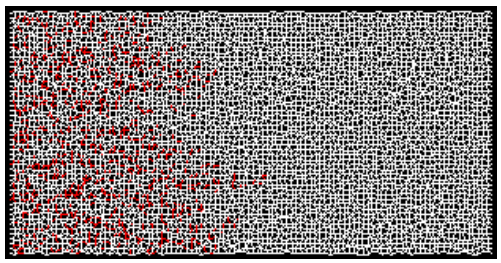

(b) *M=1.0*

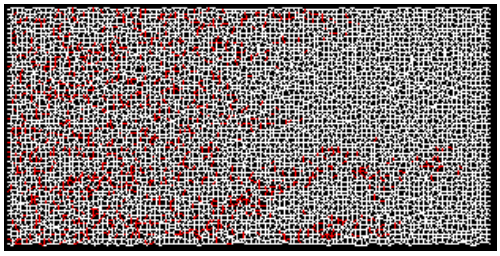

(c) *M=10.0*

Figure 5-30 Fluids configuration of ***low-rate models*** with ***Q=5.0e^{-8}m^3/s*** and various ***viscosity ratios***.

Above figures represent pores filled by different phases, and are taken when identical amount of water (0.192PV) has been injected into each network. Red is water-filled pores, white is oil-containing pores.

At this low flow rate, especially in the *M=0.1* and *M=1.0* cases, capillary forces become the dominant force – these two simulations have the similar S_w at the moment of water breakthrough, and the less even water front of the *M=1.0* case ensure a longer period of two-phase flow after water BT, hence the higher S_w at the end (Figure 5-31).

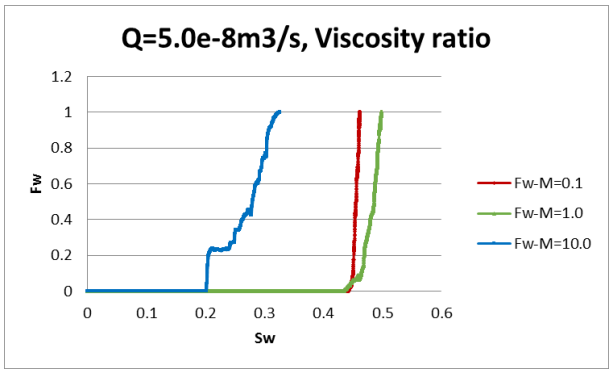

Figure 5-31 F_w-S_w curves of ***low-rate model*** (***Q=5.0e^{-8}m^3/s***, C_a=*1.47e^{-3}*) with various ***viscosity ratios***.

For the same low injection rate (*Q=5.0e^{-8}m^3/s*, C_a=*1.47e^{-3}*), the local λ in *M=0.1* case will start from 1.0 then gradually decrease (Figure 5-32 (a)); on the contrary, in *M=10.0* case, the local switch will increase to 1.0 from a lower value (Figure 5-32 (c)).

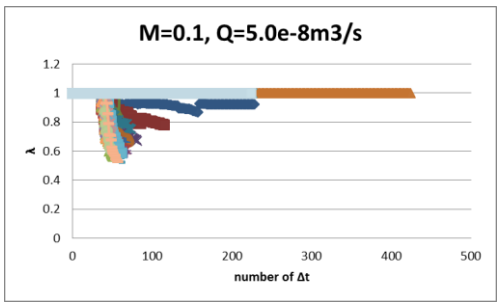

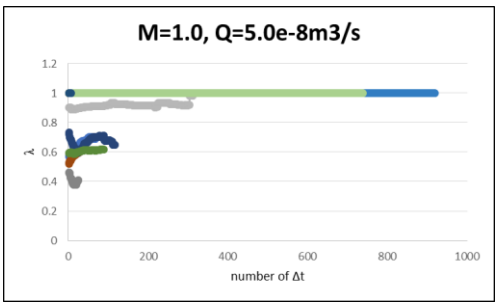

(a) *M=0.1* (b) *M=1.0*

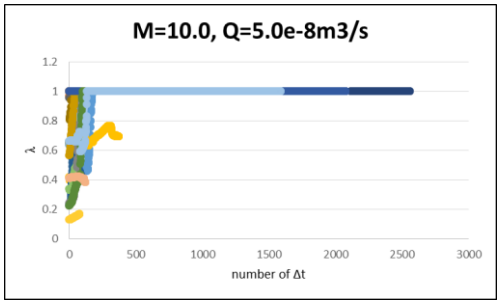

(c) *M=10.0*

Figure 5-32 Local Switch evolution in ***low-rate models*** (***Q=5.0e^{-8}m^3/s***, ***C_a=1.47e^{-3}***) and various ***viscosity ratios***.

5.4.4 Low-rate Model (Q=1.0e^{-9}m^3/s, C_a=2.94e^{-5})

Our model automatically checks the flow direction in each pore and temporally traps counter-current pores at every time step in order to eliminate negative inlet/outlet flows and retreating bulk menisci. These occur more often in the low-rate, capillary-dominated cases, especially in the completely dry initial networks as used in the current calculations. This approximation can be relaxed later if the technique of simulating mobile oil ganglion is included in this model.

In the cases with *Q=1.0e^{-9}m^3/s*, the starting global pressure drop in *M=1.0* and *M=0.1* cases are smaller than zero (as seen in Figure 5-35); injected water can only flow through very limited pathways and a large portion of pores are closed due to their counter-current flow. Worse still, in the dry network, open pores far away from the water path cannot be displaced due to a lack of water supply. Hence the displacement results are characterised by very wispy, long, thin fingers (Figure 5-33 (a) and (b)), which leads to a large volume of oil residual in the un-swept areas (Figure 5-34). In comparison to the cases with *Q=5.0e^{-8}m^3/s*, the appearance of these pathologically long fingers causes the abrupt changes in the f_w curves (see Figure 5-31 and Figure 5-34). In the unfavourable viscosity ratio (*M=10.0*) case, however, the relatively larger global viscosity requires a higher pressure drop to start displacement (Figure 5-35), which guarantees a sufficient portion of open pores and hence more of the network in a flowing state (Figure 5-33 (c)) and a better oil recovery (Figure 5-34). Later in Section 5.5.8, the pathological long fingers as shown in Figure 5-33 (a) and (b) will be avoided in systems with initial wetting films. Similar behaviours have been observed by

Weisbrod et al. (2002) during their experimental research about differences between water imbibition in initially dry sand versus prewetted sand.

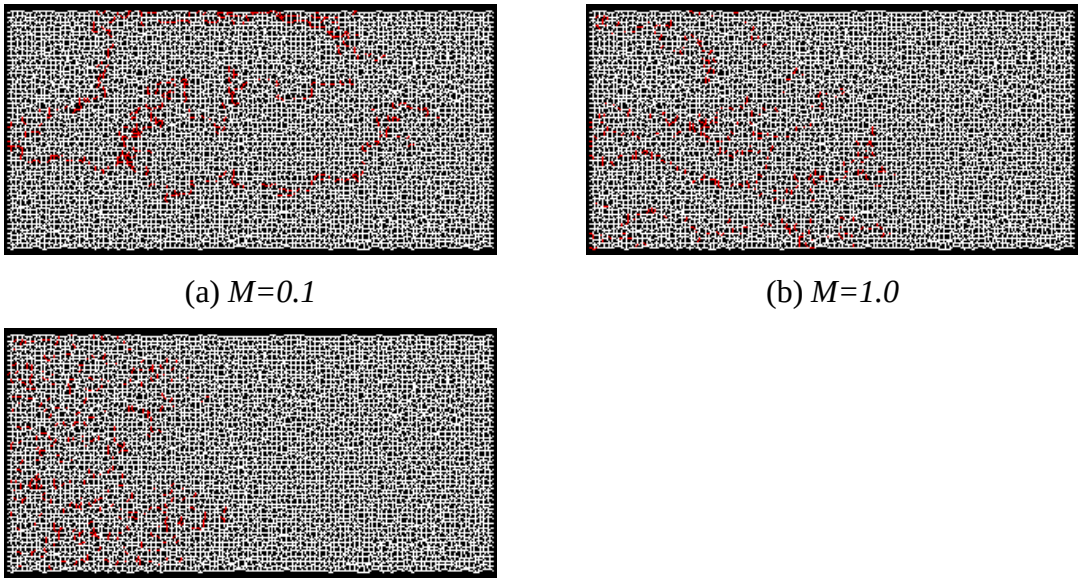

(a) *M=0.1* (b) *M=1.0*

(c) *M=10.0*

Figure 5-33 Fluids configuration of ***low-rate*** (***Q=1.0e^{-9}m^3/s***, C_a=*2.94e^{-5}*) model with various ***viscosity ratios***.

Above figures represent pores filled by different phases, and are taken when identical amount of water (0.064PV) has been injected into each network. Red is water-filled pores, white is oil-filled or partial-filled pores with wetting film.

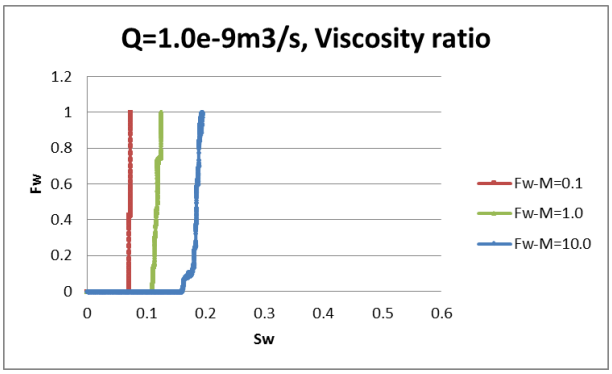

Figure 5-34 F_w-S_w curves of ***low-rate*** (***Q=1.0e^{-9}m^3/s***, C_a=*2.94e^{-5}*) model with various ***viscosity ratios***.

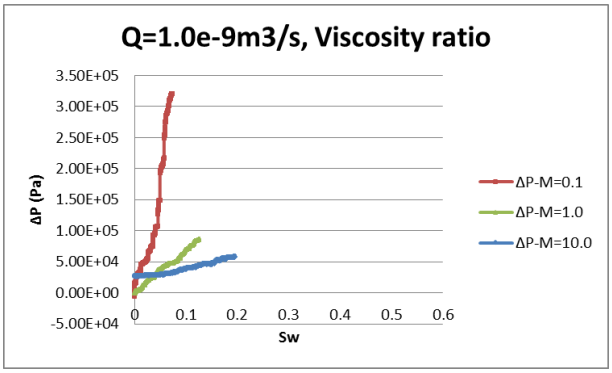

Figure 5-35 Global pressure drop of ***low-rate*** (***Q=1.0e^{-9}m^3/s***, $C_a=2.94e^{-5}$) model with various ***viscosity ratios***.

5.4.5 Constant Pressure Drop Simulations

Besides the constant flowrate protocol, the numerical imbibition displacement experiments can also be conducted by keeping the pressure drop constant while changing the injection rate, as in the quasi-static model.

To illustrate this for each viscosity ratio, we select the initial pressure drops of high-rate, intermediate-rate, and low-rate cases respectively – hence the starting injection rates are the same as their corresponding constant rate simulations (see the starting point of each curve in Figure 5-36, Figure 5-40, and Figure 5-44). After water injection, the flow rate will vary as the displacement proceeds (as controlled by the evolving conductances as a result of viscosity alteration and oil trapping).

As shown in Figure 5-36, the simulations (a) and (b) are compared to the constant flow rate cases $Q=1.0e^{-3}m^3/s$ and $Q=5.0e^{-9}m^3/s$ ($M=1.0$) respectively. Considering the global conductance reduction caused by oil-trapping, the total injection rate keeps decreasing in each constant ΔP case.

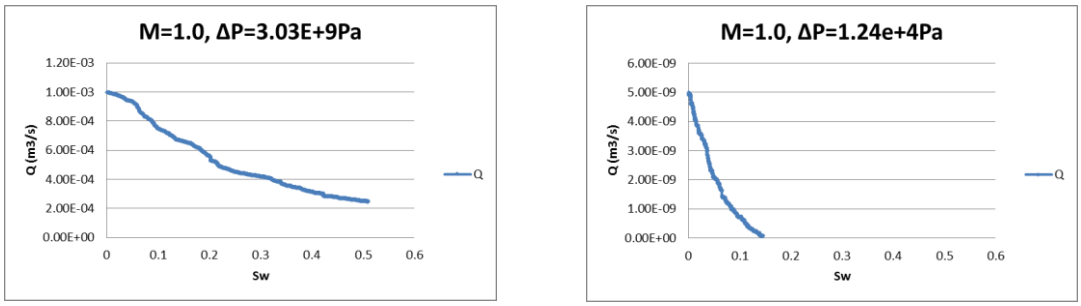

(a) $\Delta P=3.03e^9Pa$ (b) $\Delta P=1.24e^4Pa$

Figure 5-36 Total injection rates in each ***constant pressure drop*** case, ***M=1.0***.

In the high-ΔP case ($\Delta P=3.03e^{9}Pa$), the flow rate decrease is only caused by trapped oil and is not very dramatic. Therefore compared with the constant-Q cases, the differences in filling results (Figure 5-38) and water fractional flow curves (Figure 5-37 (a)) are *negligible*. In the low-ΔP case ($\Delta P=1.24e^{4}Pa$), however, as displacement proceeding, the decreasing flow rate causes increasing number of pores to have counter-current flow, and results in pathologically long fingers (Figure 5-39) – hence far *less* oil is produced compared with the constant $Q=5.0e^{-9}m^3/s$ case (Figure 5-37 (b)).

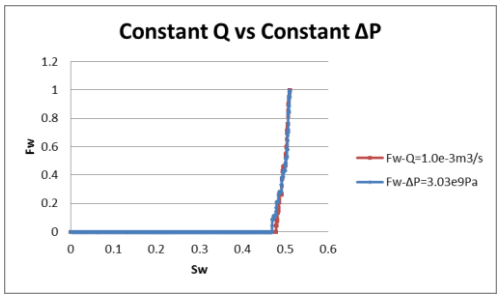

(a) $Q=1.0e^{-3}m^3/s$ vs $\Delta P=3.03e^{9}Pa$

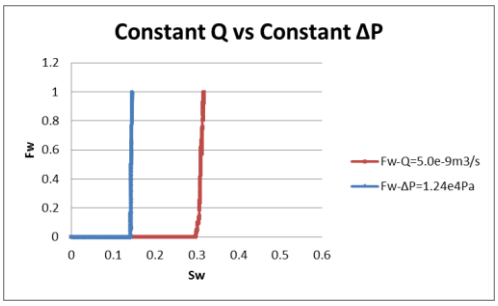

(b) $Q=5.0e^{-9}m^3/s$ vs $\Delta P=1.24e^{4}Pa$

Figure 5-37 S_w-F_w curves of each case under ***constant flow-rate*** or ***constant pressure drop***, ***M=1.0***.

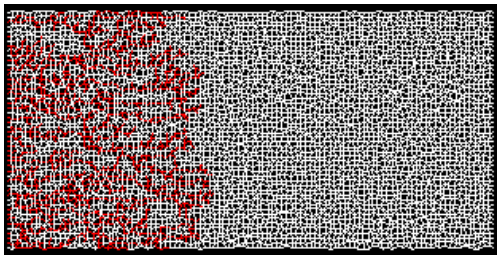

(a) $Q=1.0e^{-3}m^3/s$

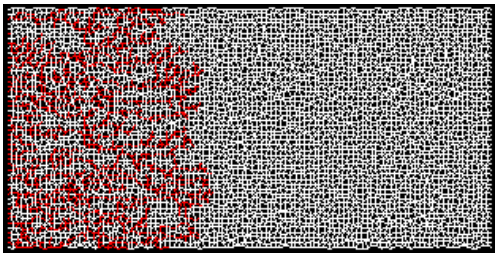

(b) $\Delta P=3.03e^{9}Pa$

Figure 5-38 Fluids configuration of $\boldsymbol{Q=1.0e^{-3}m^3/s}$ and $\boldsymbol{\Delta P=3.03e^{9}Pa}$ case, ***M=1.0***. Above figures represent pores filled by different phases, and are taken when identical amount of water (0.192PV) has been injected into each network. Red is water-filled pores, white is oil-containing pores.

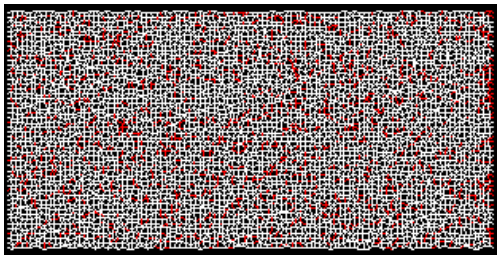

(a) $Q=5.0e^{-9}m^3/s$

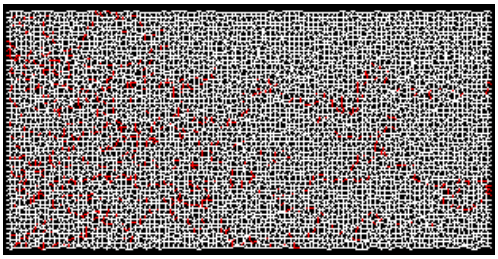

(b) $\Delta P=1.24e^{4}Pa$

Figure 5-39 Fluids configuration at the end of $\boldsymbol{Q=5.0e^{-9}m^3/s}$ and $\boldsymbol{\Delta P=1.24e^{4}Pa}$ cases, ***M=1.0***. Red represents water-filled pores and while represents pores containing oil.

Similar results can also be observed for the *M=0.1*, constant-ΔP simulations – (1) decreasing flow rate as displacement proceeds (here, the flow reductions are more dramatic than those in the unit viscosity ratio floods - besides oil trapping, the more viscous invading water will further reduce the global conductance) (Figure 5-40); (2) filling results in high-rate ($Q=1.0e^{-3}m^3/s$) and corresponding high-ΔP ($\Delta P=3.03e^8Pa$) simulations are similar (the more viscous water film is insensitive to the increasing value of local switch as flow decreases) (Figure 5-42, Figure 5-41 (a)); and (3) in the low-ΔP ($\Delta P=1.24e^4Pa$) simulation, the decreasing flow rate will cause counter-current flow and pathologically long fingers, therefore the displacement terminates at *low* S_w (in this case, even before the water front breakthrough) (Figure 5-41(b), Figure 5-43).

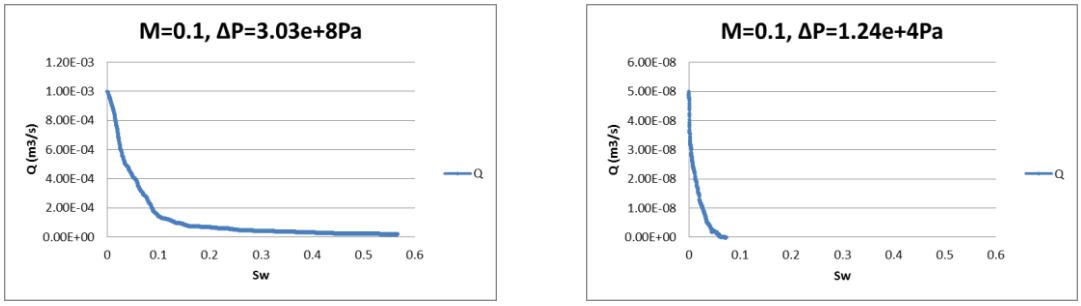

(a) $\Delta P=3.03e^8Pa$ (b) $\Delta P=1.24e^4Pa$

Figure 5-40 Total injection rates in each ***constant pressure drop*** case, ***M=0.1***.

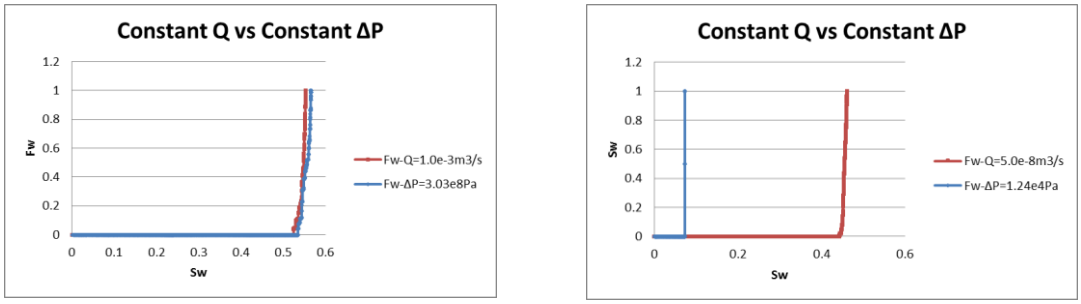

(a) $Q=1.0e^{-3}m^3/s$ vs $\Delta P=3.03e^8Pa$ (b) $Q=5.0e^{-8}m^3/s$ vs $\Delta P=1.24e^4Pa$

Figure 5-41 S_w-F_w curves of each case under ***constant flow-rate*** or ***constant pressure drop***, ***M=0.1***.

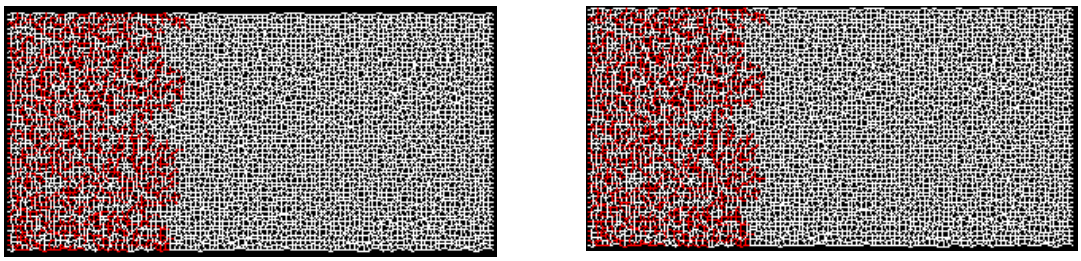

(a) $Q=1.0e^{-3}m^3/s$ (b) $\Delta P=3.03e^8Pa$

Figure 5-42 Fluids configuration of $\boldsymbol{Q=1.0e^{-3}m^3/s}$ and $\boldsymbol{\Delta P=3.03e^8Pa}$ case, ***M=0.1***.

Above figures represent pores filled by different phases, and are taken when identical amount of water (0.192PV) has been injected into each network. Red is water-filled pores, white is oil-containing pores.

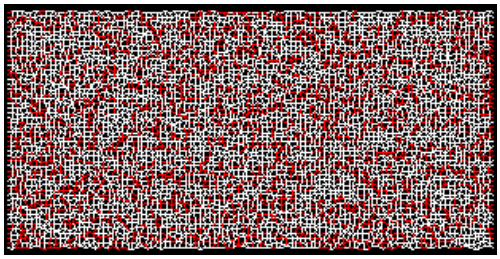

(a) $Q=5.0e^{-8}m^3/s$

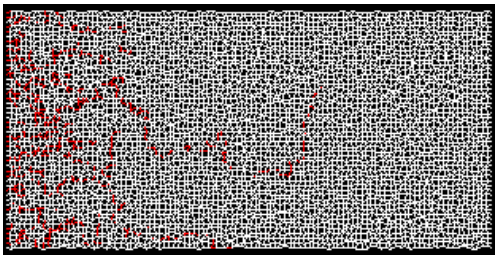

(b) $\Delta P=1.24e^{4}Pa$

Figure 5-43 Fluids configuration at the end of $\boldsymbol{Q=5.0e^{-8}m^3/s}$ and $\boldsymbol{\Delta P=1.24e^{4}Pa}$ cases, $\boldsymbol{M=0.1}$. Red represents water-filled pores and while represents pores containing oil.

In cases with unfavourable viscosity ratio ($M=10.0$), trapped oil and less viscous invading water have opposing effects on the evolution of global conductance – hence injection rate under constant pressure drop can be *increasing or decreasing*. Generally, (1) when the pressure drop is high, the less viscous water dominates and the flow rate will increase (Figure 5-44 (a)); (2) under low ΔP, the trapped oil will have more influence and the total flow rate will decrease (Figure 5-44 (c)); and (3) the opposing influences of trapped oil and decreasing global viscosity are balanced under the intermediate ΔP (Figure 5-44 (b)).

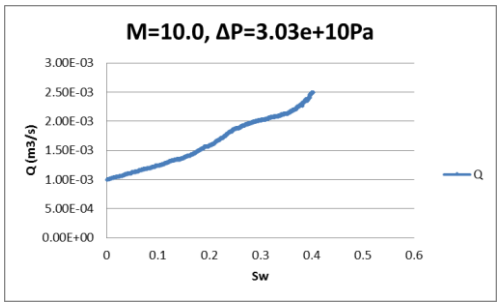

(a) $\Delta P=3.03e^{10}Pa$

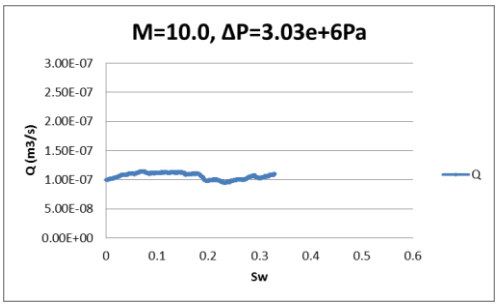

(b) $\Delta P=3.03e^{6}Pa$

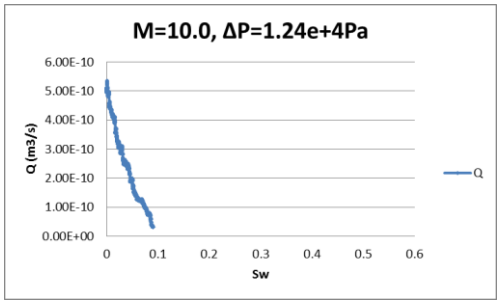

(c) $\Delta P=1.24e^{4}Pa$

Figure 5-44 Total injection rates in each ***constant pressure drop*** case, $\boldsymbol{M=10.0}$.

When $Q=1.0e^{-3}m^3/s$, the dynamic imbibition is already dominated by piston-like displacements, thus in the corresponding $\Delta P=3.03e^{10}Pa$ case, the increasing injection rate will hardly cause any changes to the filling result (Figure 5-45 (a), Figure 5-46 (a), (b)). In the $\Delta P=3.03e^{6}Pa$ case, the flow rate fluctuates around $1.0e^{-7}m^3/s$ and the filling result are affected slightly, but the total PV of produced oil is similar to that of the corresponding constant-Q floods (Figure 5-45 (b), Figure 5-46 (c), (d)). Due to the appearance of counter-current flow (Figure 5-47 (b)), oil production for the $\Delta P=1.24e^{4}Pa$ case is smaller than the $Q=5.0e^{-10}m^3/s$ case (Figure 5-45 (c)).

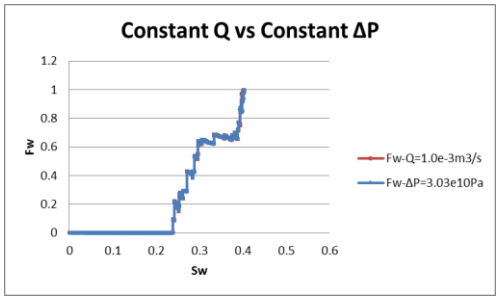

(a) $Q=1.0e^{-3}m^3/s$ vs $\Delta P=3.03e^{10}Pa$

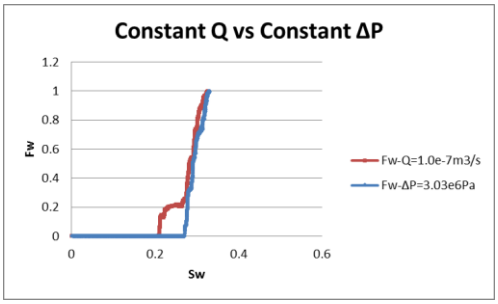

(b) $Q=1.0e^{-7}m^3/s$ vs $\Delta P=3.03e^{6}Pa$

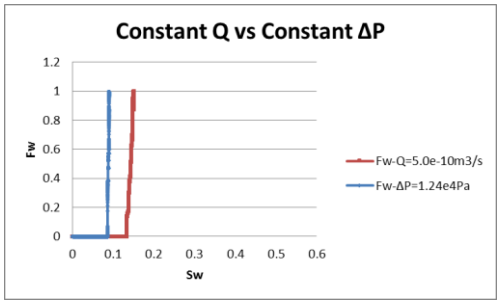

(c) $Q=5.0e^{-10}m^3/s$ vs $\Delta P=1.24e^{4}Pa$

Figure 5-45 S_w-F_w curves of each case under ***constant flow-rate*** or ***constant pressure drop***, ***M=10.0***.

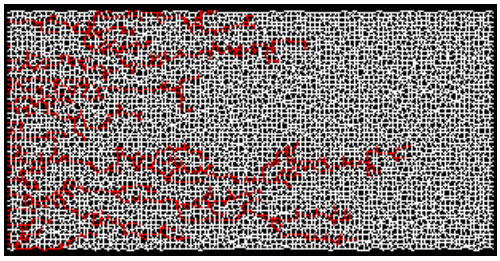

(a) $Q=1.0e^{-3}m^3/s$

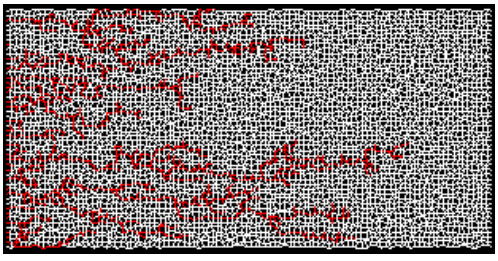

(b) $\Delta P=3.03e^{10}Pa$

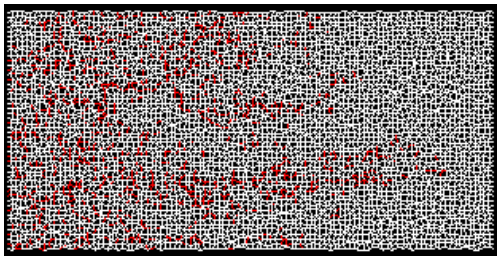

(c) $Q=1.0e^{-7}m^3/s$

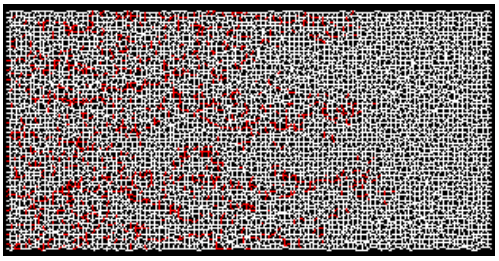

(d) $\Delta P=3.03e^{6}Pa$

Figure 5-46 Fluids configuration of of each case under ***constant flow-rate*** or ***constant pressure drop***, ***M=10.0***.

Above figures represent pores filled by different phases, and are taken when identical amount of water (0.192PV) has been injected into each network. Red is water-filled pores, white is oil-containing pores.

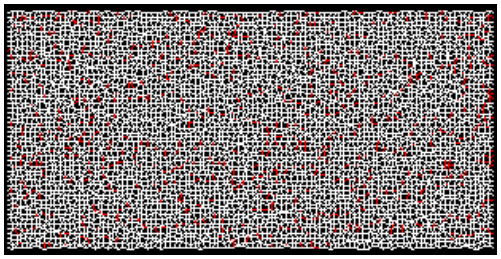

(a) $Q=5.0e^{-10}m^3/s$

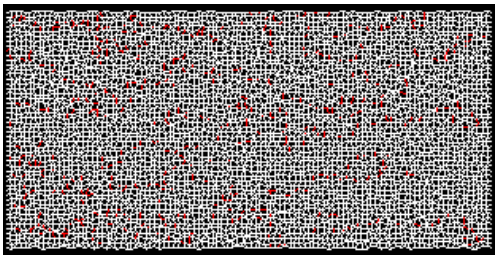

(b) $\Delta P=2.24e^{4}Pa$

Figure 5-47 Fluids configuration at the end of $\boldsymbol{Q=5.0e^{-10}m^3/s}$ and $\boldsymbol{\Delta P=2.24e^{4}Pa}$ cases, ***M=10.0***.

Red represents water-filled pores and while represents pores containing oil.

5.5 Other Parametric Sensitivities

Flow rate and viscosity ratio will only affect the capillary vs viscous force competition through varying the viscous pressure field while leaving the capillary pressure untouched. The parameters below, however, will change both forces and have a more subtle influence on the fluid configurations.

5.5.1 Pore Size

The pore size distribution (PSD) is controlled by the inscribed radius range and distribution method and here we will focus on the uniform distribution. For any given radius range, the mean radius r_{mean} and the ratio $r_{\max}/r_{\min}$ will both affect the displacement sequence. As an example, the radius range (11, 40) has $r_{\min}$ = 11μm and $r_{\max}$ =40 μm.

r_{mean} affects both the local capillary pressure and flow rate, in Section 4.9, we rearranged the formula for the capillary/viscous switch to show the relationship between λ and other system parameters explicitly, Equation 4-64. Thus the local balance between capillary and viscous forces is proportional to the cube of the pore radius, *and so more bulk displacements (smaller λ) should be expected in networks characterised by a smaller* r_{mean}. In contrast, with the same water volume in corners, the value of $R_{w\text{-}o}$ will be controlled by the pore size - a smaller r_{mean} will result in a higher $R_{w\text{-}o}$ which boosts film-swelling.

The $R_{w\text{-}o}$ scaling gives an inverse tendency compared to that of the local switch. However, from Figure 5-48 (a), (c), (e), the effect of the local switch appears to predominate the filling sequences. As the mean pore radius of the network decreases, the displacement moves from being dominated by film flow and snap-off to one characterised by viscous fingering (note that *M=10.0* here), which helps the oil production (Figure 5-49). In Figure 5-48 (b), (d), (f), the corresponding PSD bar charts also confirm that decreasing the mean radius will lead to more *bulk* movement.

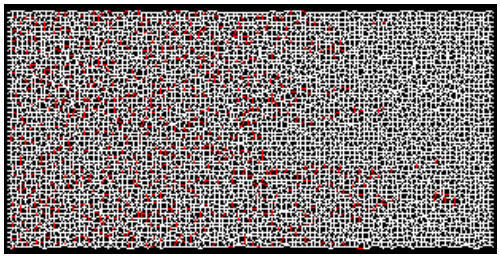

(a) (11, 40), $Ca=2.94e^{-4}$

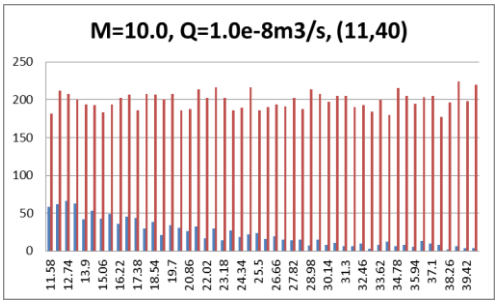

(b) (11, 40), $Ca=2.94e^{-4}$, PSD bar chart

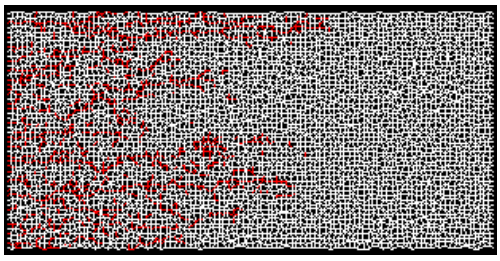

(c) (3.3, 12), $Ca=9.81e^{-4}$

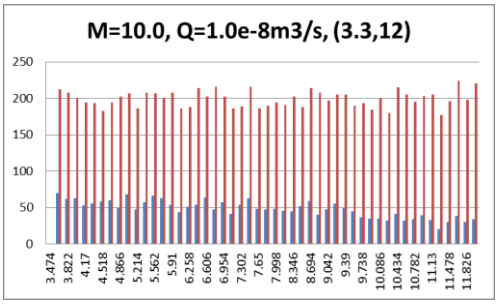

(d) (3.3, 12), $Ca=9.81e^{-4}$, PSD bar chart

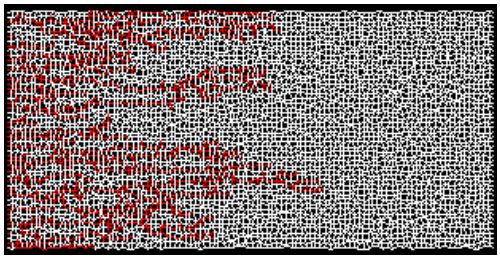

(e) (1.1, 4), $Ca=2.94e^{-3}$

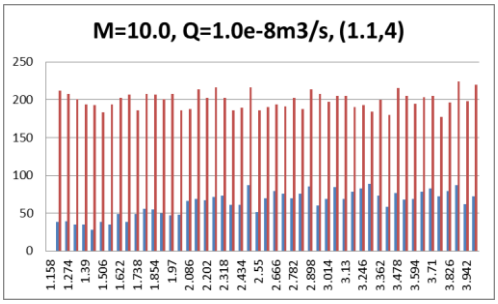

(f) (1.1, 4), $Ca=2.94e^{-3}$, PSD bar chart

Figure 5-48 Fluid configurations and PSD bar charts with various r_{mean}, $Q=1.0e^{-8}m^3/s$, $M=10.0$.

(a), (c), (e) represent pores filled by different phases, and are taken when the global water saturations are the same (S_w=0.192). Red is water-filled pores, white is oil-containing pores. (b), (d), (f) are corresponding PSD bar chart. Red is the number of all the pores within each range. Blue is the water-filled pores in each range.

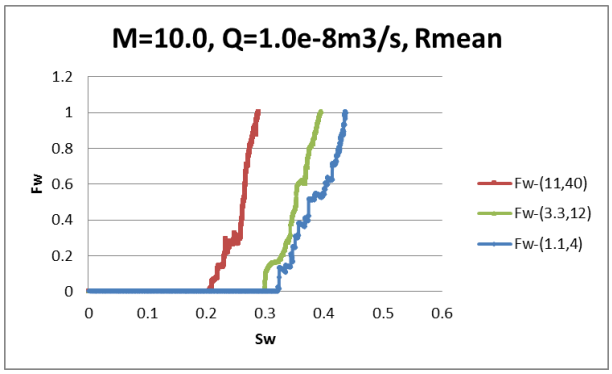

Figure 5-49 Water fractional flow curves of simulations with various r_{mean}, $Q=1.0e^{-8}m^3/s$, $M=10.0$.

A second example highlighting the importance of pore size distribution is shown in Figure 5-50. Here, a high-rate, unfavourable-viscosity-ratio simulation is presented in which the structure of the viscous fingering is radically different because of the altered pore size distribution. In the network with a wider radius range (1, 50) (larger r_{max}/r_{min} but identical mean radius), enhanced cross flow in the y-direction allows water to enter some transverse pores and several thin dendritic fingers are produced (Figure 5-50 (a)). In the system with a narrower radius range (11, 40), however, local pressure gradients in the y-direction are lower and so water tends to flow parallel to the global pressure drop in x-direction and many more fingers developed (Figure 5-50 (b)). The low r_{max}/r_{min} case also has a more uniform water front and later breakthrough, reduced trapping and better oil recovery (Figure 5-50 (c)).

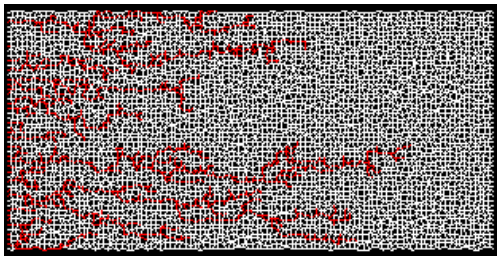

(a) PSD *(1,50)*

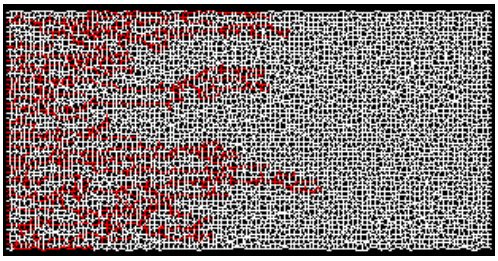

(b) PSD *(11,40)*

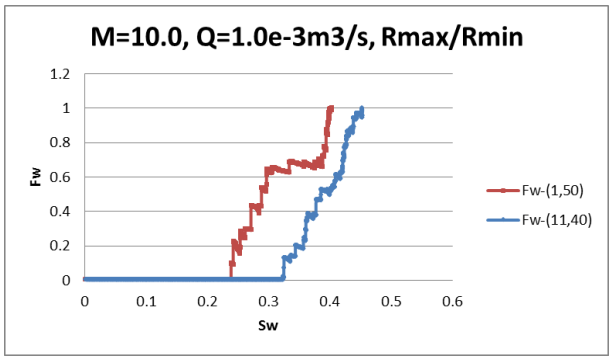

(c) F_w

Figure 5-50 Fluids configuration, PSD bar chart, and fractional flow curve of high-rate model with various $\boldsymbol{r_{max}/r_{min}}$, $\boldsymbol{Q=1.0e^{-3}m^3/s}$ ($Ca=2.94e^{1}$), $\boldsymbol{M=10.0}$.
(a) and (b) represent pores filled by different phases, and are taken when identical amount of water (0.192PV) has been injected into each network. Red is water-filled pores, white is oil-containing pores. (c) shows the final f_w-S_w curves.

Note that, for the same mean radius, $r_{\max}/r_{\min}$ will have very little influence on bulk-film competition. Thus, the extent of film swelling and snap-off tends to be the same in Figure 5-50 (a) and Figure 5-50 (b) – it is the impact of pore-scale heterogeneity on the viscous pressure field that matters the most.

Corresponding results from the low-rate simulations ($Q=1.0e^{-8}m^3/s$) are shown in Figure 5-51. Here, we see a lesser impact of pore-scale heterogeneity in determining the uniformity of the wetting front and recovery characteristics.

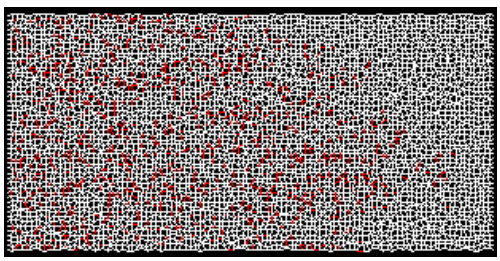

(a) PSD *(1,50)*

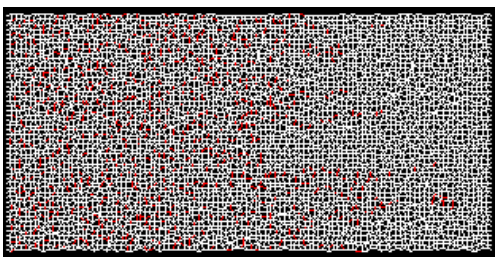

(b) PSD *(11,40)*

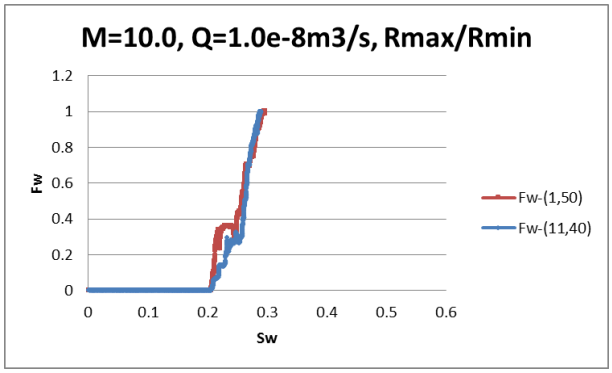

(c) F_w

Figure 5-51 Fluids configuration, PSD bar chart, and fractional flow curve of low-rate model with various $\boldsymbol{r_{max}/r_{min}}$, $\boldsymbol{Q=1.0e^{-8}m^3/s}$ ($Ca=2.94e^{-4}$), $\boldsymbol{M=10.0}$.
(a) and (b) represent pores filled by different phases, and are taken when identical amount of water (0.192PV) has been injected into each network. Red is water-filled pores, white is oil-containing pores. (c) shows the final f_w-S_w curves.

5.5.2 Pore Length

Figure 5-52 demonstrates how pore length can also affect the displacement pattern. The pore length, l, has no influence on capillary pressure but it *does* affect pore conductance and is inversely proportional to the capillary/viscous switch (λ). Therefore, as pore-length increases, more piston-like displacements (smaller λ) would be expected to occur at a fixed injection rate. The average of our base case is $\bar{l}=333\mu m$, and the comparisons are made between $\bar{l}=\bar{l}/20=16.65\mu m$, $\bar{l}=\bar{l}/3=111\mu m$, $\bar{l}=333\mu m$, and $\bar{l}=\bar{l}*2=666\mu m$.

For the case ($M=10.0$, $Q=1.0e^{-7}m^3/s$, $\bar{l}=333\mu m$) (Figure 5-52(c)), viscous fingering with some snap-off can be observed. With all other conditions fixed, reducing the pore length leads to more snap-off and capillary forces begin to control the displacement (Figure 5-52 (a) and (b)). In contrast, by doubling the pore length, snap-off and film swelling are suppressed (Figure 5-52 (d)). In the calculation of capillary numbers, the larger pore length will lead to a smaller C_a (by enlarging the cross-sectional area of the network), which contradicts the tendency predicted by the value of λ. The water fractional flow curves are shown in Figure 5-53.

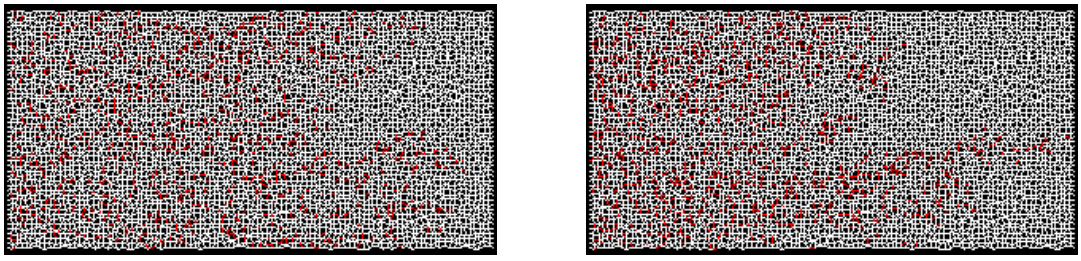

(a) $\bar{l} = 16.65\mu m$, C_a=5.89e^{-2} (b) $\bar{l} = 111\mu m$, C_a=8.83e^{-3}

(c) $\bar{l} = 333\mu m$, C_a=2.94e^{-3} (d) $\bar{l} = 666\mu m$, C_a=1.47e^{-3}

Figure 5-52 Fluids configuration of simulations with various ***pore lengths***, ***Q=1.0e^{-7}m^3/s***, ***M=10.0***.

(a)- (d) represent pores filled by different phases, and are taken the global water saturations are the same (S_w=0.192). Red is water-filled pores, white is oil-containing pores.

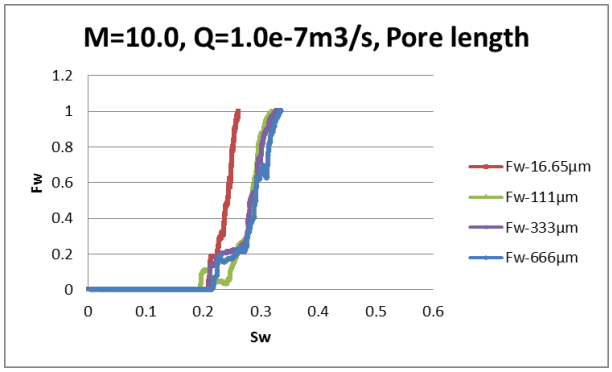

Figure 5-53 Water fractional flow curves of simulations with various ***pore lengths***, ***Q=1.0e^{-7}m^3/s***, ***M=10.0***.

5.5.3 Pore Aspect Ratio

For each pore, the local switch (λ) is proportional to the cube of inscribed pore radius and has a linear relationship with the reciprocal of pore length. Furthermore, the indicator of film-swelling, $R_{w\text{-}o}$, is governed by the pore size but is not a function of the pore length. Hence simulations with the same pore-scale aspect ratio, R_{asp} (as seen in Equation 4-65), do not necessarily have the same displacement pattern. An increasing pore radius causes higher λ and more significant film-swelling (Figure 5-54).

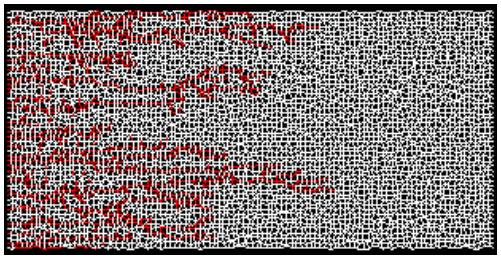

(a) PSD *(1.1, 4)*, $\bar{l} = 33.3\mu m$

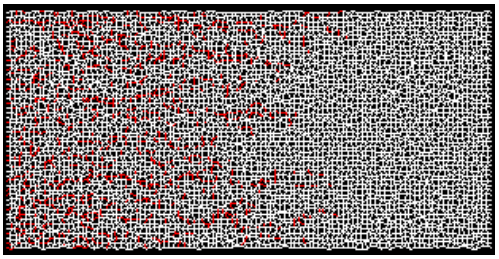

(b) PSD *(3.3, 12)*, $\bar{l} = 99.9\mu m$

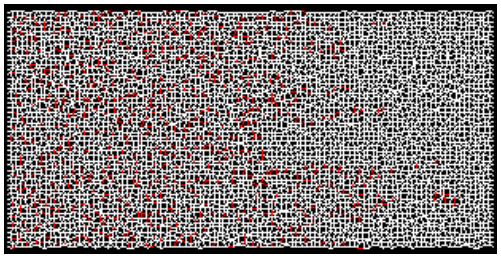

(c) PSD *(11, 40)*, $\bar{l} = 333\mu m$

Figure 5-54 Fluids configuration of models with identical pore-scale aspect ratio, ***Q=1.0e^{-8}m^3/s***, ***M=10.0***.

(a), (b), and (c) represent pores filled by different phase, and are taken the global water saturations are the same. Red is water-filled pores, white is oil-filled or partial-filled pores with wetting film.

5.5.4 Interfacial Tension, IFT

As capillary pressure is directly proportional to interfacial tension, a reduction in IFT results in a smaller switch value that will reduce the extent of film swelling. Thus water should prefer to flow through connected clusters of bulk fluid rather than through wetting films – this is confirmed by our simulations, as shown in Figure 5-55 and Figure 5-56, where snap-off is suppressed as IFT is reduced from *40mN/m* to *5mN/m*. Capillary number will also increase as IFT drops (2.94e^{-4} and 2.36e^{-3} respectively).

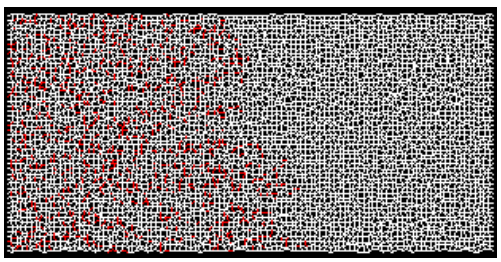

(a) *M=1.0, σ =40.0e^{-3}N/m*

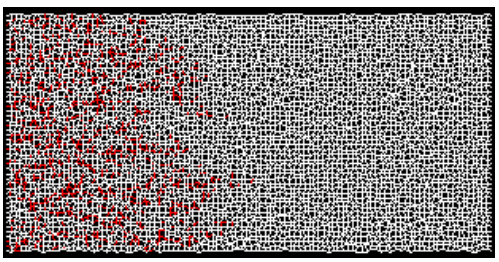

(b) *M=1.0, σ =5.0e^{-3}N/m*

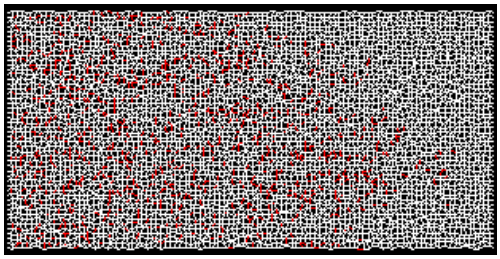

(c) $M=10.0$, $\sigma = 40.0e^{-3} N/m$

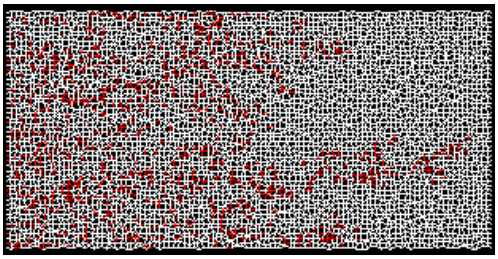

(d) $M=10.0$, $\sigma = 5.0e^{-3} N/m$

Figure 5-55 Fluids configuration of simulations with various ***interfacial tensions***, ***Q=1.0e^{-8}m^3/s***.

Above figures represent pores filled by different phases, and are taken when identical amount of water (0.192PV) has been injected into each network. Red is water-filled pores, white is oil-containing pores.

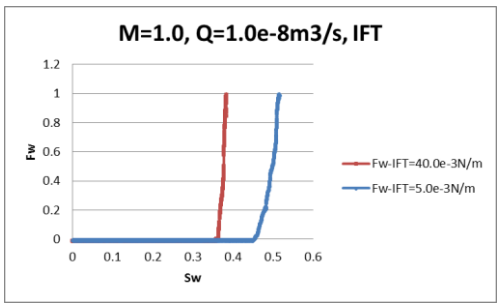

(a) $M=1.0$

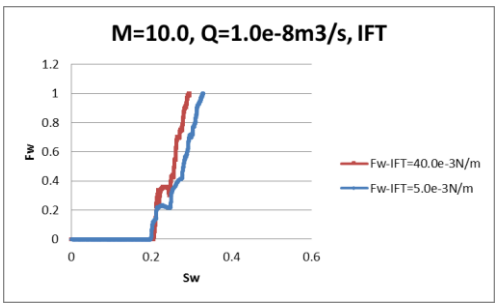

(b) $M=10.0$

Figure 5-56 Water fractional flow curves of simulations with various ***interfacial tensions***, ***Q=1.0e^{-8}m^3/s.***

Note that greater sensitivity to IFT is seen at relatively low-rates. For the high-rate, viscous-force-dominated simulations, the changing capillary number hardly affects the displacement results (Figure 5-57 (c)). Inversely, in ultra-low rate cases, where the capillary pressure is much larger than the viscous forces, the influence of IFT will once again hardly be noticed; that is, the switch in low IFT cases has already reached $\lambda = 1.0$ and therefore higher IFT will not lead to any further differences.

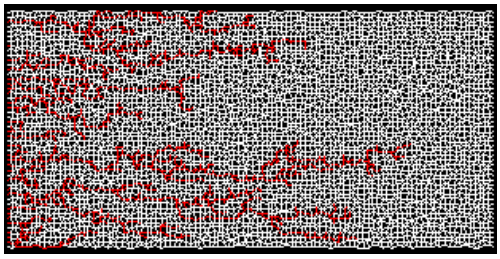

(a) $M=10.0$, $\sigma = 40.0e^{-3} N/m$

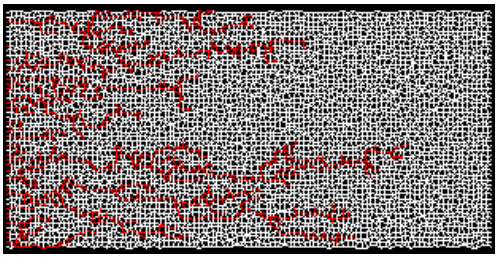

(b) $M=1.0$, $\sigma = 5.0e^{-3} N/m$

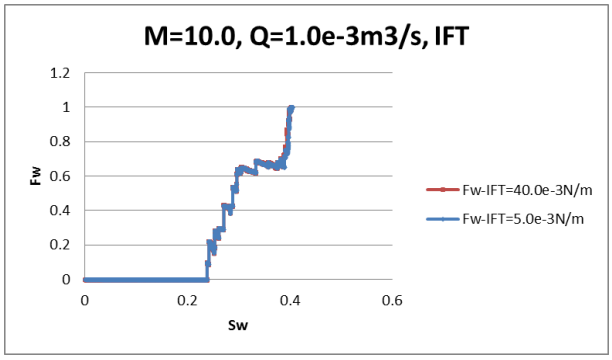

(c) F_w

Figure 5-57 Fluids configuration and F_w-S_w curves of model with various ***interfacial tensions***, ***Q=1.0e^{-3}m^3/s***.

Figure (a) and (c) represent pores filled by different phases, and are taken when identical amount of water (0.192PV) has been injected into each network. Red is water-filled pores, white is oil-containing pores. (b) and (d) are the corresponding F_w-S_w curves.

5.5.5 Pore Shape

Having carefully analysed both circular and equilateral triangle pore shapes, we now go on to generalise the pore shape still further and consider cross sections that are scalene triangles. To get a scalene triangle with $\beta_1 \geq \beta_2 \geq \beta_3$ as its half angles, the approach has been to randomly assign the values of β_1 and β_2 within two predefined ranges, and then $\beta_3 = \frac{\pi}{2} - \beta_1 - \beta_2$. The range for β_1 is $[\frac{\pi}{6}, \frac{\pi}{2})$ and that for β_2, needs to meet three conditions: (1) smaller than β_1, (2) smaller than $\frac{\pi}{2} - \beta_1$; and (3) larger than β_3.

In the system where $\theta = 0^o$, we can simplify S_1 and F_d^* to:

$$S_1 = (\sum_{i=1}^{3} \frac{1}{\tan \beta_i}) - \pi , \qquad 5\text{-}2$$

and

$$F_d^* = 1 + \sqrt{\frac{\pi}{\sum_{i=1}^{3} \frac{1}{\tan \beta_i}}} . \qquad 5\text{-}3$$

Therefore the capillary/viscous switch in scalene triangular pores can be rewritten as:

$$\lambda = \frac{3\cdot(\sum_{i=1}^{3}\frac{1}{\tan\beta_i} + \sqrt{\pi\cdot\sum_{i=1}^{3}\frac{1}{\tan\beta_i}})}{20}\cdot\frac{\sigma_{ow}\cdot r^3}{\bar{\mu}ql} \qquad 5\text{-}4$$

Based on the inequality of arithmetic and geometric means, we have

$$\sum_{i=1}^{3}\frac{1}{\tan\beta_i} \geq 3\cdot\sqrt[3]{\prod_{i=1}^{3}\frac{1}{\tan\beta_i}} \qquad 5\text{-}5$$

and so $\sum_{i=1}^{3}\frac{1}{\tan\beta_i}$ will only get to its minimum value when $\beta_1 = \beta_2 = \beta_3$, i.e. in an equilateral triangle. Hence with other conditions fixed, the equilateral triangular pore will have the smallest switch (*i.e.* be least film-dominated) than any other scalene triangle (Figure 5-58) – it also has the smallest S_1, and the highest F_d^* (Figure 3-31 (a), Figure 3-32(a)). Furthermore, when the contact angle is 0º, the displacement is actually determined by the shape factor, G_{shape}. That is, systems containing various pore shapes should give identical simulation results if the shape factors are identical; for example, in Figure 5-58, pores with half angles (60,15,15) and (40,40,10) have the same S_1, F_d^*, and local switch.

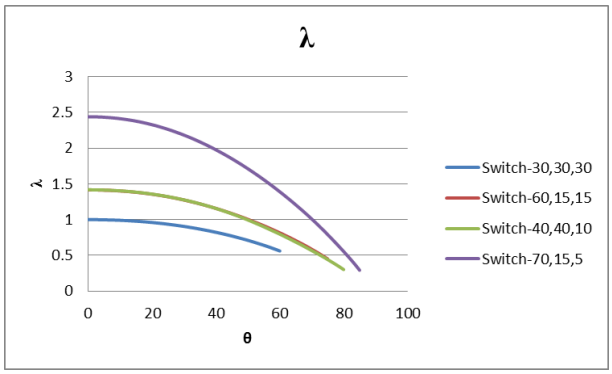

Figure 5-58 Illustration of λ for different pore shapes and contact angles. Each curve marked by half angles of corresponding pore element.

Moreover, under the same A_w, equilateral triangular pores, with the smallest cross-sectional area A and highest film conductance associate with the lowest S_1, will have the largest $R_{w\text{-}o}$ (Figure 5-59), which will encourage the extent of film swelling – in conflict with the influence of the local switch.

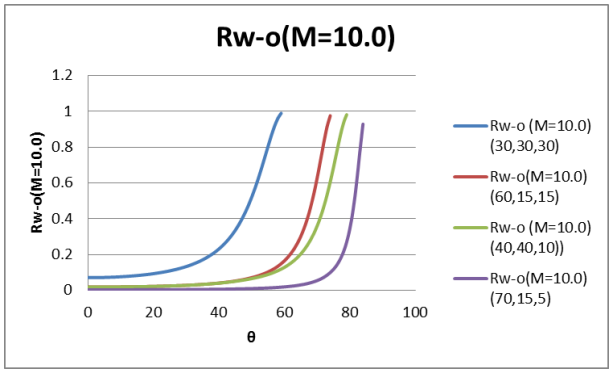

Figure 5-59 Illustration of $R_{w\text{-}o}$ for different pore shapes and contact angles. Each curve marked by half angles of corresponding pore element.

It emerges from the analysis above that *an equilateral triangle will be less capillary-dominated than a scalene triangle but will contain films that are more mobile*. Thus, the question may be posed: which effect wins out?

The results in Figure 5-60 indicate that, in most cases, systems with scalene triangular pores (distributed half angle combinations throughout the system) tend to have more snap-off compared with the corresponding equilateral-triangular-pore network (Figure 5-60 and Figure 5-61), except the low-rate case with *M=10.0* (Figure 5-61 (c) and (d)).

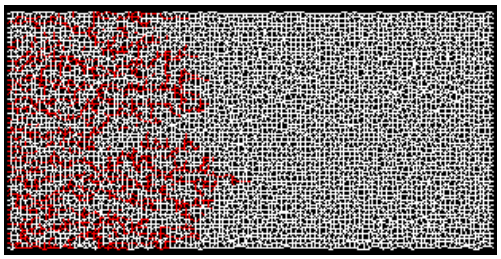

(a) E-T, $Q=1.0e^{-6}m^3/s$, $Ca=2.94e^{-2}$

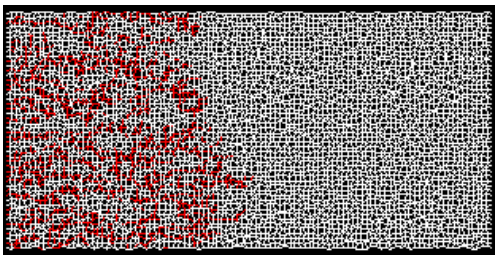

(b) S-T, $Q=1.0e^{-6}m^3/s$, $Ca=2.94e^{-2}$

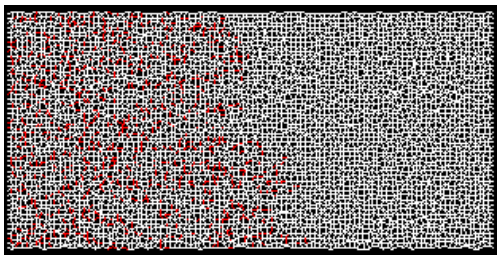

(c) E-T, $Q=1.0e^{-8}m^3/s$, $Ca=2.94e^{-4}$

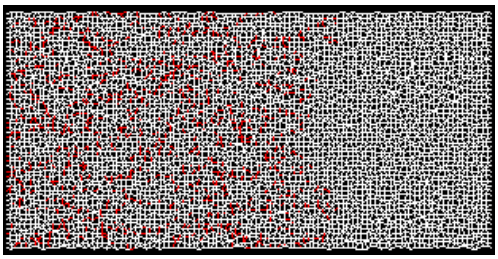

(d) S-T, $Q=1.0e^{-8}m^3/s$, $Ca=2.94e^{-4}$

Figure 5-60 Fluids configuration of simulations with various ***pore shapes***, equilateral triangle (E-T) and scalene triangle (S-T), ***M=1.0***.

Above figures are taken when the global water saturations are the same (S_w=0.192). (a)-(d) are figures of pores filled by different phases. Red is water-filled pores, white is oil-containing pores.

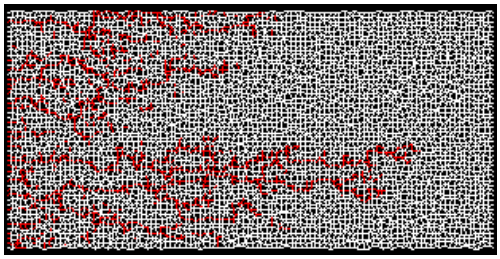

(a) E-T, $Q=1.0e^{-6}m^3/s$, $C_a=2.94e^{-2}$

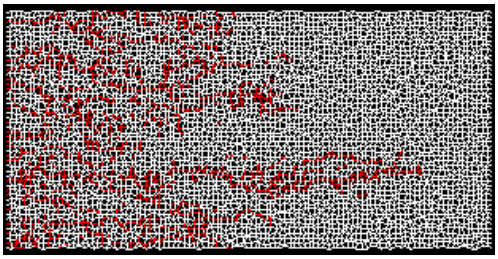

(b) S-T, $Q=1.0e^{-6}m^3/s$, $C_a=2.94e^{-2}$

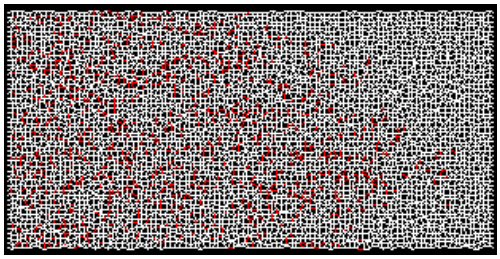

(c) E-T, $Q=1.0e^{-8}m^3/s$, $C_a=2.94e^{-4}$

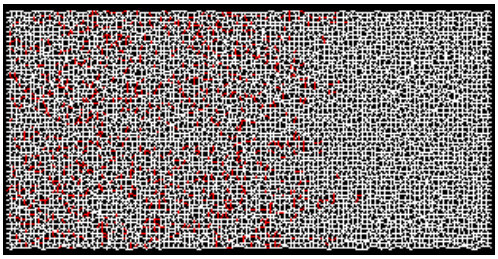

(d) S-T, $Q=1.0e^{-8}m^3/s$, $C_a=2.94e^{-4}$

Figure 5-61 Fluids configuration of simulations with various ***pore shapes***, equilateral and scalene triangle, ***M=10.0***.

Above figures are taken when the global water saturations are the same (S_w=0.192). (a)-(d) are figures of pores filled by different phases. Red is water-filled pores, white is oil-containing pores.

The influence of pore shape can also be seen in the water fractional curves which show that systems with more film-swelling and snap-off tends to experience earlier water breakthrough and lower oil recovery (Figure 5-62 and Figure 5-63).

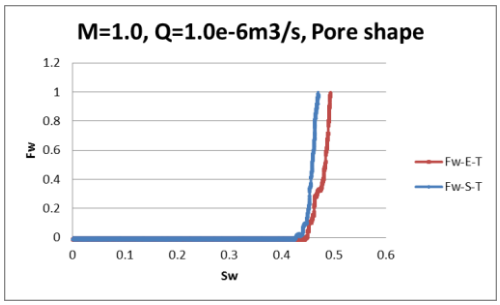

(a) $Q=1.0e^{-6}m^3/s$

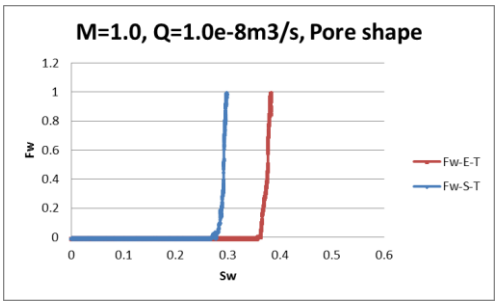

(b) $Q=1.0e^{-8}m^3/s$

Figure 5-62 F_w-S_w curves of simulations with various ***pore shapes***, equilateral and scalene triangle, ***M=1.0***.

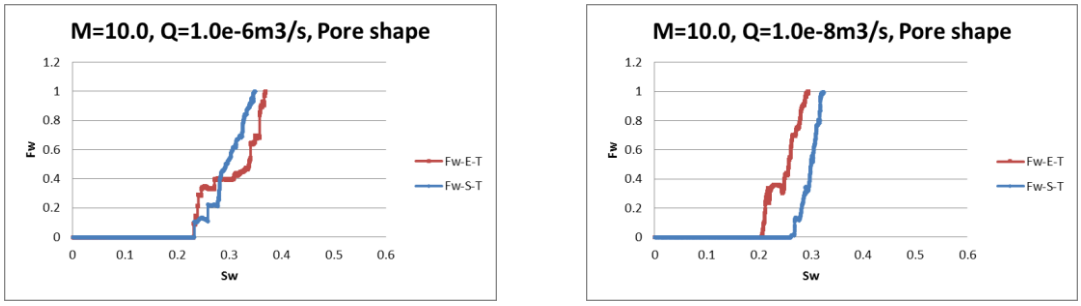

(a) $Q=1.0e^{-6}m^3/s$ (b) $Q=1.0e^{-8}m^3/s$

Figure 5-63 F_w-S_w curves of simulations with various ***pore shapes***, equilateral and scalene triangle, ***M=10.0***.

5.5.6 Contact Angle

The contact angle is not considered in the calculation of the total conductance of a pore (although it may play a role when determining the viscous pressure field). However, contact angle *can* affect the fluid displacement through the equations governing capillary pressure and wetting film conductance. The equilateral triangle has either three arc menisci (*AMs*) or no *AM* at all and, in the contact angle range $[0,60)$ where the pore has 3 *AMs*, both S_1 and F_d^* will decrease as θ increases (Figure 3-31 (a) and Figure 3-32 (a)). As a result, capillary pressure will be reduced as θ increases and so will the switch (i.e. the balance moves towards more bulk flow). If the contact angle is increased beyond 60º, the E-T pore will no longer accommodate a wetting film and water will displace oil only through piston-like advancement (with $S_1 = 0$ and $F_d^* = 2\cos\theta$) (Figure 5-64).

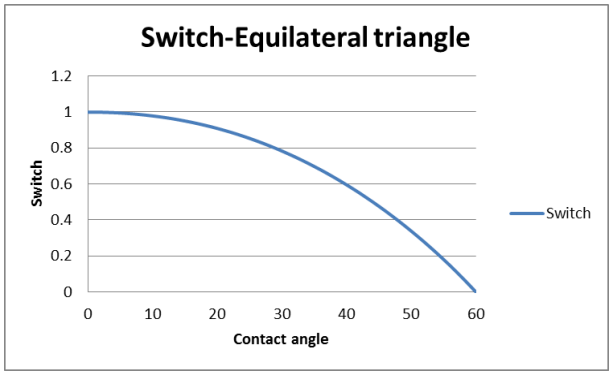

Figure 5-64 Local switch in equilateral triangle system with various contact angle

However, based on Equation 4-19, the other effect of this decreasing S_1 is a higher mobility of the wetting film, especially as θ approaches 60^o degree (as seen in Figure 5-65): with the same A_w, water film will have higher conductance as contact angle

increases. Thus, given that the smaller switch essentially suppresses film swelling in systems with large contact angles, in the dynamic model, *the extent of film swelling as contact angle increases is more complex than a unidirectional increasing or decreasing tendency*.

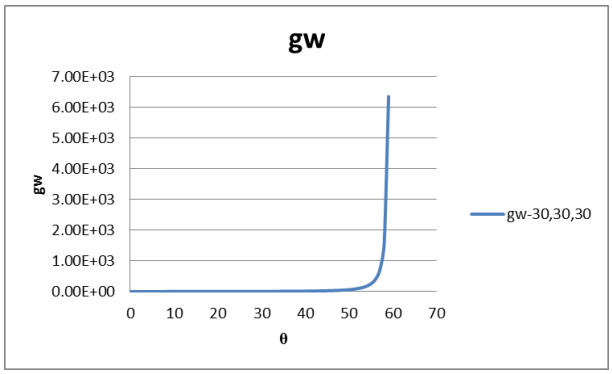

Figure 5-65 Water film conductance with various contact angle, assuming with the identical A_w.

As shown in Figure 5-66 below, compared with the base case ($\theta = 0^o$), more compact water-filled clusters emerge when $\theta = 30^o$, indicating less snap-off in this system. When the contact angle is increased to 50º, the injected water spreads throughout the system due to a higher extent of film swelling and snap-off, assisted by the higher water film conductance. When $\theta = 60^o$, corner water can no longer exist in the triangular pores and water can only displace oil through piston-like displacement.

In more realistic cases, rather than having a constant contact angle, contact angles in a system tend to be distributed. After identical amounts of water have been injected, systems with contact angles distributed within particular ranges will have transitional filling results (Figure 5-66 (b), (d), (f)). The tendency is as expected and the prior analysis stands: snap-off is restrained in the (0^o, 30^o) range due to the lower dynamic switch and will be enhanced when the contact angle is approaching 60º since wetting film conductance will grow within that range. In the case when θ is randomly distributed within 0º and 89.9º, pores with large contact angle (over 60º) will lose their capacity to accommodate wetting films, which will further prevent the upstream film from swelling (*i.e.* wetting-film trapping). Therefore, although film swelling is possible in pores with small contact angles, snap-off is still effectively reduced (Figure 5-66 (f)). Capillary number is independent of the value of contact angle and fails to capture the difference between the various cases we have just discussed.

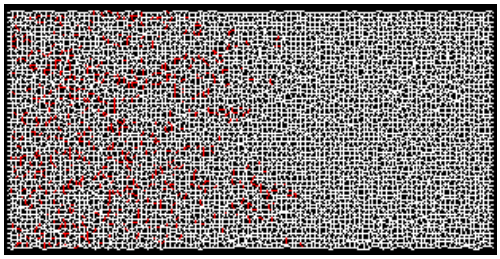

(a) $\theta = 0^o$

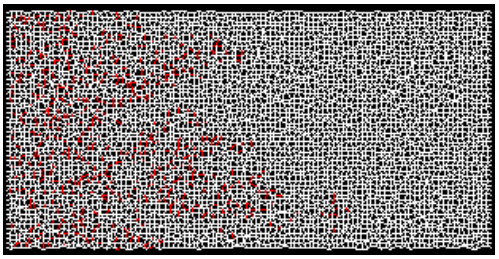

(b) $\theta \in [0^o, 30^o]$

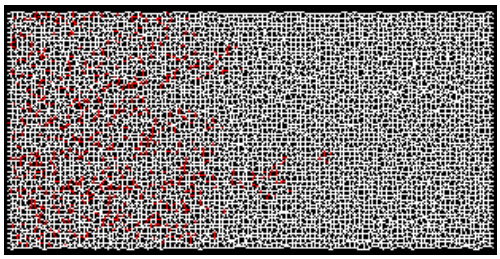

(c) $\theta = 30^o$

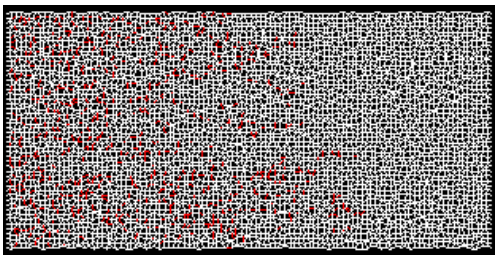

(d) $\theta \in [0^o, 60^o)$

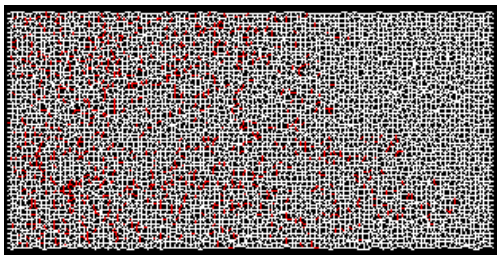

(e) $\theta = 50^o$

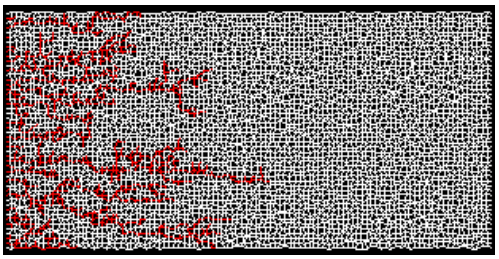

(f) $\theta \in [0^o, 89.9^o)$

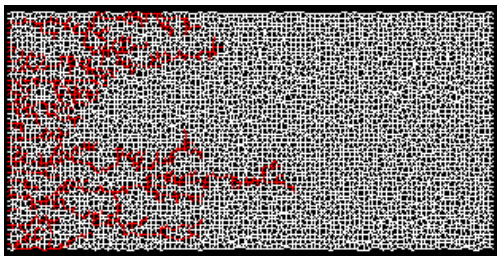

(g) $\theta = 60^o$

Figure 5-66 Fluids configuration of low-rate model with constant or distributed ***contact angles***, ***Q=1.0e^{-8}m^3/s***, ***C_a=2.94e^{-4}***, ***M=10.0***.

Above figures represent pores filled by different phases, and are taken when identical amount of water (0.128PV) has been injected into each network. Red is water-filled pores, white is oil-containing pores.

However, snap-off is still *possible* in the (*0^o,89.9^o*) case. Compared with a system with a constant contact angle of 60^o, some disconnected water clusters near the water front can be found in Figure 5-67 (a). Furthermore, in the low rate cases with contact angle exceeding 60 ^{o}, (θ=60^o and θ=80^o), although water can only invade the system in

continuous fingers, the value of contact angle can still affect the filling result – higher θ (80^o) can reduce the capillary pressure (Figure 5-67 (b) and (c)).

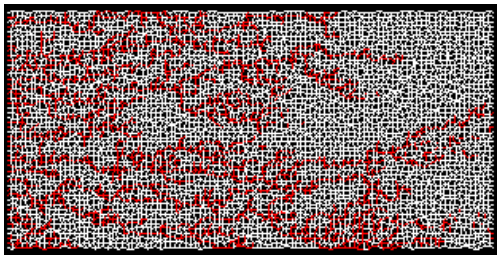

(a) $\theta \in [0^o, 89.9^o)$

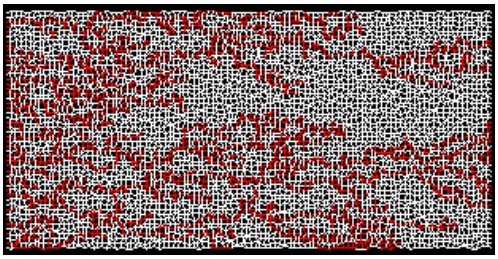

(b) $\theta=60^o$

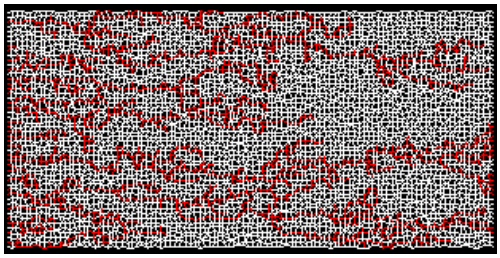

(c) $\theta=80^o$

Figure 5-67 Fluids configuration of low-rate model with high ***contact angles***, ***Q=1.0e^{-8}m^3/s***, ***C_a=2.94e^{-4}***, ***M=10.0***.

Above figures represent pores filled by different phases, and are taken when identical amount of water (0.32PV) has been injected into each network. Red is water-filled pores, white is oil-containing pores.

The extent of film-swelling and snap-off also affects the corresponding F_w-S_w curves (Figure 5-68), since generally, a higher level of snap-off can cause more trapping, earlier breakthrough and as a consequence lower oil recovery. The fingering regime will also have a significant influence on the shape of the fractional flow curves (Figure 5-68).

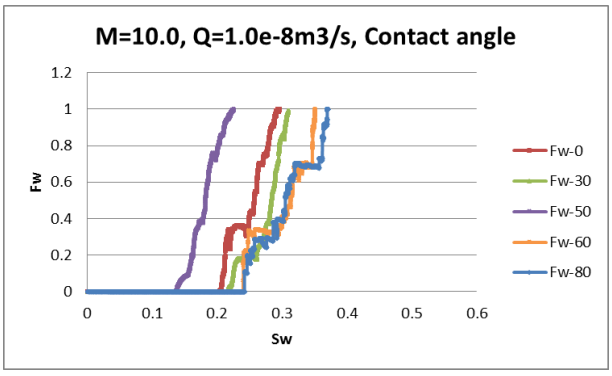

Figure 5-68 F_w-S_w curve of low-rate model with various ***contact angles***, ***Q=1.0e^{-8}m^3/s***, ***M=10.0***.

The pore scale network model distributes the pore size and contact angle uniformly and, according to Figure 5-69, it is clear that there is no correlation between contact angle and pore size.

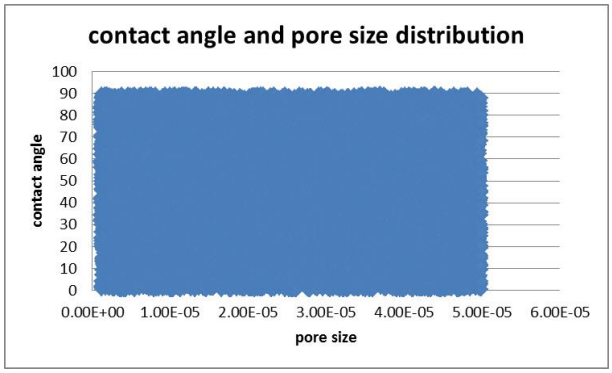

Figure 5-69 Relationship between contact angle and pore size. PSD (1,50), $\theta \in [0^o, 89.9^o)$.

As in the section above discussing circular-pores, in film-free systems with equilateral triangular pores and $\theta \geq 60^o$, flow rate can still have an influence on the filling results. In systems with unfavourable viscosity ratio (*M=10.0*), viscous fingering is the regime at high rates, while as injection rate decreases, capillary fingering appears (Figure 5-70).

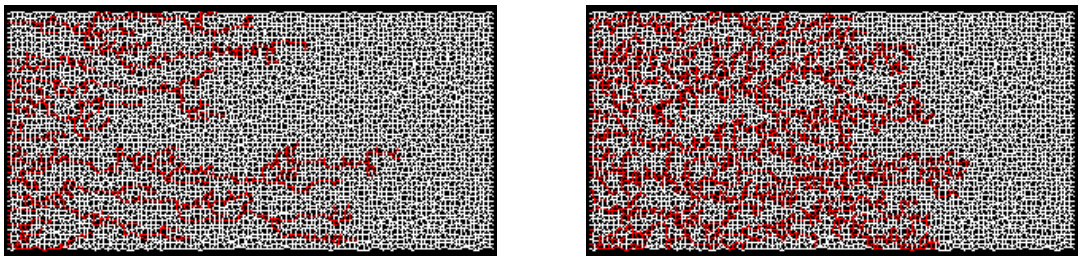

(a) $Q=1.0e^{-3}m^3/s$, $C_a=2.94e^{1}$ (b) $Q=1.0e^{-9}m^3/s$, $C_a=2.94e^{-5}$

Figure 5-70 Fluids configuration with various injection rates in system without wetting film, $\boldsymbol{\theta=60^o}$.

Above are figures of pores filled by different phases. Red is water-filled pores, white is oil-containing pores.

Figure 5-71 and Figure 5-72 also illustrate the different results found by varying flow rate (with $\theta=60^o$), i.e. viscous fingering (high rate) vs capillary fingering (low rate).

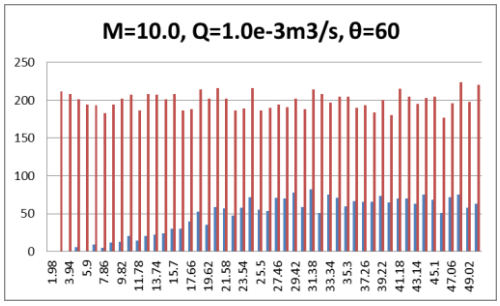

(a) $\theta = 60^o$, $Q=1.0e^{-3}m^3/s$

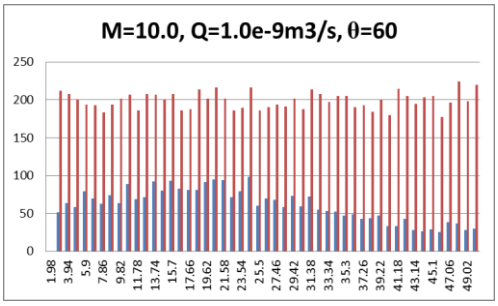

(b) $\theta = 60^o$, $Q=1.0e^{-9}m^3/s$

Figure 5-71 PSD bar chart with various injection rates in system without wetting film, ***θ=60º***.

Red is the number of all the pores within each range. Blue is the water-filled pores in each range.

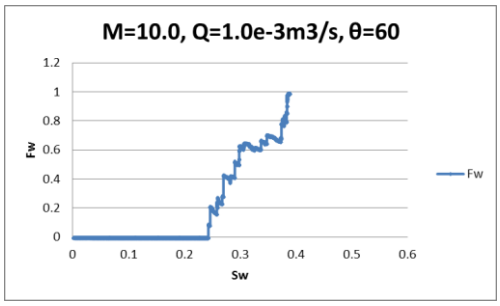

(a) $\theta = 60^o$, $Q=1.0e^{-3}m^3/s$

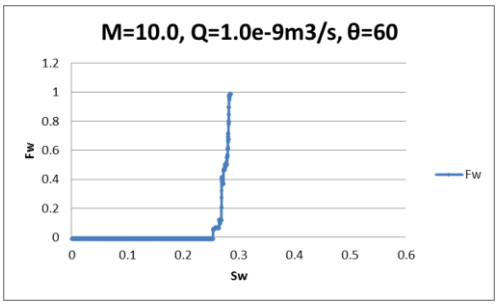

(b) $\theta = 60^o$, $Q=1.0e^{-9}m^3/s$

Figure 5-72 F_w-S_w curve at the end of each simulation with various injection rates in system without wetting film, ***θ=60º***.

For the case of scalene triangular pores, contact angle will have a more complex effect on the results. To emphasise this, a very narrow scalene triangle (half angles 70º, 15º, 5º) is chosen as it has a much smaller shape factor than that of an equilateral triangle. In this scalene triangular pore, the subdued wetting film conductance, due to the higher S_1 value, limits the extent of film swelling and snap-off, despite the fact that this has a much higher local switch in favour of film-swelling.

The scalene triangular pore system with half angle (70º, 15º, 5º) exhibits quite similar filling result to the E-T pore system; that is film swelling and snap-off are reduced when θ is constant at 30 º. For larger film conductances, when contact angle is 50º, more film swelling and snap-off can be observed compared with the $\theta=30^o$ case (Figure 5-73 and Figure 5-74). And when $\theta=80^o$, snap-off is completely subdued in the E-T system, while in S-T system, snap-off is the primary filling mechanism with the assistance of highly active wetting films.

However, in the S-T pore system, differences in filling result between $\theta=0^o$ and $\theta=50^o$ are less obvious than those displayed in equilateral triangular pore systems. The distributed pore shape (half angles) will have a much more complicated relationship with contact angle. As contact angle increases, the competition between having a lower local switch and increasing wetting film conductance is more balanced (comparing with the equilateral-triangle case), slightly in favour of the wetting film. In general, the equilateral triangular pore system appears to be more sensitive to the change of contact angle (Figure 5-73).

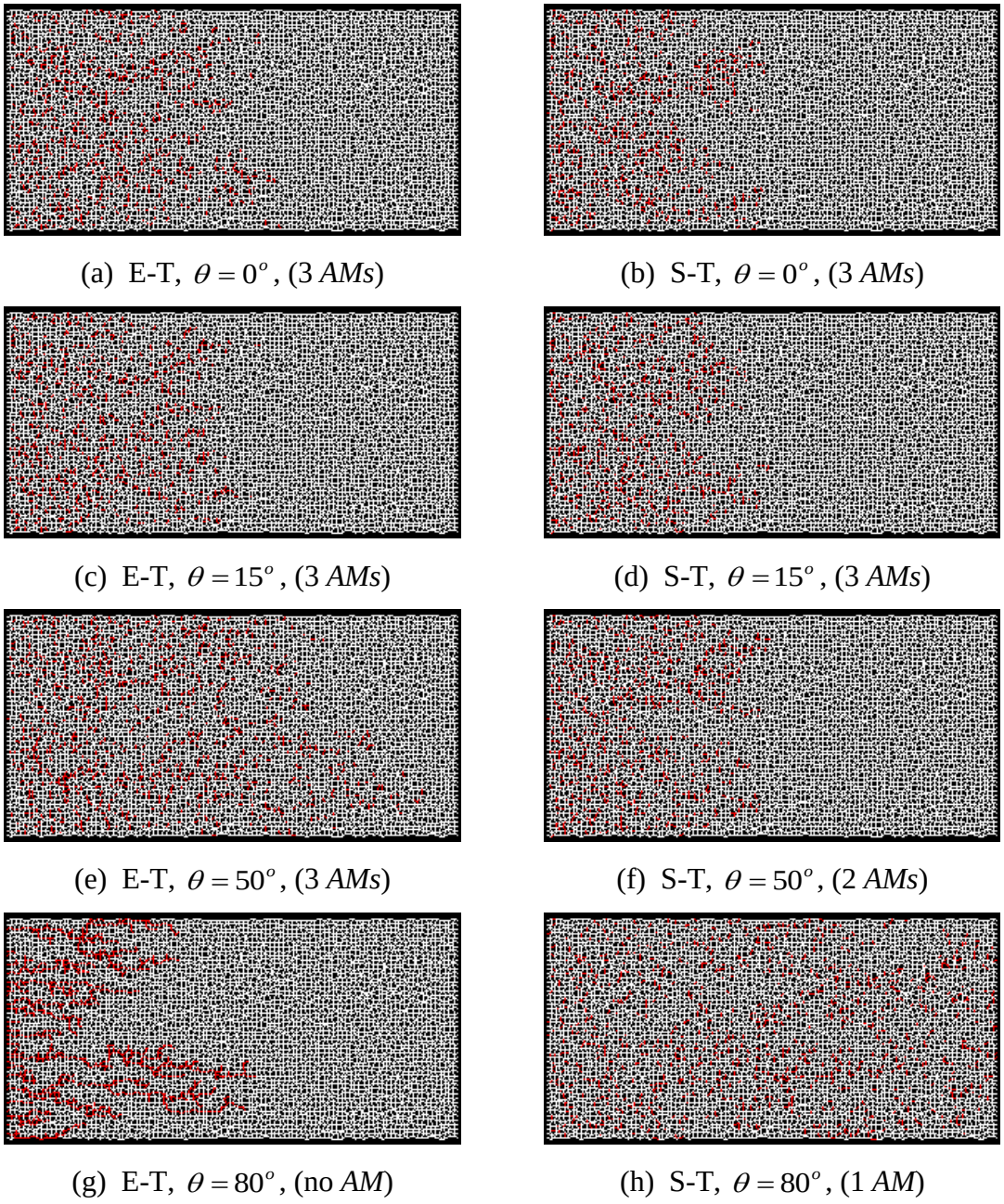

(a) E-T, $\theta = 0^o$, (3 *AMs*) (b) S-T, $\theta = 0^o$, (3 *AMs*)

(c) E-T, $\theta = 15^o$, (3 *AMs*) (d) S-T, $\theta = 15^o$, (3 *AMs*)

(e) E-T, $\theta = 50^o$, (3 *AMs*) (f) S-T, $\theta = 50^o$, (2 *AMs*)

(g) E-T, $\theta = 80^o$, (no *AM*) (h) S-T, $\theta = 80^o$, (1 *AM*)

Figure 5-73 Fluids configuration of low-rate model with various ***contact angles***, equilateral triangle and scalene triangle, half angles (70º, 15º, 5º),

Q=1.0e^{-8}m^3/s, M=10.0.

Above figures represent pores filled by different phases, and are taken when the global water saturations are the same (S_w=0.128). Red is water-filled pores, white is oil-containing pores.

The resulting water fractional flow curves are shown in Figure 5-74.

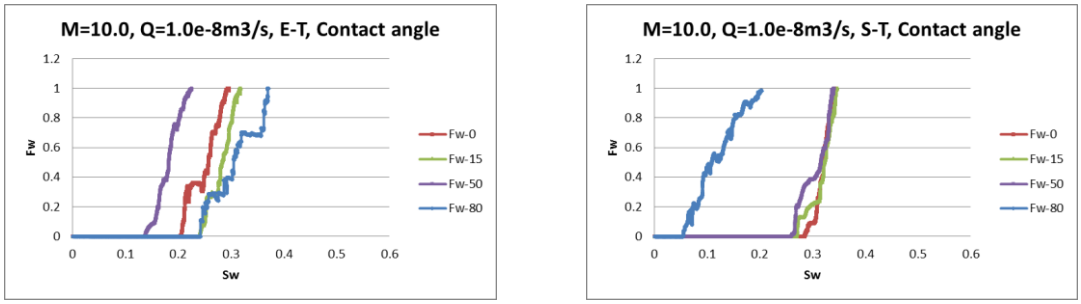

(a) E-T (b) S-T

Figure 5-74 F_w-S_w curves of low-rate model with various ***contact angles***, equilateral triangle and scalene triangle, half angles (70^o, 15^o, 5^o), ***Q=1.0e^{-8}m^3/s, M=10.0***.

5.5.7 The Resistance Factor of Solid, C_w

As the final issue in our parametric study, we consider the impact of pore wall resistance factor (C_w). Recall that the conductance of a wetting film can be expressed as:

$$G_{corner} = \frac{A_w^2}{C_w \mu_w S_1}. \qquad 5\text{-}6$$

where C_w is a dimensionless flow resistance factor that represents the reduced water conductivity close to the pore walls (notionally accounting for wall surface roughness). C_w itself has no influence on the automatic switch but, by controlling the wetting film conductance, it can still affect the fluid configurations (especially the extent of film swelling and snap-off) through the quantity, $R_{w\text{-}o}$.

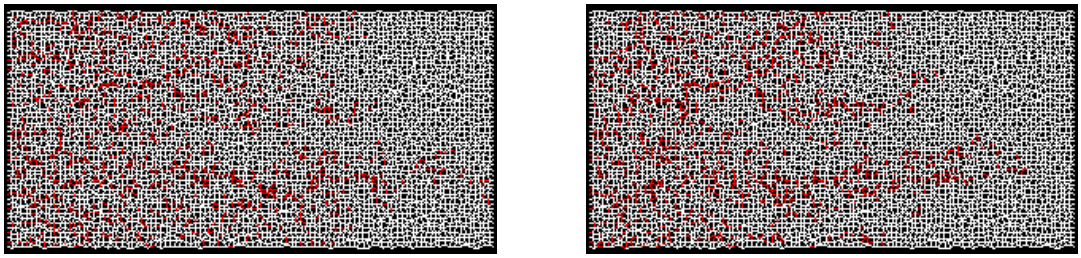

(a) C_w=*20* (b) C_w=*100*

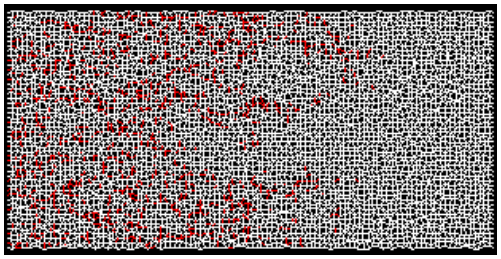

(c) C_w=*500*

Figure 5-75 Fluids configuration of simulations with various C_w, ***M=10.0***, ***Q=1.0e^{-7}m^3/s***. Above figures are taken when identical amount of water (0.192PV) has been injected into each network. (a)-(d) are figures of pores filled by different phases. Red is water-filled pores, white is oil-containing pores.

As shown in Figure 5-75 and Figure 5-76, as the resistance factor increases by a factor of 100, (a)-(c), the mobility of the wetting film is reduced. Thus less film swelling and less snap-off is observed.

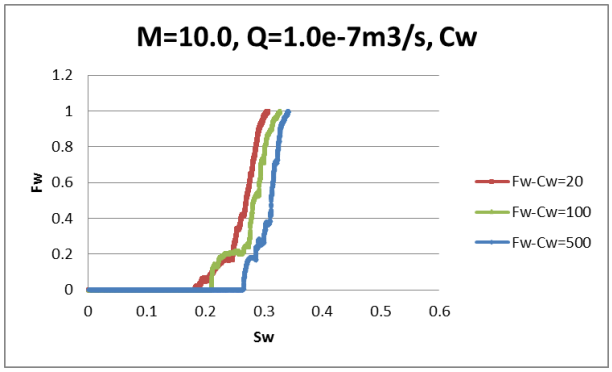

Figure 5-76 Water fractional flow curves of simulations with various C_w, ***M=10.0***, ***Q=1.0e^{-7}m^3/s***

5.5.8 The Influence of Initial Water

All of the simulations discussed so far have assumed that no initial water is present in the system prior to injection. We now relax this constraint and investigate the effect of adding some initial water to the system before water-flooding. Initial water saturation, S_{wi}, can affect the displacement by providing the invading water with better developed pathways, especially for film swelling. By contrast, in a system with no initial water, pores far away from the water front are not able to experience film swelling and snap-off due to the lack of water supply.

Before the dynamic imbibition simulation commences, we always allow the model to run quasi-static primary drainage (PD) as a preliminary stage. Thus, by choosing the

final P_c for PD, this model is able to assign each pore with the correct configuration based on an input initial water saturation. In Figure 5-77 and Figure 5-84, the network models initially have thin and uniform water films (characterised by $P_{c,max}$ at the end of PD) throughout the system– *AMs* in smallest pores simply merge.

In the high-rate ($Q=1.0e^{-3}m^3/s$, $C_a=2.94e^{1}$) models, where piston-like displacement is the main mechanism, the presence of an initial wetting film does not have a significant influence on the displacement patterns (Figure 5-77).

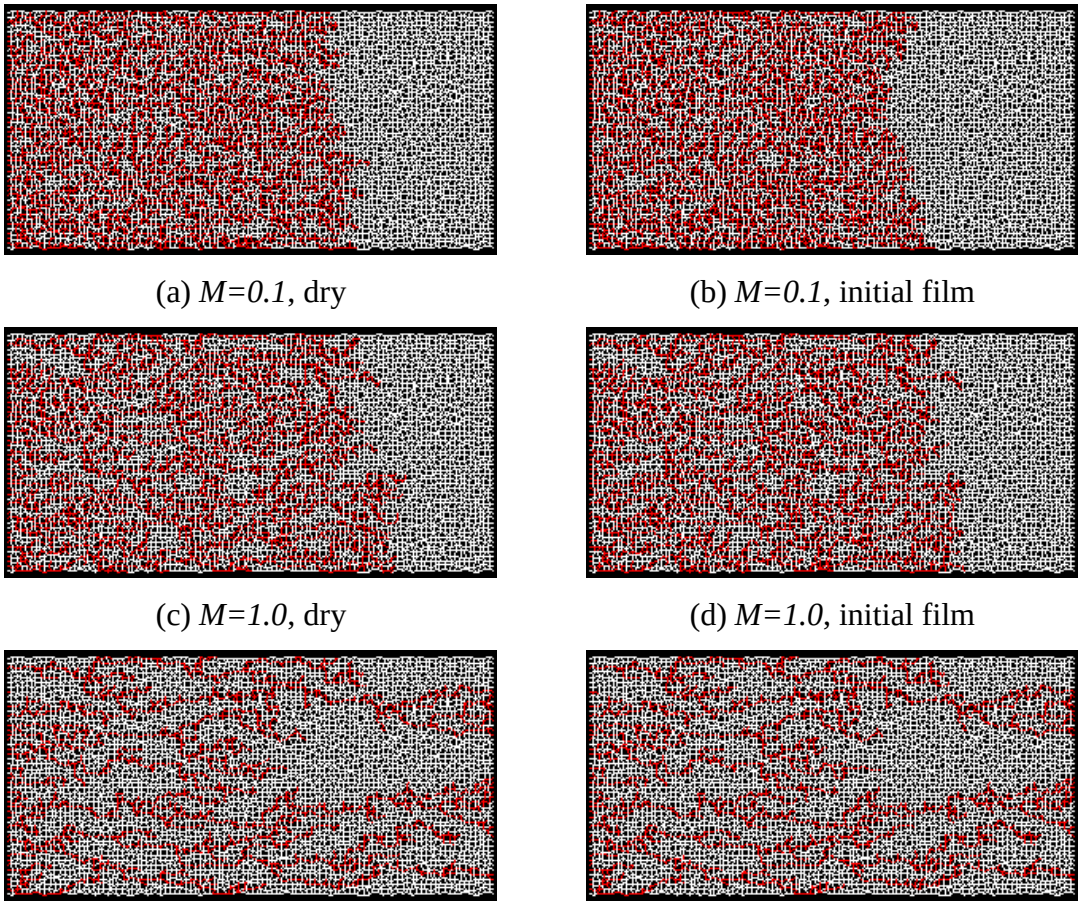

(a) *M=0.1*, dry (b) *M=0.1*, initial film

(c) *M=1.0*, dry (d) *M=1.0*, initial film

(e) *M=10.0*, dry (f) *M=10.0*, initial film

Figure 5-77 Fluids configurations of high-rate (***Q=1.0e*$^{-3}$*m*^{3}*/s***) models with or without initial water film.

Above figures are taken when identical amount of water (0.384PV) has been injected into each network. (a)-(f) are figures of pores filled by different phases. Red is water-filled pores, white is oil-containing pores.

However, the presence of some initial bulk water-filled pores can alter the shapes of viscous fingers in the high rate ($Q=1.0e^{-3}m^3/s$, $C_a=2.94e^{1}$), unfavourable viscosity ratio (*M=10.0*) models (as seen in Figure 5-78). Water-filled pores prior to imbibition can function as "nuclei" for the formation of discrete clusters of water-filled pores, which

may in turn alter the distribution of the subsequent incoming water (as seen in Figure 5-79 (b)). Also, the presence of initial water-filled pores can cause more oil trapping (Figure 5-80).

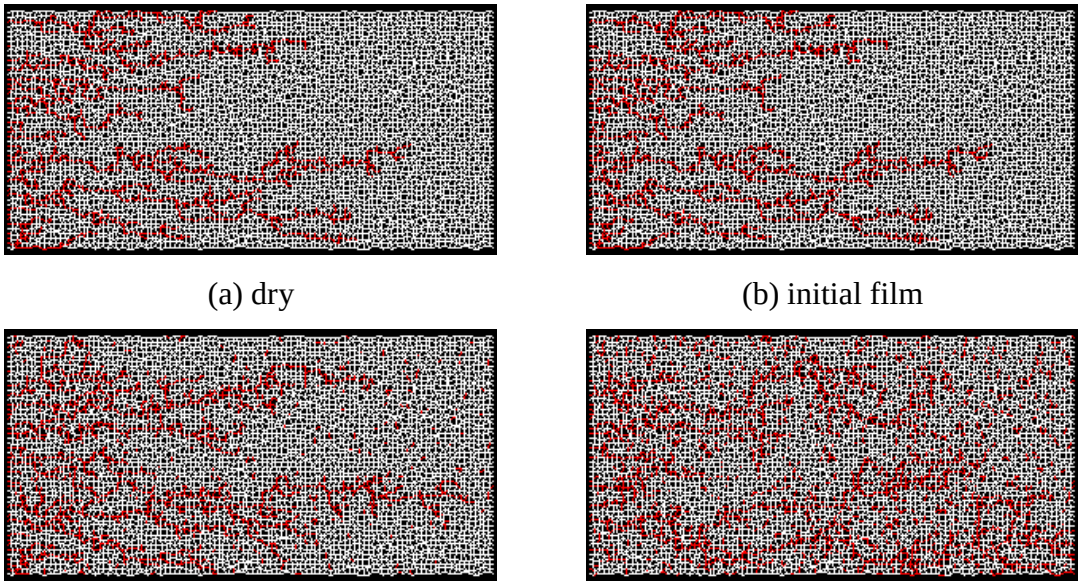

(a) dry (b) initial film

(c) S_{wi}=0.001 (d) S_{wi}=0.005

Figure 5-78 Fluids configuration with various $\boldsymbol{S_{wi}}$, $\boldsymbol{M=10.0}$, $\boldsymbol{Q=1.0e^{-3}m^3/s}$.

Above figures are taken when identical amount of water (0.192PV) has been injected into each network. (a)-(d) are figures of pores filled by different phases. Red is water-filled pores, white is oil-containing pores.

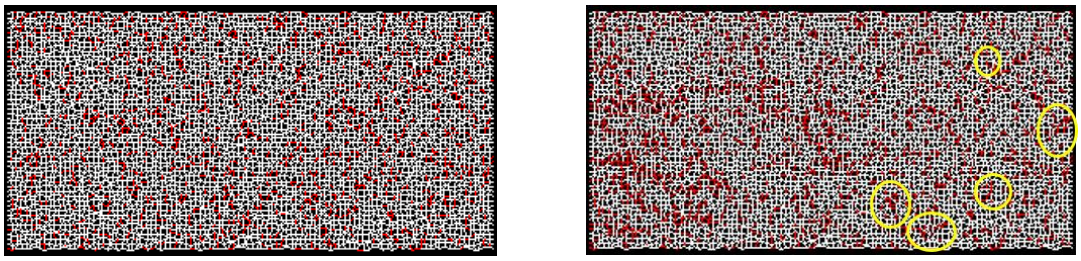

(a) S_w=0.01 (b) S_w=0.07

Figure 5-79 Fluids configuration with $\boldsymbol{S_{wi}=0.01}$, $\boldsymbol{M=10.0}$, $\boldsymbol{Q=1.0e^{-3}m^3/s}$.

Figure (a) shows the configuration at the start of simulation (S_w=0.01), figure (b) is taken when S_w=0.07. Discrete water-filled pores are circled by the yellow circles.

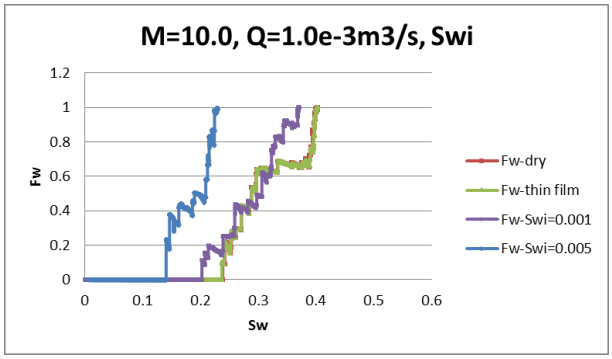

Figure 5-80 F_w-S_w curves with various ***S_{wi}, $M=10.0$, $Q=1.0e^{-3}m^3/s$***.

Furthermore, in low rate ($Q=1.0e^{-9}m^3/s$, $C_a=2.94e^{-4}$) cases, different S_{wi} can affect the displacement pattern by providing the entering water with alterative paths. The models of Figure 5-81 (c) and (d) only have thin and uniform wetting films initially; with slightly increased S_{wi}, models (Figure 5-81 (e) and (g)) begin to contain some initially water-filled pores. By encouraging film swelling and snap-off, the initial water will cause more oil trapping and worse oil production (Figure 5-82).

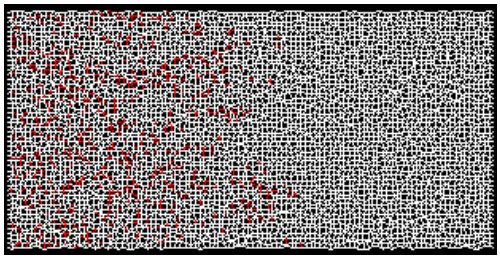

(a) dry

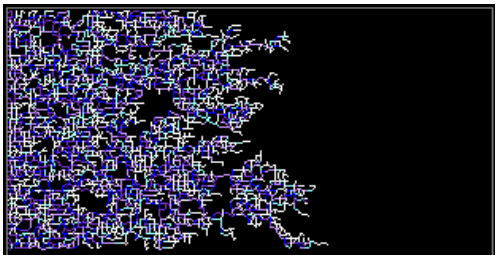

(b) dry, S_w map

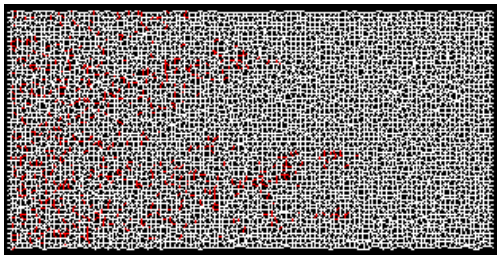

(c) initial film

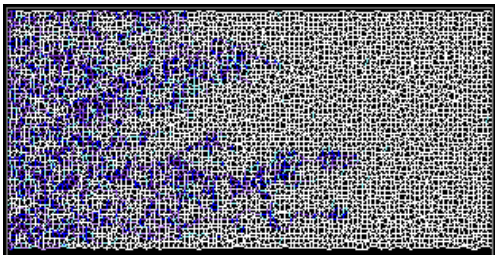

(d) initial film, S_w map

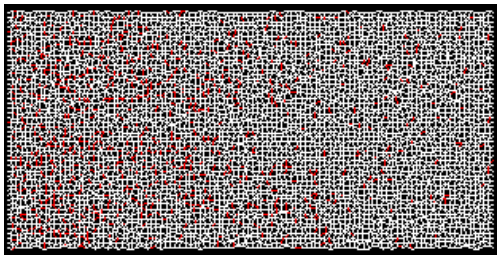

(e) S_{wi}=0.001

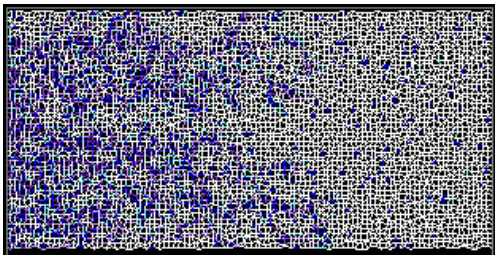

(f) S_{wi}=0.001, S_w map

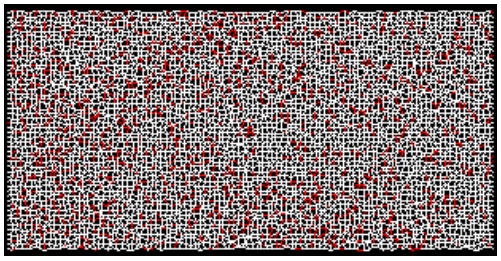

(g) S_{wi}=0.005

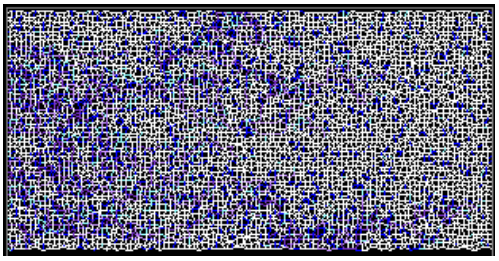

(h) S_{wi}=0.005, S_w map

Figure 5-81 Fluids configurations with various $\boldsymbol{S_{wi}}$, $\boldsymbol{M=10.0}$, $\boldsymbol{Q=1.0e^{-8}m^3/s}$.

Above figures are taken when identical amount of water (0.128PV) has been injected into each network. (a), (c), (e), (g) are figures of pores filled by different phases. Red is water-filled pores, white is oil-containing pores. (b), (d), (f), (h) are figures showing the corresponding local water saturation. As S_w increases, the colour will change in the order of black, white, light blue, light purple, dark purple, to dark blue. The black region is composed of pores with volumeless film and the dark blue pores are filled with invading water.

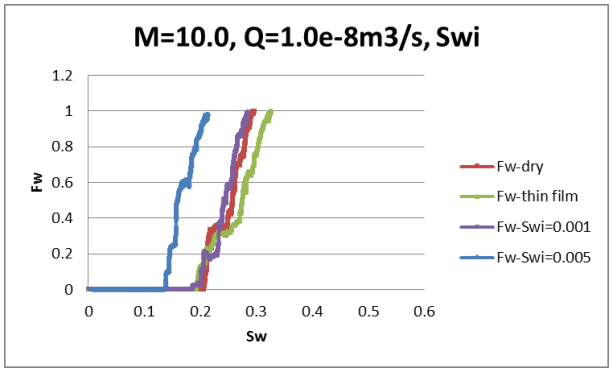

Figure 5-82 F_w-S_w curves with various $\boldsymbol{S_{wi}}$, $\boldsymbol{M=10.0}$, $\boldsymbol{Q=1.0e^{-8}m^3/s}$.

In low-rate simulation with initial water, isolated regions with film swelling and snap-off near the system outlet can be observed (as shown by the circled regions in Figure 5-83 (b) and (d)).

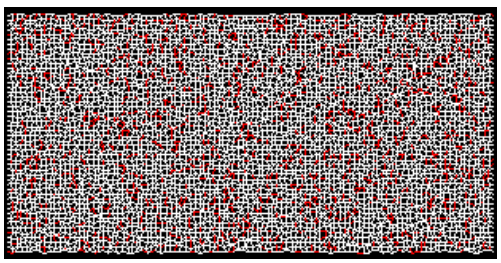

(a) Configuration, S_w=0.01

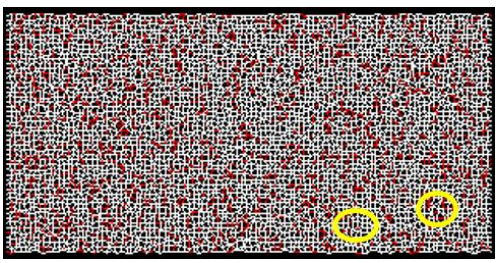

(b) Configuration, S_w=0.07

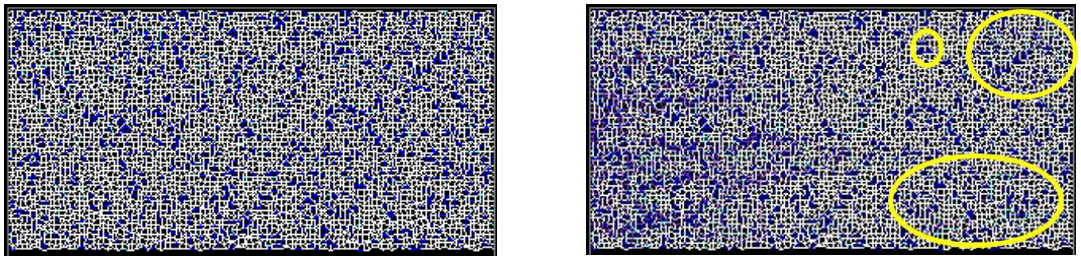

(c) Local S_w, S_w=0.01 (d) Local S_w, S_w=0.07

Figure 5-83 Fluids configuration with $\boldsymbol{S_{wi}=0.01}$, $\boldsymbol{M=10.0}$, $\boldsymbol{Q=1.0e^{-8}m^3/s}$.

Figure (a) and (b) are figures of pores filled by different phases, figure (c) and (d) are the local S_w maps. The yellow circles indicate the discrete water-filled pores in figure (b), and represent the isolated ragions with swelling films in figure (d).

In the ultra-low rate ($Q=1.0e^{-9}m^3/s$, $C_a=2.94e^{-5}$) cases, pore-scale pressure drops in systems with favourable or unit viscosity ratios are sufficiently low to cause counter-current flow and hence a large portion of pores are temporarily closed to flow. In dry networks, without the wetting film to connect pores that are open to the invading wetting phase, water can only displace oil present in the nearest open neighbours and create pathologically long thin fingers in Figure 5-84 (a) and (c), thus leaving a large percentage of areas of the network un-swept. In contrast, in systems with an original wetting film, all the open pores are connected, and so water is able to invade more pores (Figure 5-84 (b) and (d)). In the cases with $M=10.0$, local pressure drops in most of the pores are still high enough to maintain the co-current flow and leave them open to the entering water (either with or without an initial water film). The presence of original water can offer the invading water much better pathways and may also boost the snap-off process (Figure 5-84 (e) and (f)). So, to summarise, the presence of a small initial water saturation is sufficient to ameliorate some of the pathological results observed in dry systems.

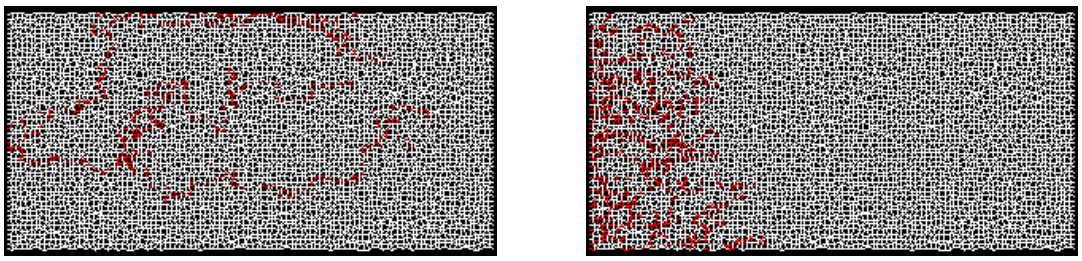

(a) $M=0.1$, dry (b) $M=0.1$, initial film

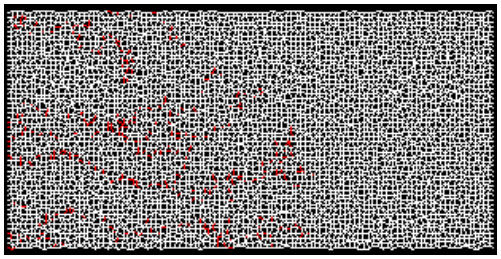

(c) *M=1.0*, dry

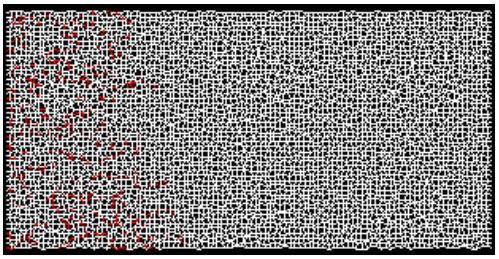

(d) *M=1.0*, initial film

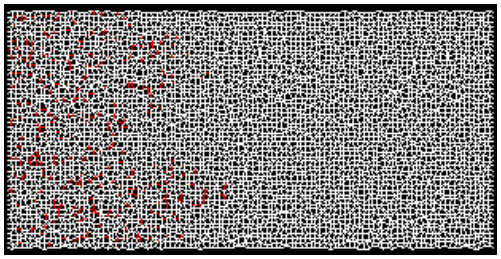

(e) *M=10.0*, dry

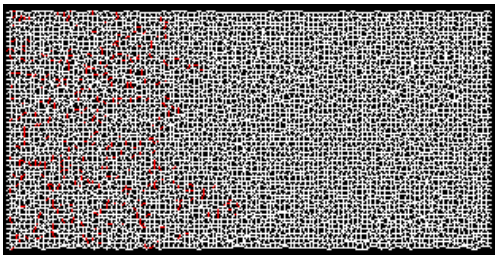

(f) *M=10.0*, initial film

Figure 5-84 Fluids configurations of low-rate (***Q=1.0e^{-9}m^3/s***) models with or without initial water film.

Above figures are taken when identical amount of water (0.064PV) has been injected into each network. (a)-(f) are figures of pores filled by different phases. Red is water-filled pores, white is oil-containing pores.

5.5.9 The Impact of Capillary Pressure in the Pressure Solver

In order to verify the fact that the long thin fingers in Figure 5-84 (a) and (c) are caused by the large proportion of closed pores (which are a result of suppressed counter-current flow), we can eliminate the capillary pressure from the pressure solver in the process of updating the pressure field and local flow rates: regardless of the presence of bulk menisci, all local flow rates are given by Equation 4-23. When $Q=1.0e^{-9}m^3/s$, $C_a=2.94e^{-5}$, the influence is dramatic (Figure 5-85) – so, inclusion of P_c in the pressure solver is the source of reversed flow and removing it will guarantee co-current flow. Water distribution in *M=10.0* cases are also different due to the altered pressure field with or without the capillary forces.

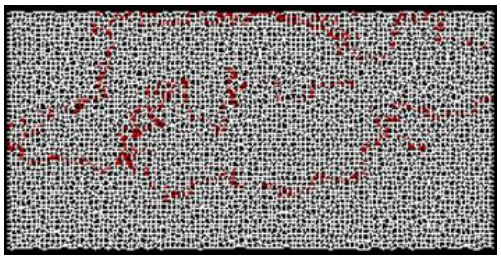

(a) *M=0.1*, P_c

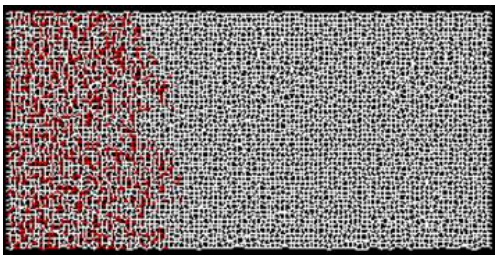

(b) *M=0.1*, No P_c

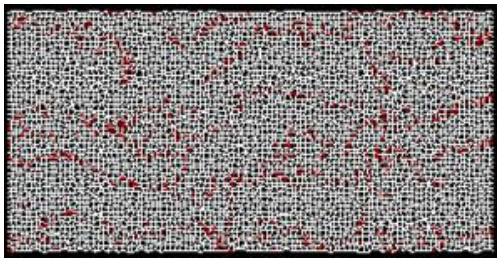

(c) *M=1.0*, P_c

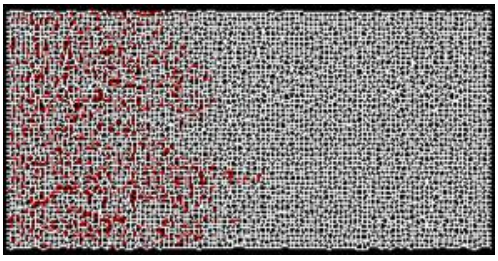

(d) *M=1.0*, No P_c

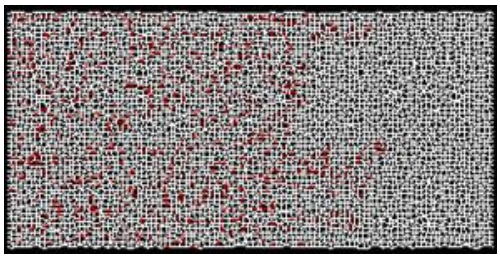

(e) *M=10.0*, P_c

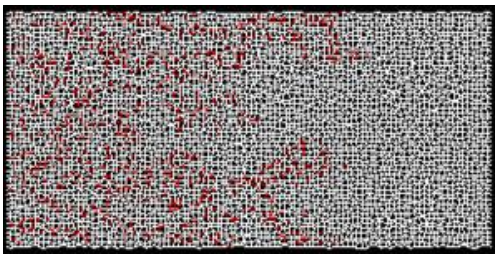

(f) *M=10.0*, No P_c

Figure 5-85 Fluids configuration with or without P_c in pressure solver, ***Q=1.0e^{-9}m^3/s***. Above figures are taken when identical amount of water (0.192PV) has been injected into each network. (a), (c), (e) are results when capillary pressure is included in pressure solver; (b), (d), (f) are the corresponding results when P_c is not considered.

Removal of P_c hardly brings any differences in the high rate cases (Figure 5-86) since viscous forces govern the displacement and P_c can be ignored.

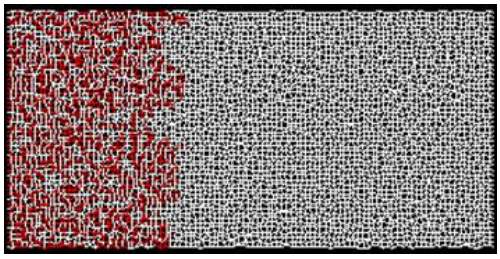

(a) *M=0.1*, P_c

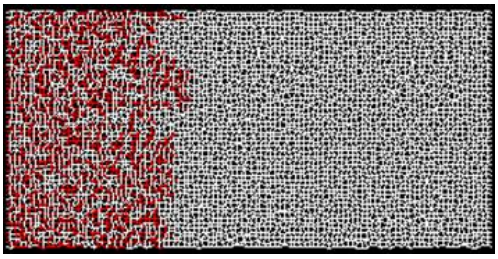

(b) *M=0.1*, No P_c

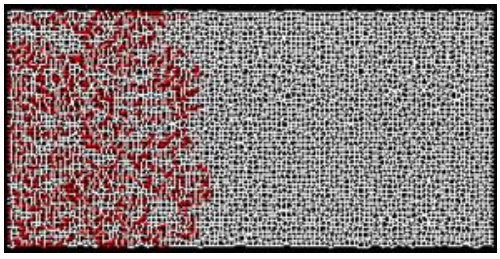

(c) *M=1.0*, P_c

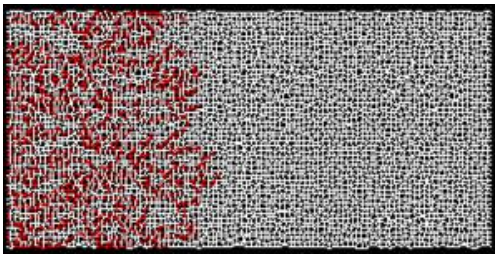

(d) *M=1.0*, No P_c

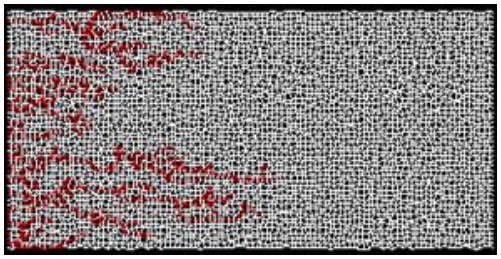

(e) *M=10.0*, P_c

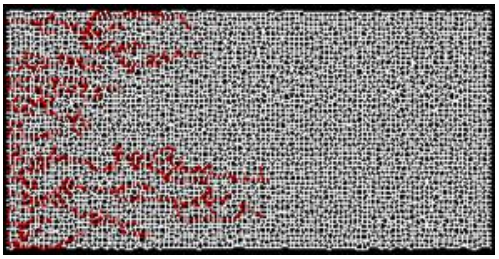

(f) *M=10.0*, No P_c

Figure 5-86 Fluids configuration with or without P_c in pressure solver, ***Q=1.0e^{-3}m^3/s***. Above figures are taken when identical amount of water (0.192PV) has been injected into each network. (a), (c), (e) are results when capillary pressure is included in pressure solver; (b), (d), (f) are the corresponding results when P_c is not considered.

5.5.10 Other Parameters

Coordination Number (Z)

For completeness, a few additional sensitivities have been undertaken. Figure 5-87 presents some simulation results in a less-connected system with a coordination number, Z = 3.6, where the fully connected 2-D network has *Z* = 4. All the results are in the same regime as their counterparts.

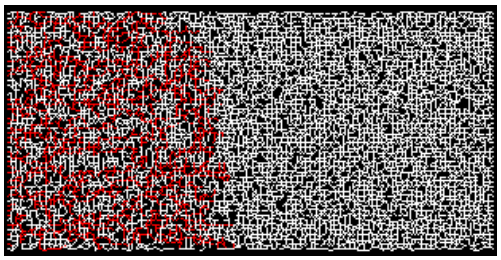

(a) *M=0.1*

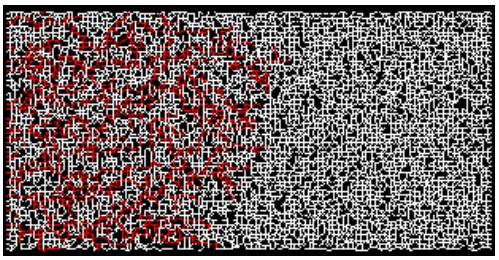

(b) *M=1.0*

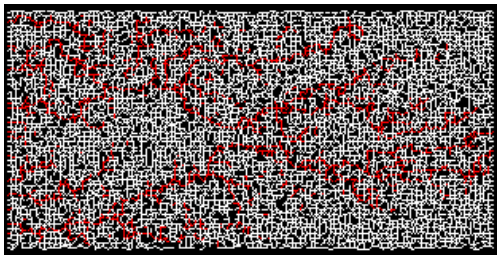

(c) *M=10.0*

Figure 5-87 Fluid configuration in the ***less-connected*** system. ***Q=1.0e^{-6}m^3/s***.

Above figures are taken when identical amount of water (0.192PV) has been injected into each network. (a)-(c) are figures of pores filled by different phases. Red is water-filled pores, white is oil-containing pores.

From the water fractional flow curves (Figure 5-88), systems with lower coordination number experience slightly earlier water breakthrough and lower oil recovery (as expected). Less connected networks provide fewer escape paths to the oil-phase and therefore result in more oil trapping.

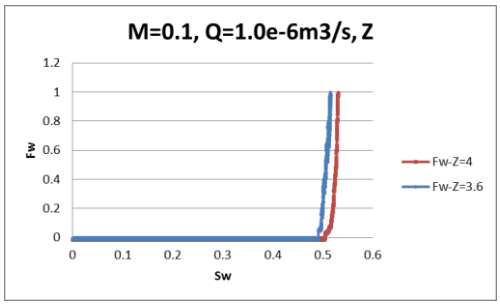

(a) *M=0.1*

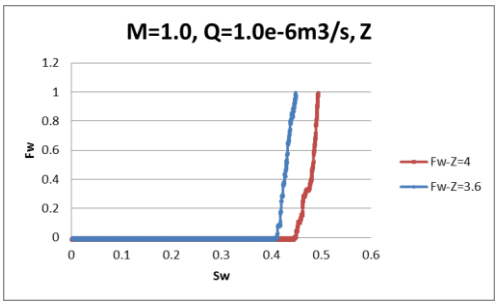

(b) *M=1.0*

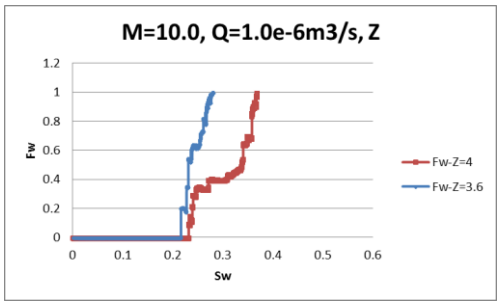

(c) *M=10.0*

Figure 5-88 F_w-S_w curves in systems with different *M* and *Z*. ***Q=1.0e^{-6}m^3/s***.

Random Seed

The pore scale network model structure and pore size distribution (within the pre-set range) are controlled by the "seed" used in the random number generator. With other conditions fixed, the pore filling results and the production data for the various systems studied with altered seeds should not show any significant differences in flow regime. Figure 5-89, Figure 5-90 and Figure 5-91 confirm this to be the case (although the precise fingering locations are seed-dependent as expected) and the simulations above are representative.

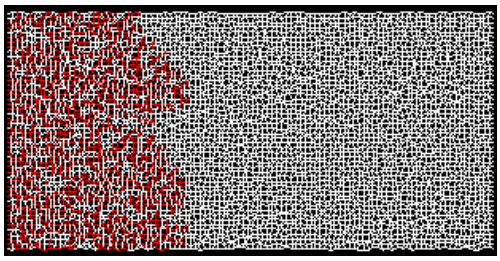

(a) *Seed=21*

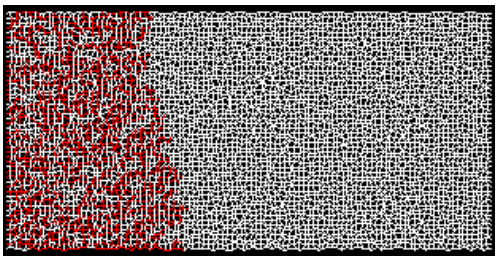

(b) *Seed=216*

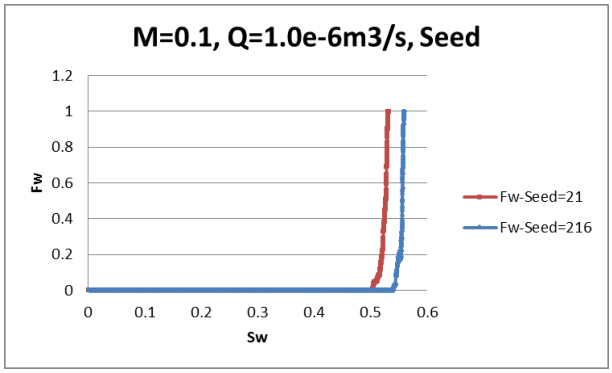

(c) F_w

Figure 5-89 Fluid configuration and F_w-S_w curves of systems with various ***seeds***, ***M=0.1***, ***Q=1.0e^{-6}m^3/s***.

Above figures are taken when identical amount of water (0.192PV) has been injected into each network. (a) and (b) are figures of pores filled by different phases. Red is water-filled pores, white is oil-containing pores. (c) shows the corresponding F_w-S_w curves.

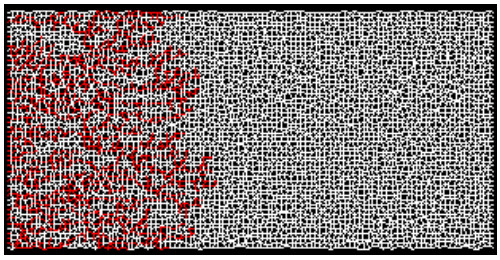

(a) *Seed=21*

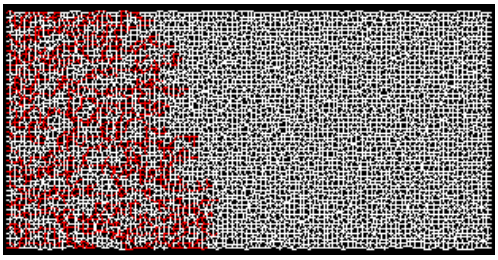

(b) *Seed=15*

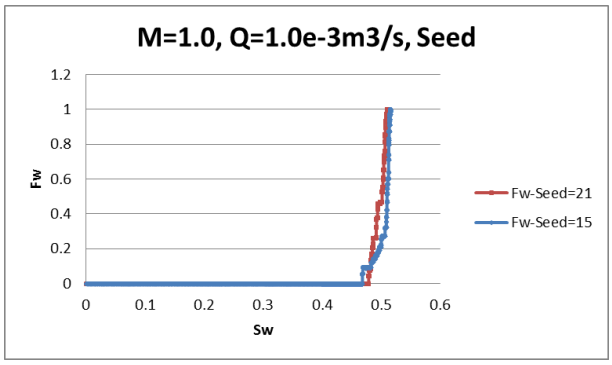

(c) F_w

Figure 5-90 Fluid configuration and F_w-S_w curves of systems with various ***seeds***, ***M=1.0***, ***Q=1.0e^{-3}m^3/s***.

The above figures are shown when identical amounts of water (0.192PV) have been injected into each network; (a) and (b) are figures of pores filled by different phases. Red denotes the water-filled pores, white is oil-containing pores. (c) shows the corresponding F_w-S_w curves.

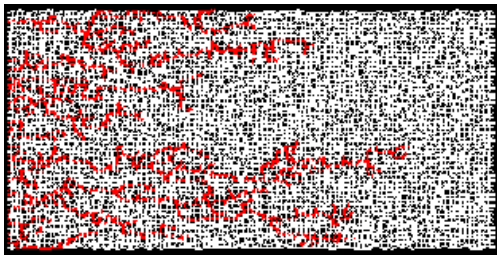

(a) *Seed=21*

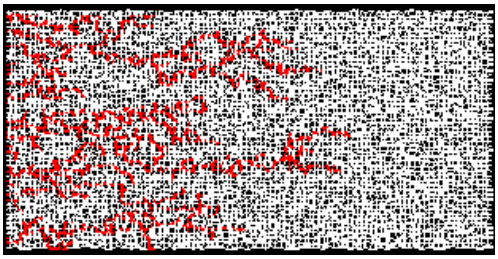

(b) *Seed=100*

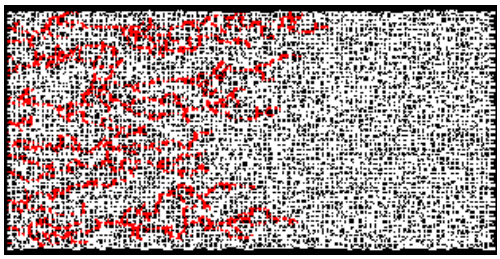

(c) *Seed=103*

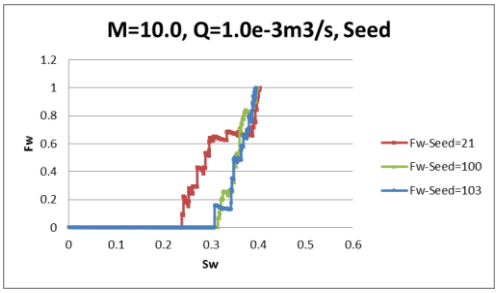

(d) F_w

Figure 5-91 Fluid configuration and F_w-S_w curves of systems with various ***seeds***, ***M=10.0***, ***Q=1.0e^{-3}m^3/s***.

Above figures are taken when identical amount of water (0.192PV) has been injected into each network. (a) - (c) are figures of pores filled by different phases. Red is water-filled pores, white is oil-containing pores. (d) shows the corresponding F_w-S_w curves.

Other than pore size distribution and pore length variation in the distorted network, the random seed in the less connected (smaller Z) network can also affect the distribution of sealed pores, thus more difference brought in by various random seeds can be expected.

5.6 Summary and Conclusions

In this chapter, this new dynamic *PNM* model quantifies the complex relationships between the physical displacement mechanisms themselves and several parameters of interest, such as the sensitivities to flow rate (Q), viscosity ratio (μ_o/μ_w), pore-size distribution (PSD), wettability state (θ), pore geometry, interfacial tension (σ), and initial water saturation (S_{wi}). The roles of all of these parameters in two phase dynamic imbibition displacements have been examined quite extensively in both 2D (this chapter) and 3D (Chapter 7) network models.

Table 5-2 lists all the parameters under investigation and shows how various controls, such as the capillary number (C_a), local switch (λ) or the extent of film-swelling ($R_{w\text{-}o}$), are affected as each factor on the left column of the table increases. Note that for the

scalene triangle, the changing tendency is compared with the equivalent equilateral-triangular pore system.

Table 5-2 Parameters and their influences

	C_a	λ	$R_{w\text{-}o}$	Film
$\lambda\uparrow$	→	↑	→	↑
$q\uparrow$	↑	↓	→	↓
$\mu_o\uparrow$	→	↓	↑	*
$r\uparrow$	↓	↑	↓	↑
$l\uparrow$	↓	↓	→	↓
$\sigma\uparrow$	↓	↑	→	↑
$C_w\uparrow$	→	→	↓	↓
$\theta\uparrow$	→	↓	↑	*
Scalene	→	↑	↓	*

↑ means increasing, ↓ means decreasing, → means no specific influence and * means the influence is non-monotonic due to opposing effects between λ and $R_{w\text{-}o}$. Film column listed the changing tendency of film swelling degree as each parameter varies.

6 3-D Results, SS and USS Relative Permeability Study

Whilst the 2D simulations presented above are very useful for visualising the various flow regimes that emerge from unsteady-state (USS) water injection, we cannot use the production and pressure drop data in a meaningful way to produce USS relative permeability curves. In this chapter, calculations are presented using the dynamic imbibition network model in 3D networks - unlike 2D networks, the simultaneous bicontinuous flow of both oil and water is possible in 3D. Therefore, such networks can be used to calculate the relative permeabilities of the system for a given PSD, pore geometry type and wettability conditions. Unsteady-state (USS) relative permeability curves can be calculated from the water fractional flow curves through Buckley-Leverett theory, particularly by applying the method of Jones and Roszelle (1978), which will be introduced below.

6.1 The Jones and Rozelle Method for Deriving Relative Permeability

The method of Jones and Roszelle (1978) is similar to the JBN method (Johnson et al. (1959)) in that it combines the Welge method (Welge (1952)) with pressure drop and flow rate data. However, the Jones-Roszelle method treats data reduction differently. This method uses a graphical approach to data processing which is useful for consistent interpretation of the data. Another unique feature of the Jones and Roszelle contribution is the derivation of the method, which is simpler than those of the Welge and the JBN methods. This method has been used to analyse the results generated by our network model to compute the corresponding dynamic relative permeabilities.

Ignoring gravity effects and capillary pressure, water and oil relative permeability (expressed as functions of saturation) are given by the equations:

$$k_{rw} = \mu_w f_{w2} / \delta_2 \qquad 6\text{-}1$$

and

$$k_{ro} = \mu_o f_{o2} / \delta_2 \qquad 6\text{-}2$$

In the above equations, the fractional flow of water or oil, f_{w2} and f_{o2}, and the effective viscosity, δ_2, must be determined as functions of saturation. These quantities must be point values, not averages and the most convenient location for their evaluation is the outlet end of the core because the fractional flow at the outlet is the same as the produced oil or water cut.

Given an initial water saturation S_{wi}, the average water saturation in the system can be calculated from

$$\bar{S}_w = S_{wi} + N_p / V_p \qquad 6\text{-}3$$

where N_p is the volume of oil produced and V_p is the total pore volume. If we denote Q_i as the cumulative injection volume W_i relative to the entire pore volume, $Q_i = W_i/V_p$, then, at each Q_i, we can draw a line tangent to the Q_i - $\bar{S}_w$ curve (Figure 6-1) and its intersection with the ordinate axis represents the saturation at the outlet end of the core after Q_i pore volume of water have been injected into the network (example of S_w-Q_i curve derived by the dynamic model is shown in Figure 6-2). The tangent construction is equivalent to the Welge equation, the derivation is described in the Appendix A of Jones and Roszelle (1978).

$$S_{w2} = \bar{S}_w - Q_i \cdot \frac{d\bar{S}_w}{dQ_i} \qquad 6\text{-}4$$

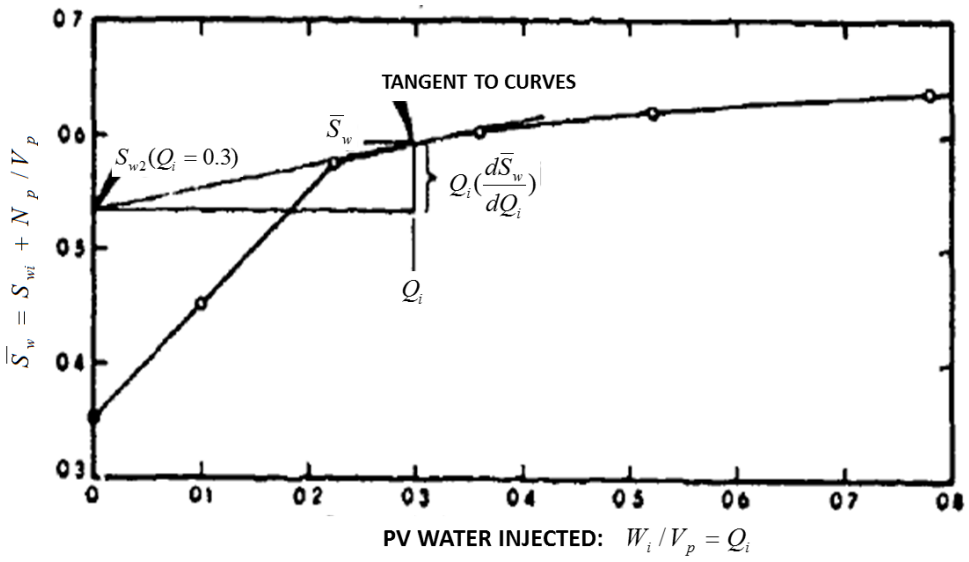

Figure 6-1 Construction for determining point saturation from average saturation (after Jones and Roszelle (1978)).

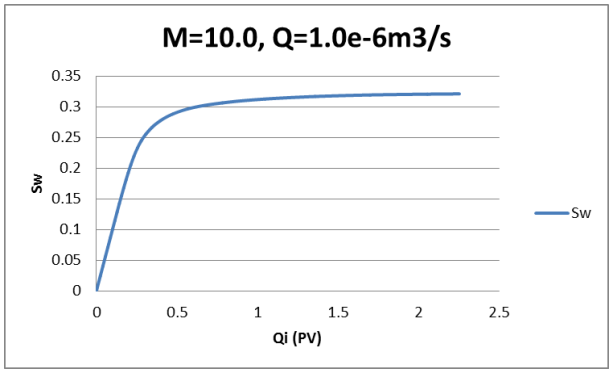

Figure 6-2 Example of S_w-Q_i curve derived by the dynamic model, S_{wi}=0.0, Q=1.0e^{-6}m^3/s, M=10.0.

Note that, before water breakthrough, the volume of injected water is equal to the volume of produced oil, i.e. $Q_i=N_p/V_p$. Thus Equation 6-3 can be written as:

$$\bar{S}_w = S_{wi} + Q_i \tag{6-5}$$

Furthermore, before water breakthrough, Equation 6-4 can also be simplified correspondingly

$$S_{w2} = S_{wi} + Q_i - Q_i \cdot \frac{d(S_{wi} + Q_i)}{dQ_i} = S_{wi} \tag{6-6}$$

Therefore, before water breakthrough, there is a linear relationship between average saturation and Q_i. All tangents drawn to the average saturation curve before water breakthrough intersect the ordinary axis at the exact initial water saturation, S_{wi}; that is, the saturation at the outlet end of the core is unchanged during a waterflood until water breakthrough. Also, the water saturation at this location is always less than the average saturation until all oil production terminates, at which time the slope of the average saturation curve becomes zero and the intercept has the same value as the average saturation.

The average effective viscosity can be calculated as

$$\bar{\delta} = \mu_s (\frac{\Delta P}{Q}) / (\frac{\Delta P_s}{Q_s}) \tag{6-7}$$

where μ_s is the viscosity of the fluid used to find the absolute permeability, and ΔP_s and Q_s are the global pressure drop and flow rate corresponding to this single-phase flooding.

Note all the parameters in Equation 6-7: μ_s, $\Delta P_s / Q_s$, and Q are all constant in the fixed injection rate models which we are studying. Thus, the *average effective viscosity* calculated here is solely determined by the global pressure drop ΔP. If we denote a constant (H),

$$H = \mu_s (\frac{1}{Q}) / (\frac{\Delta P_s}{Q_s}) \qquad 6\text{-}8$$

then

$$\bar{\delta} = H \cdot \Delta P \qquad 6\text{-}9$$

The point effective viscosity at the outlet can be derived by a similar method as that used to find the point saturation:

$$\delta_2 = \bar{\delta} - Q_i \cdot \frac{d\bar{\delta}}{dQ_i} = H \cdot [\Delta P - Q_i \cdot \frac{d(\Delta P)}{dQ_i}] \qquad 6\text{-}10$$

Now we can calculate the water and oil relative permeabilities using Equations 6-1 and 6-2. Now, before water breakthrough, f_{o2}=1 and f_{w2}=0; thus water relative permeability remains zero and the calculated k_{ro} only represents the changing tendency and velocity of global pressure drop as S_w increases and is not the actual oil relative permeability.

The unsteady-state experimental measurement can only provide relative permeability data after water breakthrough. And at the moment when all oil production terminates, the slope of the global pressure drop curve becomes zero and δ_2 has the same value as the average $\bar{\delta}$. Thus water relative permeability at this moment can be written as:

$$k_{rw} = \mu_w f_{w2} / \bar{\delta} . \qquad 6\text{-}11$$

In Equation 6-7, μ_s is the viscosity of the fluid used to find the absolute permeability and in our model $\mu_s = \mu_w$, thus

$$k_{rw} = f_{w2} (\frac{\Delta P_s}{Q_s}) / (\frac{\Delta P}{Q}) . \qquad 6\text{-}12$$

Note that at the end of simulation, f_{w2}=1 and that *ignoring capillary pressure*, $\frac{\Delta P}{Q}$ is the global conductance when oil production ends. At this moment only water and immobile

oil present in the network and, since the trapped oil occupies a portion of pathways and limits the mobility of water, $\frac{\Delta P_s}{Q_s} > \frac{\Delta P}{Q}$ and $k_{rw} < f_{w2} = 1$.

6.2 SS and USS Relative Permeability

A number of 3-D network model simulations using 20*20*20 networks have been performed to calculate oil/water relative permeabilities and study various parameters in terms of their influence on the corresponding relative permeability curves. Similar to the experimental measurements of relative permeabilities, except the inlet (left side) and outlet (right side) of the system, other surfaces are sealed to prevent flow. Unless otherwise indicated, the parameters of importance in this model will be assigned with the default values, which are listed in Table 6-1. Also, all simulations start without initial water (dry system), and continue until no further displacement is possible. The running time is determined by particular conditions (especially network size and flow rate) of the simulation: the typical running time of a 20*20*20 network will be several hours (high rate) to a day (low rate).

Table 6-1 List of default parameters used in this study (3D)

Parameter	Default value	Unit
Network size (3D)	20*20*20	Node
Coordination number (Z)	6	-
Pore size (uniform) (r)	1-50	μm
Distortion number	0.3	-
Average pore length (l)	333	μm
Pore shape/half angles (β_i)	30,30,30	degree
Wettability class	Water wet	-
Water viscosity	$1.0e^{-3}$	$N \cdot s/m^2$
Contact angle (θ)	0	degree
Interfacial tension (σ)	40.0	mN/m
Initial water saturation (S_{wi})	0.0	-
The resistance factor of solid (C_w)	100	-

6.2.1 Effect of Flow Rate and Viscosity Ratio on Dynamic Relative Permeabilities

Figure 6-3 shows the influence of both *flow rate* and *viscosity ratio* on displacements in 3D models. As was observed in our 2-D networks, decreasing the flow rate will lead to more snap-off and film swelling, as the global viscous pressure drop decreases and capillary forces become more dominant. For an unfavourable viscosity ratio ($M=10.0$), decreasing flow rates also alter the fingering patterns, which go from viscous fingering at high rates to a more uniform front composed of disconnected clusters at low rates. Capillary numbers of injection rates $1.0e^{-3}m^3/s$, $1.0e^{-5}m^3/s$, $1.0e^{-7}m^3/s$ are $5.64e^{-1}$, $5.64e^{-3}$, and $5.64e^{-5}$, respectively. Note that in the low rate ($Q=1.0e^{-7}m^3/s$) case with $M=0.1$, a large portion of pores are closed due to counter-current flow - hence the rapid spread of water-filled clusters (Figure 6-3 (c)) and worse oil production (Figure 6-4 (a)).

The 3D results with the same injection rate (especially high and intermediate rates), are in line with their 2D counterparts. Different displacement regimes – from stable displacement to viscous fingering – are observed as the viscosity ratio increases (Figure 6-3).

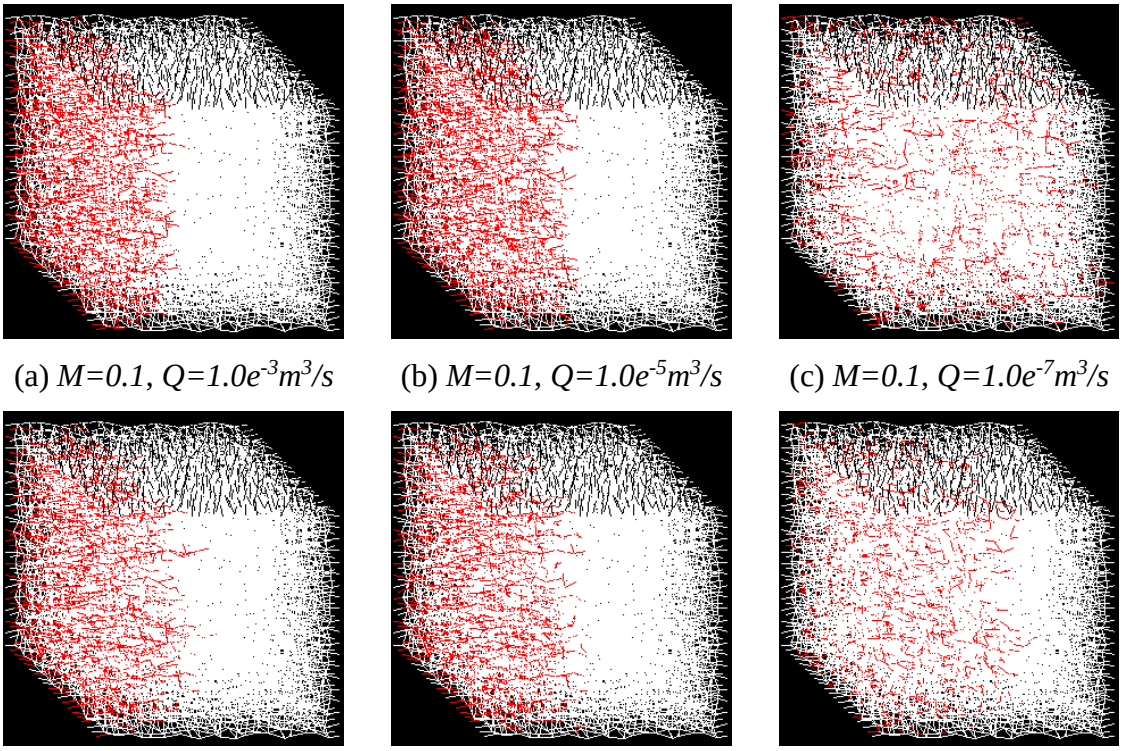

(a) $M=0.1$, $Q=1.0e^{-3}m^3/s$ (b) $M=0.1$, $Q=1.0e^{-5}m^3/s$ (c) $M=0.1$, $Q=1.0e^{-7}m^3/s$

(d) $M=1.0$, $Q=1.0e^{-3}m^3/s$ (e) $M=1.0$, $Q=1.0e^{-5}m^3/s$ (f) $M=1.0$, $Q=1.0e^{-7}m^3/s$

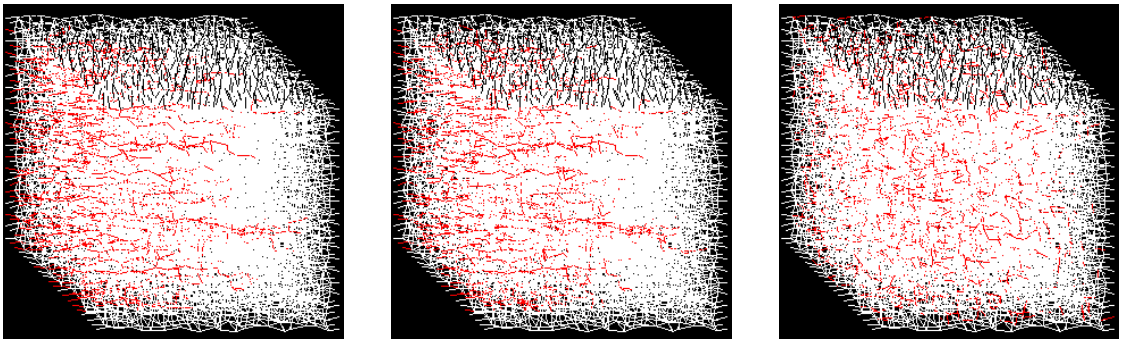

(g) $M=10.0$, $Q=1.0e^{-3}m^3/s$ (h) $M=10.0$, $Q=1.0e^{-5}m^3/s$ (i) $M=10.0$, $Q=1.0e^{-7}m^3/s$

Figure 6-3 Fluids configuration in 3-D networks with various ***viscosity ratios*** and ***flow rates***.

Figures of pores filled by different phases are taken when identical amount of water (0.162PV) has been injected into each network. Red is water-filled pores, white is oil-containing pores.

The effect of flow rate can also be seen in the water fractional flow curves (Figure 6-4), where similar results to those in our 2D simulations are observed. In high rate water injection, viscous forces predominate and water tends to replace more oil, while at low rates snap-off occurs in the smallest pores more often, and results in earlier water breakthrough and lower oil production. Moreover, viscous fingering in $M=10.0$ cases will prolong the duration of S_w increase between water breakthrough and the end of the simulation, the S_w range in which unsteady-state relative permeabilities can be produced.

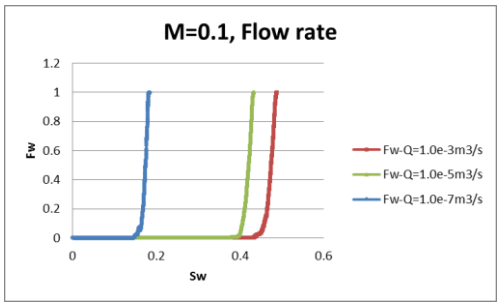

(a) $M=0.1$

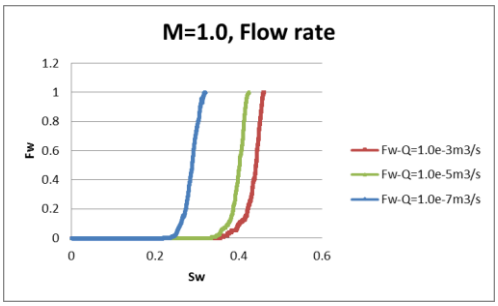

(b) $M=1.0$

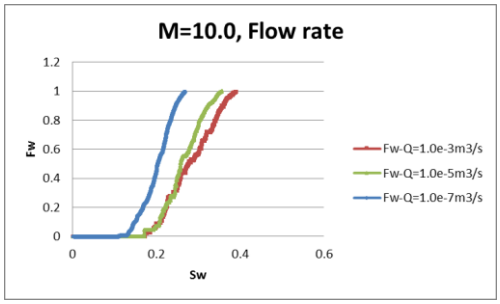

(c) $M=10.0$

Figure 6-4 F_w-S_w curves in 3-D networks with various ***viscosity ratios*** and ***flow rates***.

From Section 5.3, we update the global pressure drop to maintain a constant injection rate using the equation:

$$Q = a\Delta P + b = \bar{g} \cdot (\Delta P + \bar{P}_{c,entry}). \quad 6\text{-}13$$

Thus, we can get

$$\bar{g} = a \quad 6\text{-}14$$

and

$$\bar{P}_{c,entry} = \frac{b}{a}. \quad 6\text{-}15$$

Average conductance is clearly affected by the average viscosity and fluid configuration: in cases with unit viscosity, $\bar{g}$ reduction is caused by the trapped oil. In simulations where water is more viscous than oil (*M=0.1*), increasing viscosity also contributes to the conductance dropping in addition to the effect of the oil trapping (especially in the low-rate case, when a large portion of pores are closed due to counter-current flow). In cases with unstable viscosity ratio, decreasing viscosity and oil trapping are acting in opposite direction with $\bar{g}$ generally increasing, but this growth is limited, if not reversed, in the low-rate case as seen in Figure 6-5 (c).

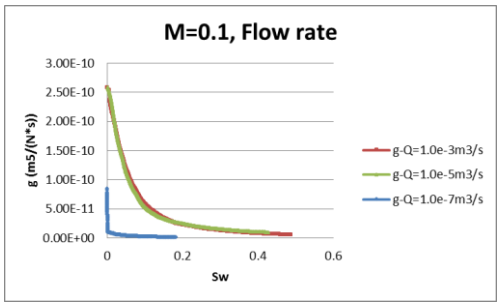

(a) *M=0.1*

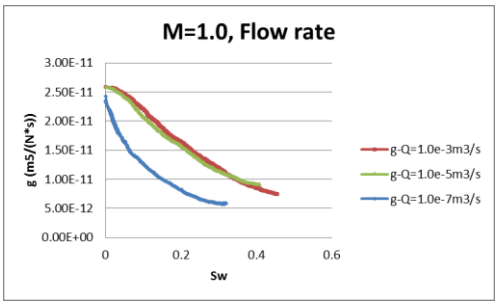

(b) *M=1.0*

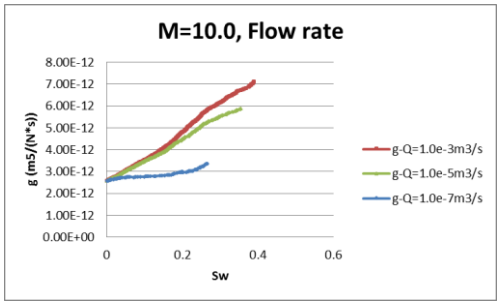

(c) *M=10.0*

Figure 6-5 Global conductance in 3-D networks with various ***viscosity ratios*** and ***flow rates***.

$\overline{P}_{c,entry}$ in Equation 6-15 corresponds to an average capillary *entry* pressure and this quantity is shown as a function of average network water saturation in Figure 6-6. Unlike the net capillary pressure in quasi-static model, $\overline{P}_{c,entry}$ does not correspond to the measured P_c in experiments using porous plate method. If the global pressure drop across the system is sufficiently high, all the inlet pores should be open to the invading bulk water at the start of each simulation, thus most of the $\overline{P}_{c,entry}$ curves begin with the same value. Except in the low rate cases with *M=0.1* and *M=1.0*, when the corresponding pressure drops are relatively low (even negative), a portion of inlet pores are closed to guarantee the positive inlet flow (see Section 4.4.2). Consequently, in Figure 6-6 (a) and (b), $\overline{P}_{c,entry}$ curves of the low rate cases start with higher values.

In networks dominated by viscous forces, $\overline{P}_{c,entry}$ will have a constant average value before water breakthrough, followed by a gradual decreasing trend as the water front leaves the system (Figure 6-6). The stable *average* capillary entry pressure before water breakthrough ($\overline{P}_{c,entry} \approx 2000Pa$) corresponds to the local capillary entry pressure of a pore with $r \approx 34\mu m$, which also confirms that bulk water will preferentially invade the larger pores in viscous force dominated simulations.

In contrast, in the low rate case, in which the capillary forces dominate, the average $\overline{P}_{c,entry}$ continually increases as the water front invades the smallest pores (with highest capillary pressure). For the *M=10.0* imbibition case (in which there are more active water films than for other viscosity ratios), $\overline{P}_{c,entry}$ increment is more obvious and can even be observed in the intermediate-rate case (Figure 6-6 (c)).

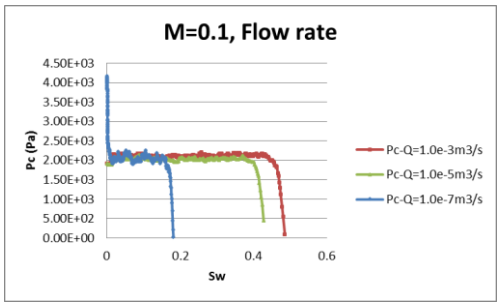

(a) *M=0.1*

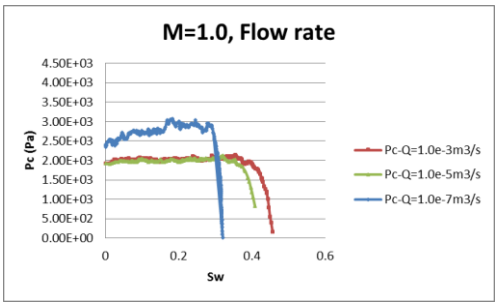

(b) *M=1.0*

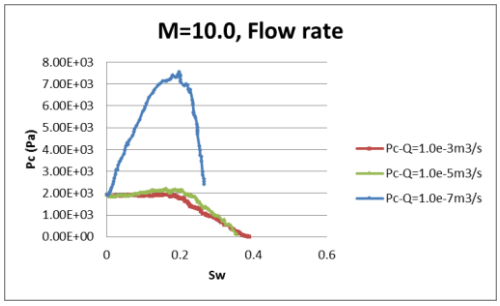

(c) *M=10.0*

Figure 6-6 Average capillary entry pressure in 3-D networks with various ***viscosity ratios*** and ***flow rates***.

Deriving the average capillary pressure from a dynamic model is not as straightforward as doing so in a quasi-static mode since the configuration change (especially film swelling) is controlled by water supply rather than by a simple sequence of capillary pressure steps. In the high-rate cases, where most of the invading water is involved in bulk flow instead of in wetting films, even the notion of average capillary pressure in a dynamic model is rather ambiguous. At other flow rates, film thickness is heterogeneous throughout the system (considering the very thin film at the front), whilst in intermediate-rate models, the local switch controls the water distribution.

The rate dependent global pressure drop, $\Delta P = Q/\bar{g} - \overline{P}_{c,entry}$, is inversely proportional to the global conductance and is also affected by the increasing $\overline{P}_{c,entry}$ in capillary dominated cases (Figure 6-7).

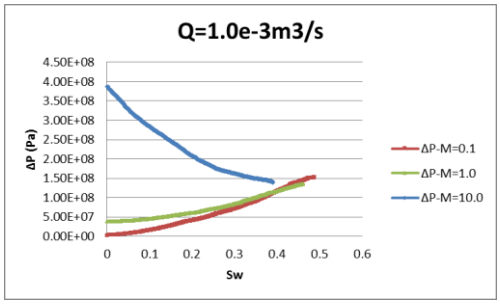

(a) $Q=1.0e^{-3}m^3/s$

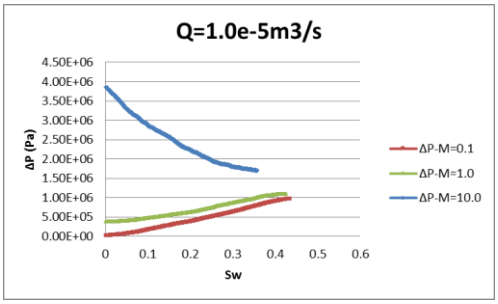

(b) $Q=1.0e^{-5}m^3/s$

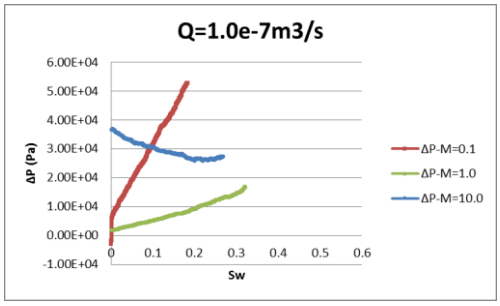

(c) $Q=1.0e^{-7}m^3/s$

Figure 6-7 Global pressure drop in 3-D networks with various ***viscosity ratios*** and ***flow rates***.

So, how do those variations in pressure drop and recovery manifest themselves in the corresponding USS relative permeabilities? Based on the Jones and Roszelle method, we can obtain the relative permeability (RP) curves using the production data - F_w-S_w and ΔP-S_w curves after water breakthrough. These quantities were recorded at the outlet end of the network in a manner similar to that used in core floods.

Once the water front (in bulk or film) reaches the outlet, k_{rw} starts to grow gradually and k_{ro} declines until the displacement process is complete. Thus the S_w range after water BT determines how much RP information can be derived from the corresponding simulation. This is directly analogous to the situation in unsteady state (USS) experimental RP curves. For simulations with favourable viscosity ratio (*M=0.1*), the stable water front sweeps the network outlet quickly with little displacement, the duration of two-phase flow at the outlet is short and we can only obtain very limited RP curves from the displacement data (Figure 6-8 (a)). Cases with unit viscosity ratio (*M=1.0*) can provide more RP information than the *M=0.1* cases. However, it is evident that when viscous fingering occurs (*M=10.0*), then this results in earlier water breakthrough and a prolonged period of two phase displacement and this has some merit in being "helpful" for extending the saturation range over which RP can be measured (as seen in Figure 6-8 (c)). However, with viscous fingers, these models tend to have "straggling" water fractional flow curves and the finite model size must be taken into consideration to eliminate this shortcoming (as seen in the 2-D f_w curves with *M=10.0*, for example Figure 5-14). Furthermore, viscous fingering actually violates one of the principal assumptions of Buckley-Leverett theory: stable displacement (but is often ignored in practice), and the resulting unstable data is difficult to interpret with the current techniques. It is also the main reason that causes the observed difference between relative permeabilities of SS and USS experiments in heavy-oil systems.

At each viscosity ratio, the decreasing injection rate will cause more film swelling and snap-off, consequently, more oil will be found trapped in the porous medium when displacement terminates. Especially in the $M=0.1$, $Q=1.0e^{-7}m^3/s$ case, the pathologically long and thin fingers are responsible for the low oil recovery and relative permeabilities of both phases. More active wetting films in low rate case will generally result in higher k_{rw} in normal cases (Figure 6-8). But it should also be noted that the low rate simulations violate the assumption of Buckley-Leverett theory that there should be no capillary pressure. Capillary end effect is another issue that will affect the unsteady-state relative permeabilities and should be avoided in experimental measurements.

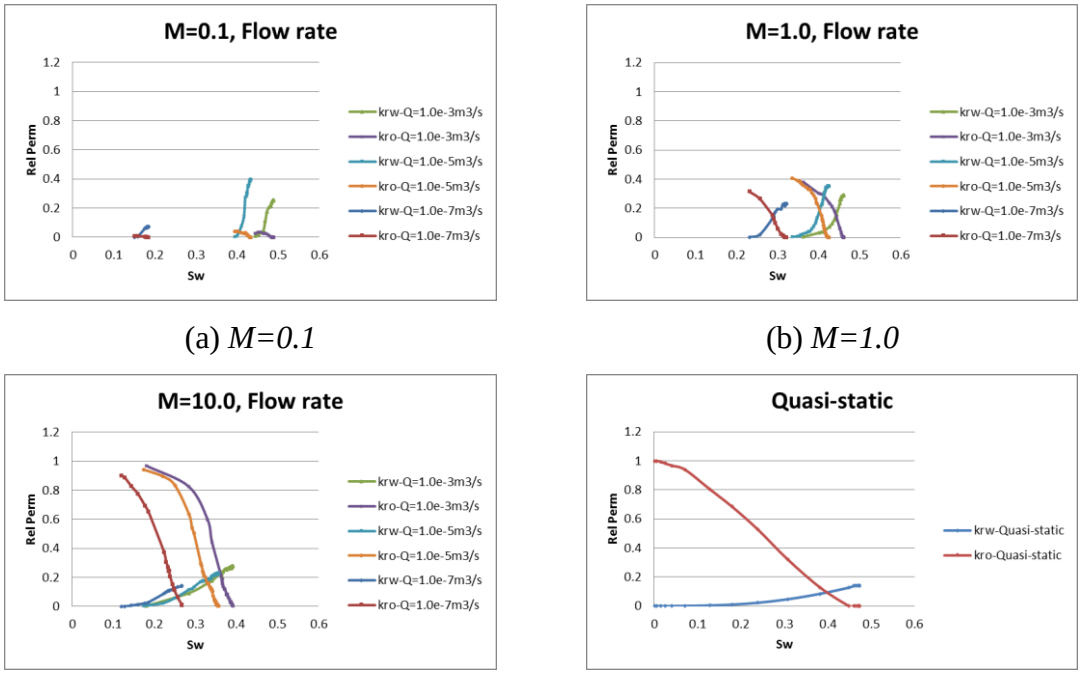

(a) *M=0.1* (b) *M=1.0*

(c) *M=10.0* (d) *Quasi-static model*

Figure 6-8 Relative Permeability curves in 3-D networks with various ***viscosity ratios and flow rates***.

For the same network structure, pore geometry, and wettability, the quasi-static relative permeability curves are unaffected by flow rate and viscosity ratio (Figure 6-8 (d)). This RP curve invariance is due to the fact that, in quasi-static models, the filling order is governed by the sequence of pore capillary entry pressures only, which is independent of these two parameters (rate and viscosity ratio). Also, at one particular P_c step, water in each pore either occupies the entire pore shape or is present as a wetting film, whose area, A_w, is also independent of flow rate and viscosity ratio.

6.2.2 Influence of the Local Capillary/Viscous Switch (λ) on USS RPs

As discussed in detail in Chapters 5 above, the rate dependent switch, λ, in each pore can be calculated automatically based on the local pressure drop and capillary pressure. In certain simulations it can also be forced to be a constant value in order to simulate an experiment with only forced piston-like displacement or only snap-off. Through controlling the balance between these primary filling mechanisms during imbibition, the switch can clearly have an effect on the relative permeability curves. Figure 6-9 illustrates these statements by showing the comparison of the intermediate-rate model ($Q=1.0e^{-5}m^3/s$) with unfavourable viscosity ratio ($M=10.0$). For this injection rate, water should displace oil through both bulk advancement and film swelling mechanisms. However, if we set λ=0.0, then film swelling is completely suppressed and, likewise, when we make λ=1.0, only snap-off occurs throughout the network. Regardless of the value of the switch, the capillary number is constant at $5.64e^{-3}$. However, it is clear from the 3D network displacement patterns in Figure 6-9 that the flows are very different and we would expect that this ***must*** have some influence of the resulting relative permeability curves.

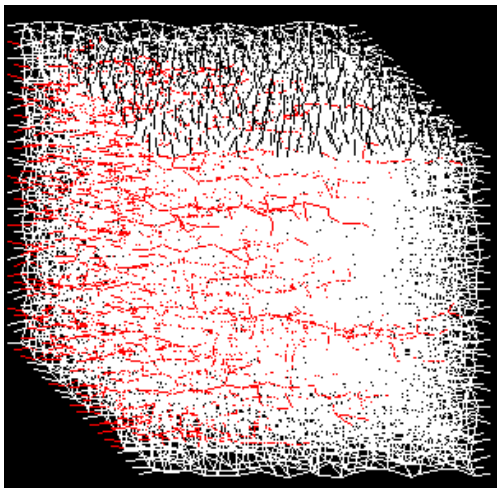

(a) λ=0.0, piston-like

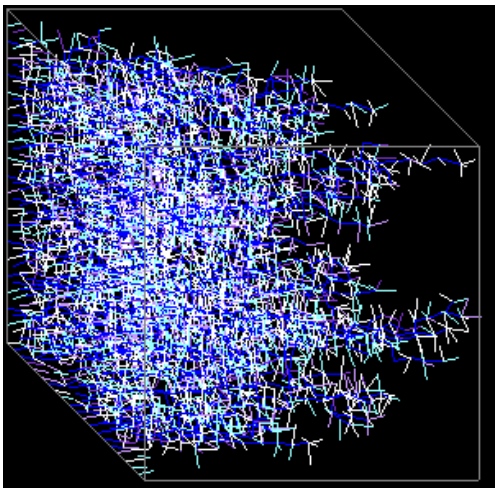

(b) λ=0.0, piston-like, S_w map

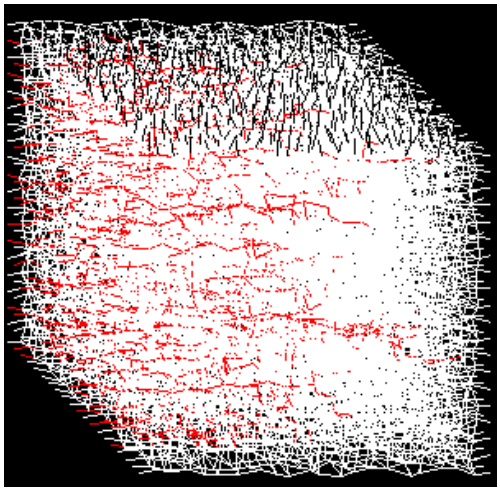

(c) automatic λ

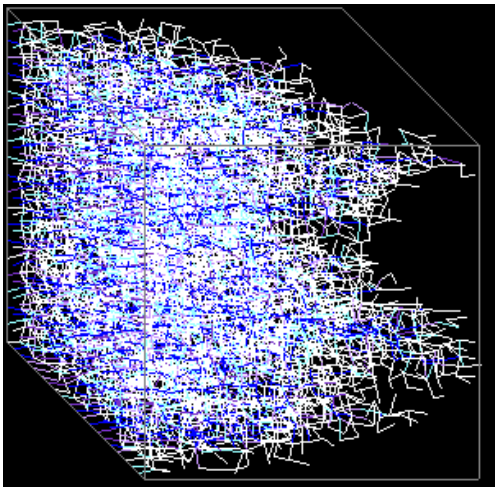

(d) automatic λ, S_w map

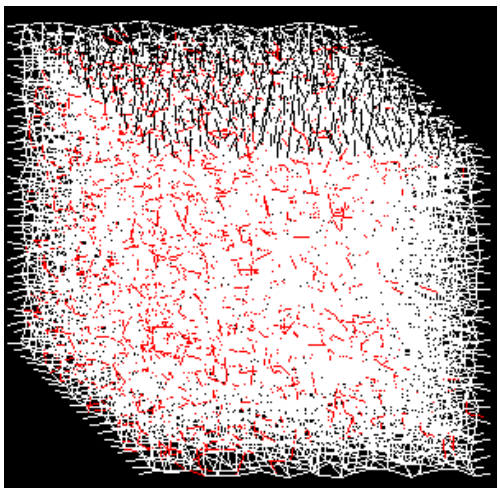

(e) λ=1.0, snap-off

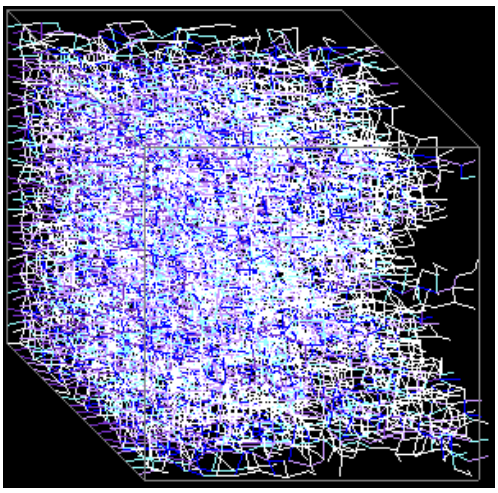

(f) λ=1.0, snap-off, S_w map

Figure 6-9 Illustrate the influence of ***switch***, ***Q=1.0e^{-5}m^3/s***, ***M=10.0***.

(a), (c), (e) are figures of pores filled by different phases, which are taken when identical amount of water (0.162PV) has been injected into each network. Red is water-filled pores, white is oil-containing pores. (b), (d), (f) are corresponding local water saturation maps.

The controlled competition between viscous forces and capillary forces can also be found in the changing tendency of average entry pressure at the water front (Figure 6-10 (b)) from which is evident that water in the viscous dominated displacement tends to fill the largest pores and advance with a stable average entry pressure. In contrast, when film-swelling and snap-off mechanisms dominate in capillary dominated displacements, the water is directed to the smallest pores with highest entry pressure.

Furthermore, higher levels of film-swelling and snap-off will lead to more severe oil-trapping as a consequence, which explains the smaller average conductance (Figure

6-10 (a)), earlier water breakthrough and worse oil recovery (Figure 6-10 (d)), as well as the slightly higher pressure drop (where the trapped-oil offsets the influence of decreasing global viscosity) (Figure 6-10 (c)).

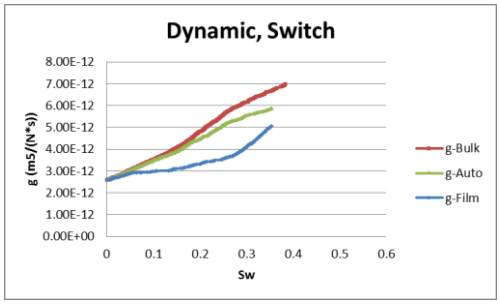

(a) $\bar{g}$

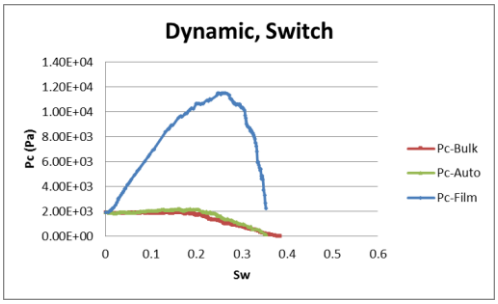

(b) $\bar{P}_c$

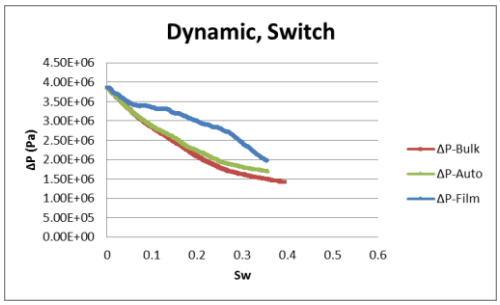

(c) ΔP

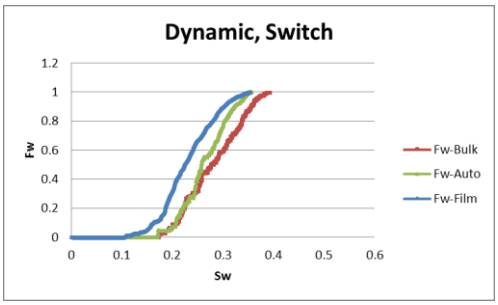

(d) F_w

Figure 6-10 Comparisons of simulations with various ***switches***, ***Q=1.0e^{-5}m^3/s***, ***M=10.0***.

Based on Buckley-Leverett theory, the model can be used to obtain the relative permeability curves (Figure 6-11) using water fractional flow (Figure 6-10 (d)) and global pressure drop data (Figure 6-10 (c)). Figure 6-11 verifies that more film swelling and snap-off will cause more oil-trapping and reduce the value of k_{ro}. Clearly, without the concept of a local switch, quasi-static RPs cannot be affected by λ.

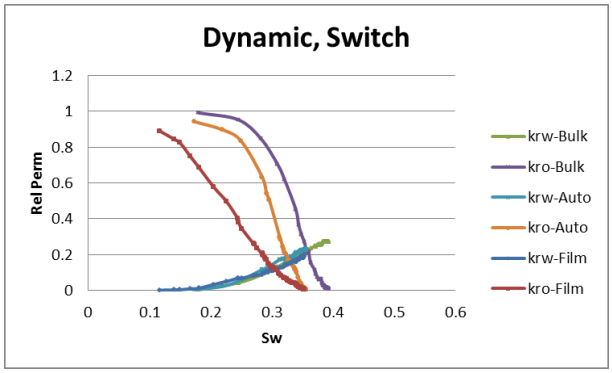

Figure 6-11 Relative permeability curves of simulations with various ***switches***, in dynamic model: ***Q=1.0e^{-5}m^3/s***, ***M=10.0***.

6.2.3 Pore Size Distribution, PSD

As found in the 2D calculations presented in Section 5.5.1, the local balance between capillary and viscous forces is proportional to the cube of the pore radius, and so *more bulk displacements (smaller λ) should be expected in networks characterised by a smaller* r_{mean} (Figure 6-12).

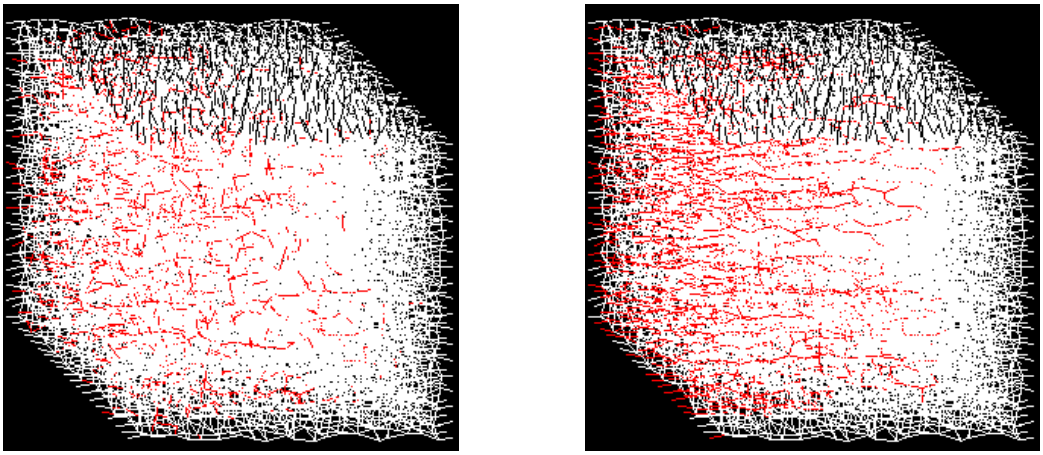

(a) (11, 40) (b) (1.1, 4)

Figure 6-12 Fluid configurations of simulations with various $\boldsymbol{r_{mean}}$, $\boldsymbol{Q=1.0e^{-6}m^3/s}$, $\boldsymbol{Ca=5.64e^{-4}}$, $\boldsymbol{M=10.0}$.

(a) and (b) are figures of pores filled by different phases, which are taken when S_w in these two systems are the same (S_w=0.16). Red is water-filled pores, white is oil-containing pores.

For the same mean radius, $r_{\max}/r_{\min}$ will have very little influence on the bulk-film competition. Thus, the extent of film swelling and snap-off tends to be the same in Figure 6-13 (a) and Figure 6-13 (b). But, in the network with a wider radius range (1, 50), enhanced cross flow in the y-direction allows water to enter more large pores and create thin dendritic fingers. In the system with a narrower radius range (11, 40), however, water tends to flow parallel to the global pressure drop in x-direction, since local pressure gradients in the y-direction and z-direction are lower (illustration of these directions are shown in Figure 3-1). The low $r_{\max}/r_{\min}$ case also has a more uniform water front and later breakthrough, reduced trapping and better oil recovery. But from the 2-D results in Figure 5-50 and Figure 5-51, it can be concluded that the difference of oil recovery is mostly found in high-rate cases, while in low-rate case, the influence of $r_{\max}/r_{\min}$ is even lesser (see also Figure 6-15 and Figure 6-17).

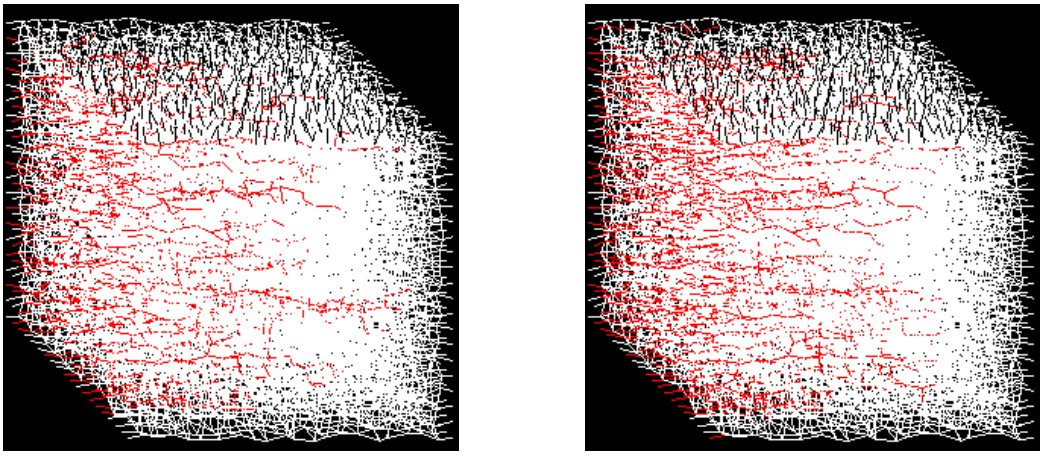

(a) (1,50) (b) (11, 40)

Figure 6-13 Fluid configurations of simulations with various **(r_{min}, r_{max})**, ***Q=1.0e^{-3}m^3/s***, ***Ca=5.64e^{-1}***, ***M=10.0***.

Figures of pores filled by different phase are taken when identical amount of water (0.162PV) has been injected into each network. Red is water-filled pores, white is oil-contained pores.

According to the expression for the local switch, λ is positively proportional to r^3 and $1/q$ – this is verified by Figure 6-12 (b) and Figure 6-13 (b): the R_{mean} in these two cases are differentiated by 1 magnitude (R_{mean}=2.55μm and R_{mean}=25.5μm); and their flow rates have a 3 orders of magnitudes difference ($Q=1.0e^{-6}m^3/s$ and $Q=1.0e^{-3}m^3/s$ respectively).

Figure 6-14 and Figure 6-15 show the F_w-S_w curves, while Figure 6-16 and Figure 6-17 show the relative permeability curves.

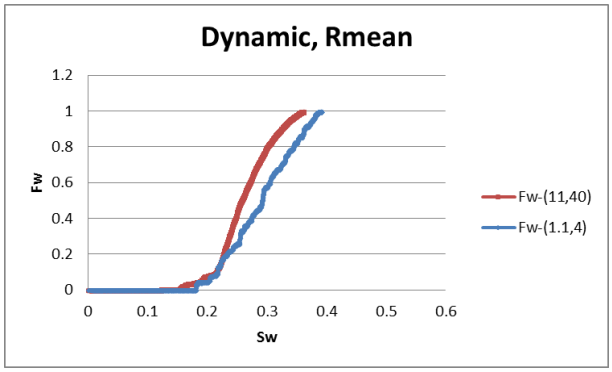

Figure 6-14 F_w-S_w curves of simulations with various ***r_{mean}***, ***Q=1.0e^{-6}m^3/s***, ***M=10.0***.

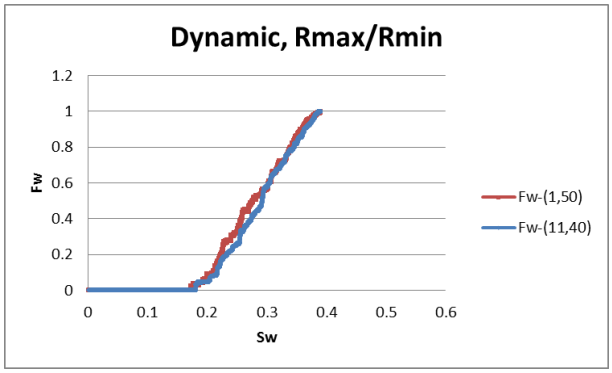

Figure 6-15 F_w-S_w curves of simulations with various **(r_{min}, r_{max})**, ***Q=1.0e^{-3}m^3/s***, ***M=10.0***.

Although mean radius has no influence on relative permeability in quasi-static model, it affects the dynamic results through interfering with the balance between the primary forces and the corresponding favoured filling mechanism; higher levels of snap-off in the (11,40) model clearly limits the oil permeability and enhances the k_{rw} (Figure 6-16 (a)).

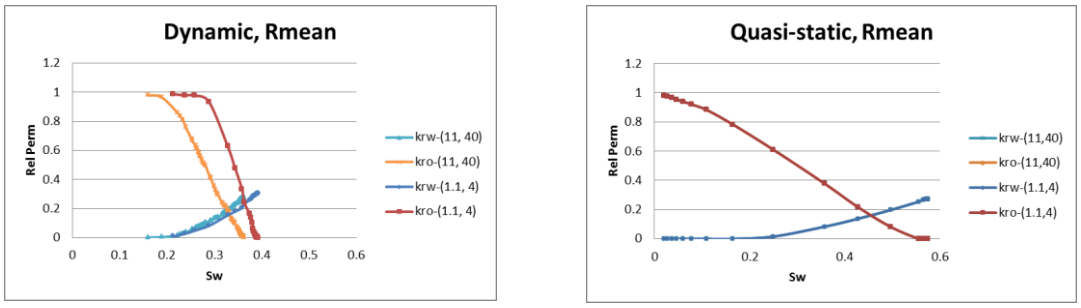

(a) Dynamic (b) Quasi-static

Figure 6-16 Relative permeability curves of simulations with various r_{mean}, in dynamic model: ***Q=1.0e^{-6}m^3/s***, ***M=10.0***.

Radius range has negligible impact on the force balance and filling mechanism competition in dynamic water flooding, although the dendritic fingers of the (1,50) case tends to reach the network outlet earlier and have a longer period of two-phase displacement at the system outlet. However, in quasi-static model, snap-off will be effectively suppressed in the (11,40) case and the water-filled pores will make larger contribution to the global water saturation due to their larger pore volumes (Figure 6-17).

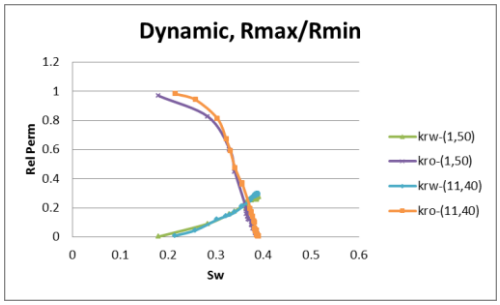

(a) Dynamic

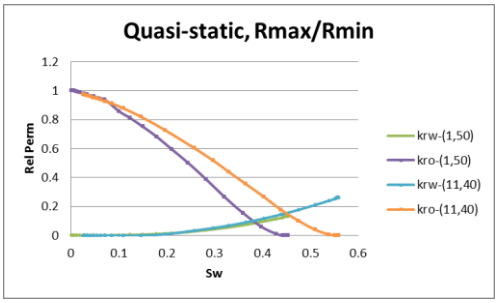

(b) Quasi-static

Figure 6-17 Relative permeability curves of simulations with various (r_{min}, r_{max}), $Q=1.0e^{-3}m^3/s$, $M=10.0$.

6.2.4 Pore Length

As discussed in Section 5.5.2, the switch value is inversely proportional to the pore length – *increasing pore length will reduce the degree of snap-off*, which contradicts the tendency predicted by the decreasing capillary number, this is confirmed by Figure 6-18 to Figure 6-20.

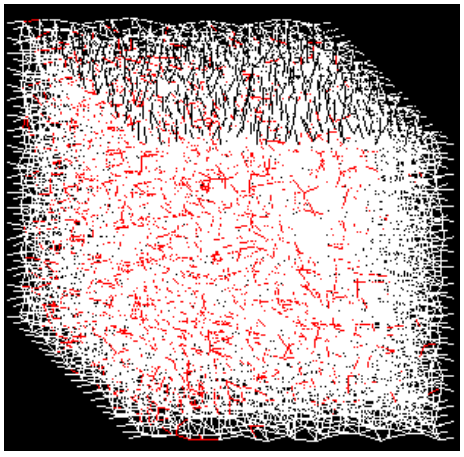

(a) $L= 16.65\ \mu m$, $C_a=2.25e^{0}$

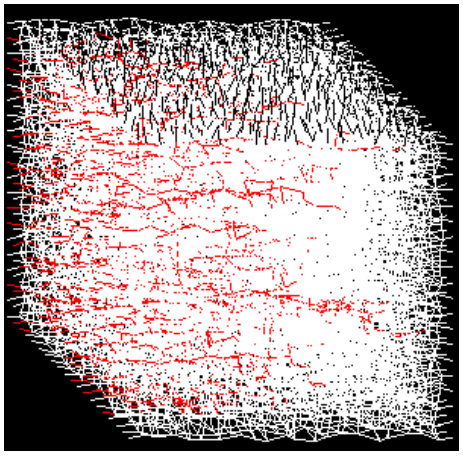

(b) $L= 333\ \mu m$, $C_a=5.64e^{-3}$

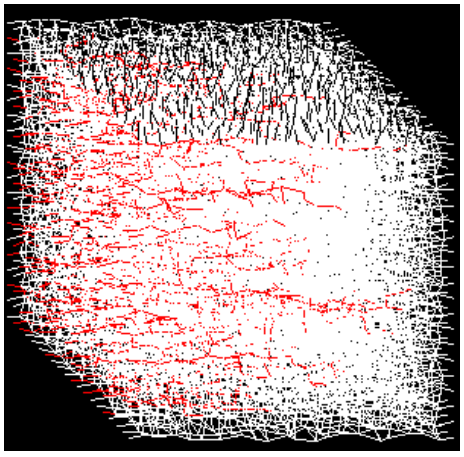

(c) $L= 999\ \mu m$, $C_a=6.26e^{-4}$

Figure 6-18 Fluid configurations of simulations with various ***pore lengths***, ***M=10.0***, ***Q=1.0e^{-5}m^3/s***.

Figures of pores filled by different phase are taken when identical amount of water (0.162PV) has been injected into each network. Red is water-filled pores, white is oil-contained pores.

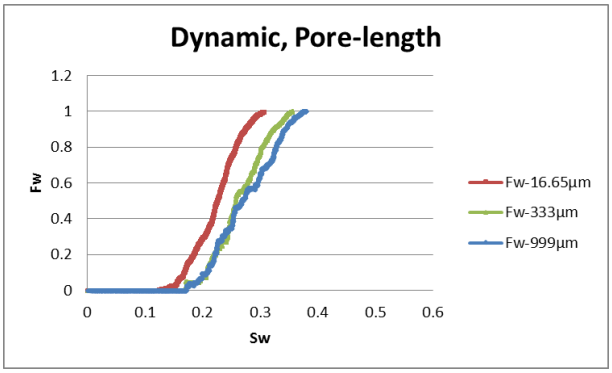

Figure 6-19 F_w-S_w curves of simulations with various ***pore lengths***, ***M=10.0***, ***Q=1.0e^{-5}m^3/s***, ***C_a=5.64e^{-3}***.

Although pore length cannot affect the quasi-static RP results, it *does* have an influence on the dynamic relative permeabilities through its effect on the local switch. Note the differences between USS models are mostly shown in oil permeability because *increasing pore length will reduce the degree of snap-off* – resulting in less trapped oil and better oil recovery (Figure 6-20).

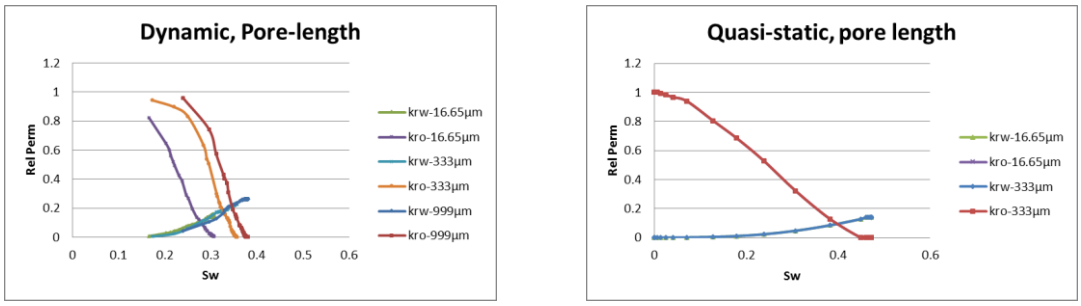

(a) Dynamic (b) Quasi-static

Figure 6-20 Relative permeability curves of simulations with various ***pore lengths***, in dynamic model, ***Q=1.0e^{-5}m^3/s***, ***M=10.0***.

6.2.5 Interfacial Tension, IFT

In the intermediate-rate models, higher IFT can slightly favour the effect of film swelling and snap-off in a given case (by increasing P_c and λ) (Figure 6-21 and Figure 6-22). In high-rate and low-rate floods, where the dominant force is viscous force and

capillary force respectively, IFT hardly has any influence (as explained in Section 5.5.4). With the same injection rate ($Q=1.0e^{-6}m^3/s$), the capillary numbers for IFT levels of $\sigma=5.0e^{-3}N/m$ and $\sigma=40.0e^{-3}N/m$ systems are $4.51e^{-3}$ and $5.64e^{-4}$, respectively.

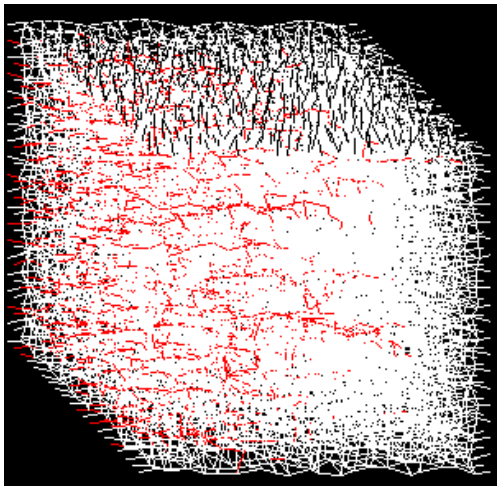

(a) σ =5.0e^{-3}N/m

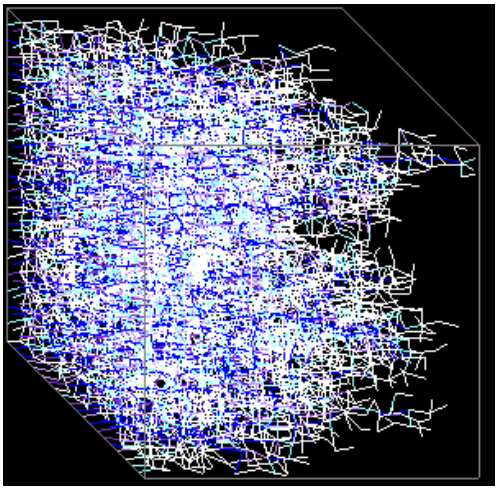

(b) σ =5.0e^{-3}N/m, S_w map

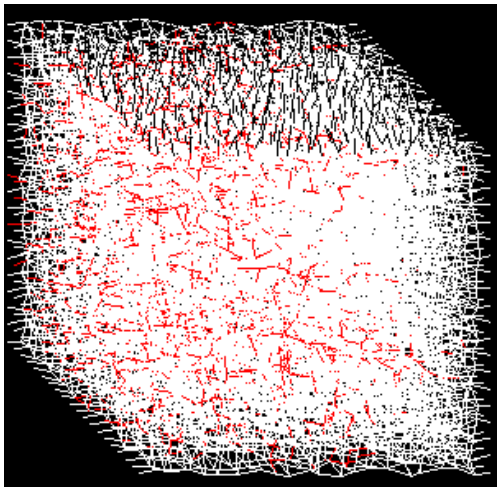

(c) σ =40.0e^{-3}N/m

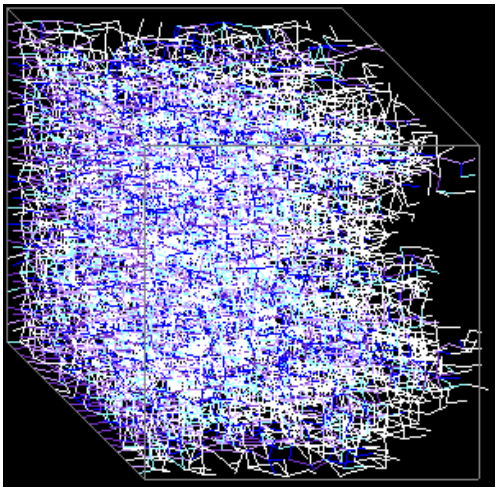

(d) σ =40.0e^{-3}N/m, S_w map

Figure 6-21 Fluid configurations of simulations with various ***IFT***, ***$Q=1.0e^{-6}m^3/s$***, ***$M=10.0$***.

(a) and (c) are figures of pores filled by different phases, which are taken when identical amount of water (0.162PV) has been injected into each network. Red is water-filled pores, white is oil-containing pores. (b) and (d) are corresponding local water saturation map.

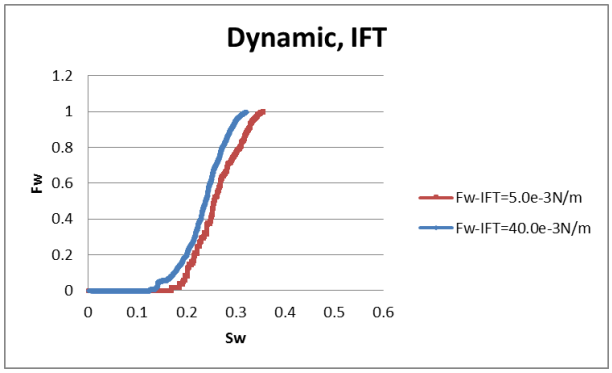

Figure 6-22 F_w-S_w curves of simulations with various ***IFT***, ***Q=1.0e^{-6}m^3/s***, ***M=10.0***.

The influence of water/oil interfacial tension is applied uniformly in each pore in a quasi-static model, and thus no alteration of the pore filling pattern can be observed. While the different k_{ro} curve in Figure 6-23(a) is due to the balance shifting between the two dominant forces in the dynamic network.

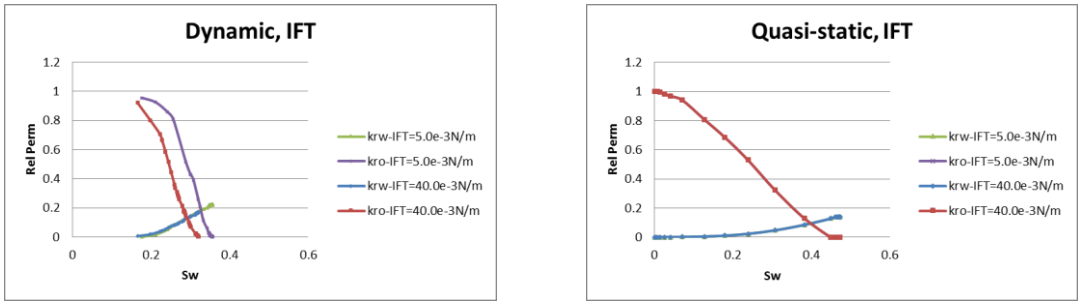

(a) Dynamic (b) Quasi-static

Figure 6-23 Relative permeability curves of simulations with various ***IFT***, in dynamic model, ***Q=1.0e^{-6}m^3/s***, ***M=10.0***.

6.2.6 Pore Shape

The comparison between equilateral triangular pores and scalene triangular pores is non-monotonic, as discussed in Section 5.5.5. Compared with an equilateral-triangular pore, the competition between a higher switch value (more snap-off) and less active wetting film determines the filling result in a scalene-triangular pore (Figure 6-24 to Figure 6-26).

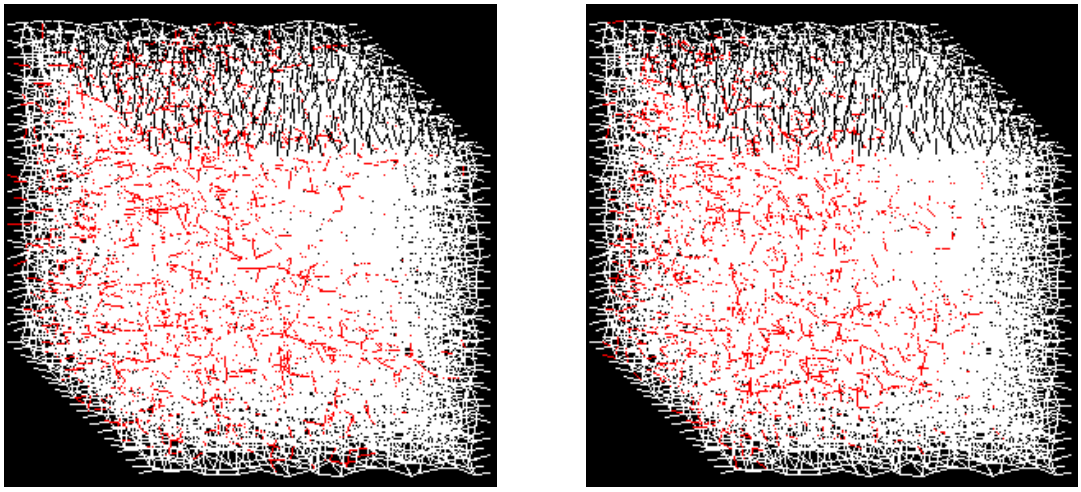

(a) equilateral-triangle (b) scalene-triangle

Figure 6-24 Fluid configurations of simulations with various ***pore shapes***, ***Q=1.0e^{-6}m^3/s***, ***Ca=5.64e^{-4}***, ***M=10.0***.

Figures of pores filled by different phases are taken when each network has the same water saturation (S_w=0.162). Red is water-filled pores, white is oil-containing pores.

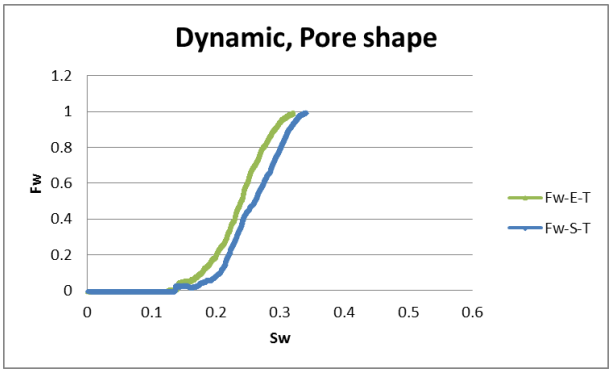

Figure 6-25 F_w-S_w curves of simulations with various ***pore shapes***, ***Q=1.0e^{-6}m^3/s***, ***Ca=5.64e^{-4}***, ***M=10.0***.

In a quasi-static model, the shifting of RP curves in systems with various pore shapes is mainly because films in each pore shape has a different ability to swell and affect local water saturation. Hence, E-T pores have less water saturation change in water imbibition (Figure 6-26 (b)).

In dynamic models, however, snap-off is completely impossible in circular pores and purely piston-like displacements can occur and this reduces the level of oil-trapping maximally, hence resulting in the best oil recovery (Figure 6-26 (a)).

As for the comparison between pores which have equilateral-triangle and scalene-triangle pore geometries, the tendency remains the same in quasi-static and dynamic models. The scalene triangle has a larger corner area which can accommodate more

water as wetting films (Figure 6-26). However, note that the difference here is obtained at certain conditions of flow rate and viscosity ratio and, for other conditions, it may be reversed. At high rates, the effect of a larger switch may overcome the slower film (through larger S_1) and generate more sparse water-filled clusters in the S-T system than in E-T system, which will reduce the corresponding oil relative permeability.

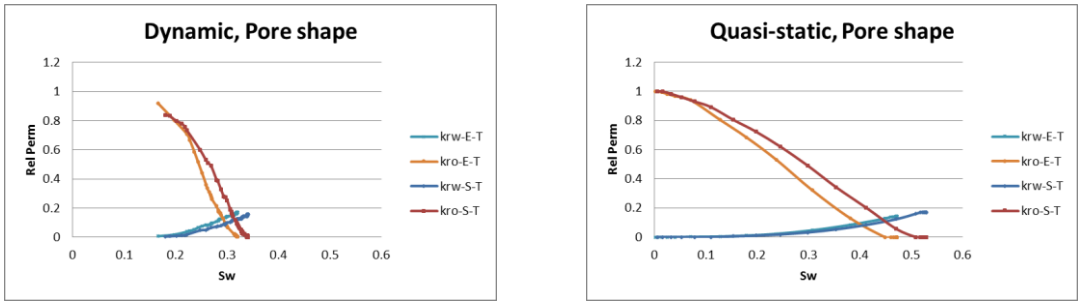

(a) Dynamic (b) Quasi-static

Figure 6-26 Relative permeability curves of simulations with various ***pore shapes***, in dynamic model, ***Q=1.0e^{-6}m^3/s***, ***M=10.0***.

6.2.7 Contact Angle

Increasing contact angle has two opposing influences: a lower λ, which will lead to more piston-like displacements, and also wetting films with higher mobility, which means more swelling and snap-off. Thus the filling pattern of each specific case is the result of this competition. Also, in systems with equilateral triangular pores, once the contact angle exceeds 60^o, pores can no longer accommodate wetting films and bulk displacement will become the only mechanism possible (Figure 6-27 and Figure 6-28). Contact angle has no effect on capillary number, with different contact angle cases at the same injection rate ($Q=1.0e^{-5}m^3/s$) having the same capillary number, $C_a=5.64e^{-3}$.

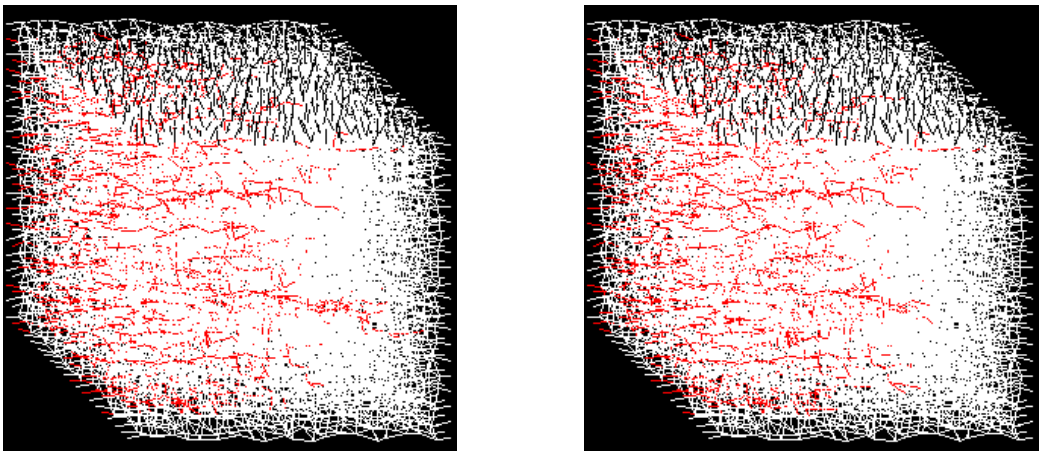

(a) $\theta = 0^o$ (b) $\theta = 30^o$

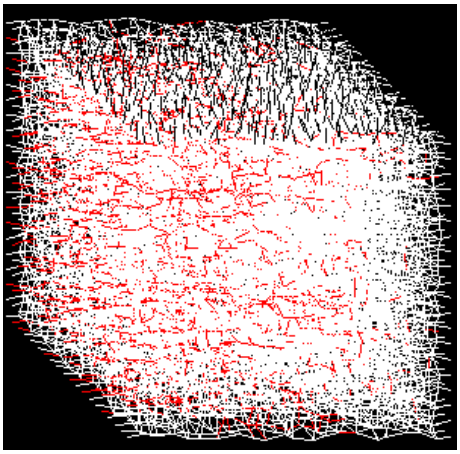

(c) $\theta = 50^o$

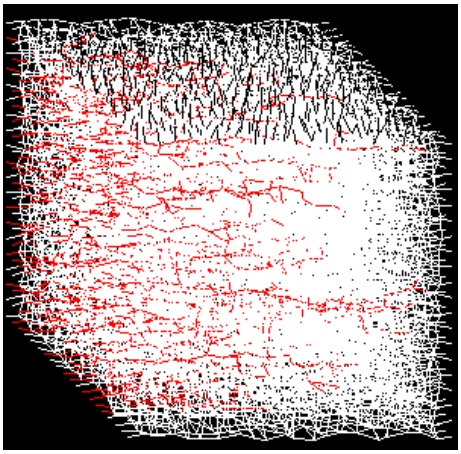

(d) $\theta = 60^o$

Figure 6-27 Fluid configurations of simulations with constant or distributed ***contact angles***, ***M=10.0***, ***Q=1.0e^{-5}m^3/s***.

Figures of pores filled by different phases are taken when identical amount of water (0.162PV) has been injected into each network. Red is water-filled pores, white is oil-contained pores.

Figure 6-28 shows the water fractional flow curves of each case and the corresponding relative permeability curves are shown in Figure 6-29.

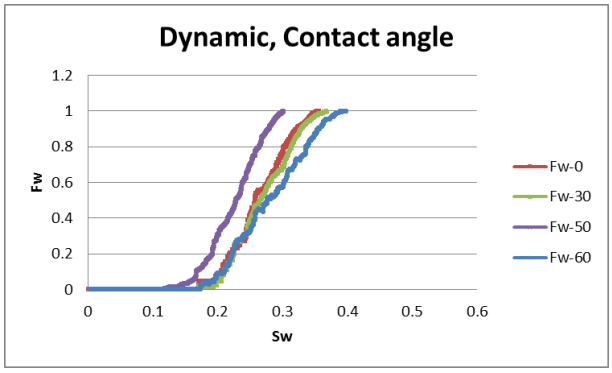

Figure 6-28 F_w-S_w curves of simulations with constant or distributed ***contact angles***, ***Q=1.0e^{-5}m^3/s***, ***M=10.0***.

In the quasi-static model, there is no local switch to simulate the competition between bulk displacement and snap-off. As θ increases, RP curves are expected to move to the left since at the same radius level, pores with higher contact angle have less water in their corners. Also, with higher contact angle, the contrast between capillary entry pressures of piston-like displacement and snap-off will be expanded (as seen in Figure 3-35 (b)), and therefore less snap-off events can be expected. And to be compared with the corresponding dynamic simulation, snap-off is not allowed in the quasi-static $\theta=60^o$ case. While if θ increases in the dynamic model, due to the opposing effect of

decreasing λ (more bulk) and smaller S_1 (more film), snap-off will be suppressed partially in $\theta=30^o$ case and completely if $\theta>60^o$, but be encouraged when the contact angle is approaching the critical 60^o. As the result of different pore-filling mechanism, suppressed snap-off is associated with better oil recovery (due to less oil trapping), and vice versa (as seen in Figure 6-29).

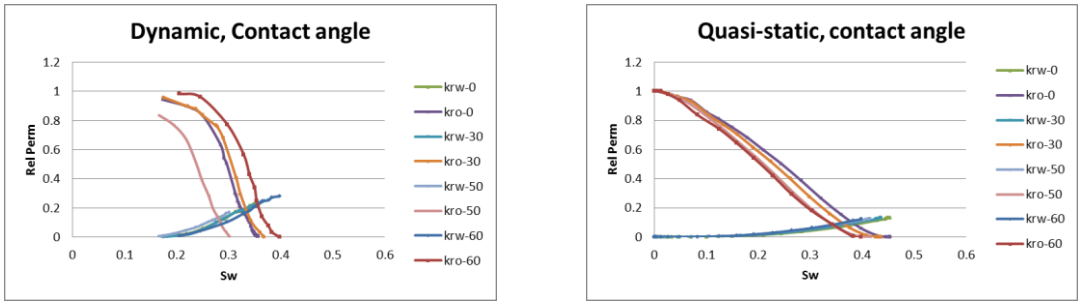

(a) Dynamic (b) Quasi-static

Figure 6-29 Relative permeability curves of simulations with various ***contact angles***, in dynamic model, ***Q=1.0e^{-5}m^3/s***, ***M=10.0***.

In comparison with the $\theta=60^o$ cases, in which only piston-like displacement is possible, film swelling and snap-off are possible in the $\theta\in[0^o,89.9^o]$ simulations (Figure 6-30, see also Figure 5-67). However, when $\theta\in[0^o,89.9^o]$, the comparison between water saturation maps of 2-D and 3-D simulations shows that higher level of film swelling can be found in the 3-D network: there are more pores with lower S_w (coloured by white or light blue) in Figure 6-30 (d) than in Figure 6-30 (b). Based on the local flow direction, a particular pore can have at most 3 and 5 downstream neighbours in 2D and 3D networks respectively – more downstream neighbours in 3D network provide more possible paths for the wetting films within (if exist) and therefore reduce the extent of film trapping.

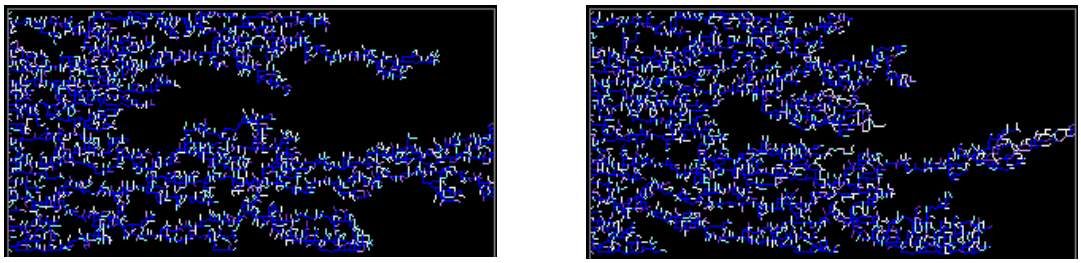

(a) 2-D, $Q=1.0e^{-8}m^3/s$, $\theta=60^o$ (b) 2-D, $Q=1.0e^{-8}m^3/s$, $\theta\in[0^o,89.9^o]$

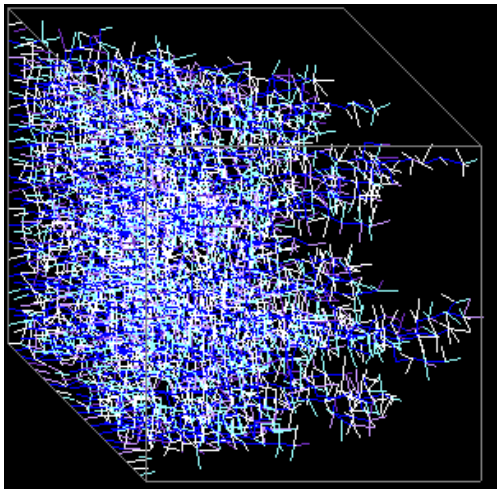

(c) 3-D, $Q=1.0e^{-5}m^3/s$, $\theta = 60^o$

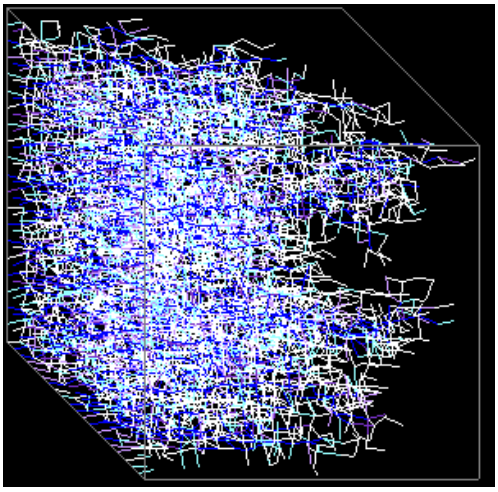

(d) 3-D, $Q=1.0e^{-5}m^3/s$, $\theta \in [0^o, 89.9^o]$

Figure 6-30 Comparisons between simulations with $\theta = 60^o$ and $\theta \in [0^o, 89.9^o]$, ***M=10.0***. 2D figures ((a) and (b)) are taken when 0.256PV of water has been injected into each network. 3D figures ((c) and (d)) are taken when 0.162PV of water has been injected into each network.

Furthermore, for scalene triangular pore systems, the distributed contact angles within [0°, 30°] and constant 30° contact angle can both reduce the level of snap-off, while when contact angle increases to θ =50°, the increasing wetting film conductance will help the snap-off process to occur, which results in the formation of more scattered water clusters.

Comparing the filling results and relative permeability curves with those of equilateral triangular pore system, the scalene triangle cases tend to have more film-swelling and snap-off (earlier breakthrough and lower oil production) (Figure 6-31 and Figure 6-32). Except for the case when the contact angle is 50°, the equilateral triangle has faster advancing wetting films helped by the high water conductance. In contrast, scalene triangular pores, due to the distributed half angles, will have a more balanced competition between the lower local switch (piston-like displacement) and higher film conductance (snap-off) as contact angle increases (Figure 6-31 (e), (f); and Figure 6-32 (b)). Generally speaking, the equilateral triangle system is more sensitive to the contact angle alteration.

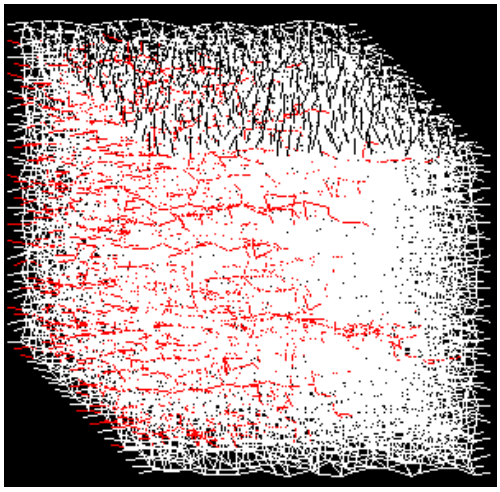

(a) E-T, $\theta = 0^o$

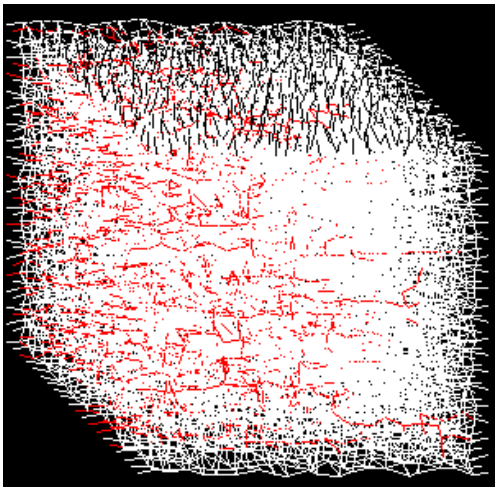

(b) S-T, $\theta = 0^o$

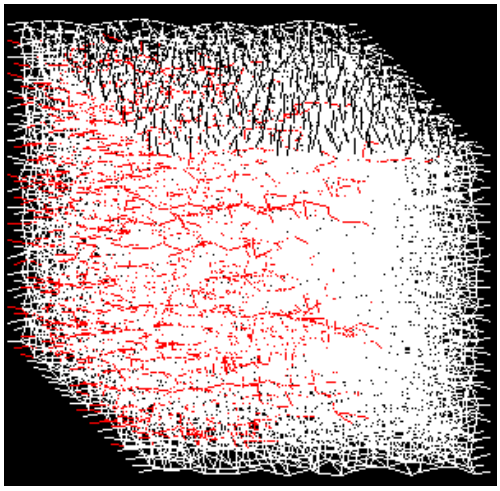

(c) E-T, $\theta = 30^o$

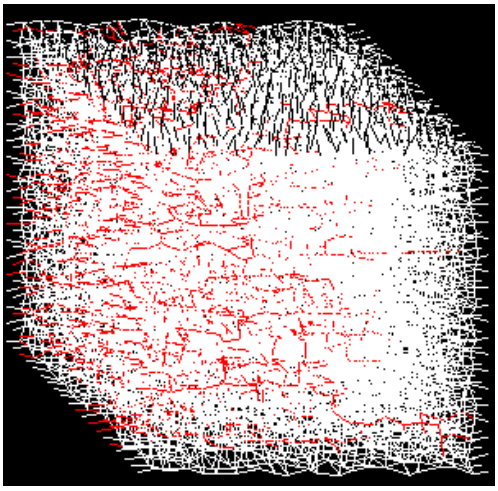

(d) S-T, $\theta = 30^o$

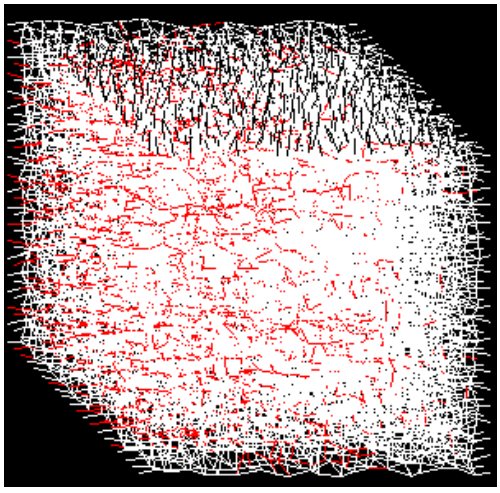

(e) E-T, $\theta = 50^o$

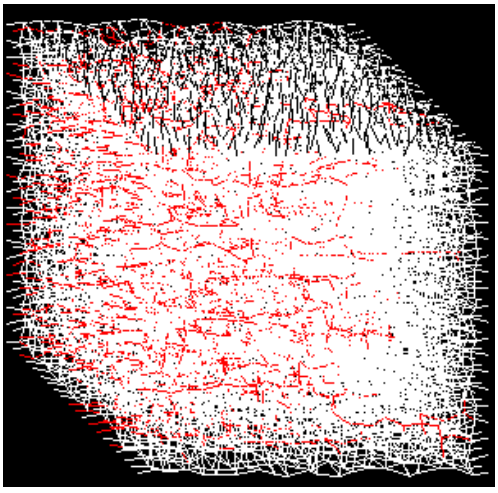

(f) S-T, $\theta = 50^o$

Figure 6-31 Fluid configurations of simulations with constant or distributed contact angle, equilateral or scalene triangular pore, $\boldsymbol{Q=1.0e^{-5}m^3/s}$, $\boldsymbol{M=10.0}$.

Figures of pores filled by different phases are taken when identical amount of water (0.162PV) has been injected into each network. Red is water-filled pores, white is oil-containing pores.

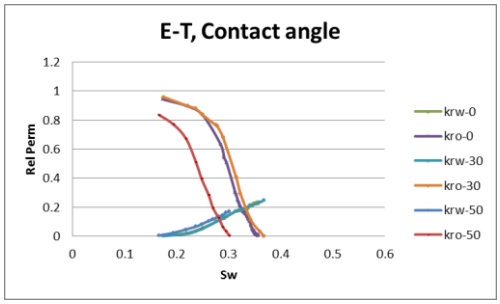

(a) E-T

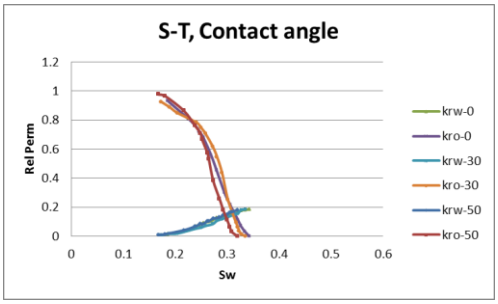

(b) S-T

Figure 6-32 Relative permeability curves of simulations with constant or distributed contact angle, scalene triangular pores, ***Q=1.0e^{-5}m^3/s***, ***M=10.0***.

6.2.8 The Resistance Factor of Solid, C_w

The resistance factor of the solid, C_w, affects the wetting film conductance since an increasing C_w will reduce the wetting film mobility and the extent of snap-off (Figure 6-33 to Figure 6-34).

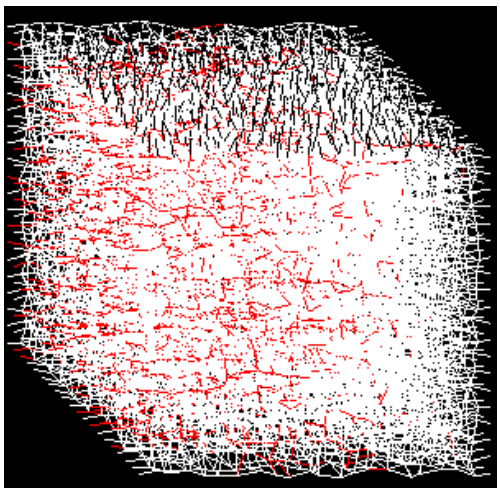

(a) C_w= *10*

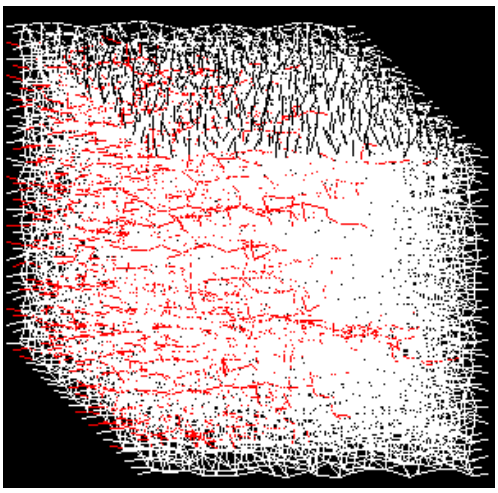

(b) C_w= *100*

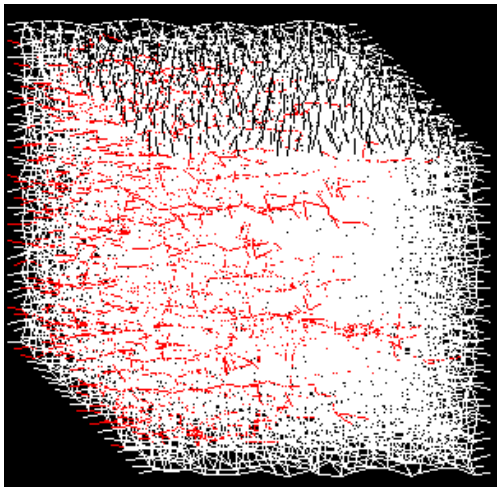

(c) C_w= *2000*

Figure 6-33 Fluid configurations of simulations with various C_w, $Q=1.0e^{-5}m^3/s$, $C_a=5.64e^{-3}$, $M=10.0$.

Figures of pores filled by different phases are taken when identical amount of water (0.162PV) has been injected into each network. Red is water-filled pores, white is oil-containing pores.

We can see that C_w hardly affects the quasi-static k_{ro} and reduces the k_{rw} slightly as it increases. However, in the dynamic model, increasing C_w can clearly help the oil-phase to flow by reducing the extent of film swelling and snap-off (Figure 6-34).

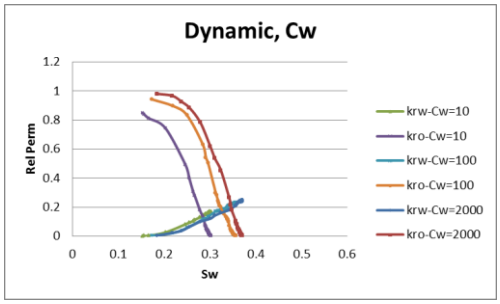

(a) Dynamic

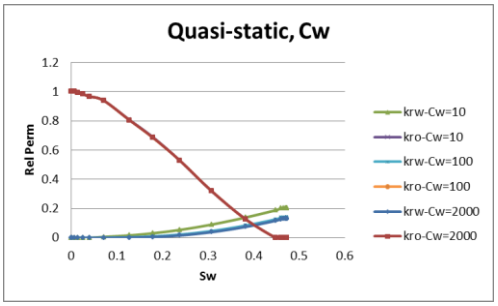

(b) Quasi-static

Figure 6-34 Relative permeability curves of simulations with various C_w, in dynamic model, $Q=1.0e^{-5}m^3/s$, $M=10.0$.

6.2.9 Initial Water, S_{wi}

Initial wetting films can provide the invading, less viscous, water phase a better pathway through the network, which can enable the smaller pores far from the water front to snap-off. Furthermore, the initially water-filled pores can work as "nuclei" for the formation of discrete clusters of water-filled pores, which may in turn alter the distribution of the subsequent incoming water (while still requiring a sufficient water

supply) (as can be seen in Figure 5-79 and Figure 5-83). However, the initially present water-filled pores will cause more oil trapping and limit the oil relative permeabilities (Figure 6-35 to Figure 6-37).

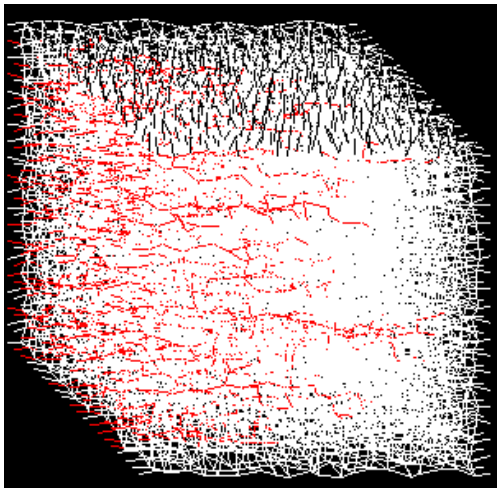

(a) no initial water

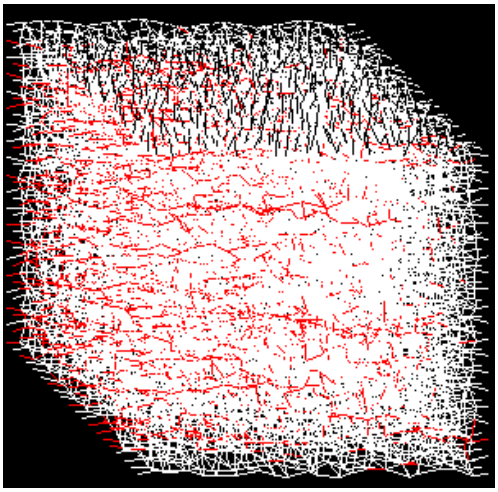

(b) S_{wi}=0.001

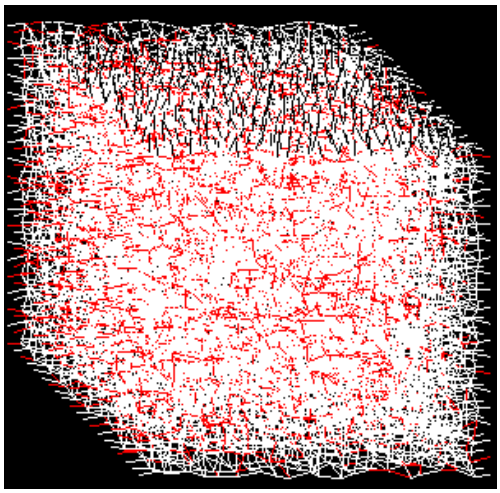

(c) S_{wi}=0.005

Figure 6-35 Fluid configurations of simulations with various $\boldsymbol{S_{wi}}$, $\boldsymbol{Q=1.0e^{-3}m^3/s}$, $\boldsymbol{M=10.0}$.

Figures of pores filled by different phases are taken when identical amount of water (0.162PV) has been injected into each network. Red is water-filled pores, white is oil-containing pores.

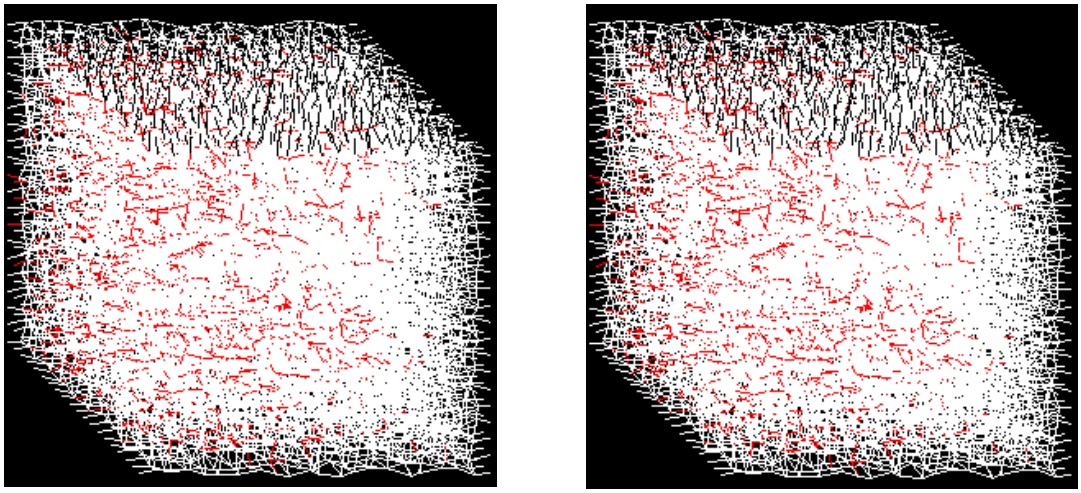

(a) no initial water (b) thin film

(c) S_{wi}=0.001 (d) S_{wi}=0.005

Figure 6-36 Fluid configurations of simulations with various $\boldsymbol{S_{wi}}$, $\boldsymbol{Q=1.0e^{-6}m^3/s}$, $\boldsymbol{M=10.0}$.

Figures of pores filled by different phases are taken when identical amount of water (0.162PV) has been injected into each network. Red is water-filled pores, white is oil-containing pores.

Note that the initial water saturation in the network cannot cause any differences between quasi-static RP curves (except for the starting S_w). But it *can* affect the dynamic relative permeabilities by providing the invading water better pathways and result in higher k_{rw}. In the cases with initial water-*filled* pores, the formation of discrete clusters of water-filled pores (in high-rate cases) and snap-off (in low-rate cases) in regions near the system outlet (as indicated by Figure 5-79 and Figure 5-83) can result in more oil-trapping, hence the reduced k_{ro} and S_{or}.

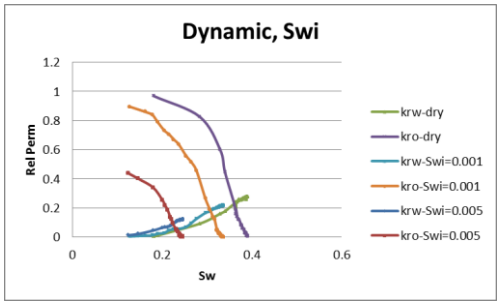

(a) Dynamic- $Q=1.0e^{-3}m^3/s$

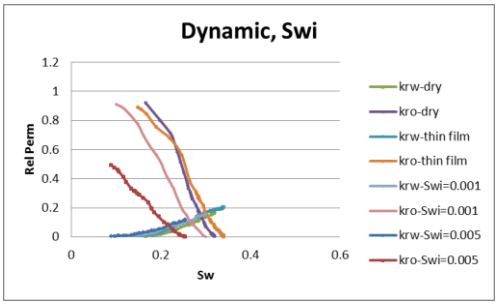

(b) Dynamic- $Q=1.0e^{-6}m^3/s$

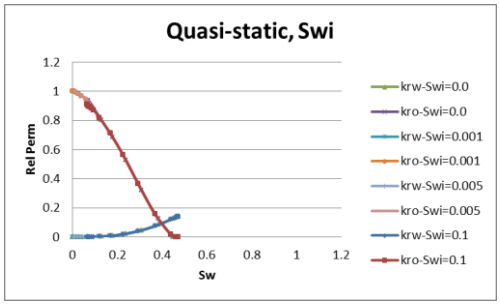

(c) Quasi-static

Figure 6-37 Relative permeability curves of simulations with various $\boldsymbol{S_{wi}}$, in dynamic model, ***M=10.0***.

In the extremely low-rate case with favourable viscosity ratio (*M=0.1*), the wetting film that is present in the network can connect the open pores and, as a result, the long thin fingers predicted originally (because of suppressed counter-current flow) in completely dry systems are absent (Figure 6-38).

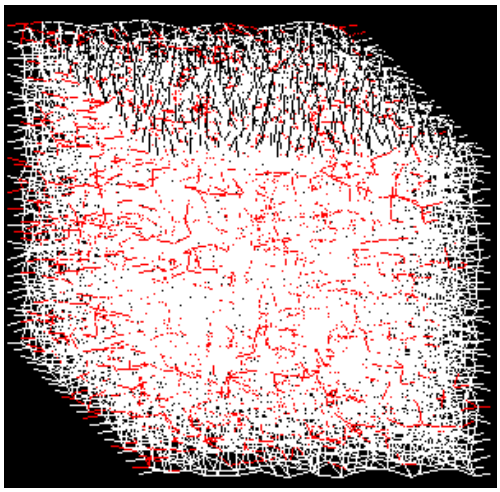

(a) no initial water

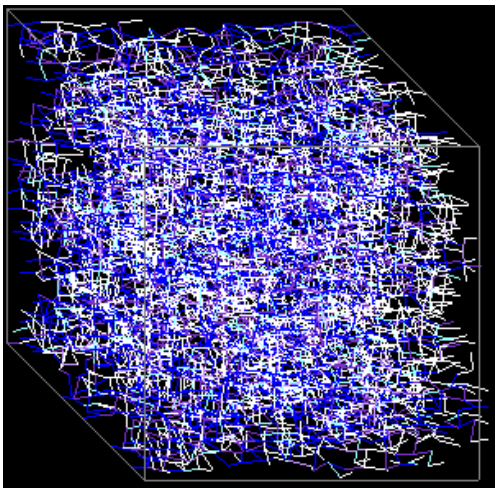

(b) no initial water, S_w map

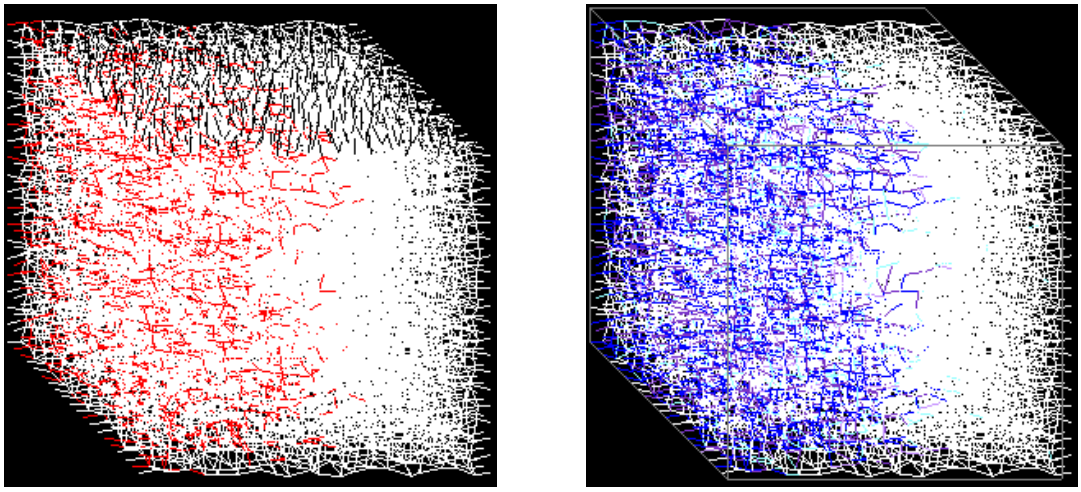

(c) thin film (d) thin film, S_w map

Figure 6-38 Fluid configurations of simulations with various S_{wi}, $Q=1.0e^{-7}m^3/s$, $M=0.1$. (a) and (b) are figures of pores filled by different phases, which are taken when identical amount of water (0.162PV) has been injected into each network. Red is water-filled pores, white is oil-containing pores. (i)-(ii) are figures of corresponding local water saturation map.

Very significant differences in water fractional curves and relative permeabilities are observed (Figure 6-39 and Figure 6-40).

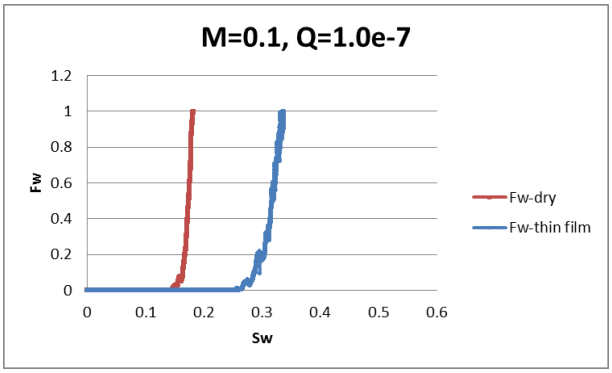

Figure 6-39 F_w-S_w curves of simulations with various S_{wi}, $Q=1.0e^{-7}m^3/s$, $M=0.1$.

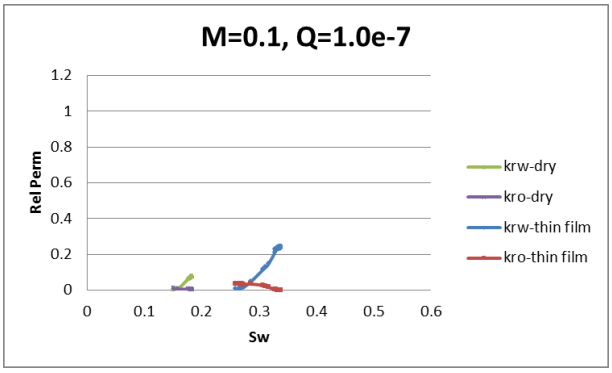

Figure 6-40 Relative permeability curves of simulations with various S_{wi}, $Q=1.0e^{-7}m^3/s$, $M=0.1$.

6.2.10 Coordination Number, Z

As discussed in the context of the 2-D model, coordination number, Z, cannot affect the competition between the dominant forces or primary filling mechanisms. Thus, at the same injection rate and viscosity ratio, the results will be within the same regimes as their corresponding fully-connected counterparts.

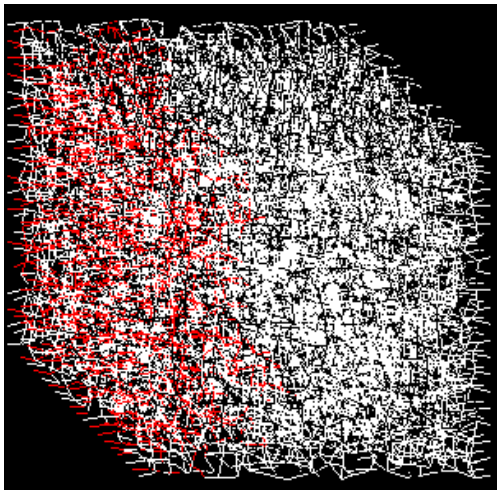

(a) $M=0.1$, $Q=1.0e^{-3}m^3/s$

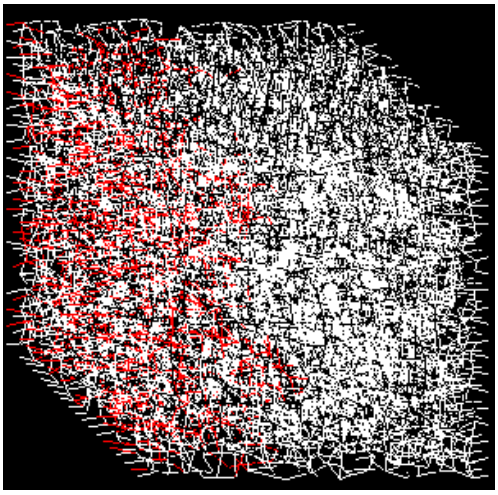

(b) $M=0.1$, $Q=1.0e^{-6}m^3/s$

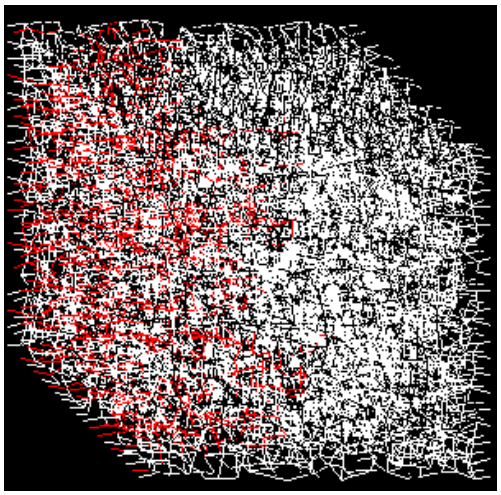

(c) $M=1.0$, $Q=1.0e^{-3}m^3/s$

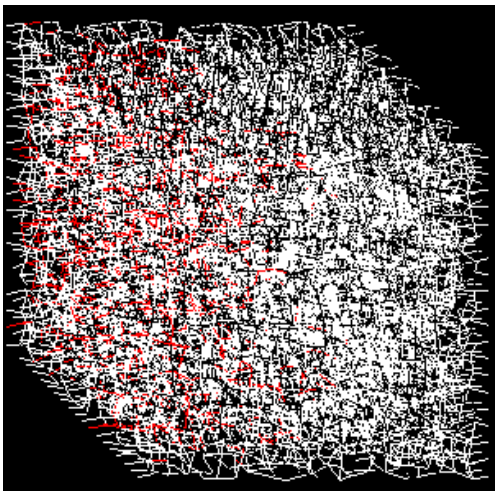

(d) $M=1.0$, $Q=1.0e^{-6}m^3/s$

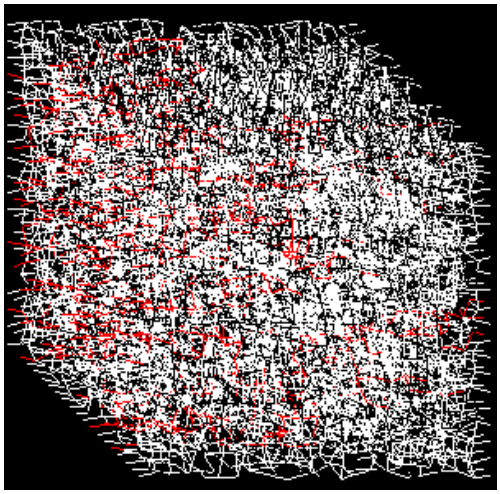

(e) *M=10.0, Q=1.0e^{-3}m^3/s*

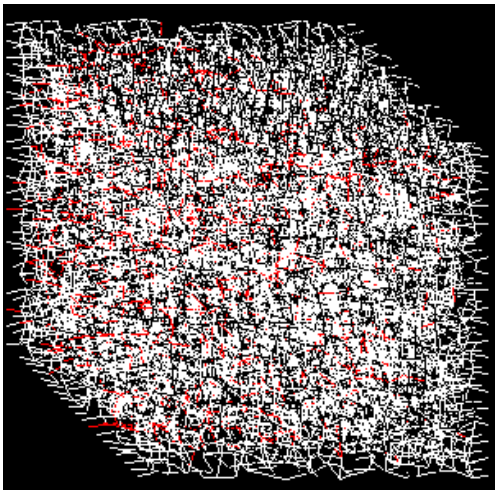

(f) *M=10.0, Q=1.0e^{-6}m^3/s*

Figure 6-41 Fluid configurations of simulations with ***Z=4***.

Figures of pores filled by different phases are taken when identical amount of water (0.162PV) has been injected into each network. Red is water-filled pores, white is oil-containing pores.

In high-rate floods, where piston-like displacement is the main filling mechanism, the water paths that are possible will be reduced in less connected networks. This will result in more severe oil-trapping and lower oil recovery (which is consistent with the quasi-static results). In low-rate floods, however, the situation may be reversed, where a lower coordination number also breaks the connectivity of the wetting films, thus making it more difficult for them to snap-off. Hence, in low rate cases, relatively more piston-like displacements may occur for coordination number Z=4 models and this may actually result in a better oil recovery (Figure 6-42).

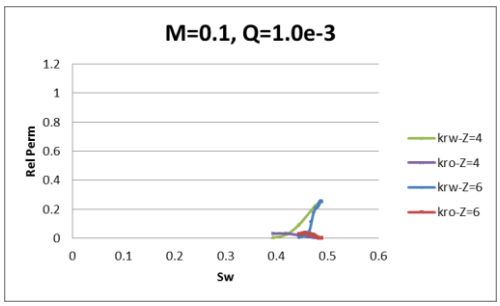

(a) *M=0.1, Q=1.0e^{-3}m^3/s*

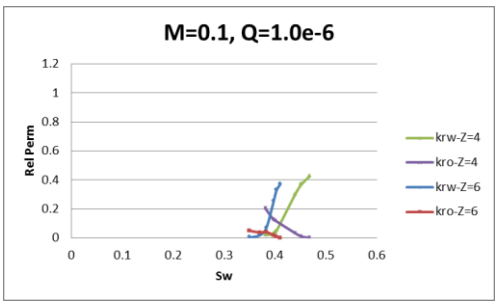

(b) *M=0.1, Q=1.0e^{-6}m^3/s*

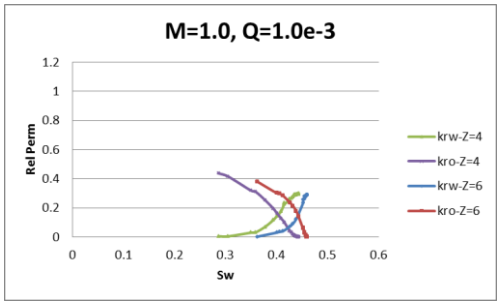

(c) *M=1.0, Q=1.0e^{-3}m^3/s*

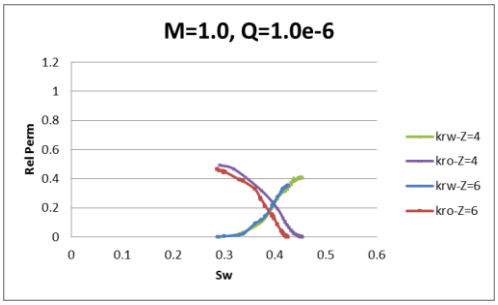

(d) *M=1.0, Q=1.0e^{-6}m^3/s*

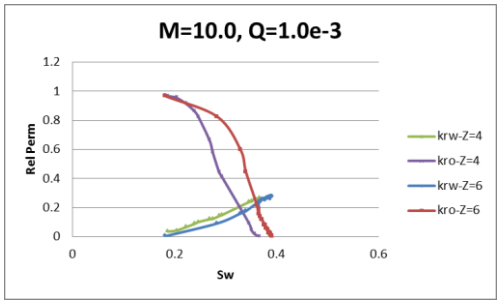

(e) *M=10.0, Q=1.0e^{-3}m^3/s*

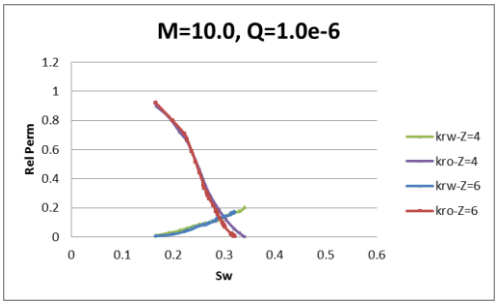

(f) *M=10.0, Q=1.0e^{-6}m^3/s*

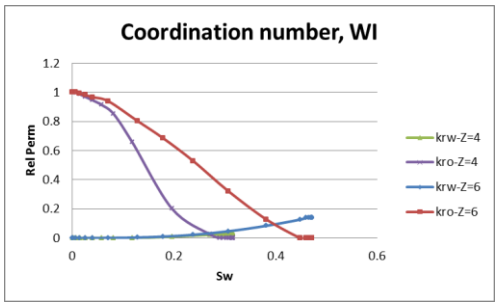

(g) quasi-static

Figure 6-42 Relative permeability curves of simulations with ***Z=4***.

6.3 Attempts to Explain the Differences between RPs of Quasi-static and Dynamic Models

From above parametric sensitivity studies, it is clear that the quasi-static and dynamic models have different sensitivities to the flow rate and viscosity ratio. And the differences between SS and USS RPs are obvious.

Sorbie and Salino (2009) identified the clear case when there would be no difference between SS and USS RPs: only purely viscous forces were present (no capillarity) and the system was 1D and homogeneous, *viz.* all the Buckley-Leverett assumptions were satisfied. However, these assumptions can be easily violated in low-rate floods (which are capillary forces dominated) and high-rate, *M=10.0* cases (due to the viscous fingering effect). Therefore, the observed difference between relative permeabilities of quasi-static model and dynamic model can be partially explained.

To avoid the issues discussed above, our model is also able to record the global fluids configuration at one particular instant and use this information to obtain the associating quasi-static relative permeabilities by conducting the *Quasi-Static* model on this distribution (see Section 3.1.6). By iterating this process, a set of quasi-static RP curves which represent the dynamic filling regimes can be obtained. In attempt to mimic the quasi-static simulation, below simulations are started with initial wetting films characterised by $P_{c,max}$ at the end of primary drainage. To eliminate the capillary end effect, similar as the actual relative permeability experiments (as seen in Figure 6-43), we only conduct the quasi-static RP calculations on the middle section (Figure 6-44). And by running the quasi-static model on the identical middle section, relative permeabilities of the quasi-static displacement can also be obtained (Figure 6-45 (d)) and compared with the corresponding USS RPs (Figure 6-45 (a)-(c)).

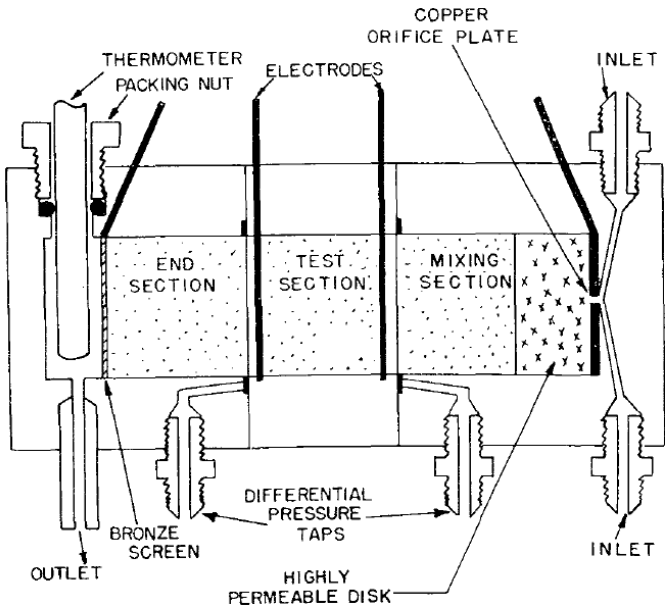

Figure 6-43 Three-section core assembly in relative permeability experiment (as seen in Geffen, et al. (1951)).

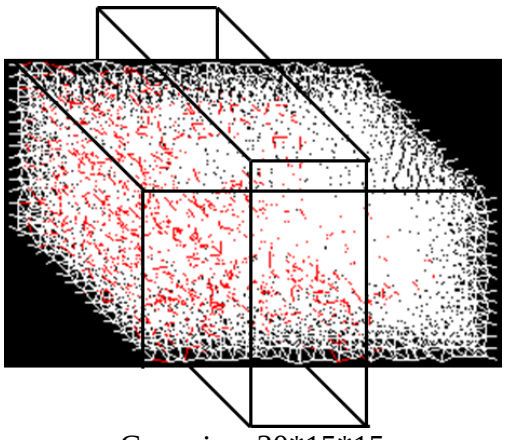

Core size: 30*15*15

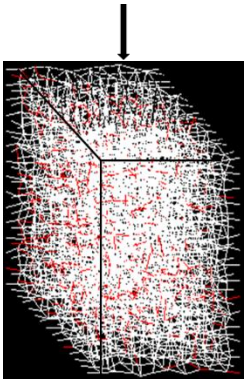

Section size: 10*15*15

Figure 6-44 Illustration of the selection of the middle section.

Although the high-rate dynamic models with *M=0.1* and *M=1.0* are free from the capillary end effect and viscous fingering effect, their obtained RPs (Figure 6-45 (a), (b)) are still different from the relative permeabilities of quasi-static model (Figure 6-45 (d)). This can be explained by the presence of stable water front in dynamic simulations: stable water front will cut off the communication of bulk oil with the system inlet at the early stage of displacement, therefore the low k_{ro} at low S_w. And before water breakthrough, without water flowing out of the system, k_{rw} will remain 0.0. Note even in the low-rate cases, influence of water front can still be observed.

In systems with unfavourable viscosity ratio (*M=10.0*), flow regimes like viscous fingering (high rate) and high level of film swelling/snap-off (low rate) result in early water breakthrough and a prolonged period of two-phase flow at the system outlet. Consequently, quasi-static relative permeabilities of the *M=10.0* case (Figure 6-45 (c)) are more similar to the RPs shown in Figure 6-45 (d). Comparison between Figure 6-45 (c) and (d) shows the same behaviours like those observed by Maini et al.(1990)): quasi-static oil relative permeabilities are generally higher than the dynamic k_{ro}, while water relative permeabilities are in the same range as those obtained in dynamic displacements.

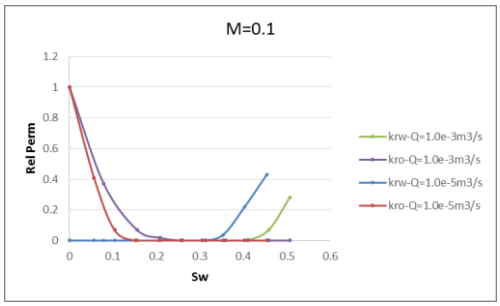

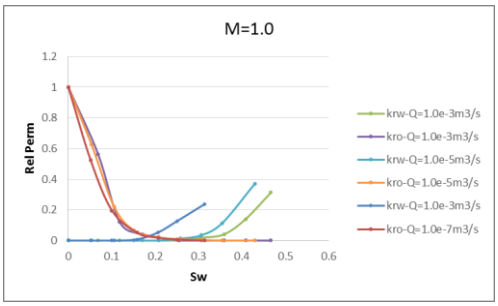

(a) *M=0.1* (b) *M=1.0*

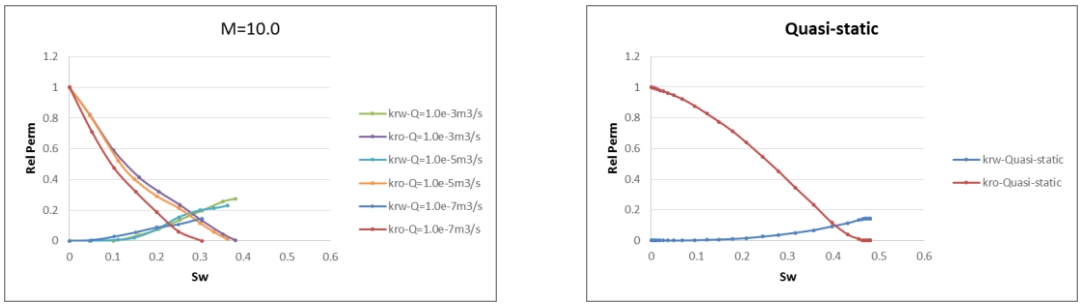

(c) *M=10.0* (d) Quasi-static model

Figure 6-45 Quasi-static relative permeabilities of the dynamic displacements (a)-(c) and relative permeabilities of the quasi-static model (d).

From Figure 6-45, it can be concluded that the technique to obtain relative permeabilities is not the only source of the observed differences between RPs of the quasi-static and dynamic models. Their filling regimes are essentially different from each other. Figure 6-46 shows the schematics of various displacement regimes: (a) quasi-static model of both snap-off and piston-like displacement, (b) quasi-static model with only snap-off, (c) stable displacement in dynamic model, (d) viscous fingering in dynamic model, and (e) film-swelling and snap-off in dynamic model. 2D simulations are compared here to emphasize the differences between various filling regimes. Note in Figure 6-46, count of red pores is not necessarily correlated to S_w, that is because (1) red only represents the water-filled pores, there is still water residing in other partial-filled (white) pores as wetting films or bulk water (Table 4-3 C-I); and (2) specific pore volume has to be taken into account in the calculation of water saturation. Also note that the 2D quasi-static simulation, unlike the 3D SS case, have more residual oil than the corresponding dynamic cases – oil is more easily trapped in the 2D network due to the snap-off near the system outlet.

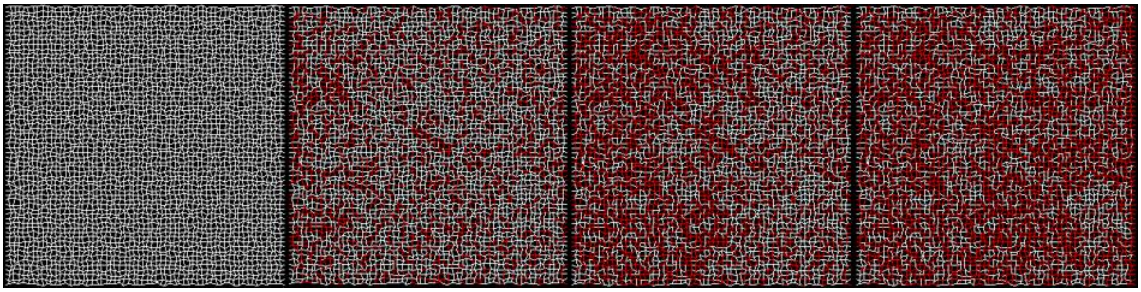

S_w=0.00027 S_w=0.089 S_w=0.178 S_w=0.242

(a) Quasi-static model – both piston-like displacement and snap-off

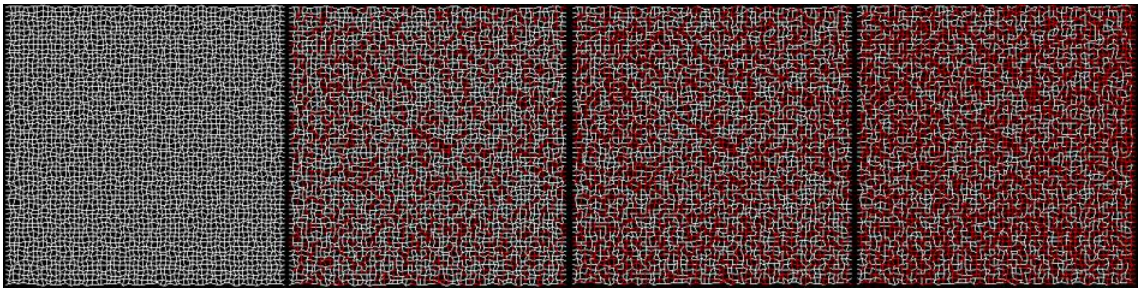

S_w=0.00027 S_w=0.089 S_w=0.178 S_w=0.264

(b) Quasi-static model – snap-off only

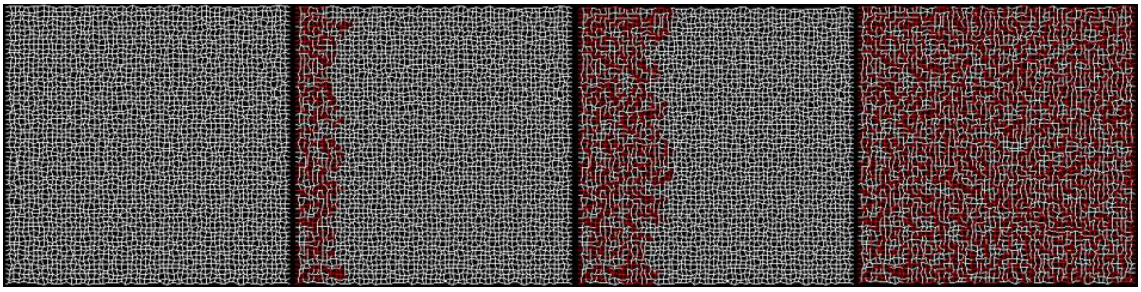

S_w=0.00027 S_w=0.089 S_w=0.178 S_w=0.596

(c) Dynamic model – stable displacement

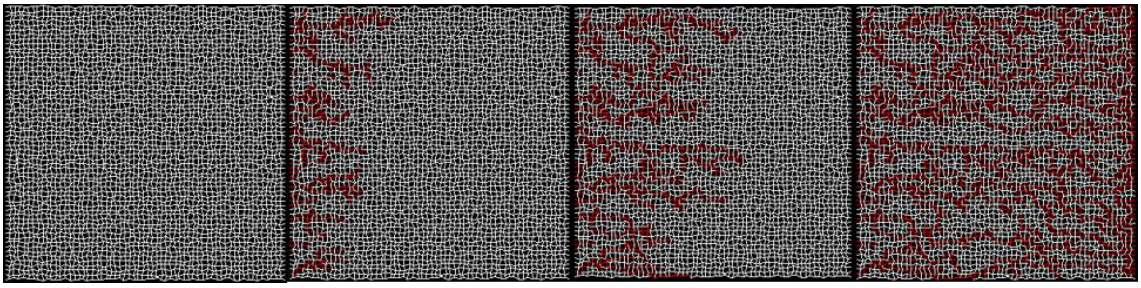

S_w=0.00027 S_w=0.089 S_w=0.178 S_w=0.419

(d) Dynamic model – viscous fingering

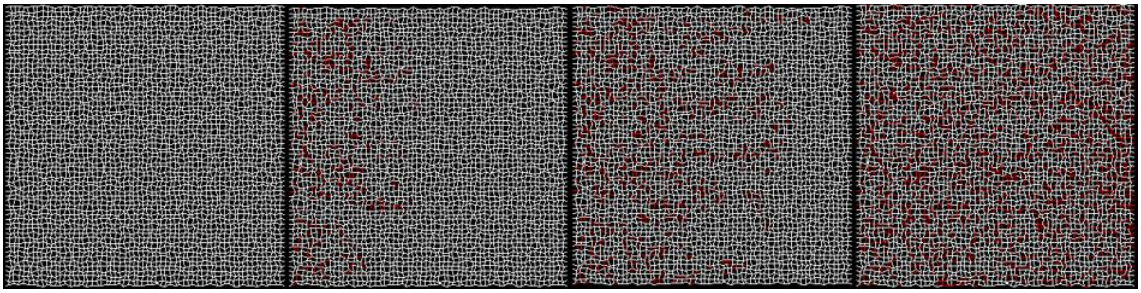

S_w=0.00027 S_w=0.089 S_w=0.178 S_w=0.367

(e) Dynamic model – film swelling and snap-off

Figure 6-46 Schematic of different displacement regimes:

(a) quasi-static model of both snap-off and piston-like displacement, (b) quasi-static model with only snap-off, (c) stable displacement in the dynamic model (high rate, *M=0.1*), (d) viscous fingering in the dynamic model (high rate, *M=10.0*), and (e) film-

swelling and snap-off in the dynamic model (low rate, *M=10.0*). Red represents water-filled pores and white represents pores containing oil.

In quasi-static model, as shown in Figure 6-46 (a) and (b), snap-off can occur everywhere throughout the network, providing the local capillary entry pressure and oil trapping status are suitable. The quasi-static model allows the user to choose the specific filling mechanism – in Figure 6-46 (a), both piston-like displacement and snap-off are possible; while in Figure 6-46 (b), water can only displace oil through snap-off.

In dynamic simulations, however, pore-filling and film-swelling require sufficient water supply – at the beginning of displacement, invading water will preferentially displace oil near the network inlet: snap-off near the outlet is not possible (see Section 4.6). Hence clear water front can be observed in the high-rate dynamic simulations: stable water front in Figure 6-46 (c), and unstable viscous fingering in Figure 6-46 (d). At low flow-rate, although invading water spreads much further (through film swelling and snap-off) than the continuous water paths in high rate cases, filling sequence of the dynamic imbibition is still not entirely controlled by the capillary forces as in quasi-static model - different filling sequences due to the requirement of water supply can still be observed (Figure 6-46 (e)).

Furthermore, due to the limitation of present pressure solver, the dynamic model assumes that there are no mobile oil ganglia and counter-current flow. Consequently, in 3D system, more oil will be trapped in low-rate dynamic model comparing to quasi-static model. Worse still, the existence of flowing-through water after water breakthrough in dynamic simulations expands the difference between S_{or} in two models: in dynamic model, once the connected path of water from the system inlet to the outlet created, a fraction of injected water (based on the current f_w) will flow through the system without displacement. And as water fractional flow increases, the portion of flowing-through water will increase as well. While in quasi-static model, based on the invasion percolation theory, the connected water path will have no influence on the newly-injected water: untrapped oil will still be displaced in the order of increasing pore size. Therefore, comparing to the dynamic simulations, more water tends to stay in the network during the quasi-static displacement.

To conclude, the different filling regimes are due to the different model assumptions. Quasi-static model is capillary-forces dominated and based on the invasion percolation algorithm. While in dynamic model, displacement is controlled by the local

competition between capillary forces and viscous forces, as well as water supply. In fact, taking water supply into consideration, the displacing regime of quasi-static water imbibition (snap-off occurs throughout the network in the order of pore size) can never be reached by dynamic model, regardless the flow rate. Therefore, the newly proposed dynamic model cannot be validated through the comparison between a normal low-rate, capillary force dominated case and the corresponding quasi-static simulation. The reasons why the dynamic low-rate cases tend to trap more oil than the corresponding quasi-static models are explained in the previous paragraph. Once this issue is solved, the comparison between quasi-static and dynamic simulations with only piston-like displacement (e.g. in system with equilateral triangular pores and $\theta>60^o$) can be used to check the validity of dynamic model.

Although the assumptions of the Buckley-Leverett theory are often violated, this theory is still used to obtain the dynamic RPs in the parametric sensitivity research above (Section 6.2) for three reasons: (1) techniques based on Buckley-Leverett theory are widely used in unsteady-state experimental measurements of relative permeabilities. (2) Obtained RP curves can provide sufficient information for the parametric sensitivity study. And (3) the technique of obtaining SS relative permeabilities of the dynamic process introduced in this section is developed in the very late stage of this study and it is not a standard technique in real experiments. The technique of selecting middle section is a standard and effective method to eliminate the capillary end effect in the low rate dynamic simulations, and should have been applied throughout. Unfortunately, due to the limited time of this research, this technique can only be applied in the future simulations – RPs of the low rate cases may be affected accordingly.

In quasi-static model, the difference brought in by various trapping mechanisms – topology trapping (Section 3.1.5) and trapping mechanisms based on local flow direction (Section 4.8) – can be ignored. However, in dynamic model, different trapping mechanisms have important influences on relative permeabilities. The technique to obtain quasi-static relative permeabilities of the dynamic process introduced here is also useful to explore the influence of trapping mechanisms. In the process of obtaining RPs, the oil trapping status of each pore (based on the flow-direction trapping mechanism) is recorded and called directly. However, it is also possible to invoke the topology trapping mechanism during this process and re-judge the oil trapping status of each element. The resulting RP curves, comparing with the curves applying the flow-direction trapping mechanism, are shown in Figure 6-47: in

high rate model, viscous forces controls the displacement and counter-current flow can hardly be seen, various oil trapping mechanisms have negligible influence on relative permeabilities (Figure 6-47 (a)). While in low-rate simulations, some former trapped oil regains mobility based on the topology trapping, therefore the higher k_{ro} (Figure 6-47 (b)). Also, if the capillary entry pressures are ignored in the process of updating the pressure field, there is no counter-current flow in the low rate cases and we are able to obtain similar RP curves under two trapping mechanisms again and more oil will be displaced compared with the simulations considering P_c in pressure solver (Figure 6-47 (c)).

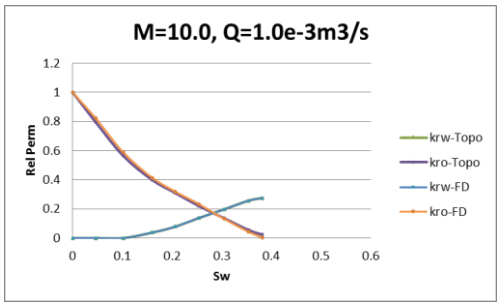

(a) high-rate

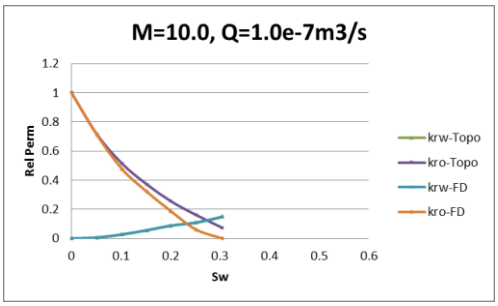

(b) low-rate

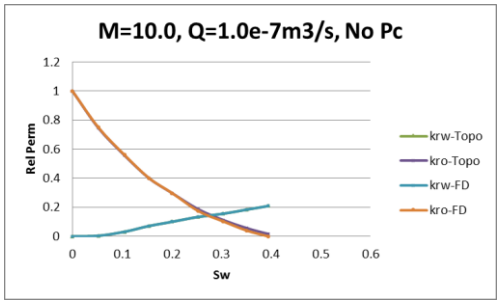

(c) low-rate, no P_c in pressure solver

Figure 6-47 Relative Permeability curves in 3-D dynamic network: topologically trapping (Topo) vs flow-direction trapping (FD). ***M=10.0***.

6.4 Summary and Conclusions

This chapter reviewed the Jones and Roszelle method, which was subsequently used by our model to obtain the dynamic relative permeability curves. In line with 2D simulations described in Chapter 5, we have run some 3D, 20*20*20 simulations to study unsteady-state relative permeabilities under different conditions. Then by comparing the dynamic RP curves with the corresponding quasi-static relative permeabilities, we concluded that the investigated parameters have different influence on the quasi-static and dynamic relative permeabilities. The main conclusions are summarised in Table 6-2.

Table 6-2 Parameters and their influence on SS and USS results

	SS	**USS**
$\lambda\uparrow$	*NA*	↑
$q\uparrow$	*NA*	↓
$\mu_o\uparrow$	→	*
$r_{mean}\uparrow$	→	↑
$l\uparrow$	→	↓
$\sigma_{ow}\uparrow$	→	↑
$C_w\uparrow$	↓	↓
$\theta\uparrow$	↓	*
Scalene	↑	*
$Z\uparrow$	↑	*

NA means the related parameter is not applicable in the quasi-static model; as the parameters in left column increase, ↑ means more film-swelling can be observed, ↓ means less film-swelling and snap-off show in the results, → means no influence, *viz.* the filling results and relative permeabilities are independent from the current quantity; * means the influence is non-monotonic due to opposing effects between λ and $R_{w\text{-}o}$.

Then, another technique to obtain quasi-static relative permeabilities of the dynamic process was introduced. Although the same technique was applied on quasi-static model and dynamic model to obtain the corresponding RPs, differences could still be observed, which confirmed that data-interpretation technique was not the only source of the observed differences. Because of the different model assumptions, filling regimes of these two models were essentially different from each other. Selected case to check the validity of dynamic model was also briefly introduced.

7 Conclusions

7.1 Pore-scale Network Models (PNM): Quasi-static and Dynamic Model

In order to explain and model observed experimental differences between steady-state (SS) and unsteady-state (USS) oil/water relative permeabilities, we studied two-phase flow in porous media in this thesis through an improved quasi-static model and a novel dynamic model.

The quasi-static *MixWet* model of McDougall and Sorbie (1994, 1995) is modified to implement angular pores with films: formulae of important parameters (cross section area, area occupied by wetting phase in corners, conductance, capillary entry pressure) of angular pores were included and more detailed film behaviours (swelling, shrinking, and trapping) were simulated in each displacing cycle. Pore filling in quasi-static model is controlled entirely by capillary forces and based on the invasion percolation theory: displacement occurs in the descending/ascending order of pore size, considering trapping.

The new dynamic pore-scale network model concentrates on simulating 2-phase displacement during water imbibition with specific intra-pore bulk and film behaviours – piston-like displacement, snap-off, coupling of bulk and film. In line with the three filling mechanisms, more complicated pore-level fluids configurations are simulated: careful management of pore conductance, local water flow and time step are included in this dynamic model. Through a newly proposed dynamic switch λ and including capillary entry pressure into the process of updating pressure field and local flow rate, this model is able to simulate the rate-dependent *local* competition between capillary forces and viscous forces under different conditions; and confirm that the *pore-scale* primary filling mechanism is determined by the dominant force (piston-like displacement under viscous forces, and snap-off because of capillary forces), which will further determine the *global* filling regimes. Furthermore, sufficient water supply is also crucial for a particular pore to be filled: at each node, the upstream spare water is distributed to swell wetting films in downstream pores. More advanced trapping mechanism based on the specific flow direction is also introduced. Then the Jones & Roszelle method is used to obtain the dynamic relative permeabilities.

7.2 Summary of Results

Multiphase flow in porous media, especially the competition between capillary forces and viscos forces, is characterised by two parameters: viscosity ratio (M) and capillary number (C_a). As the supplements of M and C_a, we introduced the local switch parameter (λ) and the indicator of film-swelling potential ($R_{w\text{-}o}$) to describe the two-phase flow in dynamic water imbibition. The above parameters (λ, C_a, M) have no influence on the steady-state permeabilities, but they determine the filling regime and resulting RPs of unsteady-state simulations:

1. In dynamic model, the value of λ determines the local competition between capillary forces and viscous forces, as well as the distribution of invading water. The value of local switch is updated automatically and rate-dependent, but in order to study the explicit influence of λ, our model also allows the switch to be assigned with constant value. Compared against the λ=0.0 (bulk displacement only) model, the λ=1.0 (purely snap-off) case has more oil trapping and worse oil production (and so k_{ro} is reduced). However, the active wetting films in λ=1.0 case increase the water relative permeability.
2. Piston-like displacement is the primary filling mechanism at high flow rates ($C_a \sim O(10^{-1})$), while at low rates ($C_a \sim O(10^{-5})$), more snap-off will be observed (principally in the smaller pores) and result in worse oil recovery. At intermediate rates (($C_a \sim O(10^{-3})$)), water will displace oil through a balance of both mechanisms. At low injection rate, bulk oil will be trapped in pores displaying counter-current flow (due to the current oil trapping algorithm), which will result in pathologically long fingers and low oil production.
3. In the dynamic model, different viscosity ratios will lead to various filling regimes. At higher flow rates, more viscous invading phase ($M<1.0$) will stabilize the front, while if $M>1.0$, viscous fingering will be observed. At intermediate and low flow rates, except for certain filling regimes, different levels of snap-off can also be found between cases with different viscosity ratios: in cases with unstable viscosity ratio ($M>1.0$), water can flow faster along the wetting films and more snap-off occurs.

   The S_w range after water breakthrough determines how much RP information can be derived from the corresponding simulation. It is evident that when viscous fingering occurs, then this results in earlier water breakthrough and a prolonged period of two phase displacement - this has some merit in being

"helpful" for extending the saturation range over which RP can be measured compared with the *M=0.1* and *M=1.0* cases. However, viscous fingering is also a main issue of unsteady-state experiments measuring relative permeability in heavy-oil system and leads to the differences observed in the SS and USS RPs.

From the parametric sensibilities study conducted in this thesis, it can be concluded that the investigated properties have different influences on SS and USS relative permeabilities. Note that during the parametric sensitivities study, simulations are generally conducted with *M=10.0*. This is due to the fact that, with unfavourable viscosity ratio, wetting films are more sensitive to the alteration the investigated parameters.

- The following parameters were found to have no influence on the quasi-static relative permeabilities, but they can affect the results in dynamic imbibition:
    1. The local balance between capillary and viscous forces is proportional to the cube of the pore radius, and so more bulk displacements (smaller λ) should be expected in networks characterised by a smaller r_{mean}. However, with the same water volume in corners, $R_{w\text{-}o}$ has an opposing effect: a *smaller* r_{mean} will result in a higher $R_{w\text{-}o}$ which *boosts* film-swelling. From the results presented above, the influence of the local switch appears to dominate the filling results. Higher levels of snap-off in the model with larger r_{mean} result in less oil production, limiting the oil permeability and enhancing the k_{rw}.
    2. Larger interfacial tension (σ), by encouraging film-swelling and snap-off in intermediate-rate floods, reduces oil relative permeability.
    3. The initial water saturation in the network cannot cause any differences between quasi-static RP curves (except for the starting S_w). However, it can affect the dynamic relative permeabilities considerably by providing the invading water better pathways, especially in the cases with initial water-filled pores, which result in higher k_{rw}, and lower k_{ro} (due to the higher level of oil-trapping). In the extremely low-rate case, the wetting film that is present in the network can connect the open pores and, as a result, the long thin fingers predicted originally (because of counter-current flow) in dry systems are suppressed.
- The following factors can affect both the SS and USS relative permeabilities:

1. In a quasi-static model, the shifting of RP curves in systems with various pore shapes is mainly because films in each pore shape have a different ability to swell and affect local water saturation. Hence, scalene-triangular (ST) pores have larger S_w increment than the equilateral-triangular (ET) pores.

   In dynamic models, due to the opposing effects between λ and $R_{w\text{-}o}$, the influence of pore shape (ST and ET) is non-monotonic but is strongly coupled to flow rate, viscosity ratio and other factors.
2. In the quasi-static model, as θ increases, RP curves are expected to move to the left since, at the same radius level, pores with a higher contact angle have less water in their corners.

   If θ increases in the dynamic model, the influence of increasing mobility of wetting films offsets the decreasing local switch; hence the influence of contact angle is non-monotonic as well: a system with $\theta=30^o$ can produce more oil than the $\theta=0^o$ base case because of the resulting enhancement of more piston-like displacements. When contact angle is 50^o, the films in the system are highly active because of the near-zero S_1 and the fact that the permeability of the oil phase is limited. For the $\theta=60^o$ case, only piston-like displacement is possible and the oil phase has the highest mobility.
3. Radius range has negligible impact on the force balance and filling mechanism competition in dynamic water flooding, but it determines the shape of viscous fingers in the high-rate cases with unstable viscosity ratio ($M>1.0$). However, in quasi-static model, snap-off will be effectively suppressed in the case with narrower radius range and the water-filled pores will make larger contribution to the global water saturation due to their larger pore volumes
4. The resistance of the solid, C_w, hardly affects the quasi-static k_{ro} but reduces the k_{rw} slightly as it increases. However, in the dynamic model, increasing C_w can clearly help the oil-phase to flow by reducing the extent of film swelling and snap-off.
5. In high-rate floods, the possible water paths will be reduced in less connected networks. This will result in more severe oil-trapping and lower oil recovery which is consistent with the quasi-static results. In low-rate cases, however, the situation may be reversed, where a lower coordination

number (Z) also breaks the connectivity of the wetting films, thus making it more difficult for them to snap-off.

7.3 Conclusions

From this work, the following conclusions can be drawn:

1. The observed differences between RPs of quasi-static model and dynamic model in this thesis can be partially explained by the fact that these two models apply different techniques to obtain the relative permeabilities. Especially in the dynamic model, assumptions of Buckley-Leverett theory can be easily violated in low-rate cases (which are capillary forces dominated) and high-rate cases with unfavourable ratio (viscous fingering effect). Furthermore, due to different model assumptions, these two models have fundamental differences in pore filling sequences, dominant forces, and oil trapping mechanisms. Therefore, agreement between RPs of these two models can hardly be seen.
2. Quasi-static and dynamic relative permeabilities have different sensitivities to the investigating parameters:
    - Quasi-static simulations are free from the influence of flow rate (Q) and viscosity ratio (M), while these two parameters have crucial impact on filling regimes and relative permeabilities of dynamic simulations.
    - Wetting films in systems with *M=10.0* are more sensitive (compared with *M=0.1* and *M=1.0* cases) to the alteration of studied parameters. Simulations with unfavourable viscosity ratios can also have longer period of two-phase flow at the system outlet after water breakthrough and provide more RP information. Therefore, the viscous unstable displacements are useful in the parametric sensitivities studies.
    - Mean radius (r_{mean}), interfacial tension (σ), initial water saturation (S_{wi}) have no influence on quasi-static simulations, but will affect dynamic displacements and the corresponding relative permeabilities.
    - Pore shape, contact angle (θ), radius range (r_{max}, r_{min}), coordination number (Z) have impact on both quasi-static and dynamic relative permeabilities, but due to the complexity of dynamic displacements, the corresponding influences are generally non-monotonic and strongly coupled to other conditions.

7.4 Future Works

The two model developed in the thesis have proven to be useful modelling tools for simulating two-phase flows in porous media, explaining and modelling observed experimental differences between steady-state (SS) and unsteady-state (USS) oil/water relative permeabilities. However, there are a number of assumptions made in these two models that can be relaxed in the future models:

- In water imbibition (quasi-static and dynamic), we do not currently consider the 'sandwich' situation, in which small amount of oil may exist between the corner water and the newly invading bulk water – we allow these pores to become fully-water-filled instead.
- Contact angle is assumed to be uniform within a particular pore, and the advancing and receding contact angle are not distinguished specifically.

  The simulations so far are conducted in water-wet network with constant or distributed contact angle within 0^o to 90^o, the inclusion of oil-wet pores will require some more coding and the mixed-wet system may be simulated in the future.
- This model only considered the displacement in purely water-wet systems (with constant or distributed contact angle between 0^o to 90^o), effect of wettability alteration (ageing) after primary drainage needs to be considered in the future work.
- The resistance factor of solid, C_w, is initially assumed to be 100; and in the later corresponding sensitivity study, the values of C_w are still assumed to be constant throughout the system. This can be relaxed later when value of C_w are determined by the specific conditions (contact angle, corner geometry and boundary condition) as estimated by Ransohoff and Radke (1988) and Zhou et al. (1997).
- In the intermediate state after the *AMs* merge with each other, water in the central ring area has a very high conductance compared with the water films. Wetting films at this stage are highly unstable, the calculation of their conductance is based on our assumption, which may be verified or corrected in the future work.
- For simplicity, the local capillary entry pressure is included into the calculation of local flow rate in pores with bulk menisci, while the local capillary pressure

based on the thickness of wetting film may be more physical, the resulting difference will be studied in later work.

- The current form of the switching parameter represents the linear relationship between capillary forces and viscous forces, which is able to correctly reproduce the filling regimes under different conditions. To validate or explore the more physical expression of λ, micromodel experiments can be performed later to look at the distribution of incoming water and occurrence of snap-off or pore filling within a single element under various conditions.
- This dynamic model doesn't consider the oil ganglia movement and retreating bulk menisci in dynamic model, bulk oil will be trapped in these two situations – this treatment may not be physical and exaggerate the oil trapping. But in later work, this restriction can be relaxed through a modified pressure solver.
- Our two PNM models concentrate on piston-like displacement, snap-off and the coupling of bulk and film (dynamic model). Another filling mechanism called pore body filling (I_z) can also be observed in water imbibition.
- The existence of connate water is proven to be very useful to eliminate the unrealistic fingering and is closer to the actual experiments measuring unsteady-state relative permeabilities. Future simulations should start with connate water.
- The technique of selecting the middle section should be applied in the future dynamic simulations, especially in the low rate cases, to eliminate the capillary end effect.
- Furthermore, this model can be adapted to the network extracted from the 3D representation of actual porous media. One task is to match the coordination number since the maximum Z in our lattice model is only six, which may be smaller than the typical number between 3 and 8. Also, out regular lattice model is composed of pore elements and volumeless nodes, which is quite different from the "pore and throat" structure in the unstructured network.
- Due to the limited time of this study, the dynamic model in this thesis has not been numerically validated. The comparison between dynamic and quasi-static simulations with only piston-like displacement can be used to check the validity of our dynamic model, if the assumption about mobile oil ganglia and counter-current flow is relaxed. Future simulations in the more physical, unstructured networks can also be used to validate the model by comparing the resulting production data and relative permeabilities with the experimental data.

Biography

Adler, P.M., Jacquin, C.G., Quiblier, J.A. (1990). Flow in simulated porous-media. *International Journal of Multiphase Flow* 16 (4), 691 – 712

Aker, E., K. J. Maloy, A. Hansen, and G. G. Batrouni (1998). A two-dimensional network simulator for two- phase flow in porous media. *Transport in Porous Media*, 32:163–186.

Aker, E., A. Hansen, and K. Maloy (2000). A numerical study of capillary and viscous drainage in porous media. Recent Research Developments. *Fluid Dynamics*, 3:45–65.

Al-Gharbi, M. (2004). Dynamic Pore-Scale Modelling of Two-Phase Flow, Ph.D. thesis, *Department of Earth Science and Engineering, Imperial College London*.

Al-Kharusi A. S. and M. J. Blunt (2007). Network extraction from sandstone and carbonate pore space images, *Journal of Petroleum Science and Engineering*, 56(4), 219-231.

Avraam, D. G., G. B. Kolonis, T. C. Roumelioitis, G. N. Constantinides and A. C. Payatakes (1994). Steady-state two-phase flow through planar and non-planar model porous media. *Transport in Porous Media*, 16:75–101.

Bakke, S. and P. E. Øren (1997). 3-d pore-scale modelling of sandstones and flow simulations in the pore networks. *Society of Petroleum Engineers Journal*, 2:136–149.

Bear, J. (1972). Dynamics of Fluids in Porous Media. New York: American Elsevier Publishing Company, 1st edition.

Blunt, M., and P. King (1990). Macroscopic Parameters from Simulations of Pore Scale Flow, *Physical Review A*, 42, 4780-4787.

Blunt, M. and P. King (1991). Relative permeabilities from two- and three-dimensional pore-scale network modelling. *Transport in Porous Media*, 6:407–433.

Blunt, M., M. J. King, and H. Scher (1992). Simulation and theory of two-phase flow in porous media. *Physical Review A*, 46(12):7680–7699.

Blunt, M. and H. Scher (1995). Pore-level modelling of wetting. *Physical Review E*, 52:6387–6403.

Blunt, M. (1997a). Effects of heterogeneity and wetting on relative permeability using pore level modelling. *Society of Petroleum Engineers Journal*, 2:70–87.

Blunt, M. (1997b). Pore level modelling of the effects of wettability. *Society of Petroleum Engineers Journal*, 2:494–510.

Blunt, M. J. (2001). Flow in porous media - pore-network models and multiphase flow. *Current Opinion in Colloid and Interface Science*, 6(3):197–207.

Blunt, M. J., M. D. Jackson, M. Piri, and P. H. Valvatne,(2002). Detailed physics, predictive capabilities and macroscopic consequences for pore-network models of multiphase flow. *Advances in Water Resources*, 25:1069–1089.

Bondino, I., S.R. McDougall, and G.Hamon, (2011). Pore- Scale Modelling of the Effect of Viscous Pressure Gradients During Heavy Oil Depletion Experiments, Paper SPE-144467, *Journal of Canadian Petroleum Technology*, 50(2), 45-55.

Bryant, S. and M. J. Blunt (1992). Prediction of Relative Permeability in Simple Porous-Media, *Physical Review A*, 46, 2004-2011.

Bryant, S. L., P. R. King, and D. W. Mellor (1993a). Network Model Evaluation of Permeability and Spatial Correlation in a Real Random Sphere Packing, *Transport in Porous Media*, 11, 53-70.

Bryant, S. L., D. W. Mellor, and C. A. Cade (1993b), Physically Representative Network Models of Transport in Porous-Media, *AIChE Journal*, 39, 387-396.

Bryant, S., G. Mason, and D. Mellor (1996). Quantification of spatial correlation in porous media and its effect on mercury porosimetry. *Journal of Colloid and Interface Science*, 177:88–100.

Buckley, S.E. and M.C. Leverett (1942). Mechanism of Fluid Displacement in Sands, *Trans., AIME* (1942) 146, 107.

Chaouche, M., N. Rakotomala, D. Salin, B. Xu, and Y. C. Yortsos (1994). Capillary effects in drainage in heterogeneous porous media: continuum modelling, experiments and pore network simulations, *Chem. Eng. Sci*. 49, 2447–2466.

Chen, J. D. and J. Koplik(1985), Immiscible fluid displacement in small networks, *J. Coll. Int. Sci.* 108, 304–330.

Christiansen, R. L., S. M. Howarth (1995). Literature Review and Recommendation of Methods for Measuring Relative Permeability of Anhydrite from the Salado Formation at the Waste Isolation Pilot Plant. REPORT SAND93-7074, UC-721.

Coenen J., E. Tchouparova and X. Jing (2004), Measurement parameters and resolution aspects of micro X-ray tomography for advanced core analysis, In Proceedings of International Symposium of the SCA, October (2004), SCA2004-36, Abu Dhabi, UAE.

Coker, D. A., S. Torquato, and J. H. Dunsmuir (1996). Morphology and physical properties of Fontainebleau sandstone via a tomographic analysis, *Journal of Geophysical Research-Solid Earth*, 101, 17497-17506.

Constantinides, G. N. and A. C. Payatakes (1991), A theoretical model of collision and coalescence of ganglia in porous media, *J. Coll. Int. Sci.* 141, 486–504.

Constantinides, G. N. and A. C. Payatakes (1996). Network simulation of steady-state two-phase flow in consolidated porous media, *AIChE J.* 42, 369–382.

Dahle, H. K. and M. A. Celia (1999). A dynamic network model for two-phase immiscible flow. *Computional Geosciences*, 3:1–22.

Darcy, H., Les Fontaines Publiques de la Ville de Dijon, Dalmont, Paris, 1856.

Dias, M. M. and A. C. Payatakes (1986a). Network models for two-phase flow in porous media: Immiscible microdisplacement of non-wetting fluids. *Journal of Fluid Mechanics*, 164:305–336.

Dias, M. M. and A. C. Payatakes (1986b). Network models for two-phase flow in porous media: Motion of oil ganglia. *Journal of Fluid Mechanics*, 164:337–358.

Dixit, A. B., S. R. McDougall, and K. S. Sorbie (1997). Pore-level investigation of relative permeability hysteresis in water-wet systems, proceedings of the 1997 SPE International Symposium on Oilfield Chemistry, SPE 37233, Soc. Of Petroleum Engineers, Houston.

Dixit, A. B., S. R. McDougall, and K. S. Sorbie, (1998). Analysis of relative permeability hysteresis trends in mixed-wet porous media using network models, proceedings of the 11th Symposium on Improved Oil Recovery, SPE 39656, Soc. Of Petroleum Engineers, Tulsa.

Dixit, A. B., S. R. McDougall, K. S. Sorbie, J. S. Buckley (1999) Pore-scale modelling of wettability effects and their influence on oil recovery. *SPE Reservoir Evaluation Eng* 1999;2:25–36.

Dixit, A. B., J. S. Buckley, S. R. McDougall, and K. S. Sorbie (2000). Empirical Measures of Wettability in Porous Media and the Relationship between Them Derived From Pore-Scale Modelling, *Transport in Porous Media*, *40*, 27-54.

Dong, M., I. Chatzis (1995), The imbibition and flow of a wetting liquid along a corners of a square capillary tube, *J. Colloid Interface Sci.*, 172,278.

Dong, H., M. Touati and M. J. Blunt (2007), Pore network modeling: Analysis of pore size distribution of arabian core samples, In SPE Middle East Oil and Gas Show and Conference, MEOS, Proceedings, Bahrain, Bahrain: Society of Petroleum Engineers (SPE), SPE 105156.

Dong, H. and M. J. Blunt (2009), Pore-network extraction from micro-computerized-tomography images, *Physical Review E - Statistical, Nonlinear, and Soft Matter Physics*, 80(3).

Dullien, F. A. L. (1992). Fluid Transport and Pore Structure. San Diego: Academic Press, 2nd edition.

Dunsmuir, J. H., S. R. Ferguson, K. L. D'Amico, and J. P. Stokes (1991). X-ray microtomography. A new tool for the characterization of porous media, proceedings of the 1991 SPE Annual Technical Conference and Exhibition, SPE 22860, Soc. of Petroleum Engineers, Dallas.

Fatt, I., (1956a). The network model of porous media I. Capillary pressure characteristics, *Trans AIME*, 207, 144-159.

Fatt, I., (1956b). The network model of porous media II. Dynamic properties of a single size tube network, *Trans AIME*, 207, 160-163.

Fatt, I., (1956c). The network model of porous media III. Dynamic properties of networks with tube radius distribution, *Trans AIME*, 207, 164-181.

Fenwick, D. H. and M. J. Blunt (1998). Three-dimensional modeling of three phase imbibition and drainage. *Advances in Water Resources*, 21(2):121–143.

Finney, J.L. (1970). Random packings and structure of simple liquids. 1. Geometry of random close packing, Proc. R. Soc. London Ser. A—Math. *Phys. Sci.* 319 (1539) 479–493.

Finney, J.L. (1970). Random packings and structure of simple liquids. II. The molecular geometry of simple liquids, Proc. R. Soc. London Ser. A—Math. *Phys. Sci.* 319 (1539) 493–495.

Gawish, A. et al. (2008). Relative permeability curves for high pressure, high temperature conditions. *Oil and Gas Business*.

Geffen, T.M., W.W.Owens, D.R.Parish and R.A.Morse (1951). Experimental investigation of factors affecting laboratory relative permeability measurements. *Trans. AIME*, 192: 99-110.

Haghighi, M., B. Xu, and Y. C. Yortsos (1994). Visualization and simulation of immiscible displacement in fractured systems using micromodels: I. Drainage, *J. Coll. Int. Sci.* 166, 168–179.

Heiba, A. A., M. Sahimi, L. E. Scriven, and H. T. Davis (1992). Percolation theory of two-phase relative permeability. *SPE Reservoir Engineering*, 7:123–132.

Held, R. J. and M. A. Celia (2001a). Modelling support of function relationships between capillary pressure, saturation, interfacial area and common lines. *Advances in Water Resources*, 24:325–343.

Hoshen, J. and R. Kopelman (1976). Percolation and cluster distribution. I. Cluster multiple labelling technique and critical concentration algorithm. *Phys. Rev. B* 14/8, 3438.

Hughes, R. G. and M. J. Blunt (2000). Pore scale modelling of rate effects in imbibition. *Transport in Porous Media*, 40:295–322.

Hui, H. and M. J. Blunt (2000). Effect of wettability on three-phase flow in porous media. *Physical Chemistry B,* 104:3833–3845.

Idowu, N. A. (2009). Pore-scale modelling: stochastic network generation and modelling of rate effects in waterflooding. PhD thesis. *Department of Earth Science and Engineering, Imperial College London*.

Jerauld, G. R., J. C. Hatfield, L. E. Scriven, and H. T. Davis (1984a). Percolation and Conduction on Voronoi and Triangular Networks - a Case-Study in Topological Disorder, *Journal of Physics C: Solid State Physics, 17,* 1519- 1529.

Jerauld, G. R., L. E. Scriven, and H. T. Davis (1984b). Percolation and Conduction on the 3d Voronoi and Regular Networks - a 2nd Case-Study in Topological Disorder, *Journal of Physics C: Solid State Physics, 17,* 3429-3439.

Jerauld, G. R. and S. J. Salter (1990). The effect of pore-structure on hysteresis in relative permeability and capillary pressure: Pore level modelling. *Transport in Porous Media*, 5:103–151.

Jiang Z., K. Wu, G. Couples, M.I.J. Van Dijke, K.S. Sorbie and J. Ma (2007), Efficient extraction of networks from three-dimensional porous media, *Water Resources Research,* 43(12).

Joekar-Niasar, V., S. M. Hassanizadeh (2012), Analysis of Fundamentals of Two-Phase Flow in Porous Media using Dynamic Pore-Network Models; A Review, *Journal of Critical Reviews in Environmental Science and Technology*, doi: 10.1080/10643389.2011.574101.

Johnson, E. F., D. P. Bossler and V. O. Naumann (1959). Calculation of Relative Permeability from Displacement Experiments, *Trans.*, AIME, 1959, 216, 370-372.

Jones, S. C. and W.O. Roszelle (1978). Graphical Techniques for Determining Relative Permeability from Displacement Experiments, *JPT* (May 1978) 807-17; *Trans.*, AIME, 265.

Kikuchi, M.M., C.C. Branco, E.J. Bonet, R.M. Zanoni, C.M. Paiva (2005). Water Oil Relative Permeability Comparative Study: Steady Versus UnSteady State. *International Symposium of the Society of Core Analysts*, Toronto, Canada, 21-25 August 2005, SCA2005-77.

Knudsen, H. A., E. Aker, and A. Hansen (2001). Bulk flow regime and fractional flow in 2d porous media by numerical simulations. *Transport in Porous Media*, 47:99–121.

Knudsen, H. A. and A. Hansen (2002). Relation between pressure and fractional flow in two-phase flow in porous media. *Physical Review E*, 65:056310.

Koplik, J. and T. Lasseter (1985). Two-phase flow in random network models of porous media. *Society of Petroleum Engineers Journal*, 25:89–100.

Kovscek, A. R., H. Wong, and C. J. Radke (1993). Pore-level scenario for the development of mixed wettability in oil reservoirs. *AIChE Journal*, 39(6):1072–1085.

Lenormand, R., C. Zarcone, and A. Sarr (1983). Mechanisms of the displacement of one fluid by another in a network of capillary ducts. *Journal of Fluid Mechanics*, 135:337–353.

Lenormand, R. and C. Zarcone (1984). Role of roughness and edges during imbibition in square capillaries. Proceedings of the 59th Annual Technical

Conference and Exhibition of the Society of Petroleum Engineers of AIME, SPE 13264, Houston, Texas.

Lenormand, R., C. Zarcone and E. Touboul (1988), Numerical models and experiments on immiscible displacements in porous media, *J. Fluid Mech*. 189, 165–187.

Lenormand, R. (1990), Liquids in porous media, *J. Phys. Condens. Matter*, 2(S), SA79.

Lindquist, W. B., S. -M. Lee, D. A. Coker, K. W. Jones and P. Spanne (1996). Medial axis analysis of void structure in three-dimensional tomographic images of porous media, *J. Geophys. Res.*, 101(B4), 8297-8310.

Lindquist, W. B. and A. Venkatarangan (1999), Investigating 3D geometry of porous media from high resolution images, *Physics and Chemistry of the Earth Part a-Solid Earth and Geodesy*, 24(7), 593-599.

Love, P. J., J. B. Maillet and P. V. Coveney (2001). Three-dimensional hydrodynamic lattice-gas simulations of binary immiscible and ternary amphiphilic flow through porous media. *Physical Review E*, 64:061302.

Maini, B., G. Coskuner, K. Jha (1990), A comparison of steady-state and unsteady-state relative permeabilities of viscous oil and water in Ottawa sand. J Can Pet Technol 29 (2). PETSOC-90-02-02.

Maloney, D., and K. Doggett (1995). Advances in steady- and unsteady-state relative permeability measurements and correlations. FY 1995. Report NIPER/BDM-0160 prepared under DOE contract DE-AC22-94PC91008, July 1995, pp. 21–28.Man, H. N. and X. D. Jing (1999). Network modeling of wettability and pore geometry effects on electrical resistivity and capillary pressure. *Journal of Petroleum Science and Engineering*, 24:255–267.

Man, H. and X. Jing (2000). Pore network modelling of electrical ressistivity and capillary pressure characteristics. *Transport in Porous Media*, 41:263–283.

Man, H. and X. Jing (2001). Network modelling of strong and intermediate wettability on electrical resistivity and capillary pressure. *Advances in Water Resources*, 24:345–363.

Marle, C. M. (1981). Multiphase Flow in Porous Media. Paris: Imprimerie Louis-Jean, 1st edition.

Mayer, R.P. and R.A. Stowe (1965). : "Mercury Porosimetry-Breakthrough Pressure for Penetration between Packed Spheres", *J. Colloid and Interface Science*, 20, 893.

McDougall, S.R. and K.S. Sorbie (1993): "The Combined Effect of Capillary and Viscous Forces on Waterflood-Displacement Efficiency in Finely Laminated Porous Media," paper SPE 26659 presented at the 1993 SPE Annual Technical Conference and Exhibition, Houston, 3–6 October.

McDougall, S. (1994), The application of network modelling techniques to steady-and-unsteady-state multiphase flow in porous media. PhD dissertation, *Heriot-Watt U.*, Edinburgh

McDougall, S. (1994), Manual Version 2, in house manual, introducing the user interface and important properties of the *MixWet* model.

McDougall, S.R., K.S. Sorbie (1995). The impact of wettability on waterflooding: pore-scale simulation. SPE *Reservoir Engineering* August, 208– 213.

McDougall, S. R., P. A. Salino and K. S. Sorbie (1997): "The effect of interfacial tension upon gasoil relative permeability measurements: interpretation using pore-scale models", SPE Annual Tech. Conf. and Exhib., SPE, San Antonio, TX (1997), SPE 38920.

Mogensen, K. and E. Stenby (1998). A dynamic pore scale model of imbibition. *Transport in Porous Media*, 32:299–327.

Mohanty, K. K. and S. J. Salter (1982a). Multiphase flow in porous media i: Macroscopic observation and modelling. Proceedings of the 57th Annual Fall Technical Conference of SPE-AIME, SPE 11018, New Orleans.

Mohanty, K. K. and S. J. Salter (1982b). Multiphase flow in porous media ii: Pore-level modelling. Proceedings of the 57th Annual Fall Technical Conference of SPE-AIME, SPE 11017, New Orleans.

Mohanty, K. K. and S. J. Salter (1983). Multiphase flow in porous media iii: Oil mobilization, transverse dispersion and wettability. Proceedings of the 58th Annual Fall Technical Conference and Exhibition, SPE 12127, San Francisco, CA.

Mohanty, K. K. and A. E. Miller (1991). Factors influencing unsteady relative permeability of a mixed-wet reservoir rock. *SPE form. Eval.*, **6**, 349-358.

Muskat, M. (1937). The flow of homogeneous fluids through porous media. New York, McGraw-Hill Book Co., Inc..

Muskat, M., and M. W. Meres (1940). Reflection and transmission coefficients for plane waves in elastic media. *Geophysics*, 5, pp. 115 - 148.

Muskat, M. (1981). Physical Principles of Oil Production. International Human Resources Development Corporation, Boston, 2nd edition.

Nguyen, V. H., A. P. Sheppard, M. A. Knackstedt, W. V. Pinczewski (2006). The effect of displacement rate on imbibition relative permeability and residual saturation. *Journal of Petroleum Science and Engineering* 52 (2006) 54-70.

Nordhaug, H. F., M. Celia, and H. K. Dahle (2003). A pore network model for calculation of interfacial velocities. *Advances in Water Resources*, 26:1061–1047.

Odeh, A.S., B.J. Dotson (1985). A method for reducing the rate effect on oil and water relative permeabilities calculated from dynamic displacement data. *J. Pet. Technol.* 2051–2058.

Okabe, H., and M. J. Blunt (2004), Prediction of permeability for porous media reconstructed using multiple-point statistics, *Phys. Rev. E.*, 70, 066135.

Okabe, H., and M. J. Blunt (2005), Pore space reconstruction using multiplepoint statistics, *J. Pet. Sci. Eng.*, 46, 121 – 137.

Okabe H. and M.J. Blunt (2007). Pore space reconstruction of vuggy carbonates using microtomography and multiple-point statistics, *Water Resour. Res.*, 43(12), W12S02.

Øren, P.-E., S. Bakke, and O. J. Avntzen (1998). Extending predictive capabilities to network models. *Society of Petroleum Engineers Journal*, 3:324–336.

Øren P.E. and S. Bakke (2002), Process based reconstruction of sandstones and prediction of transport properties, *Transport in Porous Media*, 46(2-3), 311-343.

Øren P.E. and S. Bakke (2003), Reconstruction of Berea sandstone and pore-scale modelling of wettability effects, *Journal of Petroleum Science and Engineering*, 39(3-4), 177-199.

Osoba, J. S. et al. (1951). Laboratory measurements of relative permeability, *Trans.*, AIME, Vol. 192 (1951), pp. 47-56.

Pereira, G., W. Pinczewski, D. Chan, L. Paterson, and P. Øren (1996). Pore-scale network model for drainage dominated three-phase flow in porous media. *Transport in Porous Media*, 24(2):157–166.

Piri, M. and M. J. Blunt (2002). Pore-scale modeling of three-phase flow in mixed-wet systems. Proceedings of the SPE Annual Meeting, SPE 77726, San Antonio, Texas.

Princen, H. M. (1969a). Capillary Phenomena in Assemblies of Parallel Cylinders I. Capillary Rise between Two Cylinders, *J. Colloid and Interface Science*, 30, 60.

Princen, H. M. (1969b). Capillary Phenomena in Assemblies of Parallel Cylinders II. Capillary Rise in Systems with More Than Two Cylinders, *J. Colloid and Interface Science*, 30, 359.

Princen, H. M. (1970): Capillary Phenomena in Assemblies of Parallel Cylinders III. Liquid Columns between Horizontal Parallel Cylinders, *J. Colloid and Interface Science*, 34, 171.

Quiblier, J. A. (1984). A new three-dimensional modeling technique for studying porous-media. *Journal of Colloid and Interface Science* 98 (1), 84 – 102.

Ransohoff, T. C. and C. J. Radke (1988). Laminar flow of a wetting liquid along the corners of a predominantly gas-occupied noncircular pore, *J. Coll. Int. Sci.* 121, 392–401.

Raoof, A. and S. M. Hassanizadeh (2012). A new formulation for pore-network modelling of two-phase flow. *WATER RESOURCES RESEARCH*, VOL. 48, W01514.

Rapoport, L.A., W.J. Leas (1953). Properties of linear waterfloods. *Trans. AIME* 198, 139.

Roberts, A. P. (1997). Statistical reconstruction of three-dimensional porous media from two-dimensional images. *Physical Review E* 56 (3), 3203 – 3212.

Ryazanov, A., Pore-scale network modelling of residual oil saturation in mixed-wet system. PhD thesis. *Heriot-Watt University*, Edinburgh.

Ryazanov A.V., M. I. J. van Dijke and K. S. Sorbie (2009). Two-Phase Pore-Network Modelling: Existence of Oil Layers During Water Invasion. *Transport Porous Media*, 80, 2009, 79-99.

Ryazanov, A., K. S. Sorbie and M. I. J. van Dijke (2014). Structure of residual oil as a function of wettability using pore-network modelling. *Advances in Water Resources*. 63, p. 11-21 11 p.

Skauge, A., Thorsen, T., Sylte, A., 2001. Rate selection for waterflooding of intermediate wet cores. In: Proceedings of the International Symposium of the Society of Core Analysts, Edinburgh, Scotland, 17–19 September. Paper SCA 2001-20.

Sheppard A. P., R. M. Sok and H. Averdunk (2005). Improved pore network extraction methods, In Proceedings of International Symposium of the Society of Core Analysts, Toronto, Canada, SCA2005-20.

Sheppard A. P., M. Sok, H. Averdunk, V. Robins and M. Saadatfar (2006). Analysis of Rock microstructure using high-resolution x-ray tomography, In Proceedings of International Symposium of the Society of Core Analysts, Trondheim, Norway, SCA2006-26.

Silin D. B., G. Jin and T. W. Patzek (2003), Robust Determination of the Pore Space Morphology in Sedimentary Rocks, In SPE Annual Technical Conference and Exhibition, Denver, Colorado: Society of Petroleum Engineers, SPE 84296.

Silin D. and T. Patzek (2006). Pore space morphology analysis using maximal inscribed spheres, *Physica A: Statistical and Theoretical Physics*, 371(2), 336-360.

Singh, M. and K. K. Mohanty (2003). Review: Dynamic modelling of drainage through three-dimensional porous materials. *Chemical Engineering Science*, 58:1–18.

Sorbie, K. S. and P. Salino. A (2009). Theoretical Study of the Possible Causes of Rate Dependency in Steady-State (SS) and Unsteady-State (USS) Relative Permeabilities. BP confidential report.

Spanne, P., J. F. Thovert, C. J. Jacquin, W. B. Lindquist, K. W. Jones, and P. M. Adler (1994). Synchrotron Computed Microtomography of Porous-Media - Topology and Transports, *Physical Review Letters*, 73, 2001-2004.

Touboul, E., R. Lenormand, and C. Zarcone (1987). Immiscible displacements in porous media: Testing network simulators by micromodel experiments. Proceedings of the 62th Annual Technical Conference and Exhibition of the Society of Petroleum Engineers of AIME, SPE 16954, Dallas, TX.

Valavanides, M. S., G. N. Constantinides, and A. C. Payatakes (1998). Mechanistic model of steady-state two-phase flow in porous media based on ganglion dynamics. *Transport in Porous Media*, 30:267–299.

Valavanides, M. S. and A. C. Payatakes (2001). True-to-mechanism model of steady-state two-phase flow in porous media, using decomposition into prototype flows. *Advances in Water Resources*, 24:385–407.

Valvatne, P. H.. (2004). Predictive pore-scale modelling of multiphase flow. PhD thesis, *Imperial U., London.*

Van der Marck, S. C., T. Matsuura, and J. Glas (1997). Viscous and capillary pressure during drainage: Network simulations and experiments. *Physical Review E*, 56(5):5675–5687.

Van Dijke, M.I.J., K. S. Sorbie and S. R. McDougall (2001). Saturation-dependencies of three-phase relative permeabilities in mixed-wet and fractionally-wet systems, *Adv. Water Resour.*, 24, 2001, 365-384.

Van Dijke, M.I.J. and K. S. Sorbie (2002). Pore-scale network model for three-phase flow in mixed-wet porous media, *Phys. Rev. E.*, 66, 2002, 046302.

Van Dijke, M.I.J., M. Lago, K. S. Sorbie, and M. Araujo (2004). Free energy balance for three fluid phases in a capillary of arbitrarily shaped cross-section: capillary entry pressures and layers of the intermediate-wetting phase, *J. Colloid Interface Sci.*, 277, 2004, 184-201.

Van Dijke M. I. J. and K. S. Sorbie (2006). Existence of fluid layers in the corners of a capillary with non-uniform wettability, *J. Coll. Int. Sci.*, 293(2), 455-463.

Van Wachem, B. G. and A. E. Almstedt (2003). Methods for multiphase computational fluid dynamics. *Chemical Engineering Journal*, 96:81–98.

Vizika, O., D. G. Avraam, and A. C. Payatakes (1994). On the role of the viscosity ratio during low-capillary-number forced imbibition in porous media. *Journal of Colloid and Interface Science*, 165:386–401.

Voronoi, G. (1908). Nouvelles applications des paramètres continus à la théorie des formes quadratiques. *Journal für die Reine und Angewandte Mathematik* 133 (133): 97–178. doi:10.1515/crll.1908.133.97

Weisbrod, N., M. R. Niemet, J. S. Selker (2002). Imbibition of saline solutions into dry and prewetted porous media, *Advances in Water Resources*, 25 (2002) 841–855.

Welge, H.J. (1952). A Simplified Method for Computing Oil Recovery by Gas or Water Drive, *Trans., AIME*, 195, 91–98.

Wu K.J., M.I.J. Van Dijke, G.D. Couples, Z.Y. Jiang, J.S. Ma, K.S. Sorbie, J. Crawford, I. Young and X.X. Zhang (2006). 3D stochastic modelling of heterogeneous porous media - Applications to reservoir rocks, *Transport in Porous Media*, 65(3), 443-467.

Zhou, D., M. J. Blunt and F. M. Orr, Jr. (1997). Hydrocarbon drainage along corners of noncircular capillaries, *J. Coll. Int. Sci.* 187, 11–21.